

PROBING MODEL-INDEPENDENT MODIFIED GRAVITY AND AXION DARK MATTER

A THESIS SUBMITTED TO THE UNIVERSITY OF MANCHESTER
FOR THE DEGREE OF DOCTOR OF PHILOSOPHY
IN THE FACULTY OF ENGINEERING AND PHYSICAL SCIENCES

January 2023

By
Sankarshana Srinivasan
School of Natural Sciences

Contents

Abstract	10
Declaration	12
Copyright	13
Acknowledgements	15
Supporting Publications	17
1 Introduction	19
1.1 The current picture	23
1.2 Shortcomings of Λ CDM	29
1.2.1 Nature of dark matter and dark energy	29
1.2.2 Causal contact, flatness and generation of initial conditions	30
1.2.3 Tensions in the data, new physics?	32
1.3 Introduction to modified gravity	33
1.3.1 Why modify gravity?	34
1.3.2 The landscape of models	35
1.3.3 Parameterisations and observational probes	37
1.4 Axion Dark Matter	55

1.4.1	The axion as a dark matter candidate	55
1.4.2	Experimental searches	58
1.4.3	Indirect detection: Complimentary to laboratory searches	59
2	Modified Gravity Simulations	63
2.1	Introduction	65
2.2	The Post-Friedmann formalism	69
2.3	Methodology	75
2.3.1	N -body simulations	75
2.3.2	Predicting the power spectrum on non-linear scales	80
2.4	Simulation phenomenology	93
2.5	Impact on weak-lensing observables	99
2.5.1	Computing weak-lensing observables in modified gravity	99
2.5.2	Further evaluation of fitting functions	106
2.6	Conclusion	109
3	The Road to Model-Independent Forecasts	112
3.1	Introduction	113
3.2	Methodology: ReACT Validation Pipeline	115
3.2.1	Expanded suite of simulations	116
3.2.2	Concentration-mass relation	117
3.3	Results	123
3.4	Discussion and Conclusions	131
4	Spontaneous Decay of Axions to Photons	134
4.0.1	Stimulated emission	135
4.1	Signal from virialised halos	137
4.2	Telescope sensitivity estimates	147

4.2.1	Flux Density Signal	148
4.2.2	Brightness Temperature Signal	153
4.3	Optimising target objects	159
4.3.1	Maximising brightness temperature	160
4.3.2	Minimising Integration Time	166
4.4	Observational conclusions	171
4.5	Summary	175
5	Resonant Axion Signal from Pulsars	177
5.1	Axion-photon mixing	181
5.1.1	Axion Electrodynamics	181
5.1.2	Landau-Zener	184
5.1.3	Doppler broadening	194
5.2	Ray-tracing Simulations	201
5.2.1	Frequency Broadening	203
5.2.2	Effect of Gravity	204
5.2.3	Numerical Procedure	206
5.3	Ray-tracing analysis applied to data	209
5.3.1	Limits on the axion-photon coupling	210
5.3.2	Conclusions	211
6	Time-Domain Search for Axions	215
6.1	Introduction	217
6.2	Characterising signal variability	221
6.2.1	Ray-tracing simulations	221
6.2.2	Interpolation of simulation database	223
6.2.3	Fourier analysis of profiles	227
6.3	Matched Filter	229

6.3.1	Mathematical formalism	229
6.3.2	Simulated Data	230
6.4	B0834+06: The data from the catalogue	235
6.4.1	Archival Pulsar Data from JBCA catalogue	235
6.4.2	Modelling the Data	236
6.4.3	Prior on $\theta - \alpha$ plane	239
6.4.4	Searching for the signal	243
6.5	Establishing an upper limit	245
6.6	Summary and conclusion	249
7	Conclusion	253
	Bibliography	260
.1	Convergence Tests for Simulations	303
.2	Linear growth and smoothing	305
.2.1	The Linear Growth Factor	305
.2.2	Smoothing bin-transitions	306
.3	Covariant radiative transport in plasmas	309

List of Tables

1.1	The table of cosmological parameters as reported by the Planck collaboration inferred from the Planck CMB power spectrum data, CMB lensing data and BAO (Baryon Acoustic Oscillations, see [1] for more information).	26
2.1	The simulation redshift bins of equal incremental Λ CDM growth and equalised $P(k)$ at $z = 0$	76
3.1	The binning of μ in redshift in [2].	116
3.2	Redshift bins for ReACT validation	117
4.1	Table of telescope parameters for current and planned facilities	147
4.2	Typical properties that determine the total spontaneous flux expected from a virialised object	164

List of Figures

1.1	The scale factor as a function of time	24
1.2	Summary of constraints on the axion-photon plane	60
2.1	Pipeline for calculating $P(k)$	77
2.2	Visual representation of redshift bins for the equalised growth simulations	78
2.3	Constant μ test on different fitting functions	82
2.4	Comparison of fitting functions across literature using $R(k)$	87
2.5	As in fig. 2.4, but where μ has a different value from GR in one of the earlier redshift bins.	88
2.6	Table of $\chi^2 k_{\text{fail}}$ values associated to each fitting function	90
2.7	Accuracy of ReACT for different concentration-mass relations	91
2.8	Matter power spectra from simulations with equal linear growth at $z = 0$	94
2.9	Evolution of matter power spectra as a function of redshift	97
2.10	Weak-lensing spectra from simulation pipeline	101
2.11	ReACT weak-lensing prediction vs halofit	102
3.1	Λ CDM concentration-mass relation in our simulations and in ReACT	121
3.2	$R(k)$ measured from all simulations for the validation of ReACT . .	123

3.3	The variation of k_{fail} across all simulations	125
3.4	The trends in redshift for the concentration-mass amplitude . . .	127
3.5	We show the high-redshift and low-redshift regime $c(M)$ fit to our simulation data.	128
4.1	Schematic illustration of the telescope beam relative to viralised objects	138
4.2	Brightness temperature estimates for a halo as a function of surface- mass density	142
4.3	Mass within telescope beam as a function of concentration	152
4.4	Quantifying signal strength and integration times for different ob- jects as a function halo mass and beam size	159
4.5	Quantification of surface-mass density associated to telescope beam	165
4.6	Integration times for different characteristic CDM axion mass . .	167
4.7	Projected sensitivity to axion-photon spontaneous decay	172
5.1	The Landau-Zener parameter γ as a function of axion mass	192
5.2	Analytic and numerical estimate of probability of resonant axion- photon conversion as a function of axion mass	193
5.3	Parametrization of the Doppler shift on a moving, misaligned mirror.	197
5.4	Radiated power in image plane: vacuum vs. plasma	208
5.5	Exclusion limits on $g_{a\gamma\gamma}$ from ray-tracing simulations using simu- lation data	214
6.1	An interpolated library of profiles as a function of the input pa- rameters (θ, α)	222
6.2	Phase profiles of the radiated power as a function of (θ, α)	224
6.3	Fourier Analysis of phase-profiles	226

6.4	Analysing the signal-to-noise of the signal-injected data as a function of a single input parameter	231
6.5	2-dimensional signal-to-noise analysis of signal-injected data . . .	233
6.6	Radio pulsar data modelling	237
6.7	Dynamical spectra with cuts in frequency-space	238
6.8	Pulsar beam geometry and the measured pulse-profile of B0834+06	240
6.9	Constraint on $\theta - \alpha$ plane and scaling of $g_{a\gamma\gamma}$ as a function of (θ, α)	242
6.10	The distribution of SNR values in the real data and the Gaussian noise matrix	244
6.11	The filter response as a function of the interpolated matrix of (θ, α)	246
6.12	Examples of the varying time-dependence in the profiles across the parameter space	247
6.13	The derived upper limit on the axion-photon coupling using the matched filter	248
1	Λ CDM and modified gravity convergence tests	304
2	Input modified gravity linear power spectra from modified CLASS	306
3	Redshift evolution of growth factor for different smoothing parameters	307

Abstract

The nature and dark matter and dark energy represents one of the biggest unsolved problems in fundamental physics over the next few decades. In this thesis, we discuss two subjects that attempt to explain one or both of dark matter and dark energy, modified gravity and axion dark matter. In chapter 2 we present the first model-independent cosmological N -body simulations with a time-dependent effective gravitational force parameterised by a single parameter, μ that is binned in redshift. We compute structure formation observables and show that the majority of the constraining power for future surveys is contained the non-linear regime. We find that the **ReACT** formalism is most accurately able to reproduce the non-linear matter power spectrum from our simulations. In chapter 3, we validate **ReACT** across a much larger portion of the modified gravity parameter space. We show that the accuracy of **ReACT** in the non-linear regime is dependent on the amplitude of the concentration-mass relation and that one can fit for this variation with knowledge of $\mu(z)$ and the linear growth factor $D(z)$. We describe a plan for implementing **ReACT** into a Fisher pipeline in order to perform model-independent modified gravity forecasts for time-dependent binned μ .

We review the axion as a well-motivated dark matter candidate and discuss the possibility detecting axion dark matter via its coupling to the electromagnetic sector with radio telescopes. In chapter 4, we discuss how one can optimise search

strategies to detect the two-photon decay of axions to photons, with particular focus on the stimulated emission enhancement at the galactic centre. In chapters 5 and 6, we concentrate on the resonant conversion of axions to photons in neutron-star magnetospheres. In chapter 5, we compute the one-dimensional probability of conversion of axions to photons for general dispersion relations. We show that the spectral line signal is broadened due to the rotation of the magnetosphere. We also compute the full time-dependent signal profile via ray-tracing simulations that account for the lensing of the photons as they travel through the charge density of the magnetosphere and the gravitational field of the neutron star. We use these results to update the constraints on the axion-photon coupling using Very Large Array (VLA) data of the magnetar PSR J1745-2900. In chapter 6, we describe a new technique to mine radio pulsar data for the resonant signal using a matched filter. We show that the strength of this technique is in the fact that one can efficiently scan data across a wide range of frequencies for a time-dependent signal. We find that the time-dependence of the signal is suppressed in specific regions of the input parameter space, which one can constrain using a combination of modelling assumptions of the pulsar magnetosphere and measurements of the beam width. We discuss how one can derive a limit on the axion-photon coupling using this and test our pipeline on real data obtained from the Jodrell Bank catalogue on PSR B0834+06.

Declaration

No portion of the work referred to in this thesis has been submitted in support of an application for another degree or qualification of this or any other university or other institution of learning.

Copyright

- i. The author of this thesis (including any appendices and/or schedules to this thesis) owns certain copyright or related rights in it (the 'Copyright') and s/he has given The University of Manchester certain rights to use such Copyright, including for administrative purposes.
- ii. Copies of this thesis, either in full or in extracts and whether in hard or electronic copy, may be made only in accordance with the Copyright, Designs and Patents Act 1988 (as amended) and regulations issued under it or, where appropriate, in accordance with licensing agreements which the University has from time to time. This page must form part of any such copies made.
- iii. The ownership of certain Copyright, patents, designs, trade marks and other intellectual property (the 'Intellectual Property') and any reproductions of copyright works in the thesis, for example graphs and tables ('Reproductions'), which may be described in this thesis, may not be owned by the author and may be owned by third parties. Such Intellectual Property and Reproductions cannot and must not be made available for use without the prior written permission of the owner(s) of the relevant Intellectual Property and/or Reproductions.
- iv. Further information on the conditions under which disclosure, publication and commercialisation of this thesis, the Copyright and any Intellectual Property

and/or Reproductions described in it may take place is available in the University IP Policy (see <http://www.campus.manchester.ac.uk/medialibrary/policies/intellectual-property.pdf>), in any relevant Thesis restriction declarations deposited in the University Library, The University Library's regulations (see <http://www.manchester.ac.uk/library/aboutus/regulations>) and in The University's policy on presentation of Theses.

Acknowledgements

I would like to thank my supervisor Professor Richard Battye for the valuable advice, support and knowledge he has provided me over the course of my PhD. I would also like to thank my co-supervisors Dr Daniel Thomas, Dr Jamie McDonald and Dr Francesco Pace for their invaluable help, patience, guidance and support. I also thank my advisor Professor Keith Grainge for his timely meetings, kind advice and general support.

Special thanks to Nialh McCallum, Danielius Banys and Valerio Gilles for patiently converting me from a couch-potato to a regular gym rat. Your support ensured I didn't go stir crazy during lockdown and I will always cherish the memories that we have made and hopefully continue to make together.

I thank Manish Patel, Samuel Bateman, Eunseong Lee, Raoul Hidalgo Charman, Anamaria Tigan, Maxine Russi and Alex Dyson for being such great housemates. I enjoyed cooking you all Indian food, having endless conversations in the kitchen and watching films on the projector. Your company turned the house into my second home.

The Jodrell Bank Centre for Astrophysics has been an extremely supportive and lively department. I thank Tom Sweetnam, Tom Hillier, Susmita Sett, Shruti Badole, Deepika Venkattu, James Stringer, Dominic Viatic, Luke Hart, Steven

Cotteril, Edoardo Altamura for being such wonderful friends who have made the difficult times easier to handle. I have been lucky to meet some wonderful people outside of my workplace, and I would like to thank Harry Waring, Guuske Tiktak, Luna Noguera, Priya Attra, Emily Cuffin-Munday and Debra for the fun times that we have shared.

I would also like to thank Aakanksha Agrawal, for making me so happy towards the end of my time in Manchester when my stress levels were soaring and corrections were taking forever.

Finally, I thank my parents for their constant support and faith. I could not have achieved this without you!

Supporting Publications

- **Cosmological gravity on all scales. Part II. Model independent modified gravity N-body simulations**

Srinivasan, Sankarshana ; Thomas, Daniel B. ; Pace, Francesco ; Battye, Richard

Journal of Cosmology and Astroparticle Physics, Volume 2021, Issue 06, id.016, 32 pp.

Chapter 2 is based on this article.

- **Dark matter axion detection in the radio/mm waveband**

Battye, R. A. ; Garbrecht, B. ; McDonald, J. I. ; Pace, F. ; Srinivasan, S.
Physical Review D, Volume 102, Issue 2, article id.023504

Chapter 4 and first half of chapter 5 are based on this article.

- **Radio line properties of axion dark matter conversion in neutron stars**

Battye, R. A. ; Garbrecht, B. ; McDonald, J. ; Srinivasan, S
Journal of High Energy Physics, Volume 2021, Issue 09, article id. 105

Majority of second half of chapter 5 is based on this article.

- **Towards robust constraints on axion dark matter using PSR J1745-2900**

Battye, R. A. ; Darling, J. ; McDonald, J. I. ; Srinivasan, S.

Physical Review D, Volume 105, Issue 2, article id.L021305

Last part of chapter 5 is based on this article.

Chapter 1

Introduction

In the last 30 years, the field of cosmology has seen rapid progress. Einstein's theory of gravity, General Relativity (GR) [3] forms the basis of our understanding of the Universe as a whole, its evolution and its content. The solution of Einstein's equations assuming an isotropic and homogeneous universe is encoded in the Friedmann-Lemaitre-Robertson-Walker (FLRW) metric [4–7]. The FLRW metric along with the field equations of GR form the mathematical background for all of modern cosmology.

A variety of observational evidence supports the concordant model of cosmology. Observations of the Cosmic Microwave Background (CMB), which is the relic radiation from the Big Bang (the colloquial name given to the initial event that formed the Universe) have shown that the energy density of the Universe is dominated by unknown components, namely dark energy (70%) and dark matter (25%) [1]. This is supported by measurements of the accelerated rate of expansion of the Universe through ‘standard candles’, objects whose luminosity may be calculated independent of any distance measurement. The knowledge of the luminosity and its scaling with distance allows one to calculate the distance to these

objects, thereby constructing cosmological ‘distance-ladders’ [8]. This discovery led to the addition of a cosmological constant, Λ to Einstein’s equations, which could give rise to the observed accelerated rate of expansion. However, attempts to calculate Λ by summing over the vacuum contribution in Quantum Field Theory have failed to reproduce the observed value, a disagreement of several orders of magnitude dubbed the ‘Cosmological Constant Problem’ [9]. The unknown source of the cosmological constant has been given the name dark energy.

The distribution of matter across the Universe has been mapped out by galaxy surveys through observations of weak gravitational lensing, or weak-lensing which is the bending of light of by matter along the line of sight of the observer, causing a distortion or shear of the image of the galaxies [10, 11]. This has not only confirmed that the majority of the matter content of the Universe is dominated by dark matter that interacts only via gravity (hence the name cold dark matter), but has also thrown light on the clustering of matter as a function of scale. Specifically, galaxy surveys are valuable probes of redshift-space distortions (see for e.g. [12] and references within), which is an effect that describes the apparent inconsistency in the distribution of galaxies as a function of distance, in comparison to redshift. This is explained by the Doppler effect due to peculiar motions of galaxies that are gravitationally bound to galaxy clusters.

Valuable information on the nature of non-linear structure formation, i.e., the rate of formation of haloes, their masses and their density profiles has been obtained from cosmological N -body simulations. These are simulations with particle numbers ranging from $10^7 - 10^{10}$ in volumes ranging from hundreds of Mpc^3 to a few Gpc^3 . Such simulations currently represent the best sources of knowledge on how matter clusters on so-called non-linear scales, i.e., on scales where the matter overdensity becomes large [13]. The data from these simulations suggest a Universal

density profile for all haloes in the Universe, the Navarro-Frenk-White (NFW) profile (see chapter 4 for a more detailed discussion on the NFW profile).

1.1 The current picture

Combined evidence from observational probes has given rise to a clear picture of the Universe today as well as its history. In this picture, the Universe began in a so-called Big Bang, i.e., with hot, dense initial conditions followed by a period of expansion and cooling. Perturbations in the matter distribution of the Universe lead to gravitationally bound structures that collapsed to form the galaxies observed today ¹. The gravitational evolution is as described by Einstein's field equations

$$R_{\mu\nu} - \frac{1}{2}g_{\mu\nu}R + \Lambda g_{\mu\nu} = 8\pi GT_{\mu\nu} , \quad (1.1)$$

where $R_{\mu\nu}$ is the Ricci tensor, $g_{\mu\nu}$ is the spacetime metric, R is the Ricci scalar, $T_{\mu\nu}$ is the energy momentum tensor, G the Universal gravitational constant and Λ is the cosmological constant. The homogeneous and isotropic solution to these equations gives rise to the FLRW metric

$$ds^2 = -dt^2 + a(t)^2 \left(\frac{dr^2}{1 - kr^2} + r^2 d\theta^2 + r^2 \sin^2 \theta d\phi^2 \right) , \quad (1.2)$$

where $a(t)$ is the scale factor of the Universe introduced to model the expansion of the Universe, which causes an increase in the distance between two spacetime points with time. The usual normalisation for $a(t)$ is $a(t_0) = 1$, where t_0 is the current time. Note that for notational convenience, we write $a(t) \equiv a$. One can define $a(t)$ to have units of length, which results in r and k being dimensionless. This results in the following normalisation for k , a constant that tells us the geometry of the Universe, and consequently the fate of the Universe (see

¹The origin of these perturbations is currently unknown, although the theory of cosmological inflation (see section 1.2.2 for a brief discussion on what inflation is and the motivation for it) seems to be among the best candidates for this as well as other open questions regarding the origins of the Universe. A discussion of the merits and demerits of inflation is beyond the scope of thesis.

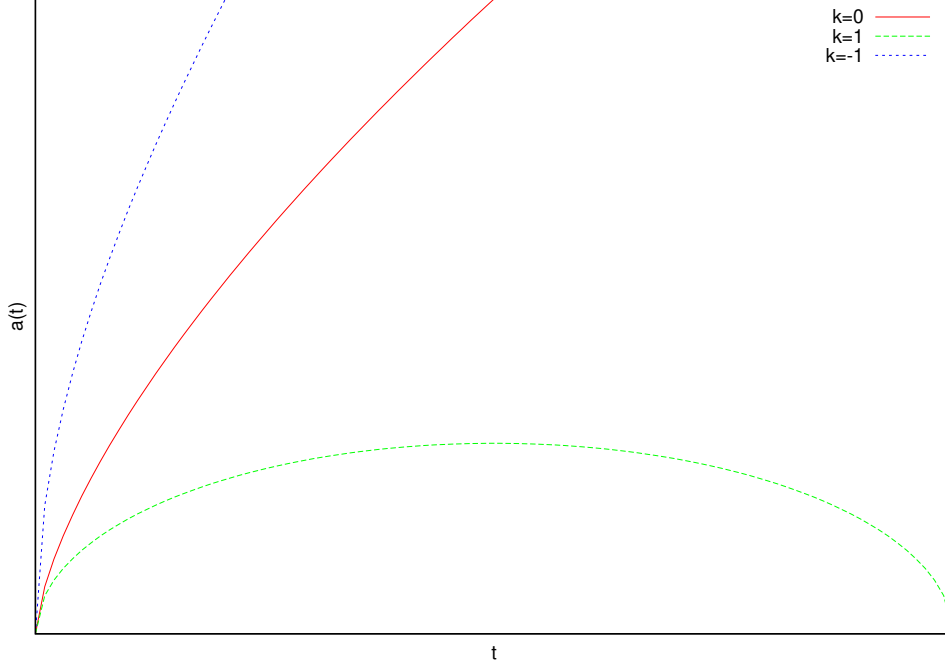


Figure 1.1: The scale factor as function of time. The $k = 1$ case corresponds to a closed universe with spherical geometry. The $k = -1$ case corresponds to an open universe with hyperbolic geometry. The $k = 0$ case corresponds to the flat, open universe. This case is corroborated by CMB measurements [1, 14].

Fig. 1.1).

$$k = \begin{cases} 1 & \text{if universe has spherical geometry and finite ,} \\ 0 & \text{if universe has flat geometry and is infinite ,} \\ -1 & \text{if universe has hyperbolic geometry and is infinite .} \end{cases} \quad (1.3)$$

On substituting the FLRW metric into Einstein's equations, one obtains the Friedmann and Raychaudhuri equations

$$H^2 = \left(\frac{\dot{a}}{a} \right)^2 = \frac{8\pi G\rho}{3} + \frac{k}{a^2} , \quad (1.4)$$

$$\frac{\ddot{a}}{a} = -\frac{4\pi G}{3} (\rho + 3p) , \quad (1.5)$$

where the dot represents a derivative with respect to time and H is the Hubble parameter that is a measure of the expansion rate, ρ is the density and p is the pressure associated to the energy-momentum fluid, respectively.

It is convenient at this point to introduce the critical density parameter, i.e., the value of the density that would just close the Universe, i.e., the value corresponding to a flat, Euclidean geometry

$$\rho_c = \frac{3H_0^2}{8\pi G}, \quad (1.6)$$

where H_0 is the Hubble parameter measured at the present time (frequently referred to as the Hubble constant). By expressing the density of the Universe as a sum over all its components and dividing by the critical density, one may rewrite the Friedmann equation in the following convenient form

$$H^2 = H_0^2 \left[\frac{\Omega_{m,0}}{a^3} + \frac{\Omega_{r,0}}{a^4} + \frac{\Omega_{\kappa,0}}{a^2} + \Omega_{\Lambda,0} \right], \quad (1.7)$$

where $\Omega_{m,0}, \Omega_{r,0}, \Omega_{\kappa,0}, \Omega_{\Lambda,0}$ are all parameters that encode the extent to which each component (matter, radiation, curvature and dark energy) of the Universe contributes to the total energy-density budget of the Universe at the present time². This relies on the assumption that the energy-momentum fluid of the Universe may be modelled as a perfect fluid, with an equation of state $p = f(\rho)$. Note that covariant conservation of energy momentum leads to the following constraint equation

$$\dot{\rho} = -3H(\rho + p). \quad (1.8)$$

It is now easy to see that for an accelerated expansion rate one would require the

²Of course, in the case of curvature, this is only a mathematical representation that is convenient for modelling purposes. The geometry of the Universe isn't associated to a physical density.

H_0 (the Hubble constant)	$67.4 \pm 0.5 \text{ km s}^{-1} \text{ Mpc}^{-1}$
$\Omega_c h^2$ (the CDM density parameter)	0.1200 ± 0.0012
$\Omega_b h^2$ (the baryon density parameter)	0.02237 ± 0.00015
σ_8 (the variance of the density fluctuations)	0.811 ± 0.006
τ (the optical depth at reionisation)	0.054 ± 0.007
$\ln 10^{10} A_s$ (amplitude of the primordial spectrum)	3.044 ± 0.014
n_s (the tilt of the primordial spectrum)	0.965 ± 0.004

Table 1.1: The table of cosmological parameters as reported by the Planck collaboration inferred from the Planck CMB power spectrum data, CMB lensing data and BAO (Baryon Acoustic Oscillations, see [1] for more information).

dominant energy-density in the Universe to exert negative pressure. Table 1.1 shows the values of the various density parameters as measured by the Planck satellite [1]. These values indicate that our Universe extremely close to being a flat, open Universe with dark energy and dark matter being the dominant components at the present time. Therefore, the cosmological model is named Λ CDM, where Λ represents the cosmological constant (dark energy) and CDM is cold dark matter.

We now have a working understanding of the evolution of the Universe to its current state that has been verified by a combination of observational probes. From the initial conditions, the Universe entered a radiation-dominated phase, during which particle began to decouple from the plasma as it cooled. The first photons that decoupled from the primordial bath form the CMB, redshifted to frequencies in the microwave band of the electromagnetic spectrum. During the radiation-dominated phase, the thermodynamic conditions were suitable for nucleosynthesis [see for e.g. [15] and references within] of heavier elements. This led to the observed vales of the Helium and Deuterium fractions today. This was followed by a matter-dominated phase, during which the majority of structure formation occurred as gravitational perturbations grew at a rate proportional to the scale factor [16]. This was followed by the current epoch, the dark-energy

dominated era, during which the Universe expands at an accelerated rate.

1.2 Shortcomings of Λ CDM

While the Λ CDM model has been remarkably successful in explaining and predicting many features of the observable Universe, there remain a few issues that it has failed address.

1.2.1 Nature of dark matter and dark energy

As mentioned before, cosmological data from a variety of sources including observations of supernovae and Cepheid variable stars in the local Universe as well as observations of the CMB have shown that the Universe is currently undergoing a period of accelerated expansion. The field equations of GR combined with a cosmological constant provide a good fit to current cosmological data, but leave several fundamental questions unanswered. Why is there a mismatch in theoretical calculations of Λ and observational data? Why does Λ dominate the energy density of the Universe now, and not at any other epoch? Does Λ vary with time/scale? If there is indeed a mysterious energy density that mimics the effects of Λ , i.e., that sources ‘repulsive gravity’, what is its origin?

All these questions represent active areas of research in fundamental physics. One possible explanation for some of these problems may be that the theory of gravity requires modification. This has led to several models of modified gravity proposed in the literature (see [17] for a review). Testing the viability of GR using current and future cosmological data is a major challenge in cosmology over the next few decades. In this thesis, we study how cosmological structure formation data on all scales can be used to probe modified gravity.

There exists a multitude of evidence for dark matter. Cosmological evidence for dark matter can be found in studies of structure formation and the CMB.

Matter perturbations are divided into a dark matter component and a baryonic component and these two components affect the CMB and structure formation differently. Dark matter perturbations are not affected by radiation, but interact purely via gravity. As a result, dark matter density perturbations can grow freely after the epoch of matter-radiation equality, forming potential wells that baryons fall into [16]. Therefore, structure formation is fundamentally driven by dark matter perturbations. Besides this, on smaller scales, galaxy rotation curves have shown that it is impossible to explain the speed at which stars orbit galaxies as a function of distance from the centre without invoking a significant dark matter component.

Meanwhile, there exist a multitude of cold dark matter candidates in the literature today [18]. However, we are yet to obtain a successful detection of a dark matter candidate [see [19] for an account of ongoing experimental searches and results]. In this work, we examine a well-motivated dark matter candidate, the axion and its detection using radio telescopes via its coupling to photons. In particular, we will focus on resonant axion-photon conversion in neutron star magnetospheres and the signal associated to this effect.

1.2.2 Causal contact, flatness and generation of initial conditions

According to the Big-Bang model, the Universe began in a hot dense state that then expanded to its current size. The *cosmological horizon* is the distance travelled by a light signal emitted at the Big-Bang epoch ($t = 0$). Two regions between which physical information can be exchanged in a time period smaller than or equal to the age of the Universe are called *causally connected* regions. Thus, the horizon size describes the size of a causally connected region, assuming

the Big-Bang happened at zero time. The ratio of the size of the horizon now and at time t_{rec} (time of recombination) is given by [20]

$$\left(\frac{l_0}{l_{t_{\text{rec}}}}\right)^2 = 1 + z(t_{\text{rec}}) \approx 1000, \quad (1.9)$$

where $z = 1/a - 1$ is the redshift parameter and l_0 is the size of the horizon today. Therefore, there are around a thousand regions in the visible Universe that have never been in causal contact. Despite this all of the Universe has about the same temperature to within one part in 10^4 , as evidenced by the CMB. This is called the horizon problem.

From Planck, we know that $|\Omega_\kappa < 0.02|$ [1]. We also know that its time evolution is given by

$$\Omega_\kappa(t) \propto \frac{1}{a^2(t)H^2(t)}. \quad (1.10)$$

Therefore,

$$\frac{\Omega_\kappa(t_0)}{\Omega_\kappa(t_{\text{rec}})} \simeq 10^{60}, \quad (1.11)$$

where t_0 is the current time. This means that the value of Ω_κ would have to be of the order of 10^{-60} in the beginning, a very unnatural fine tuning, indeed! This is called the flatness problem.

In addition to the above problems, in order to generate the observed matter distribution, one would need inhomogeneities to be present in the initial dark matter fluid at the initial time ($t = 0$). No such mechanism exists in the Λ CDM model. One possible resolution to this problem as well as the horizon and flatness problems is that the Universe initially went through a period of accelerated expansion known as inflation (inflation was originally proposed and developed by Guth, Starobinsky, Sato, Albrecht & Steinhardt and Linde [21–25], see [26] for a review

on the subject) prior to radiation domination. Such an inflationary epoch would shift the origin in conformal time (defined by $d\tau = dt/a$) far back in the past, increasing the size of a causally connected region as well as providing a natural explanation for the fine-tuning for Ω_κ . Typically, such an inflationary epoch is achieved by invoking an additional scalar field that dominates the energy density of the Universe at very early times with a negative pressure, similar to the dark energy fluid today.

1.2.3 Tensions in the data, new physics?

With the emergence of multiple data-sets used to constrain the standard cosmological model, statistical tensions have arisen in results derived from different analyses [27]. Two examples of such a tension are the Hubble tension and the σ_8 tension. The Hubble tension, that has been measured at the level of 4.5σ , is in the measurement of H_0 derived from CMB measurements [1] compared to the value derived from measurements of late Universe standard candles (type IA supernovae, Cepheid variables etc.) [28]. The σ_8 tension is in the measurement of the amplitude of the matter power spectrum $P(k)$ (see sec. 2.1) on the scale of $8 h^{-1}\text{Mpc}$ from CMB anisotropy measurements in comparison to the value derived from the analysis of galaxy clusters using the Sunyaev-Zeldovich effect [29]. These tensions have led many to believe that there exists new physics that would explain these results. On the other hand, such tensions may be alleviated by better understanding of systematic errors and uncertainties in the data or the analysis of it.

1.3 Introduction to modified gravity

General Relativity (GR) is one of the most successful theories in the modern age. It has not just withstood but indeed excelled in several tests for over a century and stands unshaken as one of the pillars of modern astrophysics and cosmology. It has been instrumental in the study of extreme astrophysical objects, like neutron stars, black holes and mergers of such compact objects and many more. Recently, the LIGO (Laser Interferometer Gravitational-Wave Observatory) and VIRGO collaborations detected and measured gravitational waves from mergers of black holes and neutron stars [30].

GR has also been a crucial tool in cosmology. The study of large scale structure and its growth in the early Universe is done on the back of GR, with perturbations of matter and radiation. Studying the growth of these perturbations in the formalism of GR forms the discipline of cosmological perturbation theory (CPT). This subject can be divided into two regimes, linear and non-linear.

In the linear regime, the evolution of perturbations is studied in the formalism of **linearised** GR. This has been done with great success, with the theory accurately predicting the details of the minute fluctuations in the CMB [1, 14, 31–34]. From these measurements of the CMB anisotropies, we have inferred the values of cosmological parameters, ushering in the age of “precision cosmology”. The current model of cosmology, the Λ CDM model is one of an expanding Universe in the background of GR, and has successfully predicted and explained several previously unknown observational features of our Universe, such as the accelerated expansion of the Universe [8, 35]. However, there is a scale at which the growth of these perturbations becomes non-linear. Then, perturbative techniques used in the linear regime are no longer applicable because of the extreme complexity

associated to the non-linearity of the growth. Therefore numerical techniques are employed to understand this regime.

1.3.1 Why modify gravity?

The motivation to modify such a well-tested model is its failure to explain the dark sector, i.e., dark matter and dark energy whose effects are modelled by Ω_c and Ω_Λ . Ideally, we would like both these parameters to be obtained within the mathematical framework of the theory itself, in a way that is consistent with quantum field theory which has been successfully used to derive the correct abundances of elements in big-bang nucleosynthesis [16]. In other words, we would like a model in which one would be able to derive the values of Ω_Λ and Ω_m at the current epoch without the need to call upon unknown entities such as dark matter and dark energy, while still being able to model accurately the gravitational interaction between objects on scales ranging from the size of the solar system to the cosmological horizon and beyond.

We know from Lagrangian and Hamiltonian dynamics that the equations of motion of a theory can be derived from an *action*. This action is defined as an integral of the Lagrange-Density \mathcal{L} . Such an action exists for GR, called the Einstein-Hilbert action

$$S = \frac{1}{16\pi G} \int \sqrt{-g}(R - 2\Lambda)d^4x + \int \sqrt{-g}\mathcal{L}_m(\psi_m, g_{\mu\nu})d^4x, \quad (1.12)$$

where the first term is the gravitational part of the action, and the second term contains the Lagrange-Density \mathcal{L}_m of the matter fields, which can be a function of the matter fields ψ_m and the metric. To derive the field equations of GR, one makes the assumptions that the weak equivalence principle, Einstein's equivalence

principle as well as the strong equivalence principle are valid. This also implies that the Ricci tensor and scalar can be written as functions of the metric alone (and not functions of the matter variables, the local environment etc.). In other words, it is assumed that $\nabla_\mu g_{\mu\nu} = 0$, where ∇_μ is the covariant derivative defined on the Riemannian manifold (see [36] for a detailed discussion). This means that the connection and all geometric quantities derived from it (the Riemann tensor, the Ricci tensor etc.) are all specified by the metric and its derivatives. The resulting geometrical structure of spacetime can be described by a Riemannian manifold, which means that we can locally study it assuming a Minkowski spacetime, which allows us to recover the laws of Special Relativity.

1.3.2 The landscape of models

Modified gravity theories are formulated in a similar manner, with an invariant action principle with respect to the metric, with a Universal coupling of all matter fields to the same metric [17]. This procedure ensures that the new theories do not violate fundamental principles that have been extremely well tested, at least to length scales of the Solar System [17].

Lovelock's Theorem Lovelock's theorem states that the **only possible** equations that are second order or less derived from an action involving the metric tensor and its derivatives are Einstein's equations with a cosmological constant. The mathematical statement of this powerful theorem is as follows

Theorem 1 *The only possible second-order Euler-Lagrange expression obtainable in a four dimensional space from a scalar Lagrange density of the form $\mathcal{L} = \mathcal{L}(g_{\mu\nu})$ is*

$$E^{\mu\nu} = \alpha\sqrt{-g} \left[R^{\mu\nu} - \frac{1}{2}g^{\mu\nu}R \right] + \lambda\sqrt{-g}g^{\mu\nu} , \quad (1.13)$$

where α and λ are constants, and $R^{\mu\nu}$ and R are the Ricci tensor and scalar curvature, respectively.

This means that if one is interested in modifying gravity, then one must

- consider additional fields for the action, other than the metric tensor.
- consider higher order derivatives of the metric tensor.
- consider higher dimensionality in the spacetime.
- not impose locality.

The last option would involve giving up on deriving the field equations from a *classical* action, i.e., non-locality typically arises from quantum fluctuations associated to the graviton leading to infrared divergences [37]. Therefore, this class of models will not be discussed.

There are many models that introduce additional fields into the action. Some well-studied examples of such models are scalar-tensor models and vector-tensor models, which, as their names suggest, introduce additional scalar [38–40] and vector fields with non-minimal couplings [41–43], respectively. Scalar-tensor models are often characterised by a coupling parameter $\omega(\phi)$ written as a function of the scalar field. The Lagrange density of a scalar field coupled to gravity via such a coupling can be written as

$$\frac{1}{16\pi} \left[f(\phi)R - \frac{\omega(\phi)}{\phi} \nabla_\mu \phi \nabla^\mu \phi - 2\Lambda(\phi) \right] + \mathcal{L}_m(\phi_m, g_{\mu\nu}) , \quad (1.14)$$

where $\omega(\phi)$ is the coupling parameter, a free function and $\Lambda(\phi)$ is a generalised cosmological constant. This theory reduces to GR in the limit $\omega \rightarrow \infty$, $\frac{\omega'}{\omega^2} \rightarrow 0$, $\Lambda \rightarrow \text{constant}$. The popular Brans-Dicke theory [44] can be obtained in the limit $\Lambda \rightarrow 0$ and $\frac{\omega}{\phi} \rightarrow \text{constant}$.

In 1974, Gregory Horndeski derived a general Lagrangian [45] that encompasses a wide variety of scalar-tensor theories including $f(R)$ gravity [46–48], Quintessence [49–58], k-essence [59–62] and a host of other theories from the general action (see [63] for a discussion). Local measurements put tight constraints on the value of ω (see section 1.3.3). Such constraints can be evaded with the help of screening mechanisms that make this coupling a function of the density of the matter field (Chameleon mechanisms) or include non-linear corrections to the coupling that can result in deviations only on large scales (Vainshtein mechanism [64]).

Vector-tensor models involve the introduction of a vector field that couples to gravity. In this case, such a vector field breaks Lorentz invariance since it picks out a preferred set of coordinates which would allow one to distinguish between inertial frames. Such a Lorentz-violating vector field is called the “aether”, which leads to these models being called Einstein-Aether models. It turns out that the aether field can have serious cosmological implications [17], it can lead to a renormalised value for the Newton’s Gravitational constant [65] and slow down the Universe expansion rate as well as lead to detectable rescaling of amplitudes of the scalar and tensor perturbations in the CMB power spectrum [66]. As a result, there are problems with trying to fit Einstein-Aether gravity to both CMB data as well as data from large-scale-structure surveys.

1.3.3 Parameterisations and observational probes

Linear parameterisations

As mentioned previously, CPT has been used with great success in the background of the FLRW metric within the framework of GR to calculate several cosmological

observables. The basic idea is to add small perturbations to the metric

$$g_{\mu\nu} = \bar{g}_{\mu\nu} + \delta g_{\mu\nu}$$

and the energy momentum tensor

$$T_{\mu\nu} = \bar{T}_{\mu\nu} + \delta T_{\mu\nu}$$

in the field equations and solve for the evolution of the perturbations, where the bar over the quantity that has identical evolution to the homogeneous background, and $\delta g_{\mu\nu}$ and $\delta T_{\mu\nu}$ are the perturbations to the metric and the energy-momentum tensor, respectively (see for example [67] for a detailed description of cosmological perturbation theory in an expanding FLRW background) In this context, ‘small’ implies that the amplitude of these perturbations are negligible in comparison to the background. Since the perturbations are assumed to be small, terms that are proportional to the product (or square) of perturbations are neglected. The scales over which such a technique is useful and applicable are known as ‘linear scales’.

Typically, the field equations for the perturbations are decomposed into scalar, vector and tensor modes (note that this step, called SVT decomposition is similar to the Helmholtz decomposition in vector calculus). The evolution of each sector is solved for separately. In addition, one also identifies two regimes for the perturbations dependent on the size of the wavelength of the Fourier modes of the perturbations relative to the cosmological horizon. The superhorizon regime refers to Fourier modes whose wavelength is larger than the Hubble horizon and vice-versa for the subhorizon regime. Of course, this implies that there exists an epoch at which any Fourier mode of a given perturbation ‘crosses over’ from superhorizon

to subhorizon. Of course, the evolution of each mode in two regimes eventually determines its observational signature, e.g., its imprint on CMB anisotropies or the matter power spectrum.

In modified gravity, one can follow a similar series of steps, except one contains additional variables in the SVT decomposition that come from extra degrees of freedom in the action. We describe two of the popular methods in the literature below.

Equation of State formalism This method involves parametrising modified gravity models on the basis of the field content in their actions, which leads to a particular equation-of-state (EoS) for the gauge invariant perturbations in the dark sector [68–70]. These EoS close the system of equations of the fluid [70]. The idea is to modify the Einstein-Hilbert action with a term which contains all the non-standard gravitational physics

$$S = \int d^4x \sqrt{-g} \left[\frac{R}{16\pi G} - \mathcal{L}_M - \mathcal{L}_d \right] , \quad (1.15)$$

where \mathcal{L}_d is the new term, called the “dark Lagrangian”. Varying the action with respect to the metric leads to the following field equations

$$G_{\mu\nu} = 8\pi G [T_{\mu\nu} + U_{\mu\nu}] . \quad (1.16)$$

All modifications to physics, i.e., all contribution to the dark Lagrangian comes from the dark-energy EM tensor $U_{\mu\nu}$ [70], which is covariantly conserved

$$\nabla^\mu U_{\mu\nu} = 0 , \quad (1.17)$$

due to the assumption that the energy momentum tensor due to the matter Lagrangian is conserved and the Bianchi identity being valid for Einstein tensor. The linear perturbation of these conservation equations (1.17) yields the general relativistic versions of the Euler and continuity equations for the velocity and density perturbations. They are written in terms of the gauge invariant density and the rescaled velocity perturbations Δ and Θ , respectively. The evolution equations for the gauge invariant density and well as velocity perturbations can be written in a way that is valid for both the conformal Newtonian gauge as well as the synchronous gauge. They are given by [71] (written in the conformal Newtonian gauge here)

$$\Delta' - 3w\Delta - 2\Pi + g_K\epsilon_H\Theta = 3(1+w)X, \quad (1.18)$$

$$\Theta' + 3\left(c_a^2 - w + \frac{1}{3}\epsilon_H\right)\Theta - 3c_a^2\Delta - 2\Pi - 3\Gamma = 3(1+w)Y, \quad (1.19)$$

where $K = \frac{k}{aH}$ and k is the wave number (or conformal momentum) of the perturbation, $c_a^2 = \frac{dp}{d\rho}$ is the adiabatic sound speed and $g_K = 1 + K^2/3\epsilon_H$, with $\epsilon_H \equiv -H'/H$ and where

$$X \equiv \phi' + \psi, \quad (1.20)$$

$$Y \equiv \psi, \quad (1.21)$$

ϕ and ψ are the usual scalar metric perturbations, i.e., the gravitational potentials that in GR are equal to each other (up to a minus sign). Finally, Π is the perturbed scalar anisotropic stress and Γ is the gauge invariant entropy perturbation. In the EoS approach, both Π and Γ will be written as linear expansions in terms of the Gauge invariant quantities, with coefficients that are dependent

only on the *homogenous background quantities*. The explicit form of these expansions depends on the modified gravity model (see [43, 71–73] for some examples on $f(R)$ and generalised Einstein-Aether theories). However, it is clear what each expansion physically implies for a system.

Effective Field Theory (EFT) Formalism This approach assumes that the weak equivalence principle is valid, i.e., there exists a metric that is universally coupled to all matter fields via the action $S_m[g_{\mu\nu}, \psi_m]$ [74] (see an alternate approach developed from this formalism [75] based on the ADM split). This action is then written in terms of the unitary gauge, where the additional degree of freedom in the form of a scalar field (since most modified gravity models can be written as the Einstein-Hilbert action + scalar) is absorbed into the metric. In other words, there are no scalar field perturbations, since the time coordinate is assumed to be a function of the scalar field. The action is given by [74]

$$S = \int d^4x \sqrt{-g} \left[\frac{M_*^2}{2} f(t) R - \Lambda(t) - c(t) g^{00} \right] + S_{\text{DE}}^{(2)}, \quad (1.22)$$

where f , Λ and c are functions of time t and the frame of reference is the Jordan frame, where the metric is universally coupled to the matter fields. by a simple Quadratic and higher order terms are encoded in $S_{\text{DE}}^{(2)}$. Note that this action is derived from the Einstein frame (where the metric is minimally coupled) by a conformal transformation $ds_{\text{Einstein}}^2 = f ds_{\text{Jordan}}^2$. When this action is expanded out to include them, we obtain (assuming the FLRW metric as defined in (1.2)

[74]

$$\begin{aligned}
S = \frac{1}{2} \int d^4x \sqrt{-g} & \left[M_*^2 f R - \rho_D = p_D - M_*^2 (5H\dot{f} + \ddot{f}) - \left(\rho_D + p_D + M_*^2 [H\dot{f} - \ddot{f}] \right) g^{00} \right. \\
& M_2^4 (\delta g^{00})^2 - \bar{m}_1^3 \delta g^{00} \delta K - \bar{M}_2^2 \delta K^2 - \bar{M}_3^2 \delta K_\mu^\nu \delta K_\nu^\mu + m_2^2 h^{\mu\nu} \partial_\mu g^{00} \partial_\nu g^{00} \\
& + \lambda_1 \delta R^2 + \lambda_2 \delta R_{\mu\nu} \delta R^{\mu\nu} + \mu_1^2 \delta g^{00} \delta R + \gamma_1 C^{\mu\nu\rho\sigma} C_{\mu\nu\rho\sigma} + \gamma_2 \epsilon^{\mu\nu\rho\sigma} C_{\mu\nu}^{\kappa\lambda} C_{\rho\sigma\kappa\lambda} \\
& \left. + \frac{M_3^4}{3} (\delta g^{00})^3 - \bar{m}_2^3 (\delta g^{00})^2 \delta K + \dots \right]
\end{aligned} \tag{1.23}$$

where $\delta g^{00} = g^{00} + 1$, δK_ν^μ is the extrinsic curvature perturbation, δK its trace, δR and $\delta R_{\mu\nu}$ the perturbation of the Ricci scalar and tensor, respectively and $C_{\mu\nu\rho\sigma}$ is the Weyl tensor. M_I , m_i , \bar{M}_i , \bar{m} and μ_i are mass parameters while λ_i and γ_i are dimensionless parameters. Note that all these are time dependent [74].

Clearly, all dark sector terms contributing to linear order are in the first line of eqn. (1.23). Similar to the EoS formalism, the coefficients of these terms depend purely on the homogeneous background, and therefore, are uniquely determined given a particular modified gravity model. Quadratic and higher order terms (from second line onwards) leave the background unchanged. Constraining their coefficients is highly dependent on clustering/screening mechanisms in the theory.

Non-linear parameterisations

The fundamental problem with studying non-linear scales in cosmology is that perturbation theory starts to become inaccurate as one starts to move from linear to non-linear scales which occurs at $k \geq 0.5h \text{ Mpc}^{-1}$. Therefore, we need to employ different techniques to try and probe non-linear structure formation in any cosmological model.

Parameterised Post-Newtonian formalism The Parameterised Post-Newtonian (PPN) formalism is one such formalism which aims to constrain modified gravity models by parameterising their weak field limit [76]. The parameters are relatively easily constrained by observations. The fundamental idea is to define a “degree of smallness”. In other words, one decides what order each individual perturbation is truncated. For the metric, one obtains

$$g_{00} = -1 + h_{00}^{(2)} + h_{00}^{(4)} + \mathcal{O}(6) , \quad (1.24)$$

$$g_{0i} = h_{0i}^{(3)} + \mathcal{O}(5) , \quad (1.25)$$

$$g_{ij} = \delta_j^i + h_{ij}^{(2)} + \mathcal{O}(4) . \quad (1.26)$$

In a similar way, we perturb the energy momentum tensor as well

$$T_{00} = \rho(1 + \Pi + v^2 - h_{00}) + \mathcal{O}(6) , \quad (1.27)$$

$$T_{0i} = -\rho v_i + \mathcal{O}(5) , \quad (1.28)$$

$$T_{ij} = \rho v_i v_j + P\delta_{ij} + \mathcal{O}(6) , \quad (1.29)$$

where Π is the ratio of the energy density to the rest mass density v is the spatial velocity of the perturbations. In addition to this, one also considers that time derivatives are of the order of the first order perturbations in magnitude, and additional scalar/vector/tensor fields are expanded up to fourth order. Ensuring that these rules for book-keeping are followed, one can derive the the full test metric given by

$$\begin{aligned} g_{00} = & -1 + 2GU - 2\beta G^2 U^2 - 2\xi G^2 \phi_W + (2\gamma + \alpha_3 + \beta_1 - 2\xi)G\phi_1 - (\beta_1 - 2\xi)G\mathcal{A} \\ & + 2(1 + 3\gamma - 2\beta + \beta_2 + \xi)G^2 \phi_2 + 2(1 + \beta_3)G\phi_3 + (3\gamma + 3\beta_4 - 2\xi)G\phi_4 , \end{aligned} \quad (1.30)$$

$$g_{0i} = -\frac{1}{2}(3 + 4\gamma + \alpha_1 - \alpha_2 + \beta_1 - 2\xi)GV_i - \frac{1}{2}(1 + \alpha_2 - \beta_1 + 2\xi)GW_i \quad (1.31)$$

$$g_{ij} = (1 + 2\gamma GU)\delta_{ij} , \quad (1.32)$$

where β , γ , ξ , β_1 , β_2 , β_3 , β_4 , α_1 , α_2 and α_3 are the PPN parameters and ϕ_W , ϕ_1 , ϕ_2 , ϕ_3 , ϕ_4 , \mathcal{A} , V_i and W_i are the PPN gravitational potentials [76]. One can clearly adapt this formalism to constrain modified gravity theories in a general way, without any particular theory in mind.

Now, we will discuss the observational constraints on the PPN parameters and potentials. These will, in turn be compared to the theoretical predictions of modified gravity models. In GR, we have that $\beta = \gamma = 1$ and $\xi = \beta_1 = \beta_2 = \beta_3 = \beta_4 = \alpha_1 = \alpha_2 = \alpha_3 = 0$.

Observations that involve null geodesics such as weak-gravitational lensing will be sensitive to the second order terms in the metric perturbations g_{00} and g_{ij} , both of which are related to the PPN parameter γ . According to the PPN formalism, the bending of light by a massive star observed is given by the expression [76]

$$\frac{(1 + \gamma)}{2}\theta_{\text{GR}} . \quad (1.33)$$

One of the tightest observational constraints on this deflection is by Shapiro, Davis, Lebach and Gregory [77] who used 2500 days worth of observations of 541 radio sources by 87 VLBI (Very Long Baseline Interferometry) sites over a period of 20 years. the result of this is

$$\theta = (0.99992 \pm 0.00023) \times 1.75'' , \quad (1.34)$$

which confirms the GR value of $1.75''$ [77]. This gives the following constraint

$$\gamma - 1 = (-1.7 \pm 4.5) \times 10^{-4} . \quad (1.35)$$

Similarly, one can also constrain γ using the differential time delay in photons as they pass through the gravitational field of a massive object (such as a star), called Shapiro light delay, given by

$$\Delta t = \frac{(1 + \gamma)}{2} \Delta t_{\text{GR}} . \quad (1.36)$$

One of the best observational constraints on this effect comes from measurements made using radio links on the Cassini spacecraft between the 6th of June and 7th of July, 2002, by Bertotti, Ies and Tortora [78]. From this experiment a time delay of $(1.00001 \pm 10^{-5}) \Delta t_{\text{GR}}$. This results in an even tighter constraint on γ given by

$$\gamma - 1 = (2.1 \pm 2.3) \times 10^{-5} , \quad (1.37)$$

which is also consistent with the prediction by GR.

Clearly, the PPN formalism is a powerful tool to constrain the local properties of modified gravity models in a general way. However, since we are interested in the cosmological behaviour of these models, we will need to go beyond local tests like terrestrial and solar system experiments.

Post-Friedmann Formalism

The corresponding version of the PPN formalism on larger scales is the Parametrised Post-Friedmann formalism, which has been used constrain the gravitational potential and shear by parametrising these quantities in a general way and comparing observational measurements of these quantities (from observations of evolution of large scale structure and gravitational shear from weak lensing) to the predictions made by different modified gravity theories. The possibility of direct comparison with observations has made this a popular approach. We are interested in making use of this formalism to constrain modified gravity models on **linear and non-linear scales**.

In linear perturbation theory, the FLRW metric with perturbations is written in the Conformal Newtonian gauge as

$$ds^2 = -a^2(\tau) [(1 + 2\psi)d\tau^2 - (1 - 2\phi)d\vec{x}^2] , \quad (1.38)$$

where ϕ and ψ are scalar potentials that are functions of space and time. We can write down the linearised conservation equations for cold dark matter (CDM), working in Fourier space and assuming adiabatic initial conditions and covariant conservation of the energy-momentum tensor [79]

$$\delta' + \frac{k}{aH}v - 3\phi' = 0 , \quad (1.39)$$

$$v' + v - \frac{k}{aH}\psi = 0 , \quad (1.40)$$

where δ is the density contrast, v the irrotational component of the peculiar velocity and primes indicate derivatives w.r.t $\ln a$. It is convenient to introduce

the co-moving density contrast

$$\Delta \equiv \delta + 3\frac{aH}{k}v. \quad (1.41)$$

Now, we have a system of equations for $\{\Delta, v, \phi, \psi\}$, which needs two more equations to be closed. These two equations are obtained from the theory of gravity which defines the relationship between the metric perturbations and how they are sourced by the perturbations of the energy momentum tensor. These equations are typically written in the modified gravity literature as

$$\frac{\phi}{\psi} = \eta(a, k), \quad (1.42)$$

$$k^2\psi = -\frac{a^2}{2M_{\text{pl}}^2}\mu(a, k)\rho\Delta, \quad (1.43)$$

where $M_{\text{pl}}^2 \equiv \frac{1}{8\pi G}$, $\eta(a, k)$ and $\mu(a, k)$ are generic functions of time and space, which parametrise the deviations from GR (in which they are both unity at late times when anisotropic stress is negligible) of a generic modified gravity theory. Thus, we now have a closed system which we can solve for the evolution of the perturbations in super-horizon and sub-horizon regimes. This treatment is valid only in the linear regime. We use the Post-Friedmann formalism to define a similar formalism on non-linear scales. The metric is expanded with perturbations to varying powers of $1/c$, where $1/c^2$ and $1/c^3$ terms are considered leading order [80]. There are two kinds of perturbations added to the background homogeneous and isotropic metric. The first is the Newtonian kind, which is an approximate solution of Einstein's equations, such that the exact non-linear equations of Newtonian dynamics will describe the evolution of these perturbations. The second kind of perturbation are relativistic. The Newtonian term will be at leading order, while the relativistic terms are higher order corrections. The

gauge used is the Poisson gauge (which is essentially the Newtonian gauge without neglecting the vector and tensor perturbations). The full metric is written as

$$g_{00} = - \left[1 - 2 \frac{U_N}{c^2} + \frac{1}{c^4} (2U_N^2 - 4U_P) \right] + \mathcal{O} \left(\frac{1}{c^6} \right) , \quad (1.44)$$

$$g_{0i} = - \frac{a}{c^3} B_i^N - \frac{a}{c^5} B_i^P + \mathcal{O} \left(\frac{1}{c^7} \right) , \quad (1.45)$$

$$g_{ij} = a^2 \left[\left(1 + \frac{2V_N}{c^2} + \frac{1}{c^4} (2V_N^2 + 4V_P) \right) \delta_{ij} + \frac{1}{c^4} h_{ij} \right] + \mathcal{O} \left(\frac{1}{c^6} \right) , \quad (1.46)$$

where the spatial Cartesian coordinates are understood as an Eulerian system of reference. In the Poisson gauge, the vector functions B_i^N and B_i^P are divergenceless and h_{ij} is a transverse and traceless tensor. Having chosen this gauge, we now have 4 degrees of freedom at leading order and 6 at higher order, two for each scalar functions U and V , two for the independent components of B_i and two for the transverse traceless tensor (which appears only as a higher order correction).

The Einstein equations

$$G_{\mu\nu} = R_{\mu\nu} - \frac{1}{2} g_{\mu\nu} R = \frac{8\pi G T_{\mu\nu}}{c^4} , \quad (1.47)$$

and the covariant conservation of energy-momentum

$$\nabla_\mu T_{\mu\nu} = 0 , \quad (1.48)$$

are used to obtain a closed system of equations. However, the large number of degrees of freedom, coupled with the non-linearity of equations makes the system too complicated to solve analytically. This then means that numerical methods are to be used to tackle the problem on non-linear scales. We aim to use

Newtonian N-body simulations to study modified gravity models on **both linear and non-linear scales**.

To use Newtonian N-body simulations, one has to derive the Newtonian limit for these equations. The Newtonian limit is the quasi-static, weak field limit of the field equations. Therefore time derivatives are attached with a factor of $\frac{1}{c}$ (low velocity). The matter content is taken to be pressureless dust, equivalent to CDM. The parameters that then describe the background fluid are the background density $\bar{\rho}$ and the density and velocity perturbations δ and v_i . We operate in the Poisson gauge, one of the few gauges that is valid on both linear and non-linear cosmological scales [81]. The vector functions B_i^N and B_i^P are divergenceless and h_{ij} is a transverse and traceless tensor (see [80] for a detailed explanation of this expansion and the physical interpretation of each term). The equations are [80]

$$\frac{1}{c^2} \frac{1}{a^2} \nabla^2 V_N = -\frac{4\pi G}{c^2} \delta \bar{\rho}, \quad (1.49)$$

$$\frac{1}{c^3} \left[-\frac{1}{2a^2} \nabla^2 B_i^N + 2\frac{\dot{a}}{a^2} \nabla_i U_N + \frac{2}{a} \nabla_i \dot{V}_N \right] = \frac{8\pi G}{c^3} \bar{\rho} (1 + \delta) v_i, \quad (1.50)$$

$$\frac{1}{c^2} \frac{2}{a^2} \nabla^2 (V_N - U_N) = 0, \quad (1.51)$$

$$\frac{d\delta}{dt} + \frac{1}{a} \nabla_i v_i (1 + \delta) = 0, \quad (1.52)$$

$$\frac{dv_i}{dt} + \frac{\dot{a}}{a} v_i = \frac{1}{a} \nabla_i U_N. \quad (1.53)$$

Note that there is a constraint equation for the vector potential B_i^N that is present at the c^{-3} order. This vector potential has been measured from N-body simulations and found to be small [82]. This further justifies, quantitatively, the use of the Newtonian approximation.

Parametrisation Therefore, neglecting the contribution of the vector potential, we are now left with two degrees of freedom in our system. The so-called “1PF” equations describe structure formation on all scales, including higher order terms in the expansion as well as terms that are structurally non-linear, i.e., terms that have the involve combinations of perturbation variables (such as $\rho\mathbf{v}$). Note that scales at which the density-field exhibits non-linearity, i.e., when the CDM density contrast is no longer small are not the same as the scales where the velocity field exhibits non-linearities (which are typically larger). Following [83], we rewrite these equations using the so-called “re-summed potentials” [80]

$$\psi_{\text{P}} = -V_{\text{N}} - \frac{2}{c^2}V_{\text{P}}, \quad (1.54)$$

$$\phi_{\text{P}} = -U_{\text{N}} - \frac{2}{c^2}U_{\text{P}}. \quad (1.55)$$

The scalar parts of the 00 component of Einstein’s equation may be expressed in Fourier space as

$$\frac{1}{c^2}k^2\tilde{\phi}_{\text{P}} + \frac{1}{c^4}[\text{non-linear terms}] = -\frac{1}{c^2}4\pi a^2\bar{\rho}G_{\text{N}}\tilde{\Delta}, \quad (1.56)$$

$$\tilde{\psi}_{\text{P}} = \tilde{\phi}_{\text{P}}, \quad (1.57)$$

So far, we have not explicitly included any departure from Λ CDM in the analysis. To make contact with the modified gravity literature, we set $G_{\text{eff}} = \mu(a, k)G_{\text{N}}$ where $\mu(a, k)$ is a potential that acts as a dimensionless potential that promotes Newton’s constant to an arbitrary function of space and time.

Usually, the Newtonian limit is obtained by imposing the condition that the timelike geodesic equation is compatible with the Newtonian equations of particle motion. This then sets $g_{00} = -(1 - 2\phi_{\text{P}}/c^2)$ where ϕ_{P} is identified to be

the Newtonian gravitational potential ϕ_N [16, 36] in the case of GR. This is the “passive” approach to gravitational physics, where one calculates the response of matter to a given gravitational field. However, in N-body simulations, we have a given matter distribution from which we calculate the gravitational field and the particle dynamics, updated at regular time-steps. Therefore, the field equations define the order of metric terms rather than the geodesic equation. This approach is called the active approach [80]. Therefore, consider the trace reversed Einstein equations

$$R^\mu_\nu = \kappa \left(T^\mu_\nu - \frac{1}{2} T \delta^\mu_\nu \right) + \Lambda \delta^\mu_\nu , \quad (1.58)$$

the trace of which (given our parametrisation) is given by

$$\frac{1}{c^2} \frac{1}{a^2} \nabla^2 (\phi_P - 4\psi_P) = \frac{12\pi G_{\text{eff}}}{c^2} \bar{\rho} \delta . \quad (1.59)$$

However, when we consider the Newtonian limit for slowly moving massive particles, i.e., the relativistic four-velocity of the CDM particles $u^\mu = (1, 0, 0, 0)$. Then, the only relevant geodesic equation is

$$\frac{d^2 \mathbf{x}}{dt^2} + 2 \frac{\dot{a}}{a} \dot{\mathbf{x}} = -\frac{1}{2} c^2 (g^{i\nu} \partial_\nu g_{00}) . \quad (1.60)$$

Note that this is not true for relativistic particles like photons. However, it does apply to matter, and effectively implies that

$$\frac{d^2 \mathbf{x}}{dt^2} + 2 \frac{\dot{a}}{a} \dot{\mathbf{x}} = \frac{1}{a(t)^2} \nabla \phi_P , \quad (1.61)$$

i.e, the evolution of massive particles only depends on ϕ_P . This means that we

can redefine our parametrisation (1.56, 1.57) as

$$k^2\phi_{\text{P}} = -4\pi\mu(a, k)G_{\text{N}}a^2\bar{\rho}\Delta, \quad (1.62)$$

$$\frac{\tilde{\phi}_{\text{P}}}{\phi_{\text{P}}} = \eta(a, k), \quad (1.63)$$

Therefore, we have only one degree of freedom that is relevant for the N-body simulation, while the second degree of freedom can be explored in post-processing (via ray tracing techniques used in weak lensing, for example).

Constraining modified gravity

A variety of observational probes have been used to constrain and test modified gravity. As mentioned earlier, local measurements including observations of the solar system are useful to impose bounds deep in the non-linear regime, i.e., on small scales. Cosmological datasets on large-scale structure that have been previously used to test Λ CDM e.g., CMB anisotropies, weak-lensing etc. have proven useful to test parameterised approaches where a set of functions capture the deviations from GR. Such approaches encompass a significant portion of the model-space, but the constraints themselves are not as strong as those that one would obtain when concentrating on individual models.

Furthermore, such cosmological constraints are often limited to linear or quasi-linear scales since we currently do not have the tools to predict non-linear large-scale structure observables for parameterised approaches. Model-specific studies allow insight into non-linear behaviour, via dedicated N -body simulations (see [84] for a detailed study of the various software that exists in the literature and the results associated with each).

In addition, there also are a variety of astrophysical datasets such as galaxy cluster

abundance, redshift space distortions, compact object mergers etc. See [85] for a detailed description on the various datasets and how they have been used to establish constraints.

In this work, we will study N -body simulations with a time-dependent effective gravitational parameter in the Post-Friedmann formalism, with $\mu = A(a, k)$ where $A(a, k) \equiv A(a)$. In chapter 2, we calculate the matter power spectra from our simulations and compare different approaches in the literature that predict the matter power spectrum for arbitrary $\mu(z)$. We quantify the accuracy of each approach, finding the **ReACT** formalism [86, 87] to be the best performing candidate and compute weak-lensing observables from the matter power spectra in the simulations as well as using the spectra from the **ReACT** and **halofit** [88–90] approaches in the literature. We also reflect on the impact of these results on the performance of future surveys in the context of model-independent constraints of modified gravity.

In chapter 3 we validate the **ReACT** formalism over a significantly wider region of parameter space in $\mu(z)$. We use this validated package to perform model-independent forecasts on time-dependent modified gravity for an LSST-like survey.

1.4 Axion Dark Matter

1.4.1 The axion as a dark matter candidate

The origins of the axion can be traced back to the strong CP problem in Quantum Chromodynamics (QCD). The QCD lagrangian contains a Charge and Parity (CP) conjugation violating term which can be written as

$$L_{\text{QCD}} = \mathcal{L}_{\text{pert}} + \mathcal{L}_{\theta} = \mathcal{L}_{\text{pert}} + \theta \frac{g^2}{32\pi^2} G^{a\mu\nu} \tilde{G}_{\mu\nu}^a, \quad (1.64)$$

where $\mathcal{L}_{\text{pert}}$ is the full perturbative QCD Lagrangian and the parameter θ violates CP symmetry, g is the gauge coupling, $G_{\mu\nu}^a$ is the gluon field tensor and $\tilde{G}_{\mu\nu}^a$ its dual. This CP violation results in a non-zero value for the electric dipole moment of the neutron. This dipole moment is experimentally constrained to be very small, $d_n \leq 3 \times 10^{-26} \text{ ecm}$ [91], which translates into the constraint $\theta \leq 3 \times 10^{-10}$, in other words, terms containing θ are negligible in QCD, which means QCD is close to being CP invariant, if not exactly invariant. Indirect CP violation in the standard model has been seen in the case of kaon decay [92]. Why does nature conspire that QCD must be CP invariant? This is the strong CP problem.

An elegant solution to this problem was suggested by R.Peccei and H.Quinn [93], where θ is promoted to a scalar field and a new symmetry is introduced called the PQ symmetry, which is broken in the early Universe during the PQ phase transition. This introduces a new scalar field, mediated by the corresponding Nambu-Goldstone boson, the axion. Therefore, θ can then naturally be relaxed to zero as the Universe evolves and QCD is CP invariant at the present day. The first axion model proposed by Weinberg and Wilczek [94, 95] was ruled out by collider experiments, since the coupling of the axion to other sectors was too strong. Subsequently two models, the KSVZ [96, 97] and DFSZ [98, 99] emerged

establishing a family of models of so-called “invisible axions”, since they are so weakly interacting. There exist two well-known non-thermal mechanisms that produce a cosmological abundance of axions in the early Universe [100–107]. This makes the axion a well-motivated dark matter candidate.

For a specific model there is a relation between the axion-photon coupling $g_{a\gamma\gamma}$ and the axion mass m_a , which depends on the choice of E/N , which is the ratio of electromagnetic and colour anomalies [108]

$$g_{a\gamma\gamma} = 5.1 \times 10^{-14} \text{ GeV}^{-1} \left(\frac{m_a c^2}{250 \mu\text{eV}} \right) \left| \frac{E}{N} - 1.92 \right|. \quad (1.65)$$

The KSVZ model has $E/N = 0$, while DFSZ model has $E/N = 8/3$ making the latter more weakly coupled to photons.

Misalignment mechanism

During the QCD transition, the axion becomes massive, caused by the axion scalar field rolling down a potential well until its value is minimised. However a number of zero-mode bosons are produced as the field oscillates about its minimum energy configuration, i.e., a Bose-Einstein condensate is formed. This produces a cosmological population of axions that was recently computed as

$$\Omega_a h_{100}^2 \approx 0.54 g_\star^{-0.41} \theta_i^2 \left(\frac{f_a}{10^{12} \text{ GeV}} \right)^{1.19}, \quad (1.66)$$

where $g_\star \approx 10$ is the number of relativistic degrees of freedom during the re-alignment process, θ_i is the initial angle of misalignment, h_{100} is defined by the Hubble constant $H_0 = 100 h_{100} \text{ km sec}^{-1} \text{ Mpc}^{-1}$ and f_a is the axion decay constant which is related to the axion mass, m_a , by $m_a c^2 = 6 \mu\text{eV} (f_a / 10^{12} \text{ GeV})^{-1}$

(see also [109–112] for other recent treatments of this issue). Recent measurements of the CMB by the *Planck* satellite [1, 14] yield an estimate for the CDM density, $\Omega_c h_{100}^2 \approx 0.12$. Assuming that this is the case, taking into account the uncertainty in the value of g_\star and the standard assumption $\langle \theta_a^2 \rangle = \pi^2/3$, we can predict a mass range of $19 \mu\text{eV} \leq m_a c^2 \leq 23 \mu\text{eV}$.

Such a choice of θ_a is made assuming that its value as a function of space is random and is eventually ‘averaged’ due to the Hubble expansion. However, such an assumption is not really a firm prediction at all. In inflationary scenarios one would expect a random value anywhere in the range $0 < \theta_a \leq \pi$ ³. One might expect that, in order to avoid an anthropic solution to the strong CP problem [114], there is a lower limit for θ_a and hence $10^{-2} < \theta_a < \pi$. In this case, we come up with a wider prediction for the range of masses from misalignment, $6 \times 10^{-3} \mu\text{eV} < m_a c^2 < 6 \times 10^2 \mu\text{eV}$.

String decay

An alternative production mechanism involves the formation of topological defects, i.e., cosmic strings. Since the axion field exists in a $U(1)$ vacuum manifold post the spontaneous symmetry being broken, a network of cosmic strings is formed via the Kibble mechanism [106, 107]. The radiation of this network of strings yields an abundance of axions that dominates the matter density of the Universe if the PQ symmetry is broken after inflation. Assuming this is the case, the resultant abundance contains a contribution from long strings and loops [115, 116] and is given by

$$\Omega_a h_{100}^2 \approx \left[1 + 10J \left(\frac{\alpha}{\kappa} \right) \right] \Delta \left(\frac{f_a}{10^{12} \text{GeV}} \right)^{1.18}, \quad (1.67)$$

³Note that inflationary axion cosmology predicts isocurvature perturbation modes in the CMB, which is an excellent way of constraining such models [113].

where α is the loop production size relative to the horizon, κ quantifies the rate of decay of the string loops, $J(x) = x^{3/2} [1 - (1+x)^{-3/2}]$ and $1/3 < \Delta < 3$ is the theoretical uncertainty associated with the QCD phase transition. This estimate was recently refined [114], notably improving the estimate of Δ and making the assumption that $\alpha/\kappa = 0.5 \pm 0.2$ to deduce $100 \mu\text{eV} < m_a c^2 < 400 \mu\text{eV}$ under the assumption that the axions are the cold dark matter. Note that this axion mass range cannot be probed by standard axion haloscope experiments (see below).

1.4.2 Experimental searches

Laboratory searches for axions may be traced back to P. Sikivie’s landmark paper in 1983 where he first described the idea of using cavity detectors to detect the axion flux from the Sun (helioscopes) and the local dark matter ‘wind’ (haloscopes) [117]. Essentially, one designs cavities with large magnetic fields that couple to specific modes of the axion field, producing microwave/radio photons (in the case of haloscopes) and X-ray photons (in the case of helioscopes). In the case of helioscopes, the bounds on the axion-photon coupling are dependent on the model used to describe the axion production mechanism in the Sun. On the other hand, haloscopes rely on measurements of the local dark matter flux.

The CERN Axion Solar Telescope (CAST) [118] is currently in operation and is responsible for the most stringent broadband bounds on $g_{a\gamma\gamma}$ i.e., bounds that span across a large range of axion mass. Meanwhile, various haloscope experiments such as the Axion Dark Matter Experiment [119–122] (ADMX), Haloscope At Yale Sensitive To Axion CDM (HAYSTAC) [123–125] have established very stringent bounds that exclude axions with couplings as weak as the KSVZ and DFSZ models, but over very a small range of axion mass.

One drawback of the conventional haloscope cavity detectors is that the resonant coupling imposes a lower limit on the size of the cavities that may be manufactured, which implies a hard upper limit on axion mass that can be probed using such devices. Recently, a hybrid method was proposed that does away with the idea of resonant coupling in favour of enhancing the signal by introducing dielectric media into the experimental setup. The basic idea is that the coupling of the axion to electromagnetic sector induces EM waves at the boundaries of dielectric surfaces (i.e., boundaries where the dielectric constant changes). It is possible to boost the signal by inserting a number of dielectric discs into the experimental apparatus [126]. This setup is known as the dielectric haloscope, and is the approach adopted by the MAgnetized Disk and Mirror Axion eXperiment (MADMAX) collaboration [126, 127].

Clearly, a lot of work remains to be done in order to explore the regions of the $g_{a\gamma\gamma} - m_a$ parameter space that have not yet been probed, especially the range of axion masses that are predicted by the misalignment and string decay mechanisms. See fig. 1.2 for a summary of the constraints that is by no means all-encompassing, but displays a reasonably up-to-date picture of the current situation in the field.

1.4.3 Indirect detection: Complimentary to laboratory searches

Laboratory searches for axions have come a long way in the last few decades. Although they have managed to achieve to achieve extremely sensitive detector designs, they require a large amount of time to scan across the range of axion masses associated to the CDM parameter space. Indirect methods of detecting axions via astrophysical magnetic fields could inform such efforts by providing a

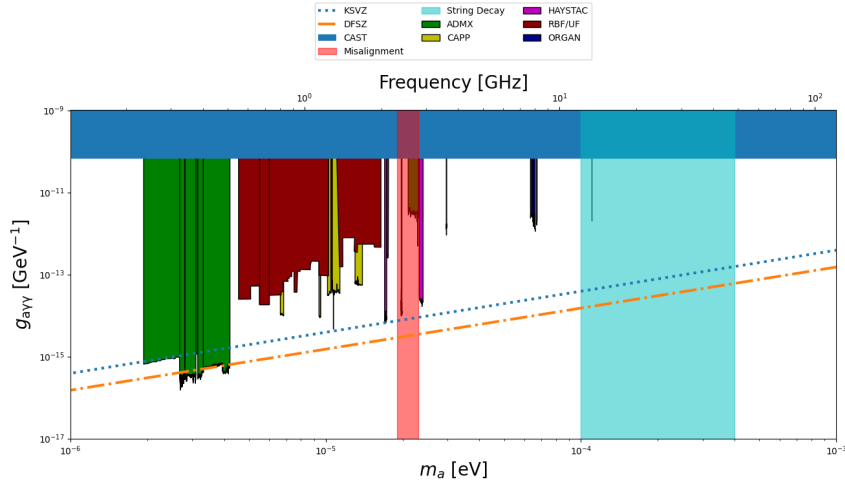


Figure 1.2: A summary of the constraints on the axion-photon coupling as a function of axion mass. The red and cyan regions represent the prediction for the CDM axion mass range according to the misalignment and string decay mechanisms [114], that assume that $\Omega_a = \Omega_{\text{CDM}}$, i.e., that axions make up the entire fraction of CDM observed today. The dark blue exclusion is from the CERN CAST helioscope [118]. The green and purple exclusions are from the ADMX [119–122] and HAYSTAC [123–125] haloscopes, respectively. The yellow exclusions are from the CAPP haloscope based in South Korea [128–130, 130, 131]. The dark red are from the RBF/UF haloscopes [132, 133]. Finally, the dark blue limits from the ORGAN collaboration [134, 135].

a much smaller window in axion mass/frequency where they are likely to achieve a positive detection.

One can study the signal from the spontaneous decay of axions to photons. Assuming axions be the CDM of the Universe, one can calculate the flux density signal that would be observable from the CDM halo of an object such as a galaxy cluster, since the spontaneous decay time is known to be

$$\tau_a = 6.8 \times 10^{24} \text{ s} \frac{(m_a/\text{eV})^{-5}}{(E_{\text{PQ}}/N - 1.95/0.72)^2}, \quad (1.68)$$

where E_{PQ} is the electromagnetic anomaly of the PQ symmetry. Clearly, this signal is quite weak. However, over a small range in frequency, there exists an enhancement of this signal via stimulated emission from ambient photons at the same frequency (e.g., CMB, galactic radio emission, synchrotron emission etc.). In chapter 4, we study the different ways of measuring this signal and clarify optimal observational strategies for the future.

Compact objects have long been known to offer a useful avenue in which to probe axions and ALPs in a variety of ways [136–144]. Neutron stars (NSs) in particular offer an exciting opportunity for increasing the possibility to detect axion dark matter by allowing axions to resonantly convert into radio photons in their magnetospheres, which relies on resonant conversion at some critical radius r_c where the plasma mass of the photons in the magnetosphere, $\omega_p = m_a$, the axion mass. Historically, these ideas can be dated to a proposal by Pshirkov and Popov [145], while the more general question of mixing of axions with photons in neutron star magnetospheres was also considered in [146]. More recently, the subject has seen a renewed interest [147–153]. In chapter 5 we study the conversion probability associated to the resonant conversion, the propagation of

the resultant photons out from the magnetosphere in the presence of gravity and characterise the shape of the signal.

Using our analysis in chapter 5, we identify target pulsars in the Jodrell Bank Centre for Astrophysics (JBCA) pulsar catalogue and perform a matched-filter analysis on the data to search for a signal in the time-domain in chapter 6. Such a technique allows one to optimise to specific time-dependence that is predicted, and will only become more powerful as the theoretical understanding of the shape of the signal improves.

Chapter 2

Modified Gravity Simulations

2.1 Introduction: Model-independence and non-linear scales

We are currently in a data-intensive era for cosmology. The next few decades in cosmology will see an unprecedented amount of data on large-scale-structure (LSS) generated by a multitude of experiments such as the *Euclid* satellite ¹, the Vera Rubin Observatory ², the Nancy Roman Space Telescope ³ and the Square Kilometre Array (SKA) ⁴ on a variety of cosmological scales. Designing tests of gravity and the dark energy paradigm that make efficient and effective use of this data represents one of the big challenges for cosmologists going forward. In the modified gravity context, the model-space is vast (see section 1.3.2 for more details). To combat this problem, a number of parameterisations of modified gravity were introduced and studied (see sec 1.3.3). A key assumption for most of these formalism is that one is restricted to the “linear” regime, where perturbations (particularly density perturbations) are small. These have been constrained with multiple observational probes [1, 8, 35, 154–157], but no deviation from Λ CDM has been detected universally. However, the restriction to linear scales significantly limits what these parameterisations can achieve ⁵.

This restriction could prove to be a severe limiting factor, since upcoming cosmological surveys will generate a multitude of data on non-linear cosmological scales. Until now, various studies of structure formation were carried out by performing N -body simulations in specific modified gravity models, such as $f(R)$ gravity [160] or Dvali-Gabadadze-Porrati (DGP) gravity [161]; for a review,

¹<https://www.euclid-ec.org>

²<https://www.lsst.org>

³<https://roman.gsfc.nasa.gov>

⁴<https://www.skatelescope.org>

⁵Note that some recent works [158, 159] are valid on non-linear scales; we will return to these and contextualise them later in this work.

see [162, 163]. While these studies are valuable in understanding the behaviour of the respective models in the non-linear regime, they do not allow one to rule out significant regions of the modified-gravity model space. Furthermore, these studies do not allow us to perform a robust *null test* of GR, unlike model-independent approaches.

Therefore, it is crucial to establish a model-independent approach towards testing modified gravity on all cosmological scales. Recent work [83] used the Post-Friedmann formalism [80] to design a rigorous approach to modified gravity that is valid on all cosmological scales. Modified gravity models are typically parameterised by two parameters in linear theory. The post-Friedmann approach extends these linear theory parameterisations in a manner that can be consistently simulated and interpreted on all scales. In this work we explore the non-linear phenomenology of this model-independent approach using N -body simulations. Crucially, a careful choice of the parameters ensures that we can run simulations characterised by a single parameter, and include the effect of the other in post-processing (see sections 2.2 and 2.5 for more details).

Combined with the simulations, we also present a critical comparison of the fitting functions capable of predicting the matter power spectrum $P(k)$, which is the 2-point correlation function of density contrast defined according to

$$\langle \delta(\tilde{\mathbf{k}}) \delta(\tilde{\mathbf{k}}') \rangle = (2\pi)^3 P(k) \delta^3(\tilde{\mathbf{k}} + \tilde{\mathbf{k}}'), \quad (2.1)$$

for arbitrary modified gravity parameters. Due to the computational cost of N -body simulations, such fitting functions will prove to be crucial in understanding the phenomenology of modified gravity and its effect on not only the matter power spectrum, but also on weak gravitational lensing (or simply weak-lensing).

This point is especially important since upcoming surveys will measure galaxy clustering (which provides information on the matter power spectrum) and cosmic shear: the apparent distortion of the shapes of galaxies due to the deflection of light by the distribution of mass along the line-of-sight on non-linear scales. As such, being able to compute these weak-lensing observables from our simulations and any fitting functions is also of paramount importance.

The plan of the chapter is as follows. In section 2.2, we describe the theoretical background, including an introduction to the Post-Friedmann formalism and a discussion of some features of our approach and their impact on the simulations. We then provide a description of our N -body pipeline in section 2.3 as well as a discussion on the performance of the different fitting-functions. We present the phenomenology of the simulations in section 2.4. In section 2.5, we compute weak-lensing observables in our approach from the simulations and examine the performance of the fitting functions in this context. We present our concluding remarks in section 2.6.

2.2 The Post-Friedmann formalism

Post-Newtonian expansions have been known to be effective in testing departures from GR deep in the non-linear regime (see section 1.3.3 for a discussion of the PPN formalism in this context). The Post-Friedmann formalism, first introduced in [80] is a $\frac{1}{c}$ expansion of the flat, homogeneous and isotropic FLRW metric and gravitational potentials, specifically designed to describe the relativistic corrections to the ‘Newtonian limit’, i.e., the weak-field, low-velocity quasi-static approximation of GR where time derivatives in the metric are down weighted in the metric expansion. The applicability of the Newtonian limit to sub-horizon scales in Λ CDM has been well-tested and leading order corrections to the Newtonian limit have been shown to be negligible [164, 165]. See section 1.3.3 for a detailed derivation of the parameterisation that we adopt for our simulations, which we repeat here for convenience

$$k^2 \phi_{\text{P}} = -4\pi\mu(a, k)G_{\text{N}}a^2\bar{\rho}\Delta, \quad (2.2)$$

$$\frac{\tilde{\phi}_{\text{P}}}{\phi_{\text{P}}} = \eta(a, k), \quad (2.3)$$

where $\mu(a, k)$ is the dimensionless parameter that promotes Newton’s gravitational constant to an arbitrary function of space and time and $\eta(a, k)$ is the slip parameter that affects photon geodesics. The key point to be made here is that these equations are valid on all sub-horizon cosmological scales and may be applied across a wide range of modified gravity models. See section VA in [83] for a detailed algorithm that defines the procedure to be followed to ensure that a specific modified gravity model fits into this framework. Practically speaking, most ‘ Λ CDM-like’ models, i.e., models that have a valid weak-field limit with a vanishing vector potential are consistent with our mathematical framework.

An important point to note the evolution of matter is governed by eq. (1.62) alone (see section 1.3.3), and therefore one can run N -body simulations with a single modified gravity parameter μ , while modelling the effects of η in post-processing.

We adopt the ‘maximally phenomenological pixels’ approach described in [83], where we express the parameters (μ, η) as piecewise constant functions in a set of bins, or pixels, in time and space. This technique has been successfully used for modified gravity [166–168], and has also been used to constrain the dark matter equation of state in a model-independent fashion [169]. In this work, we run N -body simulations with a pixelised μ . Since the accelerated expansion of the Universe is a late time effect, we assume that $\mu = \eta = 1$ at early times and that they only differ from unity deep into matter domination. This is theoretically consistent with experiments that study modified gravity using time and space dependent pixels for the two parameters. This scheme then allows one study a large class of modified gravity theories, since it is possible to run a large number of N -body simulations with different values for pixelised functions $\mu(a, k)$ and $\eta(a, k)$. In particular, $f(R)$ [170] fits within this approach. Moreover, the works ([158, 171]) can be re-interpreted in this framework as specifying the functional forms of μ that occur for some commonly studied models with screening mechanisms.

A similar and promising extension of the linear theory parameters to a much wider range of scales was developed in [159], which applies to all models that fit into a Parameterised Post Newtonian (PPN) formalism [76]. The functional form that μ assumes in this approach is such that it has scale dependent features on linear scales, but is purely time-dependent on non-linear scales, due to the

restriction to theories that fit into the PPN framework. Another promising proposal to address parameterising modified gravity theories on non-linear scales was proposed in [158]. This theoretical setup maps specific modified gravity models to known screening mechanisms via detailed spherical collapse calculations. This formalism was recently implemented to run phenomenological N -body simulations of $f(R)$ gravity without having to solve for the additional dynamical scalar field [171]. Explicitly, one would derive functional forms for $\mu(a, k)$ that originate from specific screening mechanisms. We note that our approach is by design less restrictive in the modified gravity parameter space. However, compared to the two approaches described above, our approach suffers from the drawback that it is not designed to identify the specific underlying model that causes a deviation from GR.

With all these points in mind, in this work we take the first step toward a fully model-independent treatment of modified gravity with N -body simulations. We run N -body simulations where μ is a piece-wise constant function composed of independent bins or pixels in time and space which can be varied independently of each other. Essentially, this ensures that one is maximally agnostic about the theoretical details that cause any modifications to gravity that appear in the matter power spectrum. Note that this approach has been applied successfully in linear theory for modified gravity [172] and also generalised constraints on dark matter [173]. As mentioned earlier, we can run the N -body simulations with a single modified gravity parameter μ , and only require the second parameter when computing the observables from the simulation outputs (see section 2.5 for a more detailed discussion of how our simulations can be used to probe both parameters). Since we restrict ourselves to sufficiently sub-horizon scales, the Newtonian approximation allows us to set $\tilde{\Delta} = \tilde{\delta}$, as is typical in Newtonian

N -body simulations.

We will focus on models of modified gravity with a purely time-dependent μ . Whilst the full time- and scale-dependent analysis would employ a similar analysis outlined in this work, it would involve a significantly more complicated modification to the N -body mechanism. Moreover, the purely time-dependent μ case is of considerable interest in its own right for several reasons. The time-dependent case serves as a bridge between linear and non-linear studies, due to the fact linear growth factor remains purely time-dependent. This allows one to separate the phenomenology arising from scale-dependent modifications on linear scales (with time-dependent modifications on non-linear scales), and those that arise from the scale- and time-dependent modifications on linear and non-linear scales. This was shown in [73] for a general class of modified gravity models on linear scales. We will return to this point later in this work (see eq. (2.4) and the discussion following for further details on the utility of maintaining scale independence on linear scales). We leave the full time- and scale-dependent analysis for future work.

Previous studies of phenomenological N -body simulations were carried out in [174–178]⁶. As discussed in [83], the interpretation of these simulations is murky, particularly in the details of their connection to linear parameterisations, and their signature on non-linear scales in particular modified gravity theories. By working from eq. (2.3) and the derivation and framework of [83], we avoid these possible problems, although we note that some of these earlier simulations are justified *post-hoc* by [83]. The works [176, 177] restrict themselves to smaller regions of parameter space, while the studies [174, 175] are similar to ours in

⁶As noted in [83], scalar field models typically arrive at a modified Poisson equation as well, so N -body simulations that seek to treat scalar field models quite generally (e.g. [179–181]) will be naturally similar to the code modifications we discuss here, although the justification and interpretation is different.

the sense that they concentrate on a purely time-dependent μ , although these simulations were run with a constant value for μ throughout the simulation. For this simplified setup, the authors in [174] derive a fitting function to calculate the power spectrum for arbitrary values of μ (see the appendix in [174] for details). In this work we explore the validity of the fitting function derived in [174], and other fitting functions in the literature, which attempt to reproduce the non-linear matter power spectrum $P(k)$ for modified gravity models.

Our simulations are the first to explore the phenomenology of μ having *different values in multiple redshift bins* through the simulation. This means that our method allows one to be sensitive to any time variation that μ may assume, irrespective of theoretical prejudices/biases. A similar analysis was conducted in [182], but this work did not involve N -body simulations. Moreover, this work employed the `halofit` formalism [88–90] and the Hu-Sawicki parameterisation that incorporates screening effects in the non-linear regime [183], which we explicitly show in this work is ill-suited to predicting the matter power spectrum for generic $\mu(z)$.

As noted, an advantage of a purely time-dependent μ is that the linear growth factor D is purely time-dependent, as in Λ CDM. We use this property in section 2.4 to isolate the differences in the phenomenology due to the different epochs at which modified gravity is ‘turned on’, and provide analytic checks of the simulations on large scales. It is also useful for comparing to different Λ CDM simulations, and when considering the “pseudo spectrum” in `ReACT` (see section 2.3). We solve for the linear growth factor $D(z)$ using

$$D'' + \left(2 + \frac{H'}{H}\right) D' - \frac{3}{2} \frac{\mu \Omega_{\text{m}} a^{-3}}{E(z)^2} D = 0, \quad (2.4)$$

where \prime denotes a derivative with respect to the logarithm of the scale factor a and $E(z)$ is the dimensionless Hubble function.

2.3 Methodology

2.3.1 N -body simulations

In this section we present the details of the N -body simulations and code modifications, as well as the tests and consistency checks we performed. We use the publicly available N -body code **GADGET-2** [184] as the basis for our N -body pipeline. **GADGET-2** and associated modifications have been used extensively in the literature to run a wide variety of dark matter-only simulations [185–187]. We restrict ourselves to dark matter-only simulations in order to understand modified gravity phenomenology in the absence of complications arising from baryonic physics. We present a summary of our numerical pipeline in the flowchart presented in fig. 2.1. We will now discuss the main branch of this pipeline in detail.

GADGET-2 implements a TreePM algorithm that involves a split of the gravitational force computation into a long-range and short-range force. We modify both the long-range and the short-range force in the algorithm. We follow a similar procedure as in [188], where we have a modified Poisson equation with a time-dependent μ parameter whose value is determined depending on the redshift of the simulation(s). We now describe the time evolution of μ within our simulations.

For the phenomenological pixels that we are considering, the μ function is split into a set of piece-wise constant redshift bins, i.e., each with a constant value for μ . In order to explore the phenomenology of this approach as well as make contact with earlier work [174], we run a suite of simulations with a simple “1-2-4” hierarchy of pixels. In other words, we split the simulation redshift interval $0 \leq z \leq 50$ into 1, 2, and 4 redshift bins of equal incremental growth in Λ CDM.

Number of bins	Redshift	μ	
1	0-50	1.044	0.956
2	0-7.0	1.100	0.900
	7.0-50	1.080	0.920
4	0-2.1	1.256	0.746
	2.1-7.0	1.167	0.837
	7.0-19.2	1.162	0.842
	19.2-50.0	1.161	0.843

Table 2.1: The redshift bins of equal Λ CDM growth according to the procedure described in the text, where we have the same linear growth at $z = 0$ when one of the bins is “switched on” for one, two and four bin(s). The μ values in each bin such that $P(k)$ at $z = 0$ when only that bin is turned on, is identical to $P(k)$ at $z = 0$ in the case when only the reference bin is turned on.

Note that while this choice does not necessarily cover much of the parameter-space, but crucially allows us to test the non-linear response to identical linear power spectra with different $\mu(z)$. We choose the values of μ in each bin such that the linear growth factor at $z = 0$ is equal when $\mu \neq 1$ in one of our redshift bins exclusively, with $\mu = 1$ in all the other bins (see table 2.1 and fig. 2.2 for the redshift bins and the respective μ values that correspond to each of them). The widths of each bin are chosen such that, for our cosmological parameters, there is equal growth in each bin in a Λ CDM universe. We reiterate this parameter space is multi-dimensional, which means that simultaneously covering a large portion of the parameter space while isolating non-linear behaviour is a difficult task. We focus on the latter in this work, as our intention is to understand the phenomenology.

We use 2nd order Lagrangian perturbation theory [189] to generate our initial conditions at $z = 50$ for all our simulations, via the 2LPTic code [190]. We only consider modifications to gravity from the starting redshift of the simulations, since at early times modifications to μ can be constrained by observations of the CMB [172]. This allows us to use the same initial conditions (and therefore

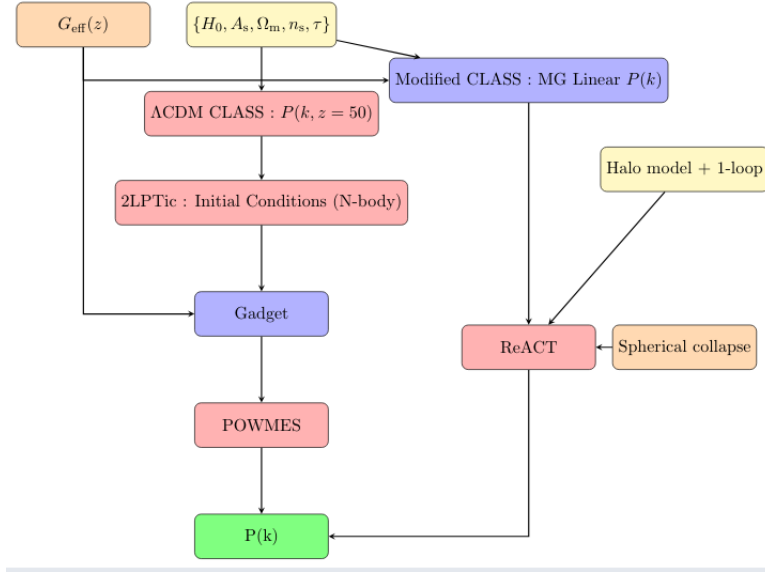


Figure 2.1: Flowchart of the numerical pipeline that we implemented. We establish initial conditions at $z = 50$, which are then evolved up to $z = 0$ using **GADGET-2**. Blue panels represent codes that we have modified, while red panels are codes that are used in their publicly available form. The modified gravity parameters are in orange, while Λ CDM parameters are in cream. The central branch represents our numerical simulation pipeline, while the right hand branch denotes our most successful pipeline for fitting the simulations (see section 2.3.2 for more details).

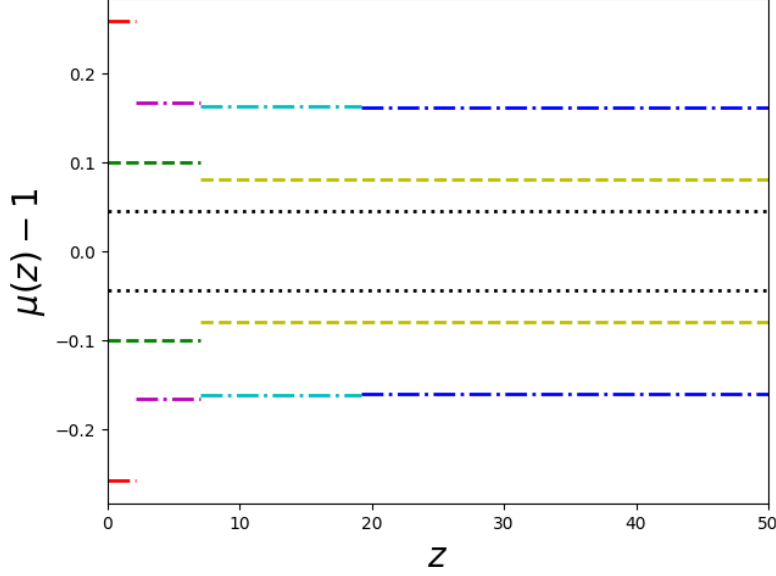


Figure 2.2: We illustrate the redshift evolution of μ in our simulations. Dotted lines represent the case where μ is constant through the simulation (one bin), dashed lines represent the case where there are two bins in redshift, while dot-dashed lines represent the case where there are four bins in redshift.

realisations) for modified gravity and Λ CDM, allowing us to focus on the phenomenology due to the modified gravitational evolution. We take advantage of these identical initial conditions as this allows us to present our results in terms of ratios of matter power spectra [191] for further details).

In order to demonstrate convergence in our simulations, we present ratios of the matter power spectrum as this allows one to neglect realisation-dependent effects [191]. We run all our simulations in a cosmological box of side $250 \text{ Mpc } h^{-1}$. (see appendix .1). For all our simulations, we use a Λ CDM initial power spectrum created using the CLASS code [192] at $z = 50$, with the following parameters $\Omega_m = 0.315$, $\Omega_\Lambda = 0.685$, $h = 0.674$, $n_s = 0.9619$ and $\sigma_8 = 0.811$. Note that we have tested that variation of the standard Λ CDM parameters at the level of 1% has no effect on our results.

In order to ensure that we do not have any systematic errors introduced into our

simulations due to a discontinuous transition in $\mu(z)$ we implement smoothing in **CLASS** as well as **GADGET-2**. We found that over the range of values we considered for the smoothing parameter, the differences between the smoothed and un-smoothed case were smaller than 0.1% (see appendix .2.2).

In addition to our suite of modified gravity simulations, we run a separate set of simulations with modified initial conditions such that we obtain Λ CDM matter power spectra with the same linear growth at $z = 0$ as our modified gravity simulations. These simulations have a modified value of $\sigma_8 = 0.883$ and $\sigma_8 = 0.742$, for the simulations with $\mu > 1$ and $\mu < 1$, respectively. This ensures that for each modified gravity simulation we analyse, we also have a Λ CDM simulation with an identical linear growth at $z = 0$. Crucially, this ensures that the **ReACT** fitting function that we explore later in section 2.3.2 predicts exactly the ratio of matter power spectra in modified gravity w.r.t. to Λ CDM spectra with matched linear growth at the same redshift. We refer to these Λ CDM spectra as ‘pseudo’ spectra. These simulations have the same initial seed as our standard Λ CDM simulations.

To measure the matter power spectrum from the output of our simulations, we use the publicly available **powmes** code [193, 194]. For notational convenience, we define the ratio $S(k) = P(k)/P_{\Lambda\text{CDM}}(k)$ to be the ratio of the matter power spectrum measured from our simulations to the Λ CDM power spectrum and $R(k) = P(k)/P_{\text{pseudo}}(k)$ to be the ratio of the modified gravity matter power spectrum from the simulations to the Λ CDM power spectrum with the same linear growth factor.

Note that we have primarily discussed the central branch of the flowchart in fig. 2.1 in this section; we now turn to the right hand side branch of the pipeline in section 2.3.2.

2.3.2 Predicting the power spectrum on non-linear scales

N -body simulations are too computationally expensive to be used to forecast and perform data analyses for upcoming surveys. In lieu of this issue, in this section we test the performance of various theoretical formulations that attempt to predict the full non-linear matter power spectrum for an arbitrary $\mu(z)$. We do this by comparing their respective accuracy in the reproduction of the ratio of the modified gravity matter power spectra with respect to the Λ CDM matter power spectrum as measured from our simulations, more specifically, we compare the quantity $R(k)$ as predicted by the fitting functions and with our measurement from the simulations. As mentioned before, this allows us to remain independent of realisation-dependent effects.

The results in [174] provide hints that knowledge of the linear power spectrum is insufficient to completely calculate the matter power spectrum on non-linear scales. This has important consequences for the fitting functions. In section 2.4 we show explicitly that in our framework simulations with identical linear matter power spectra can show significant differences in their non-linear power spectra from varying $\mu(z)$ (see appendix .2.2).

We consider the following formalisms as candidates for predicting the non-linear matter power spectrum:

- case 1 - the fitting function obtained in [174];
- case 2 - the standard halo model as in eqs. (2.6),(2.7) with a Sheth-Tormen mass function [195, 196];
- case 3 - the `halofit` fitting procedure [88];
- case 4 - the halo model reaction formalism [87] (ReACT).

We will now briefly describe each case.

Case 1: Cui et. al.

To our knowledge, the only fitting function in the literature based on an arbitrary μ is that presented in [174]. As noted earlier, this fitting function was estimated assuming a constant μ through the simulations, which is not the case in our simulations in general. Nevertheless, we investigate the performance of this fitting function in the context of our simulation results. The fitting function is given by

$$R(x, \mu) = \exp \left\{ ((1 - \mu)B(\mu)x^{C(\mu)}) \right\} , \quad (2.5)$$

where $R(x, \mu)$ as mentioned in the main text is the ratio of the matter power spectrum in modified gravity relative to the Λ CDM pseudo spectrum (with equal linear growth). $B(\mu) = 0.0429 + 0.133\mu^{-4}$, $C(\mu) = 0.573$ and $x = \Delta^2(k, z, \mu = 1)$ is the dimensionless power spectrum $P(k)k^3/(2\pi)$. The main feature of this function is that it predicts $R > 1$ when $\mu < 1$ and vice-versa when $\mu > 1$. In other words, this fitting function assumes that the non-linear evolution is slower when the growth rate is increased due to μ being larger than its value in Λ CDM, and vice versa. While we have observed a similar behaviour in some of our simulations, we find that this is not true in the general case.

We demonstrate in fig. 2.3 that one can reproduce with reasonable success the matter power spectrum in the case where μ is constant throughout the simulation time period.

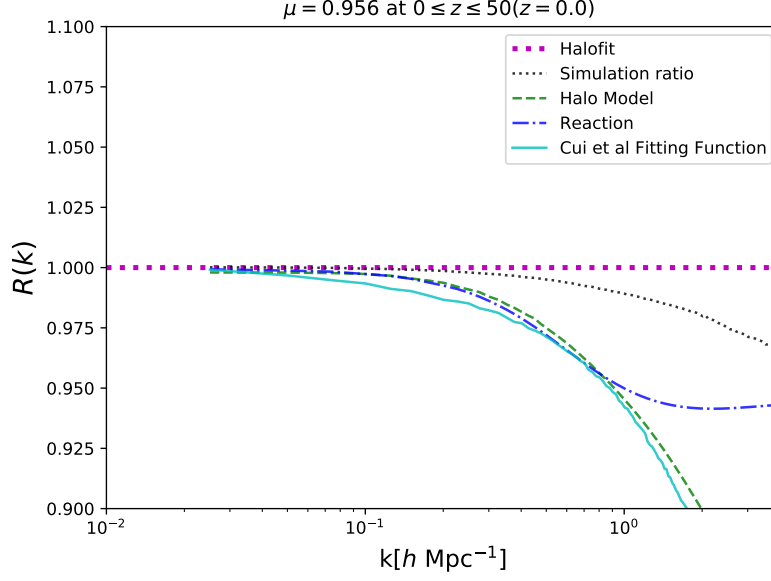


Figure 2.3: The ratio of the matter power spectrum in the simulation with $\mu = 0.956$ throughout the simulation period. The Cui et al. fitting function [174] is designed to model the power spectrum in this case, where μ is constant.

Case 2: Halo model

The standard halo model consists of the 1-halo term, given by

$$P^{1h}(k) = \int dm n(m) \left(\frac{m}{\bar{\rho}} \right)^2 |u(k|m, z)|^2, \quad (2.6)$$

which is the contribution to the power spectrum from a single halo, along with the 2-halo term given by

$$\begin{aligned} P^{2h}(k) &= \int dm_1 n(m_1) \left(\frac{m_1}{\bar{\rho}} \right) |u(k|m_1, z)| \int dm_2 n(m_2) \left(\frac{m_2}{\bar{\rho}} \right) \\ &\times |u(k|m_2, z)| P_{hh}(k, z|m_1, m_2), \end{aligned} \quad (2.7)$$

which is the contribution from 2 different haloes, where $n(m)$ is the mass function, $u(k, z|m)$ is the Fourier transform of the density profile dark matter haloes of mass m at redshift z and P_{hh} is the halo power spectrum, related to the two-point-correlation function of the haloes themselves and quantifies the interaction

between two haloes. Of these, the first term dominates on small non-linear scales, i.e., at large k , while the 2-halo term dominates on large scales. Note that the 2-halo term is usually well approximated by the linear matter powers spectrum in the literature.

In order to compute the 1-halo term, we calculate the mass function and the bias term assuming a time-dependent μ according to the Sheth-Tormen procedure [195, 196] and perform the integrals in eqs. (2.6) and (2.7). We then obtain the full non-linear matter power spectrum by summing up the 1-halo term and 2-halo term. As a cross-check we ensured that our results are replicated by summing the 1-halo term and the linear matter power spectrum.

Increasing the value of μ increases the rate of structure formation which means that haloes form earlier, resulting in smaller concentration parameters associated to the haloes. Since the Fourier transform of the density profiles is directly proportional to the concentration parameter, the contribution from the 1-halo term is smaller, resulting in a lack of power on smaller scales [174] (with the opposite taking place for $\mu < 1$).

Case 3: Halofit

We also consider the `halofit` fitting procedure [88–90] that is commonly used for a Λ CDM Universe. It is important to note that the fitting procedure is entirely derived from the linear power spectrum in `halofit`. This clearly introduces a degeneracy, i.e., all $\mu(z)$ that lead to the same linear growth at $z = 0$ are indistinguishable.

Case 4: Halo model reaction

The halo model reaction formalism integrates a modified halo model and the spherical collapse model together to predict the matter power spectrum on non-linear scales. As mentioned before, the halo model suffers from a lack of accuracy on quasi-linear scales as in the original recipe. The authors go one step further to address this problem via the reaction term, given by

$$\mathcal{R}(a, k) = \frac{[(1 - \epsilon(z))e^{-k/k_*(z)} + \epsilon(z)] P_{\text{mg}}^{\text{lin}}(z, k) + P_{\text{mg}}^{\text{1h}}(z, k)}{P_{\text{pseudo}}^{\text{hm}}(z, k)}, \quad (2.8)$$

where the subscript ‘pseudo’ represents the pseudo spectrum and k_* is computed from perturbation theory [197]. Therefore, the quantity \mathcal{R} , the so-called reaction, is a ratio of halo-model power spectra. In order to obtain a prediction of the modified gravity power spectrum, one simply multiplies \mathcal{R} by the full non-linear Λ CDM pseudo spectrum. To understand how well **ReACT** captures our simulations, we use the **ReACT** code to calculate $R(a, k) = P_{\text{mg}}/P_{\Lambda\text{CDM}}^{\text{pseudo}} = \mathcal{R}$.

The quantity \mathcal{R} has the following basic features:

- On linear scales, $\mathcal{R} \rightarrow 1$ by construction since the pseudo-spectrum has the same linear growth as the modified gravity spectrum.
- On small non-linear scales the reaction is given by the ratio of the 1-halo terms, i.e., $\lim_{k \rightarrow k_{\text{nl}}} \mathcal{R} \rightarrow P_{\text{mg}}^{\text{1h}}(z, k)/P_{\text{pseudo}}^{\text{1h}}(z, k)$.

The reaction term in eq. (2.14) may be computed from the following equations

$$P_{\text{pseudo}}^{\text{hm}} = P_{\text{pseudo}}^{\text{lin}} + P_{\text{pseudo}}^{\text{1h}}, \quad (2.9)$$

$$\epsilon = \lim_{k \rightarrow 0} \frac{P_{\text{mg}}^{\text{1h}}(z, k)}{P_{\text{pseudo}}^{\text{1h}}(z, k)}, \quad (2.10)$$

$$k_*(z) = -\bar{k} \left(\ln \left[\frac{A(\bar{k}, z)}{P_{\text{mg}}^{\text{lin}}(z, k)} - \epsilon(z) - \ln(1 - \epsilon(z)) \right] \right), \quad (2.11)$$

$$A(k, z) = \frac{P_{\text{mg}}^{\text{1-loop}}(z, k) + P_{\text{mg}}^{\text{1h}}(z, k)}{P_{\text{pseudo}}^{\text{1-loop}}(z, k) + P_{\text{pseudo}}^{\text{1h}}(z, k)} P_{\text{pseudo}}^{\text{hm}}(z, k) - P_{\text{mg}}^{\text{1h}}(z, k), \quad (2.12)$$

where the 1-loop terms may be computed from Fourier transforming the Poisson equation [86, 87]

$$-k^2 \phi(a, k) = \frac{3\Omega_{\text{m}}(a)aH(a)}{2} \mu(a, k) \delta(a, k) + \tilde{S}(a, k), \quad (2.13)$$

where the source function $\tilde{S}(a, k)$ encodes non-linear corrections to the Newtonian Poisson equation that appear at higher order. Essentially, one can derive $\tilde{S}(a, k)$ for specific models and the corresponding screening mechanisms that operate on the relevant scales. The authors in [86] calculate $\tilde{S}(a, k)$ for $f(R)$ and DGP gravity in order to reproduce the full non-linear matter power spectrum in modified gravity. Note that the **ReACT** code is set up to automatically calculate $\tilde{S}(a, k)$ for these two models and Λ CDM (where it is zero).

In contrast to [86], our work is designed to understand the phenomenology while remaining model-agnostic and therefore, we neglect any screening mechanisms and indeed any scale dependent corrections to the Poisson equation given in eq. (2.3). Therefore, in order to reproduce the matter power spectrum in our formalism within the **ReACT** code, we only modify the μ parameter and set $\tilde{S}(a, k) = 0$ and indeed all the other modified gravity parameters within the code to their

respective values in Λ CDM. This simplifies the numerical implementation of the **ReACT** while still being able to estimate the non-linear effects of modifying μ . In this case, we are able to directly calculate the reaction term for our case of independent redshift pixels for μ

$$P_{\text{mg}}(z, k) = \mathcal{R}(z, k) P_{\text{pseudo}}(z, k), \quad (2.14)$$

where P_{pseudo} is the Λ CDM ‘pseudo’ power spectrum with identical linear growth to P_{mg} .

Comparison of performance of fitting functions

In figs. 2.4 and 2.5, we show the ratio of the quantity $R(k)$ (i.e., the ratio of the modified gravity matter power spectrum to the pseudo Λ CDM matter power spectrum) as predicted by the fitting functions with respect to the same quantity computed from the simulations. Note that the focus is on understanding the constraining power contained in the non-linear power spectrum, separate from the linear power spectrum and not on the viability of the models under consideration. We have chosen a subset of our simulations that is representative of the performance of the different fitting functions we consider. Clearly, we see that the fitting function in [174] fails to predict the correct non-linear behaviour when μ is not a constant value throughout the simulation. As expected, the **halofit** prediction is identical for all the simulations, since they all have identical linear growths. In other words, the simulations where the **halofit** performs better than **ReACT** are the cases where modified gravity parameters coincidentally result in a matter power spectrum that is already very close to that of Λ CDM. We show that on average, this accidental success is not typically replicated in the general case. We see that while the **ReACT** formalism doesn’t always predict the non-linear

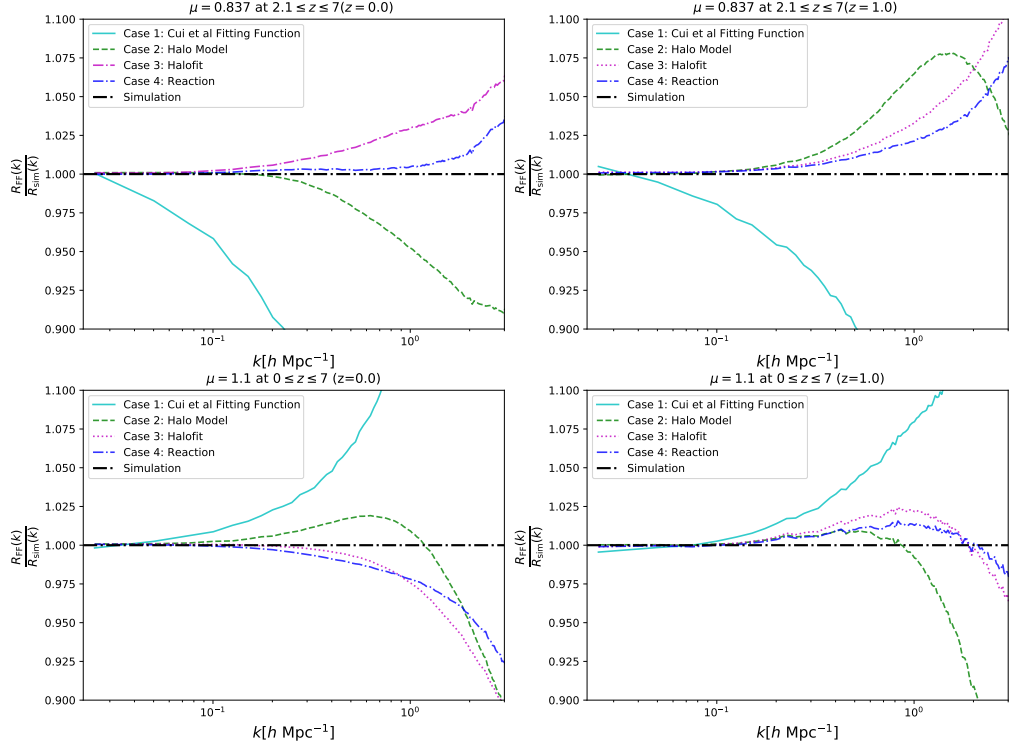


Figure 2.4: The ratio of the quantity $R(k)$ as predicted by the various fitting functions (as indicated by the superscript ‘FF’) with respect to the same quantity computed from the simulations (as indicated by the superscript ‘sim’). It is clear that the cyan line from the fitting function of [174] fails for all cases. The green dashed curve is the simple application of the halo model as shown in eqs. (2.6) and (2.7). It is important to note that the **halofit** prediction (magenta dotted) is actually identical for all the simulations, since they all have identical linear power spectra. In all the panels, we can clearly see the **ReACT** curve (blue dot-dashed) is accurate to within 5% across almost the entire range of scales up to $\sim 3 h \text{ Mpc}^{-1}$.

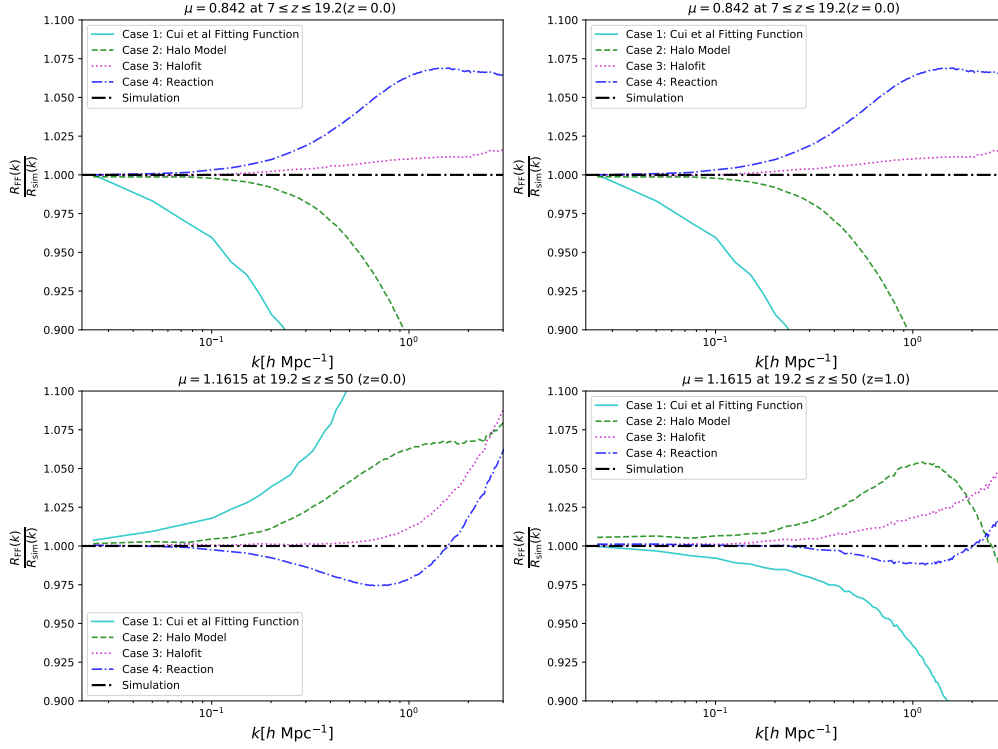


Figure 2.5: As in fig. 2.4, but where μ has a different value from GR in one of the earlier redshift bins.

trend perfectly, it appears to be consistently within 5% of the simulations. Since we are only interested in understanding the modified gravity phenomenology, we do not vary Λ CDM parameters in this work. We leave the full validation of **ReACT** across Λ CDM and modified gravity parameter space to future work.

We use the following least-square statistic to quantify the agreement between the various fitting functions with our simulations

$$\chi^2 = \frac{1}{N} \sum_{k=0.02 \, h \, \text{Mpc}^{-1}}^{k=k_{\text{cut}}} [R_{\text{sim}}(k) - R_{\text{FF}}(k)]^2, \quad (2.15)$$

where $N = 160$, with the sampling in Fourier space being approximately logarithmic, as in **powmes** and k_{cut} is a wavenumber cut-off that we choose. The subscript ‘sim’ implies the ratio as measured in our simulations and the subscript

‘FF’ implies the ratio as predicted by the various fitting functions. We employ a cut-off at $k_{\text{cut}} = 3 h \text{ Mpc}^{-1}$, which is the theoretical threshold up to which the **ReACT** formalism is supposed to be accurate [87]. Note that this scale is within the region of validity of our simulations (see fig. 1), which is $k_{\text{cut}} = 5 h \text{ Mpc}^{-1}$. We show the χ^2 statistic with both wavenumber cut-offs in fig. 2.6. This indicates that the **ReACT** formalism provides the best fit to our simulations, as evidenced by the fact the red line is largest in the majority of the cases presented. Note that since we plot the negative logarithm, a larger bar corresponds to a better fit. We also note that due to the failure of the Cui et al. [174] (see eq. (2.5)) even at small k to capture the results of our simulations, we don’t include their fitting function in this figure.

We also show the wavenumber k_{fail} at which the quantity $R_{\text{FF}}(k)/R_{\text{sim}}(k)$ deviates from unity at the level of 3 and 5 %, respectively in the right panel of fig. 2.6. Note that this probes the validity in k -space of each fitting function, while the χ^2 statistic is an indicator of the accuracy of each fitting function within this region of validity. The combination of k_{fail} and χ^2 throws light on the applicability of a fitting function to future forecasts.

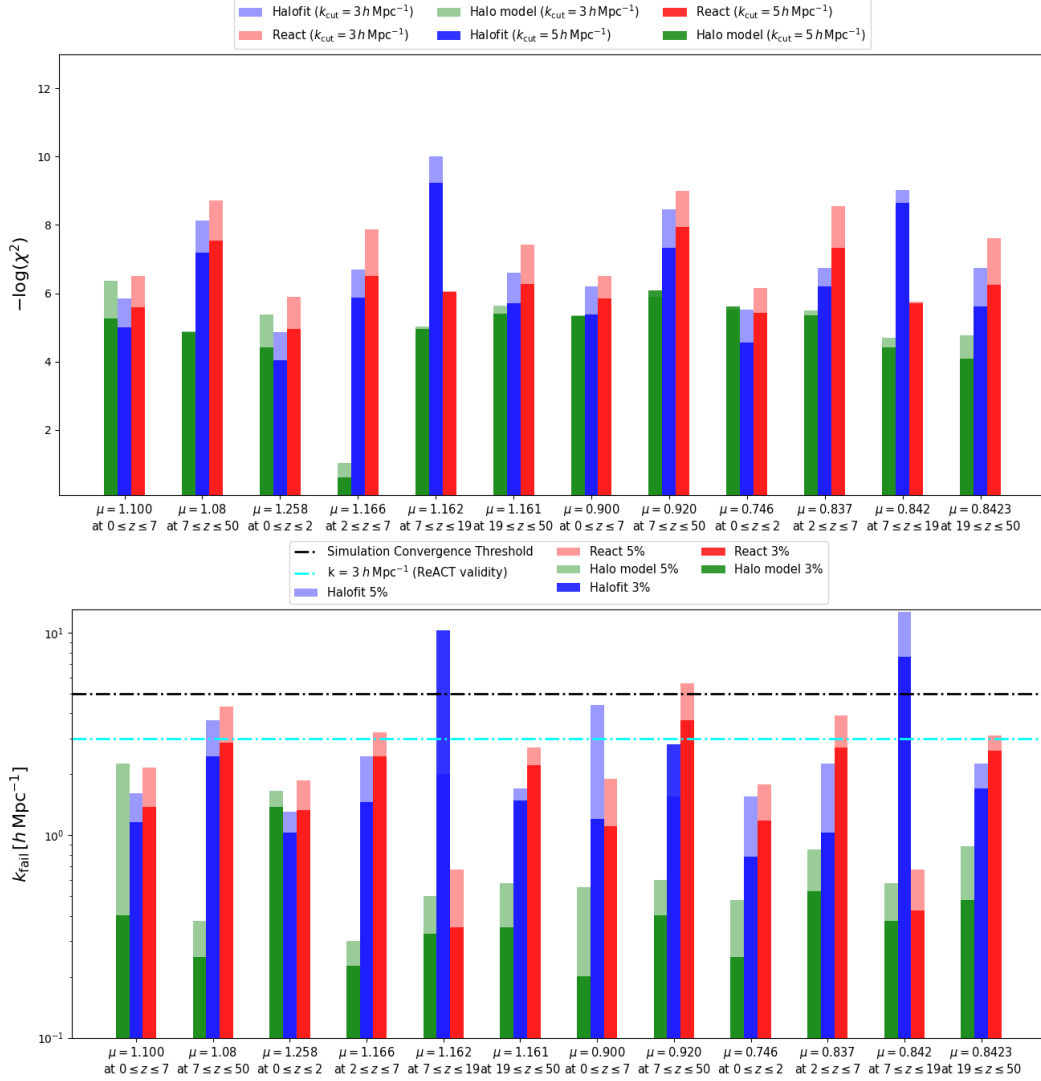


Figure 2.6: In the top panel, we show the values of the least square statistic for the different fitting functions as defined in eq. (2.15). We obtained these values by employing $k_{\text{cut}} = 3 h \text{ Mpc}^{-1}$ and $k_{\text{cut}} = 5 h \text{ Mpc}^{-1}$, which represent the wave number up to which the ReACT formalism is designed to operate and the wave number up to which we have converged results from our simulations, respectively. Clearly, the red bar is larger than the other bars in the majority of the simulations which implies that the ReACT formalism is typically the best fit over the range of scales (note that since we plot the negative logarithm, a larger bar is a better fit). In the bottom panel, we plot the wavenumber at which the quantity $R(k) - 1$ is at 3% and 5%, respectively. The results are consistent with the left panel, with the red bar being the largest for the majority of the simulations. This shows that the ReACT formalism allows one to probe deeper into the non-linear regime.

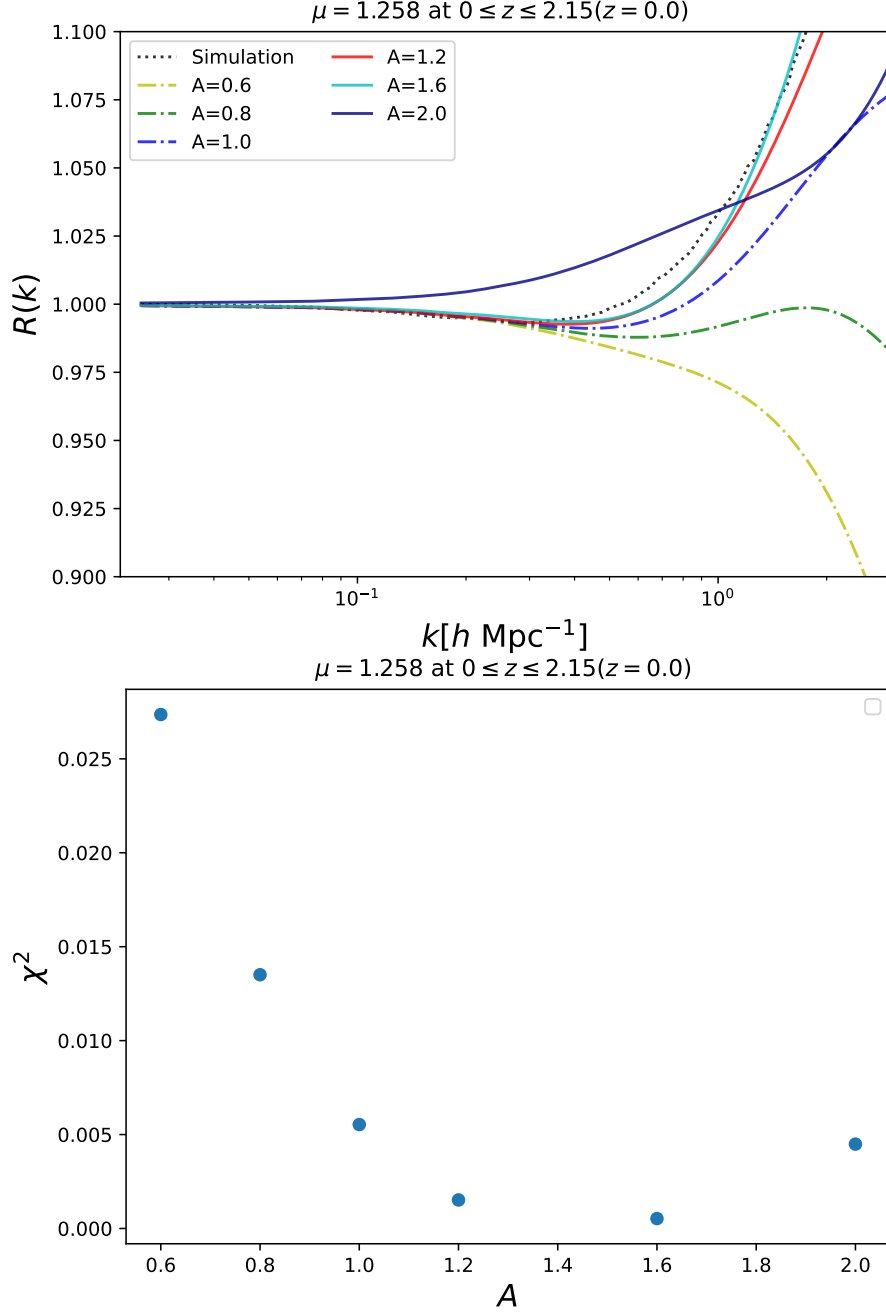


Figure 2.7: We display the ratio of the power spectra with respect to one of our simulations for several values of the parameter A in the top panel. The solid cyan line (which corresponds to $A = 1.6$) is the best fit, with the smallest χ^2 parameter, as can be seen by the plot on the bottom panel. While this behaviour was hinted at in various works in the literature [174], to our knowledge this is the first time that such an analysis has been carried out for the general model-independent case time-varying μ . We leave the analysis of varying A as a function of μ and the resulting rigorous validation of this modification to future work.

2.4 Simulation phenomenology

In this section, we discuss the phenomenology from our full suite of simulations with the fourteen different forms of $\mu(z)$. Our goal is to understand the variation in the non-linear matter power spectrum as a function of $\mu(z)$. We remind the reader that the redshift bins in our simulations are fixed by requiring that the linear growth in Λ CDM is identical for all the bins. In each simulation, we switch on μ in one and only one redshift bin and tune the value of μ such that the linear growth at $z = 0$ is identical in all our simulations.

In the top row of fig. 2.8, we present the ratio $S(k)$ (at redshift zero) of the power spectra from all the simulations to the Λ CDM spectrum with the same initial conditions. We note that while the ratio relative to the pseudo-spectrum $R(k)$ is the most appropriate ratio for the fitting functions in the previous section, here we focus on $S(k)$ because it throws light on the different structure formation histories of the simulations with respect to Λ CDM. By design, the lines in these plots are all equal on linear scales (for small k). We observe two distinct features in $S(k)$, present on quasi-linear scales and non-linear (large k) scales respectively. Firstly, we consistently see a rise (or dip, depending on whether $\mu > 1$ or $\mu < 1$) in power across all simulations on quasi-linear scales at the level of $\sim 20\%$ (at $0.1 h \text{ Mpc}^{-1} \leq k \leq 1 h \text{ Mpc}^{-1}$). This is followed by a “split” behaviour on small (non-linear) scales, where the power depends on the range of redshifts over which the modified gravity effects were switched on, and the simulations with $\mu \neq 1$ at large redshifts exhibit the opposite behaviour to the case where it is switched on at small redshifts. This is due to varying halo formation times and inter-halo clustering, as we will discuss later in this section.

The quasi-linear behaviour may be attributed to the difference in growth histories

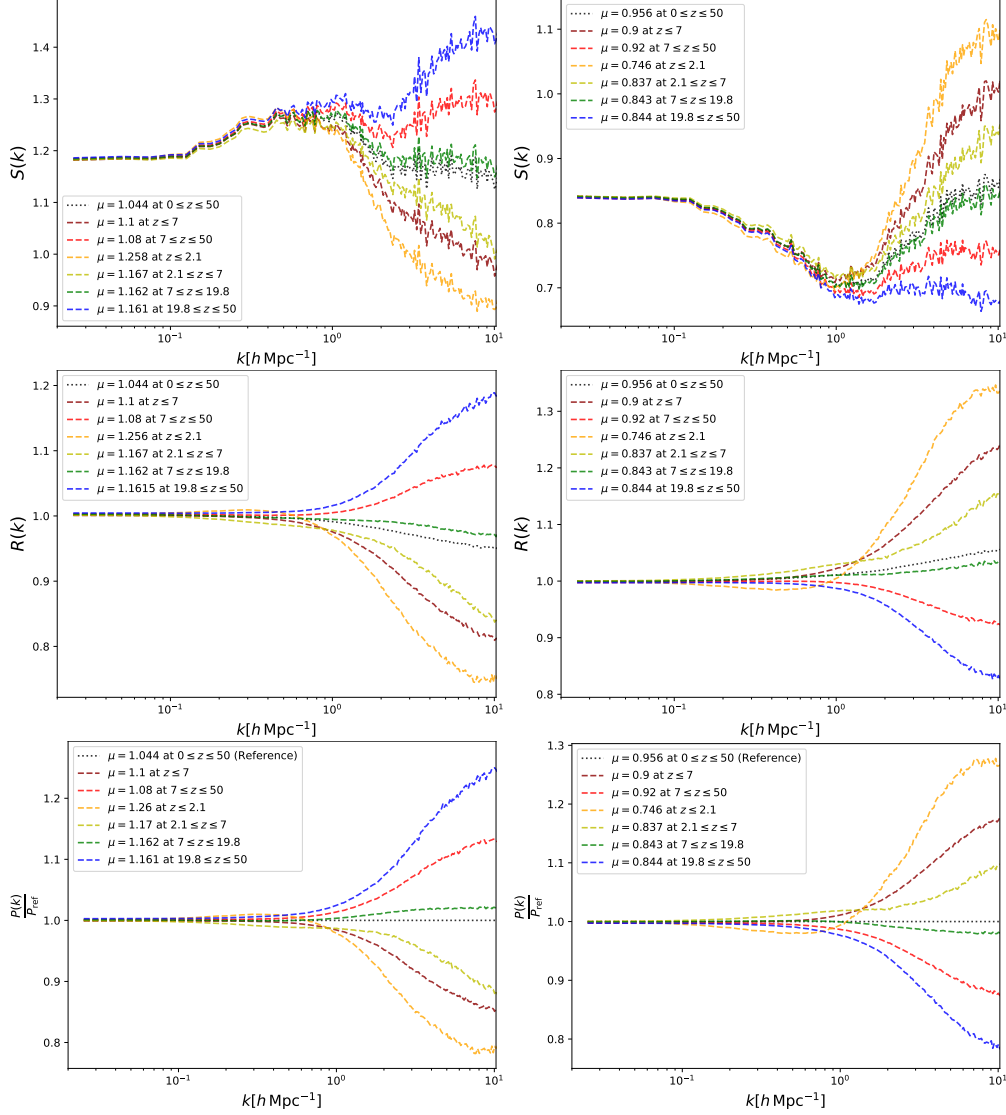


Figure 2.8: *Top row:* The ratio of the power spectra from all the simulations to the Λ CDM power spectrum at $z = 0$. Note that we see a quasi-linear bump in these due to the mismatch in linear growth, which is absent in the other rows. We see the multi-dimensionality of the parameter space in display here since we have 6 different unique non-linear power spectra for the same linear power spectrum as the case where μ is constant throughout the simulation as studied in [174]. *Middle row:* The quantity $R(k)$, the ratio of the matter power spectra from the different simulations to the pseudo Λ CDM power spectrum with the same linear growth. *Lower row:* Ratio of power spectra at $z = 0$ from all the simulations to the power spectrum at $z = 0$ from the reference simulation with a constant μ throughout, with redshift bins according to table 2.1.

between Λ CDM and the different simulations, since the effect of a different growth rate is more pronounced on quasi-linear scales compared to linear scales. We illustrate this using the middle panels of fig. 2.8, where we compute the ratio of the matter power spectrum in our simulations to the pseudo power spectrum. This quasi-linear feature is significantly diminished, since the pseudo power spectrum has the same linear growth at $z = 0$, so by construction the increased effects of the changed growth are mostly removed. This is why the pseudo power spectrum is a good comparison point when examining fitting functions. The same quasi-linear behaviour is seen in the bottom panel, where we compute the ratio of the matter power spectra relative to a reference simulation where μ is held constant in redshift.

We now turn to the non-linear split behaviour that we see in all of the rows. On small scales the lines diverge, depending on the redshift range during which $\mu \neq 1$ in each simulation. In particular, the simulations where $\mu \neq 1$ at earlier times, continues the trend expected from linear scales, that $\mu > 1$ increases the power and vice versa for $\mu < 1$. However, varying μ at low redshifts introduces the opposite effect to linear theory. For example, $\mu > 1$ at late times actually leads to a lack of power on non-linear scales. This results in “crossing points” with respect to Λ CDM, i.e. scales below which the power spectrum is actually reduced, despite equal initial conditions and $\mu > 1$. This implies that the state of clustering when μ is modified, in terms of how much structure has already formed and on what scales, is important for understanding the final clustering spectrum on small scales at redshift zero. Since we obtain intrinsically different shapes for the power spectra for different values of μ with identical linear growths, the discussion on concentration factors in [174] is insufficient to explain the physics of these simulations. These plots clearly show that any fitting procedures that

predict the non-linear matter power spectrum purely from the linear spectrum will fail to capture non-linear effects accurately.

We can examine this small-scale issue in more detail by looking at the redshift evolution of the matter power spectrum in our simulations. In fig. 2.9, we show the ratio of the power spectra from the simulations to the Λ CDM spectrum, at all of our output redshifts. There is a clear transfer of power over time from small scales to large scales. This is demonstrated in the top row where the peak/trough (depending on whether $\mu > 1$ or $\mu < 1$) in the ratio of the power spectra shifts to the left, i.e., to larger scales as one steps forward in redshift (from high redshift to low redshift). In the bottom panels, this transfer of power persists, although we see it manifested as a phenomenon that ‘evens out’ the power over large and small scales. This transfer of power indicates the formation of larger structure in the universe causing power to be deposited on larger scales. Comparing the position and height of this peak/trough provides information on the rate of structure formation and the gravitational interaction at different epochs. On comparing the behaviour of the magenta, black and red lines in the top row with the bottom row, we also see the reinforcement of our earlier result, that there is an excess of power in the non-linear regime when $\mu > 1$ at high redshift, and vice versa at low redshift (this behaviour is mirrored when $\mu < 1$). We now consider these two cases in more detail.

Structure formation in the Universe is hierarchical, with smaller halos being formed before larger ones. Therefore, modifying μ at early times impacts the power spectrum on the smallest scales as demonstrated in the bottom row of fig. 2.9 where there is a substantial peak in $S(k)$ on small scales at high redshift $z = 4$ and $z = 5$. This is due to the fact that only the smallest halos were in

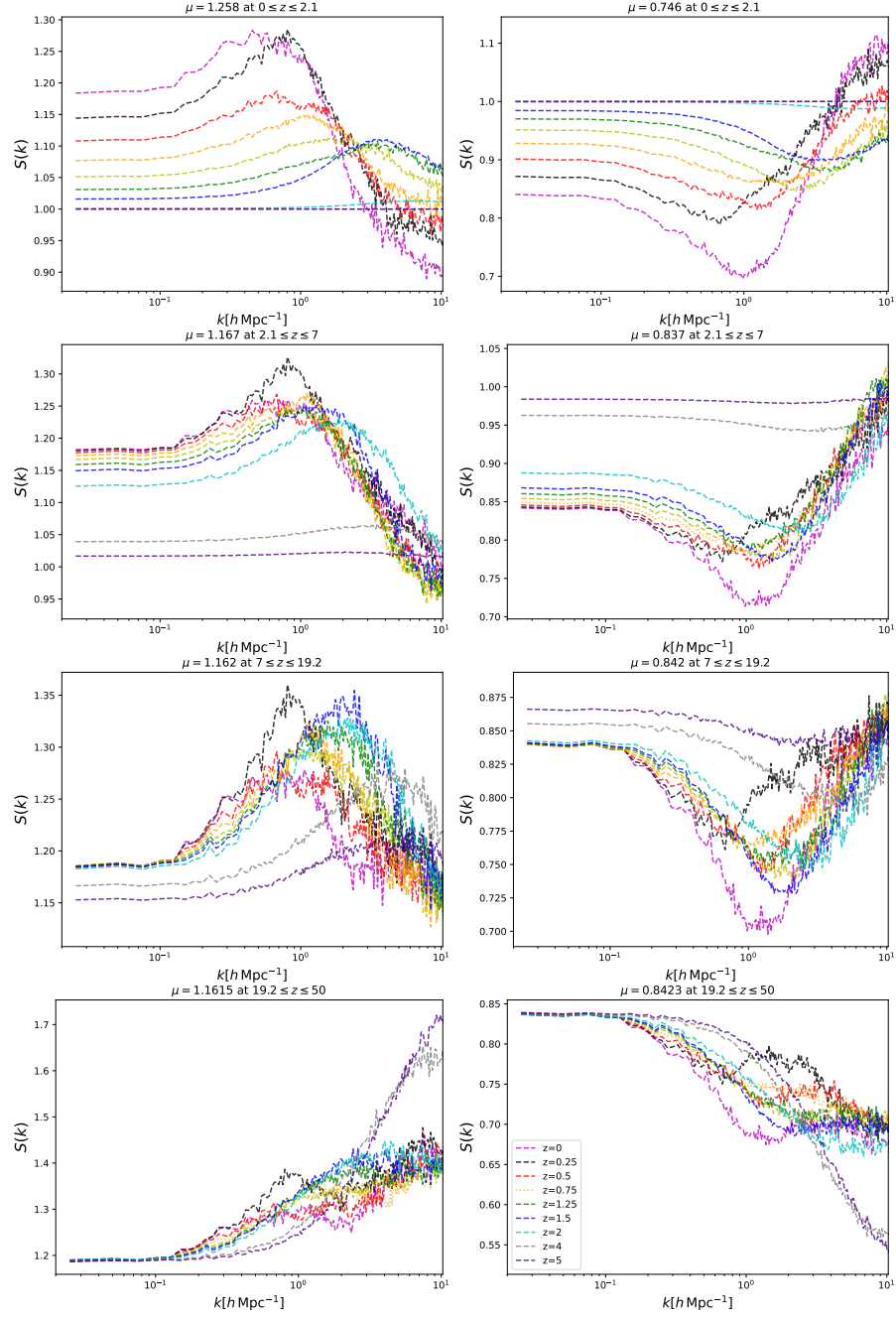


Figure 2.9: The ratio of the power spectra at all the redshifts output from our simulations relative to the Λ CDM power spectrum at the same respective redshifts, for the case where we have 4 bins in μ but the same linear growth at $z = 0$. These figures highlight the hierarchical nature of structure formation and its varying influence on the power spectrum depending on whether μ is switched on early in the simulation or later. In the former case, we have an early modification of the non-linear power spectrum, the imprint of which can be noticed at $z = 0$, while in the latter case, the late switching on of μ , introduces interaction between already formed structures resulting in non-intuitive shapes for the matter power spectrum.

the process of formation. Effectively, the increase in the rate of structure formation at early times causes smaller halos to be formed earlier. The formation of larger structure only takes place when growth reverts to the Λ CDM rate. As one steps forward in redshift, one sees that this small scale peak is diminished, but not totally destroyed. As larger halos start to form, mergers begin to take place leading to a gradual shift in power towards larger scales. However, there is still an excess of power at $z = 0$ on small scales, as a signature of the enhanced structure formation at earlier times.

Modifying μ at late times introduces additional complexity, since at late times, larger structures have started to form. Therefore, increasing/decreasing the strength of gravity massively impacts the interaction between larger halos, i.e., halo power spectrum as seen by the aforementioned shift in the peak of the power spectrum to the left in the top row of fig. 2.9. Physically, this means that the interaction between halos depletes power on smaller scales and deposits power on intermediate/large scales. Therefore, there is a transfer of power from smaller scales to larger scales (and of course the opposite happens when $\mu < 1$). This further validates the behaviour of the orange, dark red and yellow lines in fig. 2.8, where the small scale behaviour is opposite to that on linear scales. We note that the middle rows in fig. 2.9 contain a mix of the two limiting cases described in the above paragraphs.

2.5 Impact on weak-lensing observables

2.5.1 Computing weak-lensing observables in modified gravity

We now discuss the impact of varying μ in different redshift bins on the observables. In this section we compute the weak-lensing convergence power spectrum from the output of our simulations, and examine the impact of having predictions that are not restricted to linear scales. Furthermore, we also discuss how one can probe our two-parameter family approach to modified gravity from the output of our simulations.

The weak-lensing convergence power spectrum can be computed from the matter power spectrum and the modified gravity parameters from section 2.2 using the following expression

$$C_\ell = \frac{9H_0^4\Omega_m^2}{4c^4} \int_0^{\chi_{\max}} d\chi \frac{1}{a^2(\chi)} g^2(z) \frac{\mu^2(1+\eta)^2}{4} P_\delta(\ell/\chi), \quad (2.16)$$

where P_δ is the matter power spectrum, η is the second modified gravity parameter that affects the photon geodesics and χ is the comoving angular diameter distance to the source along the line of sight. This equation is derived using the standard procedure of solving for null geodesics in the perturbed FLRW metric, in order to express the convergence in terms of the metric potentials, but we then replace the potentials by substituting the modified Poisson equation in eq. (2.3). We stress that in order to compute the matter power spectrum, one requires no knowledge of η . Therefore, we need only model μ in our N -body simulations. We will return to this point shortly. In practice, the above integral is truncated at the distance χ_{\max} corresponding to the maximum source redshift the survey is

sensitive to. In this work, we concentrate on the auto-power spectra. The additional complications involved in the analysis of the cross-power spectra requires a full statistical forecast, which is beyond the scope of this work.

The function $g(z)$ is a filter function that depends on the redshift distribution of the background galaxies and is typically written as

$$g_i(z) = \int_z^\infty dz' \left(1 - \frac{\chi(z)}{\chi(z')} \right) n_i(z'). \quad (2.17)$$

We use the standard expression for the source galaxy redshift distribution given by [198]

$$n(z) \propto \left(\frac{z}{z_0} \right)^\alpha \exp \left[- \left(\frac{z}{z_0} \right)^\beta \right]. \quad (2.18)$$

We adopt a Euclid-like binning of the source number density into 10 equi-populated bins according to eq. (2.18) with $z_0 = 0.9/\sqrt{2}$, $\alpha = 2$ and $\beta = 3/2$, where we have assumed an average source density $\bar{n}_g = 30 \text{ arcmin}^{-2}$ [2, 199–202]. Due to the fact that the **ReACT** formalism is only valid at $z < 2.5$, we concentrate only on the first tomographic bin, i.e., $0 \leq z \leq 0.4$. The error bars are obtained by computing the following [202]

$$\delta C_\ell^{ij} = \sqrt{\frac{2}{f_{\text{sky}}(2\ell + 1)}} \left(C_\ell^{ij} + \frac{\sigma_\epsilon^2}{\bar{n}_i} \right), \quad (2.19)$$

where $f_{\text{sky}} = 0.7$ is the fractional sky coverage, $\sigma_\epsilon = 0.21$ is the variance of the observed ellipticities and \bar{n}_i is the surface galaxy density of each bin. Essentially, we combine the Poisson shot noise contribution with cosmic variance to obtain the total uncertainty on the power spectrum, P_κ .

Note that since this involves an integration along the line of sight, one needs to compute the matter power spectrum at multiple redshifts and interpolate between

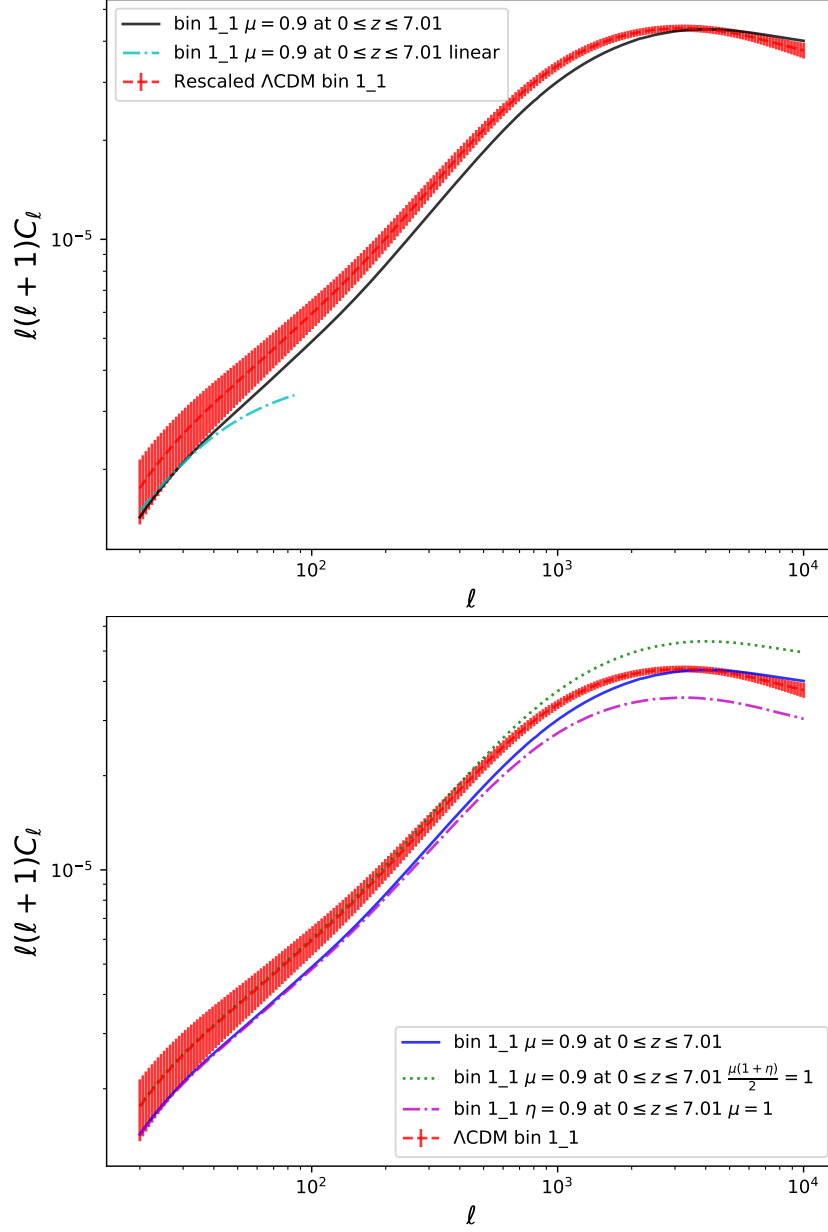


Figure 2.10: In the top panel, we show the weak lensing auto-power spectrum for a particular tomographic bin from Λ CDM (red-dashed) and from the simulations with $\mu = 0.9$ at $0 \leq z \leq 7.01$ (blue solid). Note that we are using the Λ CDM simulation with rescaled initial conditions at $z = 50$. In the bottom panel, we show three different curves with the same μ bin, but with different values of η . The first curve has $\eta = 1$ (blue solid). The second has $\eta = 0.8$ such that the prefactor $\mu(1 + \eta)/2 = 1$ as in Λ CDM (green-dotted), such that the modified gravity effects only enter through the modified P_δ . Finally, we show the case where $\mu = 1$, but $\eta = 0.8$ at $0 \leq z \leq 7$, which has a different shape, i.e., different scale dependence on non-linear scales. Therefore, we show how our approach may be used by future missions to put constraints on both μ as well as η . We stress that by explicitly going to non-linear scales, we are able to break the degeneracy between η and μ that exists in linear theory.

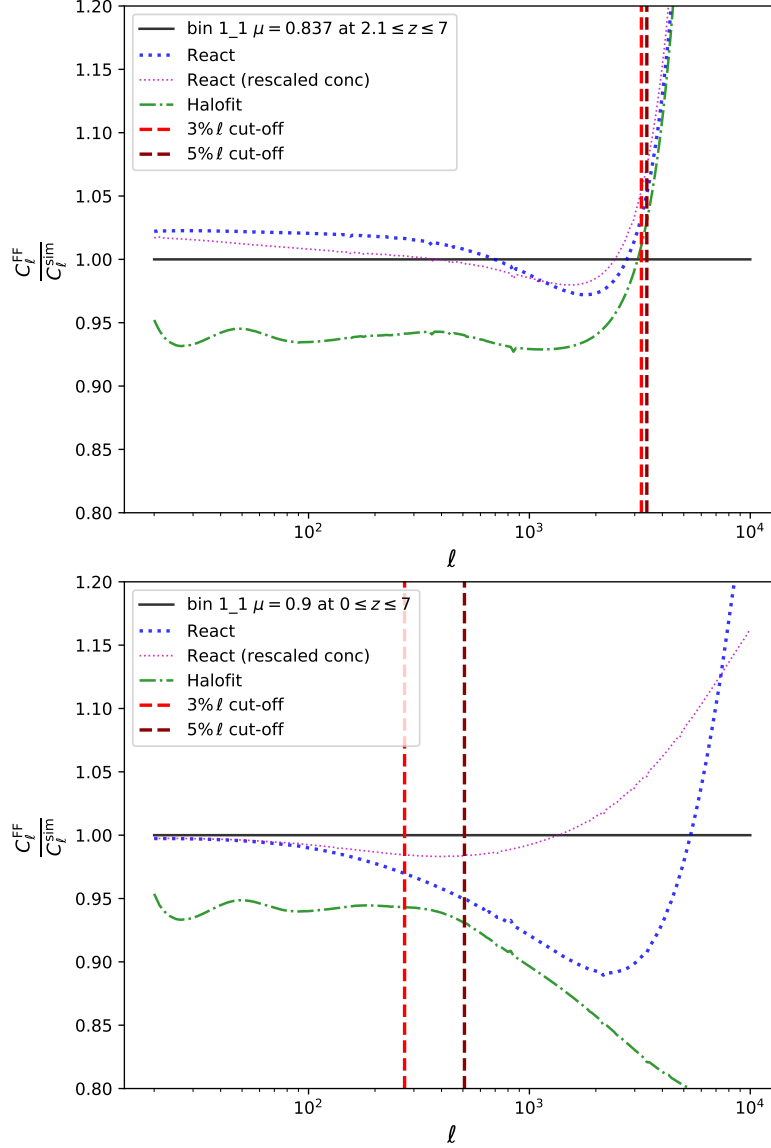


Figure 2.11: We show the ratio of the convergence power spectra obtained from the matter power spectra as predicted by the **ReACT** (blue-dotted) and **halofit** (green dot-dashed) formalisms with respect to those obtained from the simulation matter power spectra. The superscripts ‘FF’ and ‘sim’ imply ‘fitting function’ and ‘simulation’, respectively. We immediately see that **halofit** performs significantly worse than **ReACT** even at low ℓ , where it fails at the level of $\sim 5\%$. The vertical lines indicate the value of ℓ at which the **ReACT** curve deviates from the simulation curve at the level of 3% and 5%, respectively. We choose two simulations that capture the variation in the ℓ cut-offs in our sample of simulations. In the left panel is the simulation with the largest ℓ cut-offs in our sample of simulations. In the right panel, we show a simulation with one of the smallest ℓ cut-offs. The better performance of the **ReACT** formalism over **halofit** in such a model-independent analysis of modified gravity on non-linear scales is clearly demonstrated. We also show the curve with the concentration parameter modified (see fig. 2.7) which seems to further improve the **ReACT** fit, see text for details.

them to compute the integral in eq. (2.16). To do this, we make use of the `project_2d` module in the `Cosmosis` numerical library [203]. We compute both the linear and non-linear matter power spectrum from our simulations at $z_{\text{pk}} = \{0, 0.25, 0.5, 0.75, 1.0, 1.25, 1.5, 2.0\}$ which are then used as input to perform the integral in eq. (2.16) assuming the tomographic source redshift distribution given by eq. (2.18). Following eq. (2.16), we multiply the input power spectra that we are interpolating between by the corresponding value of $\mu^2(1 + \eta)^2/4$ at each redshift.

We compute the convergence power spectra from both linear matter power spectra and the non-linear matter power spectra from our simulations, and compare them with the Λ CDM convergence power spectrum with Euclid-like error bars. On the left hand panel of fig. 2.10, we show the convergence power spectra as computed from the output of one of our simulations. Note that for this plot, we only consider a variation in μ , and we set η to its Λ CDM value ($\eta = 1$). We see that on large scales, i.e., small ℓ , the modified gravity spectrum is within the Λ CDM error bars, while the spectrum on non-linear scales is outside the error bars. Moreover, the linear spectrum deviates from the non-linear spectrum below $\ell = 100$. This shows the strong increase in constraining power that can be achieved by using non-linear scales: not only are there many more scales that can be used, but also the errors are typically smaller on those scales. These results emphasise the importance of developing simulations and fitting functions for model-independent modified gravity, as examined in section 2.3.

We note that comparing our modified gravity parameterisation (with parameters that are only time dependent) to Λ CDM for a single observable is slightly non-trivial, because one has a free choice of which redshift to make the linear

matter power spectra agree at. For our weak-lensing comparison, using the lowest redshift tomographic bin, we choose to focus on the case where the two linear spectra are equal at redshift zero (i.e. the Λ CDM simulation with rescaled initial conditions at $z = 50$). We make this choice for several reasons. It minimises the linear theory difference between the two curves, allowing us to focus on the additional information from non-linear behaviour/scales and, as long as the linear theory behaviour is similar at low redshift, the exact redshift at which they are equal is unimportant since lensing combines information from multiple redshifts. Our conclusions about the relative sizes of errors on difference scales, and the relative numbers of scales that contribute in each regime, are unchanged if a different choice is made. We will extend our analysis to a full parameter forecast for upcoming surveys in future work, which will allow this issue of parameter degeneracies to be examined in detail.

We now generalise our results to using our simulation output to probe the effects of both μ and η . As mentioned before, since the input matter power spectra from the simulations are unaffected by $\eta \neq 1$, we may model the effects of it in post-processing. In other words, the evolution of matter fluctuations is driven solely by μ , but the trajectory of photons through this distribution is affected by both η and μ . Therefore, we can effectively ignore η whilst running our N -body simulations without any loss of generality, essentially getting $P_\delta(k)$ as a function of μ only. We then use eq. (2.16) to compute the weak-lensing observables for both parameters.

As shown in eq. (2.16), the effect of varying η is captured solely by the prefactor $\mu^2(1+\eta)^2/4$. Therefore, one would expect that a variation of η would result in an overall shift of the power spectrum. If one were to concentrate on purely linear scales, this is exactly the same as varying μ due to the fact that a time-dependent

μ also simply shifts the matter power spectrum in the vertical direction(s). As a result, there is a degeneracy between time-dependent η and μ in linear theory. By explicitly going to non-linear scales, we break this degeneracy since we have already shown that a time-dependent μ introduces scale-dependent features in the matter power spectrum, and therefore in the weak-lensing convergence spectrum via P_δ in eq. (2.16), whereas η introduces no such scale dependence.⁷

The breaking of this degeneracy is clearly shown in the right panel of eq. (2.16), where we show the Λ CDM convergence spectrum with error bars, along with two different curves obtained from the same simulation, with identical $\mu(z)$, but different values of η . The green-dotted line is obtained by setting $\mu^2(1+\eta)^2/4 = 1$ (as in Λ CDM). The solid blue line is obtained directly from the simulation, i.e., $\eta = 1$. We see that varying η while keeping μ constant leads to an overall different amplitude of the convergence spectra. We also explicitly show that if one reverts to the Λ CDM value of $\mu = 1$ while keeping the prefactor $\mu(1+\eta)/2$ the same as in the blue line, one obtains the same shape for the power spectrum as the Λ CDM case. This can also be seen by comparing the shapes of the blue line and the green-dotted line which have identical $\mu(z)$. Thus, it is clear that the scale dependent effects from a time-dependent μ breaks the degeneracy between the two parameters that exists on linear scales, allowing the two parameters to be distinguished from each other and from their Λ CDM values. We note that the linear theory degeneracy should persist in both the auto-power spectra and the cross-power spectra. However, we leave the full behaviour of the cross-power spectra as a function of varying η and μ to future work.

These results not only show how weak-lensing observables can be constructed from

⁷In principle, η does introduce a small scale dependence due to weighting of the non-linear spectra at different times by different amounts, but this will be much smaller than the scale dependence caused by μ on non-linear scales.

our simulations for the full (μ, η) parameter space, but also further highlight the importance and gain of using non-linear scales.

2.5.2 Further evaluation of fitting functions

We can extend the earlier analysis of the fitting functions, by examining how well they capture the non-linear behaviour of the weak-lensing observables. We focus on the two fitting functions that performed the best in section 2.3.2, i.e., the **ReACT** formalism and the **halofit** fitting procedure.

In general we find that the better performance of **ReACT** compared to **halofit** is further demonstrated when looking at the weak-lensing observables, compared to when directly examining the matter power spectrum. In particular, similarly to section 2.3.2, we quantify the quality of the fitting functions by calculating the ℓ_{fail} value (rather than k_{fail} as in section 2.3.2) at which the fitting function first fails by 3 (or 5) %. The ℓ_{fail} values at which **ReACT** fails by 3% are in the range $250 \leq \ell_{\text{fail}} \leq 4000$, however **halofit** typically fails at the 3% level even for very low ℓ . For a given fitting function, we find little correlation between the k and ℓ values at which the fitting function fails in each simulation, due to the range of k and redshift values at which the matter power spectrum contributes to the weak-lensing convolution.

To illustrate this performance, we plot the results for two representative simulations: one where **ReACT** performs well to higher ℓ , and one where it fails at much lower ℓ , approximately corresponding to the best and worst cases we studied. These simulations are shown in fig. 2.11, where we show the ratio of the convergence power spectra calculated from the matter power spectra predicted by the fitting function and the simulation respectively. These plots show that **halofit** performs worse than **ReACT**, failing at the level of $\sim 5\%$ even at low ℓ . This poor

performance of `halofit` when computing weak-lensing observables is common across all simulations.

In these plots, the vertical lines show the ℓ_{fail} values, i.e., where the **ReACT** curve deviates from the simulation curve at the level of 3% and 5%, respectively. The left panel shows a simulation where the **ReACT** curve is accurate to $\ell \sim 5000$ while on the right, cut-offs are an order of magnitude smaller. These ℓ_{fail} values give an indication of the ℓ range where **ReACT** can be used to fairly reliably predict the weak-lensing observables for model-independent modified gravity studies. As described in section 2.3.2, we expect this performance to be improved by adjusting the concentration parameter. To demonstrate this, we include an additional curve where the concentration parameter has been modified according to the discussion at the end of section 2.3.2 (see fig. 2.7 for more details). As expected, it appears that weak-lensing observables can be accurately computed to higher ℓ using this process, however we leave a detailed examination of this to future work.

These results, in combination with those in section 2.3.2, show that phenomenological modified gravity analyses with current data can be carried out without restricting to linear scales (e.g. [68]) or carrying out a linearisation procedure as in [204]. For these purposes, our results show that **ReACT** is the best performing fitting function (including outperforming `halofit`), particularly when using weak-lensing observables. In future work we will extend this initial analysis to quantitatively examine a much wider range of parameter space, in preparation for analysing the data for upcoming surveys.

2.6 Conclusion

In this chapter, we have presented N -body simulations with a time-dependent strength of gravity μ , based on a framework for examining modified gravity in a model-independent way across all cosmological scales [83]. The key results are a presentation of the phenomenology of these simulations, an evaluation of existing fitting functions for capturing this phenomenology, and a demonstration of the application and importance of this framework for weak-lensing observables.

We modified the `GADGET-2` N -body code [184], and ran a series of simulations with piecewise-constant bins in redshift for μ . See section 2.3 for more details and table 2.1 for the redshift bins and the μ values in each bin.

The only fitting function calibrated from N -body simulations for the matter power spectrum on non-linear scales in phenomenological modified gravity was presented in [174]. We investigated the performance of this fitting function, as well as the Λ CDM halofit fitting procedure, the standard halo model of structure formation [see eqs. (2.6),(2.7)] and the halo model reaction [86,87]. We compared the ratio of the modified gravity matter power spectrum to the so-called ‘pseudo’ Λ CDM power spectrum as predicted in the various formalisms to the same ratio measured from our simulations. We quantified the accuracy of each formalism by calculating the least square statistic χ^2 and k_{fail} , the wavenumber of first failure (see fig. 2.6) for each fitting function. We found that the halo model reaction formalism performed significantly better than the others, with the notable exception being the case where the modified gravity parameters are such that the resulting power spectrum is co-incidentally very similar to the Λ CDM case. We also see qualitative evidence (see fig. 2.7) supporting the theoretical expectation that to achieve precision in forecasting modified gravity matter power spectra, one needs

to modify the Λ CDM concentration-mass relationship. We will extend the investigation presented here to a full parameter space examination and validation of the ReACT approach and the concentration issue in future work.

We present the matter power spectra from our simulations in section 2.4. Figs. 2.8 and 2.9 show that a purely time-dependent μ induces scale-dependent features in the matter power spectrum, as reported in [174] for a simpler case. Our results also show that the shape of the power spectrum on quasi-linear as well as non-linear scales depends not only on the value of μ , but also on the redshift at which it is ‘switched on’ (i.e., different from unity) and the duration of such a modification. Most notably, we see that introducing a modification in μ at early times produces a power spectrum that either lacks ($\mu < 1$) or has excess power on the quasi-linear scales ($\mu > 1$) and vice-versa on non-linear scales, respectively. We also noticed that the peak in the power spectrum relative to Λ CDM shifts to larger scales (lower k) as one steps forward in time (from high redshift to low redshift).

To understand the physics that leads to these results, we first note that modifying μ at different epochs and for different periods of time affects the redshift at which non-linear structure starts to form. Combining this with our results indicates that a *transfer of power* occurs from smaller to larger scales or vice versa, depending on when and for how long μ is modified. This is due to the fact that at early times, the very first haloes are in the process of forming, which means that changing the rate of structure formation affects the smaller cosmological scales since those are the haloes forming at that time. Therefore, when one returns to Λ CDM structure formation at late times, one sees a marked difference in the power spectrum. However, if one introduces a change in the rate of structure formation at late times, when galaxies have already formed, one is then affecting

the rate at which the largest haloes form, via mergers. Therefore, one sees a unique change in both the quasi-linear as well as the non-linear scales of the matter power spectrum, for a given time evolution of μ .

Finally, we show the impact of these phenomenological modifications to gravity on weak-lensing observations that will be generated in future experiments like the *Euclid* satellite (see fig. 2.10 and the discussion attached). We show that the constraining power of these experiments in the context of modified gravity is strongly dependent on the data obtained from non-linear cosmological scales, both in terms of the number of scales that are accessible and the sizes of the errors on the different scales. We further show how we can use weak-lensing observables to probe the two-parameter $\mu - \eta$ family of modified gravity models using the output of our simulations [see fig. 2.11]. We find that by explicitly going to non-linear scales one breaks the degeneracy between these two parameters that exists on linear scales [see right panel of fig. 2.10]. We also extend our analysis of the fitting functions to the weak-lensing context, again finding that the **ReACT** formalism performs the best. This shows that phenomenological modified gravity analyses with current data can be carried out without restricting to linear scales or carrying out a linearisation procedure.

The model-independent approach, first elucidated in [83], and further developed here, is not a priori restricted to particular regions of model space or types of theories, and has the potential to be a powerful null test of the Λ CDM+GR paradigm. The simulations and results presented here are an important step towards realising this, and using all of the data in future surveys to put model-independent constraints on the laws of gravity that operate in the Universe.

Chapter 3

The Road to Model-Independent Forecasts

3.1 Introduction

We have shown in the previous chapter that one of the key challenges in the next decade is to take advantage of the constraining power associated to data on non-linear scales. In the modified gravity context, one not only requires a parameterisation that is rigorously validated on all scales, but also robust predictions across the parameter-space for the relevant cosmological observables. In the previous chapter, we have already outlined such a parameterisation [see section 2.2 and eq. (2.3) for more details], which we implemented in N -body simulations with independent redshift bins for the effective gravitational parameter $\mu(z)$. This is the first step towards understanding the effect of modifying μ on the matter power spectrum. We also found that the **ReACT** formalism was able to accurately reproduce the matter power spectrum from our simulations. We quantified this using the k_{fail} parameter which indicates the scale up to which the power spectrum in our simulations agrees with the **ReACT** prediction. More precisely, k_{fail} specifies the scale at which the quantity $R(k)$, i.e., the ratio of the matter power spectrum in the modified gravity simulations relative to Λ CDM with linear growth equalised (see section 2.3.1) as predicted by the fitting function disagrees with the value measured in the simulations at some threshold accuracy.

In this chapter, we run a suite of N -body simulations designed to test and validate **ReACT** over the $\mu(z)$ parameter space in section 3.2.1. We compare the **ReACT** prediction for $R(k)$ to that obtained from our simulations. Furthermore, we measure the concentration-mass relation in our Λ CDM simulations and define a parameterised expression that we use to represent $c(M)$ in our simulations in section 3.2.2. We then implement this expression into **ReACT** and vary the fitting parameters to maximise k_{fail} for all of our simulations. We present the results of this procedure in 3.3. Finally, we discuss how one could implement this machinery

into a Fisher forecast and possible extensions to this work in section 3.4.

3.2 Methodology: **ReACT** Validation Pipeline

In the previous chapter, we made a particular choice in the way we sampled the modified gravity parameter space, i.e., bins with equalised Λ CDM growth and μ values tuned to obtain the same linear $P(k)$ at $z = 0$. This highlighted the fact that it is possible to obtain entirely different non-linear behaviour in $P(k)$ for the same linear $P(k)$, depending on the epoch and length of time of the modification to gravity in addition to the value of μ . We explained that is due to the fact that structure formation in the Universe is hierarchical, with small halos forming first, followed by larger halos. Therefore, the range of scales affected by the modification of gravity varies depending on the mass of halos forming during the modification. The key point to be taken away from this analysis is that it is theoretically inconsistent to use fitting procedures that predict the non-linear matter power spectrum based on the linear spectrum, such as halofit. Our analysis indicated that the **ReACT** formalism is able to predict $R(k)$ [and therefore $P(k)$] in our simulations.

However, one would require a larger sweep across the parameter space to demonstrate that the accuracy of **ReACT** is robust across different choices of $\mu(z)$. Furthermore, from the point of view of a cosmological forecast and hence ultimately when applying the formalism to real data, one would need consistency over the range of scales over which the accuracy of **ReACT** remains relatively constant. In particular, this would translate to a cut in ℓ up to which the accuracy is below the goal threshold chosen for future galaxy surveys such as *Euclid* and the Vera Rubin Observatory. With this in mind, we define an expanded suite of simulations that we run in order to rigorously validate **ReACT**.

Δz_{bin}	μ
$0 \leq z \leq 1$	1.108
$1.0 \leq z \leq 1.5$	1.027
$1.5 \leq z \leq 2.0$	0.973
$2.0 \leq z \leq 2.5$	0.952
$2.5 \leq z \leq 3.0$	0.962

Table 3.1: The binning of μ in redshift in [2].

3.2.1 Expanded suite of simulations

The most recent cosmological parameter forecast in the context of modified gravity with binned $\mu(z)$ was done in [2] (see table 3.1). The justification for this choice is that since dark energy domination is a late time effect, modifications to μ should also only occur at low redshifts. Of course, this might be viewed as a theoretical bias. In addition, the size of the redshift bins was chosen to be constant.

As mentioned before, we note that this parameter-space is multi-dimensional, with the value of μ , the bin endpoints and the bin widths all representing possible degrees of freedom. In order to enable a natural comparison to Λ CDM, we opt to keep the Λ CDM incremental growth in each bin constant, while maintaining a bin structure that is similar to table 3.1 in order to facilitate comparison of results. We run simulations with 4 different values of μ in each bin, namely $\{0.8, 0.9, 1.1, 1.2\}$. Our goal is to not only maximise the k_{fail} achieved with **ReACT** but also ensure a consistent value across all our simulations. We noted in the previous work modifying the concentration-mass relationship increased the range of scales over which **ReACT** could accurately reproduce simulation results. We now describe the pipeline we use to model the $c(M)$ relation in this work.

Δz_{bin}	μ_1	μ_2	μ_3	μ_4	σ_8^1	σ_8^2	σ_8^3	σ_8^4
$7 \leq z \leq 5.4$	0.8	0.9	1.1	1.2	0.7896	0.8002	0.8215	0.8321
$5.4 \leq z \leq 4.1$	0.8	0.9	1.1	1.2	0.7896	0.8002	0.8216	0.8322
$4.1 \leq z \leq 3.0$	0.8	0.9	1.1	1.2	0.7889	0.7999	0.8218	0.8329
$3.0 \leq z \leq 2.1$	0.8	0.9	1.1	1.2	0.79	0.8004	0.8213	0.8318
$2.1 \leq z \leq 1.47$	0.8	0.9	1.1	1.2	0.7915	0.8012	0.8205	0.8302
$1.47 \leq z \leq 0.91$	0.8	0.9	1.1	1.2	0.7937	0.8023	0.8194	0.8281
$0.91 \leq z \leq 0.43$	0.8	0.9	1.1	1.2	0.7977	0.8043	0.8175	0.8241
$0.43 \leq z \leq 0$	0.8	0.9	1.1	1.2	0.8052	0.8081	0.8136	0.8165

Table 3.2: We show the redshift bins (left column) in our simulations. For each redshift bin, we run 4 simulations in which μ takes the values $\{0.8, 0.9, 1.1, 1.2\}$ in the bin and $\mu = 1$ for all other redshifts. Note that for each μ value, we run a set of 8 simulations, each of which contains one bin where μ is switched on. The idea behind this plan is to sample the $\mu - z$ parameter space broadly, while still testing the response of the code to subtle changes in redshift range during which μ is switched on. This should also allow us to check if there are any degeneracies associated to the non-linear matter power spectrum in this parameter space. Note that these are all bins with equal Λ CDM growth, i.e., $D(z_{i-1})/D(z_i) = D(z_i)/D(z_{i+1}) = \text{constant} = 1.26$.

3.2.2 Concentration-mass relation

Over the last few decades, N -body simulations of the Λ CDM model have shown that the density profile of dark matter halos is well-described by the Navarro-Frenk-White (NFW) density profile [205], given by

$$\rho(r, r_s, \rho_s) = \frac{\rho_s}{r/r_s(1 + r/r_s)^2} \quad (3.1)$$

where the two free fitting parameters ρ_s and r_s are the scale density and radius, respectively. The scale density may be related to the critical density by the dimensionless parameter $\delta_c = \rho_s/\rho_c$ which associates each halo to a characteristic overdensity. The scale radius indicates where the logarithmic slope of the profile has the isothermal value of -2 . The total mass of the halo is determined assuming

that halo is virialised, is obtained by integrating the density profile

$$M_{\text{vir}} = 4\pi\rho_s r_s^3 \int_0^c \frac{dx}{x(1+x)^2}, \quad (3.2)$$

$$= 4\pi\rho_s r_s^3 \left[\ln(1+c) - \frac{c}{1+c} \right], \quad (3.3)$$

where $x = r/r_s$ is the integration variable, the upper limit of which defines the concentration $c = r_{\text{vir}}/r_s$. This parameter is simply an alternative measure of the characteristic overdensity associated to each halo and for a given mass, the two are related by

$$\delta_c = \frac{\Delta_{\text{vir}}}{3} \frac{c^3}{\ln(1+c) - c/(1+c)}, \quad (3.4)$$

where the virial radius and mass are conventionally related by the overdensity parameter Δ_{vir} . There are different conventions adopted for this relation, depending on whether the overdensity parameter is defined relative to the critical density parameter or the background density $\rho_b = \Omega_m \rho_c$. Our results indicate that modifying μ at different epochs and for different lengths of time will affect different halos of different masses in a non-trivial way, depending on the typical value of the mass of the halos forming and merging during the modification. This suggests that there is a re-ordering of sorts of the typical values of $\{\delta_c, \Delta_{\text{vir}}\}$ associated to a given M_{vir} . Modifying the concentration-mass relation would capture some of this phenomenology. In order to measure the concentration-mass relation in our simulations, we need to estimate the mass of the halos within our simulation volume as well as their radii.

Halo-finder The problem of identifying halos and measuring their properties from raw simulation data in an efficient manner is a well-studied one, with several so-called ‘halo-finders’ publicly available [see [\[206\]](#) and references within for a

detailed discussion of the various approaches to identify halos and measure their properties]. Specifically, we make use of the Rockstar halo-finder code [207], which makes use of the Friends-of-Friends (FOF) algorithm. In other words, the particles residing in a density peak above a pre-determined threshold are identified to constitute a halo. In addition, Rockstar also makes use of phase-space velocity information to accurately assign particles to halos in mergers and in centres of large clusters (see [207] for more details). The virial mass of a halo is calculated according to the following prescription

$$M_{\text{vir}} = \Delta_c \rho_c \frac{4\pi r_{\text{vir}}^3}{3}, \quad (3.5)$$

where Δ_c is given by [208]

$$\Delta_c = 18\pi^2 + 82x - 39x^2 \quad (3.6)$$

$$x = \frac{\Omega_m(1+z)^3}{E(z)^2} - 1, \quad (3.7)$$

where $E(z) = \Omega_m(1+z)^3 + \Omega_\Lambda$. For our simulations, we set that the minimum number of particles required for an object in the simulation to be considered a halo is 1000. Thus, the code now simply counts up all the particles in each halo and determines the total mass and the corresponding virial radius using eq. (3.5). The code then fits an NFW profile to each halo to determine the the scale radius r_s . Thus, we calculate the concentration parameter $c = r_{\text{vir}}/r_s$.

For the Λ CDM model, the concentration-mass relation has been measured and validated from a suite of N -body simulations [209] and is given by

$$c(M) = C_0 \left(\frac{M}{10^{12} h^{-1} M_\odot} \right)^{-\gamma} \left[1 + \left(\frac{M}{M_0} \right)^{0.4} \right], \quad (3.8)$$

where $C_0 = 10.2$, $\gamma = 0.1$, $M_0 = 10^{17} h^{-1} \text{ M}_\odot$. We compare the concentration-mass relation above for Planck cosmological parameters with the $c(M)$ measured from our simulations and the $c(M)$ relation in **ReACT** in fig. 3.1, given by [86]

$$c(M) = \frac{c_0}{1+z} \left(\frac{M}{M_*} \right)^{-\alpha}, \quad (3.9)$$

where $c_0 = 9.$, M_* is the stellar mass computed by imposing a condition on the peak height $\nu(M_*) = 1$ of the Sheth-Tormen mass function and $\alpha = -0.13$. Therefore, we verify that our simulations are not only representative of results previously obtained in the literature, but also that we are able to reproduce $c(M)$ in **ReACT** with the expression in eq. (3.8).

We now implement eq. (3.8) into the **ReACT** framework with varying C_0 (keeping the other fitting parameters constant) to maximise the k_{fail} parameter for all the different simulations. Essentially, the goal is to obtain a fitting function for C_0 for arbitrary $\mu(z)$ that allows a more accurate calculation of $R(k)$ and hence, of the matter power spectrum.

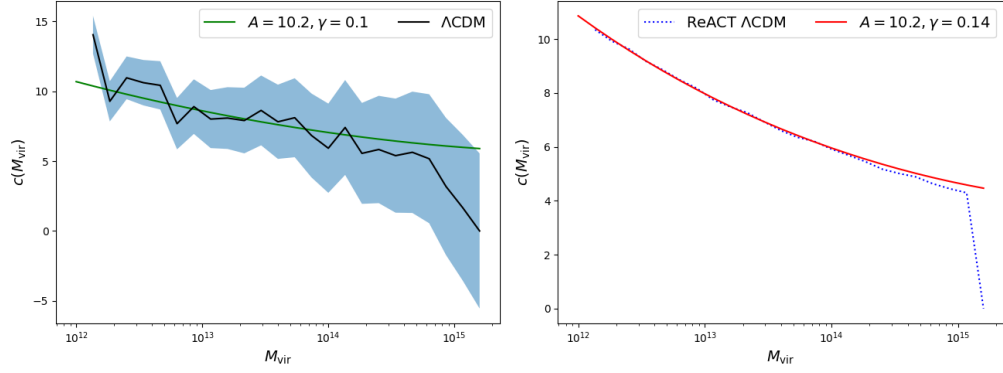


Figure 3.1: In the left panel, we present the concentration-mass relation measured from our ΛCDM simulations and the Multidark fit for the Planck parameters [209]. There is significant scatter in the simulation data, which can be driven down by averaging over more realisations of the initial conditions. In the right panel, we reproduce the ReACT $c(M)$ using the expression in (3.8). This allows us to express the concentration-mass relation in our modified gravity simulations as a ratio relative to the ΛCDM ReACT case.

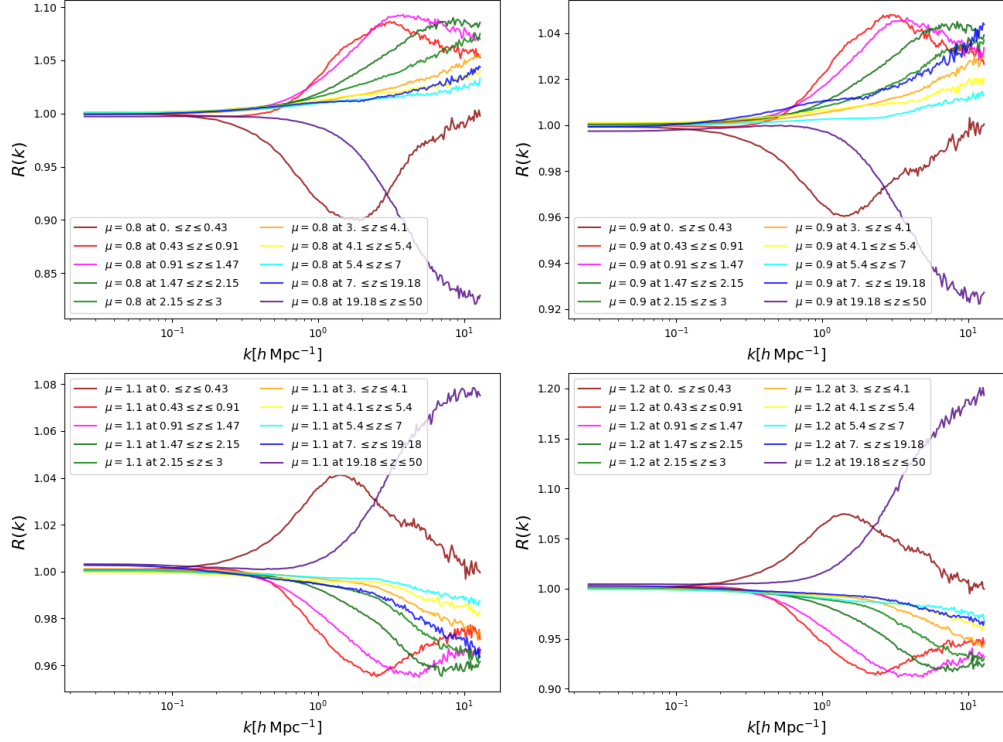


Figure 3.2: The ratio $R(k)$ for the various $\mu(z)$ presented in table 3.2. In this plot, one clearly sees the three regimes defined in the text, with the two extremes where the matter power spectrum differs from Λ CDM the most represented by the bins where μ is modified at $z < 2$ and $z > 19$. The transition regime at the intermediate redshifts are associated to smaller ‘corrections’ to the re-scaled Λ CDM case.

3.3 Results

In this section, we show the results of measuring the matter power spectrum from our suite of simulations. We perform a 1-parameter fit for the concentration-mass relation to maximise the k_{fail} for all $\mu(z)$. We do this by varying the amplitude parameter C_0 in eq. (3.8). Not only does this allow us to capture the varying phenomenology of our simulations more accurately using **ReACT**, but also allows our analysis to be insensitive to realisation-dependent effects due to the fact that we present our $c(M)$ in terms of a ratio relative to the **ReACT** relation in eq. (3.9). This ties back to our discussion in the previous chapter where we presented all our results in terms of the ratio of matter power spectra $R(k)$ for the same reason.

We remind the reader that in order to compute $R(k)$, one needs the modified gravity $P(k)$ as well as the Λ CDM $P(k)$ with equalised linear growth.

In fig. 3.2 we present $R(k)$ for the different $\mu(z)$ in table 3.2. We see from the results that one may define three broad regimes in redshift when one modifies μ based on the behaviour of the non-linear matter power spectrum. The relative differences from the Λ CDM spectrum are quite large in the two extreme cases, i.e., when $\mu \neq 1$ at low redshifts $z < 2$ and at high redshifts $z > 19$. The effect on the power spectrum from a low-redshift modification is opposite to the case when μ is modified at high redshift. This behaviour is consistent with our earlier results with greater redshift resolution in the transition regime, where the relative difference to Λ CDM decreases with increase in the redshift at which the modification occurs. We note that this pattern is broken by the lowest redshift bin, i.e., $0 \leq z \leq 0.43$, matter power spectrum associated to this redshift seems to mimic the earliest redshift bin, but over a larger range of scales. We note that this behaviour is connected to the duration of the modification and the scales at play.

As mentioned in the previous chapter, the redshift evolution of the typical mass of the halos determines the scale at which $P(k)$ is affected. Smallest halos form first, which means modifying the rate of structure formation at early times affects the smallest scales. Conversely, at late times, larger halos form from mergers of small halos. Therefore, modifying structure formation at these times induces a transfer of power from non-linear to quasi-linear scales. This qualitative argument can be made quantitative by varying the concentration-mass relation with varying $\mu(z)$. The behaviour in the smallest bin may be connected to the fact that at redshifts close to $z \leq 0.5$, the Universe is in the dark-energy dominated phase, where structure formation effectively is ‘frozen in’.

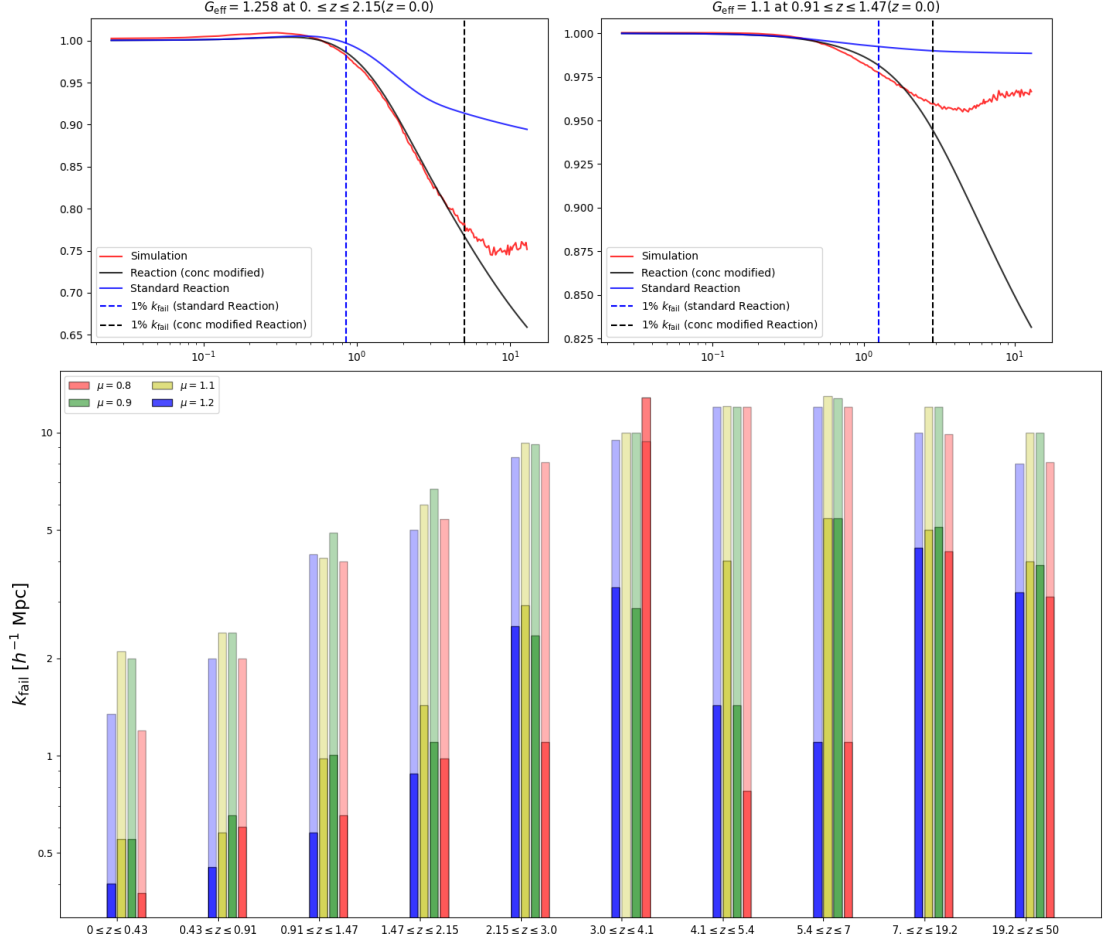


Figure 3.3: We show in the top panel examples of the extent of variation of the k_{fail} parameter when the concentration-mass relation in **ReACT** is modified. In the bottom panels, we show the k_{fail} parameters for all our simulations, before (solid) and after (transparent) the concentration amplitude modification. We see across all simulations that there is a significant improvement in k_{fail} post-modification. In all bins except the two lowest redshift cases, we see that we are able to achieve a k_{fail} larger than the **ReACT** accuracy threshold scale, i.e., $k = 3 h \text{ Mpc}^{-1}$.

We now discuss the procedure that we adopt to modify the $c(M)$ relation in **ReACT** in order to obtain a better fit to our simulation results. As we did before, we use the k_{fail} parameter to quantify the accuracy with which **ReACT** captures the simulation results. We vary the amplitude of the $c(M)$ relation to maximise k_{fail} . We show in fig. 3.3 some examples of this procedure, particularly the variation in k_{fail} before and after the modification of the concentration. We show the histogram of k_{fail} values for all of our simulations in the bottom panel of fig. 3.3. With the variation of the amplitude of the concentration-mass relation, we are able to achieve $k_{\text{fail}} > 3 h^{-1}\text{Mpc}$ (the scales over which **ReACT** is formally applicable) for the majority of our simulations, except for the two lowest redshift bins (modulo complications arising from baryonic physics). In these, cases, we still see a significant improvement that allows one to probe deeper into the non-linear regime.

In ΛCDM , it has been observed from simulations that the concentration-mass relation is a power law with a mildly negative exponent. In other words, $c(M)$ slowly decreases with halo mass. This is because at late times, the accretion of mass only occurs around the outer edges of halos, outside the scale radius. Conversely, at early times, the mass accretion is relatively uniform. Since more massive halos form at late times, larger halos are associated with smaller values of concentration and vice-versa for small halos. This argument may be extended to a qualitative prediction for three redshift regimes that we identified earlier. Note that this means the extent to which the ΛCDM concentration parameter is modified is redshift-dependent. [209].

The discussion below applies to the case where $\mu > 1$ without loss of generality. In the case of the low-redshift modification of μ , we see a transfer of power from

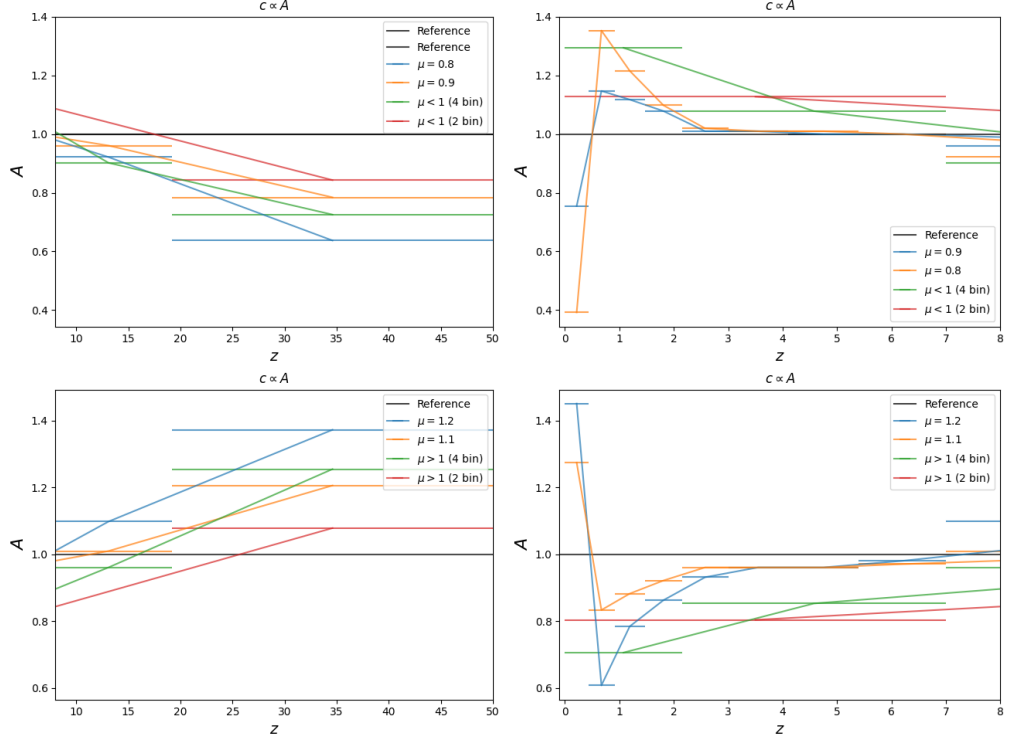


Figure 3.4: In the left panels, we show the ratio of the amplitude A relative to Λ CDM at for the simulations at which μ is modified at $z < 8$ and vice-versa in the right panels. The horizontal bars indicate the width of the redshift bin in which μ was modified in the simulation. As mentioned in the text, we see that due to a transfer of power to larger scales, i.e., an excess of larger halos, the concentration decreases (increases) when $\mu > 1$ at low z . Conversely, the concentration increases relative to Λ CDM, when $\mu > 1$ at high z , since mass accretion is more uniform at these epochs. The opposite behaviour is seen when $\mu < 1$.

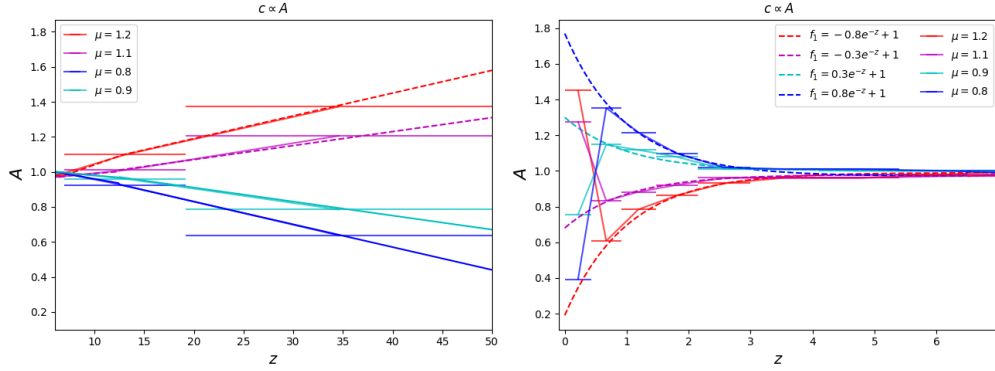


Figure 3.5: We show the high-redshift and low-redshift regime $c(M)$ fit to our simulation data.

the non-linear scales to quasi-linear scales in the case when $\mu > 1$ (and vice-versa for $\mu < 1$). Therefore, one would expect that the concentration should decrease relative to Λ CDM. One expects the exact opposite when μ is modified early in redshift, where the concentration relative to Λ CDM should be larger. In the transition regime, one would expect a negligibly small correction to the Λ CDM $c(M)$, a prediction that is made even more apparent by noting that the k_{fail} values for this regime are already above the convergence threshold for our simulations. Of course, the pattern is broken at the lowest redshift bin, where there is a massive upturn in the concentration relative to Λ CDM.

In fig. 3.4, we compute the ratio of the amplitudes of the concentration-mass relation in all the simulations corresponding to the largest k_{fail} values relative to the Λ CDM value in **ReACT** C_0 in eq. (3.9). In this case, we compute the amplitude associated to a simulation where μ is switched on in a particular redshift bin at the midpoint of the bin with error bars that span the redshift range of the bin. We see that our simple qualitative predictions are borne out in the different regimes in redshift in which μ is modified. We fit for this behaviour in **ReACT** so as to design a pipeline that is able to predict the matter power spectrum for arbitrary $\mu(z)$. The goal is to implement this into a Fisher forecast.

In order to fit the behaviour of the concentration in the two regimes, we split the redshift range into two regimes. An important phenomenological result that applies across all of our simulations in the previous chapter as well as this one is that the impact on the matter power spectrum is greater when μ is modified at the extreme ends of the redshift range, relative to when μ is modified in the intermediate regime. Our general expectation for the function form for the $c(M)$ fit is

$$A = F(\mu)G(D(z)) , \quad (3.10)$$

where $D(z)$ is the Λ CDM growth factor. In other words, a given choice for $D(z)$ implies a very specific redshift dependence for the amplitude of the concentration-mass relation that gives the correct shape for the matter power spectrum.

For our suite of simulations in this chapter, $D(z) \simeq 1.26$ in our redshift bins. Therefore, we have a fixed redshift dependence for all of our simulations, that we expect to be explicitly broken by our previous simulations. In the first regime, i.e., $0 \leq z \leq 7$, we use an exponential function

$$f_1(z) = C_1 e^{-z} + C_2 , \quad (3.11)$$

where $C_1 > 0$ when $\mu < 1$ and vice-versa for $\mu > 1$ and $C_2 \simeq 1$. In the second regime, i.e., we use a simple linear relationship

$$f_2(z) = C_3 z + C_4 . \quad (3.12)$$

where again, $C_3 > 0, C_4 = 0.9$ for $\mu < 1$ and $C_3 < 0, C_4 = 1.1$ for $\mu > 1$. We implement this procedure for our suite of simulations in fig. 3.5. Of course, at $z < 0.4$ our fit fails to capture the upturn of the concentration. A higher

resolution examination of this range of redshifts and the impact of varying μ with this range would be required to fit for this behaviour.

3.4 Discussion and Conclusions

In the next few decades, experiments such as the *Euclid* satellite and the Vera Rubin observatory will generate a huge amount of data on the non-linear scales of structure formation where the density contrast δ can be arbitrarily large. In order to make best use of this data to test GR, one needs robust predictions for cosmological observables across all scales. We presented in the previous chapter the first N -body simulations of arbitrary models of modified gravity with a time-dependent effective gravitational parameter μ . We used the **ReACT** formalism to predict the cosmological observables for arbitrary $\mu(z)$. In order to carry out a rigorous forecast for specific galaxy surveys, **ReACT** requires validation, a problem that we tackled in this chapter.

We presented an extended suite of N -body simulations to validate the **ReACT** fitting function across the parameter space. Our suite of simulations outlined in table 2.1 is designed to test the accuracy of **ReACT** for varying values of μ switched ‘on’, i.e., $\mu \neq 1$ ($\mu = 1$ in GR) at different epochs, each associated to a different duration in redshift. This leads to varying phenomenology, a subset of which we explored in the previous chapter. As before, we computed the ratio $R(k)$ of the matter power spectrum measured from our simulation to the so-called pseudo Λ CDM power spectrum i.e., with equalised linear growth at $z = 0$. We quantified the agreement of the **ReACT** prediction for $R(k)$ relative to the measurement from our simulations using the k_{fail} parameter, i.e., the first value of k at which the accuracy of **ReACT** falls below the 1% threshold.

We noted in the previous chapter that the modification of the concentration-mass relation in **ReACT** leads to a better fit to our simulation data. We achieved this by varying the amplitude of the $c(M)$ in **ReACT** [see fig. 2.7 and the related

discussion]. In order to rigorously test and validate this hypothesis. We also measure the concentration-mass relation in our simulations. We used the **Rockstar** code [207] to measure the halo properties of the dark matter halos in our simulations. We then showed that the $c(M)$ measured in our Λ CDM simulations matched the prediction in the literature [209] (see eq. (3.8) and fig. 3.1). We also reproduced the Λ CDM concentration mass relation in **ReACT**. This allowed us to study the phenomenology associated with $\mu(z)$ by amplitude of $c(M)$ relative to Λ CDM.

It is now well-established from studies of N -body simulations that $c(M)$ is a slowly decreasing power law in Λ CDM, due to the fact that mass accretion is not uniform across the halo at late times, in contrast to early times. We argued in the previous chapter that due to the hierarchical nature of structure formation, the imprint of $\mu(z)$ depends on the mass of the halos forming at the epoch of modification. We identified three regimes in redshift; modifying μ in each regime may be associated to a different effect on $P(k)$. Modifying μ at high redshifts affects the non-linear tail of matter power spectrum, since only the smallest halos form during those times. In contrast, modifying μ at low redshifts when smaller halos merge to form larger halos affects quasi-linear scales. There is a smooth transition in the intermediate redshifts, in which the effect of the matter power spectrum relative to Λ CDM is relatively small compared to the other two regimes. This qualitative argument indicates the origins of the correlation between concentration-mass relation and imprint of $\mu(z)$ on $P(k)$.

In fig. 3.3, we showed that the variation of the amplitude of $c(M)$ leads to significant improvement in the k_{fail} parameter associated to **ReACT** across all our simulations. Modifying structure formation at early times leads to an excess of smaller halos, and therefore $c(M)$ should increase relative to Λ CDM (assuming

$\mu > 1$, the opposite is true for $\mu < 1$) and vice-versa for late redshifts. We showed that for a given choice of $D(z)$, the redshift dependence is fixed and the variation with μ is linear. We presented a fitting function for the variation of the $c(M)$ that we implemented in **ReACT**.

A natural next step is to generalise the concentration-mass fit for varying $D(z)$. In order to explore this parameter space, we plan to run simulations with $D(z) \sim \{0.8, 2.6\}$, i.e., half and double the value of incremental linear growth in table 3.2. Not only will this allow us to generalise the $c(M)$ fit, but also explore the extreme low-redshift upturn described in section 3.3. The results from this analysis will facilitate the implementation of this pipeline into a Fisher forecast. This will not only allow us to obtain model-independent constraints on modified gravity parameters, but also insight on specific time bins that particular surveys are sensitive to.

Chapter 4

Spontaneous Decay of Axions to Photons

In this chapter, we discuss axion dark matter detection via spontaneous decay. In section 4.1 we discuss axion observations in virialised structures and outline the targets with the best prospects for axion decay detection. In order to present estimates of the signal strength we will set up a strawman object which is a galaxy with a virial mass, $M_{\text{vir}} = 10^{12} M_{\odot}$, virial radius $R_{\text{vir}} = 100 \text{ kpc}$ at a distance $d = 5 \text{ Mpc}$ and a velocity width of 200 km sec^{-1} which corresponds to an object similar to the nearby galaxy Centaurus A [210]. We have chosen these values to be broadly consistent with the model for the virial radius ($\propto M_{\text{vir}}^{1/3}$) from a given mass that we will use later in the subsequent discussion. As part of that discussion, we focus on our suggestion that the basic signal strength will be relatively independent of the object mass. Such an object would be expected to have an average surface mass density $\Sigma_{\text{vir}} \approx M_{\text{vir}}/(\pi R_{\text{vir}}^2) \approx 0.07 \text{ kg m}^{-2}$ over an angular diameter of $\theta_{\text{vir}} = 2R_{\text{vir}}/d \approx 40 \text{ arcmin}$. We will see that this value, which we will use in the subsequent signal estimates, is probably quite conservative and

that values up to a thousand times larger than this might be accessible in some objects, albeit over smaller areas, typically in the centre of the object. The basic conclusion will be that it will be difficult to imagine a telescope with a single pixel receiver system achieving a limit on $g_{a\gamma\gamma}$ better than that from CAST. In order to be competitive with the CAST limit, we find that it is easier to optimise future experiments if one quantifies the signal in terms of the brightness temperature, rather than the flux density. We show that the brightness temperature is proportional to the surface-mass-density Σ_{beam} associated with the telescope beam, which makes it clear that future experiments must target the centres of virialised objects where this quantity is the largest possible value. From our analysis, the main conclusion is that the larger surface-mass density at the galactic centre/Virgo cluster centre coupled with large amounts of radio emission at the relevant frequencies could enhance the signal enough to probe couplings below the CAST limit. With this in mind, we argue that the large surface-mass-density of the galactic centre or the Virgo cluster centre offer the best chance of improving current constraints on the axion-photon coupling via spontaneous decays.

4.0.1 Stimulated emission

The decay of axions into two photons can be enhanced in the presence of a photon background and, by contrast to the enhancement due to magnetic fields, this may be very significant. References [211, 212] have shown that the effective decay lifetime can be reduced to $\tau = \tau_{2\gamma}/(1 + \mathcal{F}_{\gamma}^{\text{eff}})$ where $\mathcal{F}_{\gamma}^{\text{eff}}$ is the photon occupation number associated to the relevant sources considered. Sources of photons include the CMB, the radio background and galactic emission with $\mathcal{F}_{\gamma}^{\text{eff}} =$

$\mathcal{F}_{\text{CMB}} + \mathcal{F}_{\text{radio}} + \mathcal{F}_{\text{gal}} + \dots$ For the CMB, this is given by

$$\mathcal{F}_{\text{CMB}} = 2 \left[\exp \left(\frac{m_a c^2}{2k_B T_{\text{CMB}}} \right) - 1 \right]^{-1}, \quad (4.1)$$

where $T_{\text{CMB}} = 2.725 \text{ K} = 235 \mu\text{eV}/k_B$ which can be approximated by $\mathcal{F}_{\text{CMB}} \approx 4k_B T_{\text{CMB}}/(m_a c^2)$ for $m_a c^2 \ll 470 \mu\text{eV}$ which can provide a potentially very significant enhancement of the signal. The CMB and the radio background are both isotropic sources, and so the factor \mathcal{F} is easily worked out to be proportional to the brightness temperature measured by experiments [213, 214].

The contribution from the radio background is very uncertain for a number of reasons. Firstly, making absolute measurement of the background temperature is inherently difficult. But perhaps more important is that this measurement is made from the point of view of telescopes on Earth and it may not be the same elsewhere in the Universe and also at higher redshifts. In principle, it would be necessary to model the sources contributing to the radio background and quantify the uncertainty in order set limits on $g_{a\gamma\gamma}$.

A dedicated study of specific sources, which might be easier to model than the overall background, could result in significant effective enhancement in values of \mathcal{F} for the axion masses between 1 and 20 $\mu\text{eV}/c^2$. [212] suggested that $\mathcal{F}_{\text{source}} \approx I_{\text{source}}/E_\nu^3$ where $E_\nu = hf_{\text{obs}}$ is the energy of the photons. We will adopt this relation for our later order-of-magnitude estimates of the signal from the galactic centre including the enhancement due to diffuse radio emission (eg. synchrotron emission) as well as the radio background.

4.1 Estimates of the signal amplitude for axion decay from virialised halos

Clearly the first and most important task in determining whether or not dark matter axions can be detected via spontaneous decays is to obtain a reliable estimate for the strength of the resulting signal. Let us consider a virialised halo of mass M and at redshift z . We further assume that axions constitute its whole mass. The total bolometric flux from the object is

$$\int S_{\text{tot}} df_{\text{obs}} = \frac{L_{\text{obs}}}{4\pi[r(z)]^2} = \frac{N_{\text{a}}E_{\text{obs}}}{\tau_{\text{obs}}} \frac{1}{4\pi r(z)^2}, \quad (4.2)$$

where $r(z)$ is the comoving distance to redshift z , S_{tot} the total flux density, $E_{\text{obs}} = 2hf_{\text{emit}}/(1+z)$ and $\tau_{\text{obs}} = (1+z)\tau_{2\gamma}/(1+\mathcal{F}_{\gamma}^{\text{eff}})$ are the emitted photon energy and decay life-time in the observer's frame, respectively and $\mathcal{F}_{\gamma}^{\text{eff}}$ is the photon distribution discussed in the previous section. The luminosity in the observer's frame is $L_{\text{obs}} = N_{\text{a}}E_{\text{obs}}/\tau_{\text{obs}}$ and $N_{\text{a}} = M/m_{\text{a}}$ is the number of axions in the halo. One can obtain an estimate of the observed flux density by assuming that all the flux is detected (the point source approximation) and that it is equally distributed across a bandwidth Δf_{obs} , effectively assuming a top-hat line profile, in the observer's frame

$$S_{\text{tot}} = \frac{Mc^2}{4\pi[d_{\text{L}}(z)]^2\tau_{2\gamma}\Delta f_{\text{obs}}}(1+\mathcal{F}_{\gamma}^{\text{eff}}), \quad (4.3)$$

where $d_{\text{L}}(z) = (1+z)r(z)$ is the luminosity distance to redshift z . We note that this formula is equivalent to that for the emission of neutral Hydrogen due to the spin-flip transition under the exchange of M with the neutral Hydrogen mass, M_{HI} , and $\tau_{2\gamma}$ with the effective lifetime of the spin state.

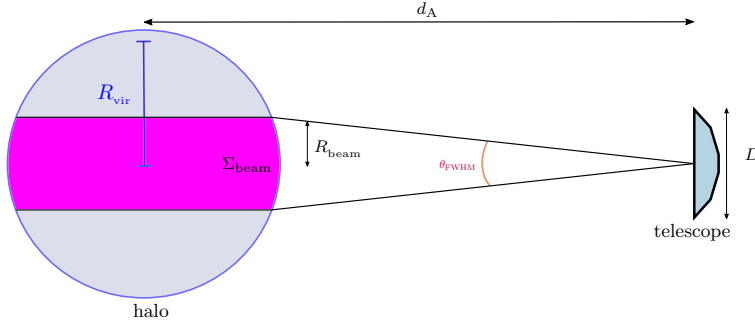


Figure 4.1: Schematic illustration of the telescope beam of width R_{beam} given in eq. (4.5) and virialised halo with surface density Σ and virial radius R_{vir} .

Neither of the assumptions will be true in reality. The assumption of a top-hat frequency profile should only lead to a small correction if Δf_{obs} is set by the velocity width of the halo $\Delta v/c = \Delta f_{\text{obs}}/f_{\text{obs}}$. From first principles, this is set by the halo mass as $\Delta v \propto M^{1/3}$. In what follows, it will be convenient to specify the measured value of Δv for a specific object rather than calculate it self-consistently from the halo mass. For typical values, and a halo at redshift z , we find

$$\begin{aligned} \Delta f_{\text{obs}} &= \frac{f_{\text{emit}} \Delta v}{c(1+z)}, \\ &\approx \frac{20 \text{ MHz}}{1+z} \left(\frac{\Delta v}{200 \text{ km sec}^{-1}} \right) \left(\frac{m_a c^2}{250 \mu\text{eV}} \right). \end{aligned} \quad (4.4)$$

Typical receiver systems can produce spectra with the resolution in eq. (4.4) in all but the most extreme situations. The question of whether one is sensitive to flux from the entire halo is more complicated. Unless the telescope beam is larger than the projected angular size of the cluster, the total flux-density can be less than that of eq. (4.3) as illustrated in fig. 4.1. Let us now estimate the importance of finite angular resolution.

We define R_{beam} as the *radius* corresponding to the Full-Width Half-Maximum

(FWHM) angular *diameter* $\theta_{\text{FWHM}} \approx \lambda_{\text{obs}}/D$, where λ_{obs} is the observed wavelength and D is the effective diameter of the observing telescope. In the case of a single dish telescope this is the actual size, whereas for an interferometer it will be given by the longest baseline. The beam radius can be estimated by $R_{\text{beam}} = d_A(z) \sin(\theta_{\text{FWHM}}/2)$, where $d_A(z)$ is the angular diameter distance which can be expanded for small θ_{FWHM} to give

$$R_{\text{beam}} = \frac{hr(z)}{Dm_a c}, \quad (4.5)$$

$$\approx 0.5 \text{ kpc} \left(\frac{r(z)}{5 \text{ Mpc}} \right) \left(\frac{D}{100 \text{ m}} \right)^{-1} \left(\frac{m_a c^2}{250 \mu\text{eV}} \right)^{-1},$$

where we have adopted a fiducial diameter of 100 m such as for the Green Bank Telescope (GBT). If $M_{\text{beam}} \leq M_{\text{vir}}$ is the mass enclosed in the projected cylinder, then the observed flux density will be

$$S_{\text{beam}} \approx 4 \mu\text{Jy} (1 + \mathcal{F}_\gamma^{\text{eff}}) \times \left(\frac{\tau_{2\gamma}}{8 \times 10^{35} \text{ s}} \right)^{-1} \times$$

$$\left(\frac{\Delta f_{\text{obs}}}{20 \text{ MHz}} \right)^{-1} \left(\frac{M_{\text{beam}}}{10^{12} M_\odot} \right) \left(\frac{d_L(z)}{5 \text{ Mpc}} \right)^{-2}. \quad (4.6)$$

If we substitute (1.68) and (4.4) into (4.6) we find that

$$S_{\text{beam}} \approx 4 \mu\text{Jy} (1 + \mathcal{F}_\gamma^{\text{eff}}) \left(\frac{g_{a\gamma\gamma}}{10^{-10} \text{ GeV}^{-1}} \right)^2 \times$$

$$\left(\frac{m_a c^2}{250 \mu\text{eV}} \right)^2 \left(\frac{M_{\text{beam}}}{10^{12} M_\odot} \right) \times$$

$$\left(\frac{\Delta v}{200 \text{ kmsec}^{-1}} \right)^{-1} \left(\frac{d_L(z)}{5 \text{ Mpc}} \right)^{-2}. \quad (4.7)$$

From this we see that, if $\mathcal{F}_\gamma^{\text{eff}} = 0$, the expected flux density is $\propto m_a^2$ for a fixed value of M_{beam} . This reflects the fact that the size of the object which is inside the beam depends on m_a via the fact that $f_{\text{obs}} \propto \theta_{\text{FWHM}}$. This is an undesirable

feature of using the flux density to assess the detectability of the axion signal, although it is possible to take into account the dependence of M_{beam} on θ_{FWHM} . Note that there will be additional dependence on m_a from $\mathcal{F}_\gamma^{\text{eff}}$; for example, there is a component from the CMB which is $\propto m_a^{-1}$.

It is possible to express the expected signal in terms of the intensity I , or equivalently the Rayleigh-Jeans brightness temperature

$$I = \frac{2f_{\text{obs}}^2 k_B T_{\text{RJ}}}{c^2}, \quad (4.8)$$

and we shall see that this is a much clearer way of quantifying the signal. For a source of axions at redshift z with surface mass-density $\Sigma = \int \rho_a dl$, taking into account that the flux density is the integral of the intensity over the solid angle subtended by the source, the integrated line intensity is given by

$$\int I_{\text{beam}} df_{\text{obs}} = \frac{c^2 \Sigma_{\text{beam}}}{4\pi \tau_{2\gamma} (1+z)^4} (1 + \mathcal{F}_\gamma^{\text{eff}}), \quad (4.9)$$

where the appropriate surface mass density is that integrated over the beam profile of the telescope, Σ_{beam} . To obtain this expression, we used eq. (4.3) and Etherington's reciprocity theorem $d_L(z) = (1+z)^2 d_A$, as the solid angle of the object is defined as $\Delta\Omega = R^2/d_A^2$. For the surface mass-density $\Sigma_{\text{beam}} = \Sigma_{\text{vir}} \approx 0.07 \text{ kg m}^{-2}$ of our strawman object, we can deduce an intensity

$$I_{\text{beam}} \approx \frac{3 \text{ mJy sr}^{-1}}{(1+z)^4} (1 + \mathcal{F}_\gamma^{\text{eff}}) \left(\frac{\tau_{2\gamma}}{8 \times 10^{35} \text{ sec}} \right)^{-1} \times \left(\frac{\Delta f_{\text{obs}}}{20 \text{ MHz}} \right)^{-1} \left(\frac{\Sigma_{\text{beam}}}{0.07 \text{ kg m}^{-2}} \right), \quad (4.10)$$

and a brightness temperature

$$T_{\text{RJ}}^{\text{beam}} \approx \frac{100 \text{ pK}}{(1+z)^2} (1 + \mathcal{F}_\gamma^{\text{eff}}) \left(\frac{\tau_{2\gamma}}{8 \times 10^{35} \text{ sec}} \right)^{-1} \times \left(\frac{\Delta f_{\text{obs}}}{20 \text{ MHz}} \right)^{-1} \left(\frac{m_a c^2}{250 \mu\text{eV}} \right)^{-2} \left(\frac{\Sigma_{\text{beam}}}{0.07 \text{ kg m}^{-2}} \right). \quad (4.11)$$

This can be simplified by substituting in eqs. (1.68) and (4.4) to yield

$$T_{\text{RJ}}^{\text{beam}} \approx \frac{100 \text{ pK}}{1+z} (1 + \mathcal{F}_\gamma^{\text{eff}}) \left(\frac{g_{a\gamma\gamma}}{10^{-10} \text{ GeV}^{-1}} \right)^2 \times \left(\frac{\Sigma_{\text{beam}}}{0.07 \text{ kg m}^{-2}} \right) \left(\frac{\Delta v}{200 \text{ kmsec}^{-1}} \right)^{-1}. \quad (4.12)$$

This expression does not have any explicit dependence on m_a and tells us that the key parameters dictating the signal strength are $g_{a\gamma\gamma}$, $\Sigma_{\text{beam}}/\Delta v$ and $\mathcal{F}_\gamma^{\text{eff}}$. The only dependence on m_a is via the observation frequency and consequently the size of the area over which Σ_{beam} is computed. The size of the signal could be larger than this for our strawman object which is relevant to an average over the virial radius - see subsequent discussions.

As a prelude to more detailed discussions of specific telescopes in the next subsection, we comment that a typical flux density of $S_{\text{beam}} = 4 \mu\text{Jy}$ might seem to be a quite accessible number for future large radio telescopes - many papers report detection of radio signals in the μJy range using presently available facilities. Conversely a brightness temperature of $T_{\text{RJ}}^{\text{beam}} = 100 \text{ pK}$ is very low and much weaker than any value usually discussed. These numbers can be reconciled in realising that the flux density is averaged over a region $\Omega \approx \pi(R_{\text{vir}}/d)^2 \approx 1.2 \times 10^{-3} \text{ sr}$ and it is also worth noting that most published radio detections are for bandwidths much larger than 20 MHz. In the subsequent discussion we will argue that it is easier to understand whether the signal is detectable by considering the intensity

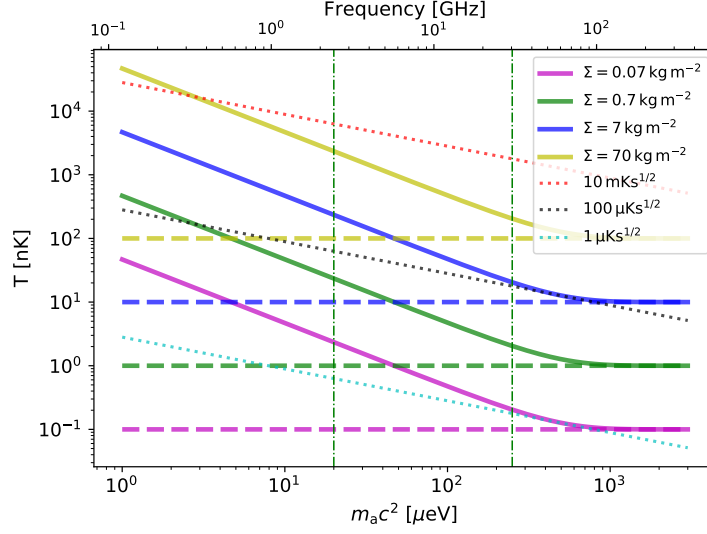


Figure 4.2: Estimates of the brightness temperature for a halo as a function of axion mass including spontaneous decay and the enhancement due to stimulated emission from the CMB (solid lines) and the pure spontaneous decay (dashed lines). We have fixed $g_{a\gamma\gamma} = 10^{-10} \text{ GeV}^{-1}$ which is close to the CAST limit and is the goal signal level. We have also fixed $\Delta v = 200 \text{ km s}^{-1}$ and used different values for $\Sigma_{\text{beam}} = 0.07, 0.7, 7$ and 70 kg m^{-2} which lead to brightness temperatures $\approx 100 \text{ pK}, 1, 10$ and 100 nK respectively for $m_a \gg 470 \mu\text{eV}$ where spontaneous decay is dominant. For lower values of m_a , we see the increase $\propto m_a^{-1}$ due to stimulated emission from the CMB which could be added to other sources such as the radio background and galactic emission. We have also included some sample noise levels (dotted lines) due to 1 year of integration time with instantaneous sensitivities of $10 \text{ mK s}^{1/2}$, 100 and $1 \mu\text{K s}^{1/2}$ at $m_a c^2 = 250 \mu\text{eV}$ with the scaling $m_a^{-1/2}$ necessary for a fixed velocity width. The two vertical lines represent $m_a c^2 = 20 \mu\text{eV}$ and $250 \mu\text{eV}$, respectively, which are illustrative values that we have used in the text.

or brightness temperature and that this gives a clearer picture of the potential for detection.

We can also calculate the background intensity due to all axions in the Universe with comoving density ρ_a

$$I_{\text{back}} = \frac{c^2 \rho_a}{4\pi [r(z)]^2 \tau_{2\gamma} f_{\text{emit}}} \frac{dV}{dz d\Omega}, \quad (4.13)$$

where $\frac{dV}{dzd\Omega} = cr(z)^2/H(z)$ is the comoving volume element and $H(z)$ is the Hubble parameter at redshift z . Using this we can deduce a background brightness temperature

$$T_{\text{RJ}}^{\text{back}} = \frac{3h^3c^5}{8\pi^2k_B G} \frac{H_0\Omega_a}{\tau_{2\gamma}} \left(\frac{1}{m_a c^2} \right)^3 \frac{(1+z)^2}{E(z)}. \quad (4.14)$$

Assuming that $\Omega_a h_{100}^2 \approx 0.12$ and $h_{100} = 0.7$, we obtain

$$\begin{aligned} T_{\text{RJ}}^{\text{back}} &\approx 0.3 \text{ pK} \frac{(1+z)^2}{E(z)} \left(\frac{m_a c^2}{250 \mu\text{eV}} \right)^{-3} \left(\frac{\tau_{2\gamma}}{8 \times 10^{35} \text{ s}} \right)^{-1}, \\ &\approx 0.3 \text{ pK} \frac{(1+z)^2}{E(z)} \left(\frac{g_{a\gamma\gamma}}{10^{-10} \text{ GeV}^{-1}} \right)^2. \end{aligned} \quad (4.15)$$

In making this background estimate we have ignored possible stimulated emission which would, of course, contribute at lower frequencies as was the case for the signal from virialised halos. The fact that this value is significantly lower than that for a halo means that there will be enough contrast to detect the signal from a halo against the background.

One can recover eq. (4.15) by substituting the background value for $\Sigma/\Delta v$ into (4.12). This background value is given by

$$\frac{d\Sigma}{dv} = \rho_a(z) \frac{dl}{dv} = \frac{(1+z)^3}{E(z)} \frac{\rho_a(0)}{H_0}, \quad (4.16)$$

so that at $z = 0$ this is $\rho_a(0)/H_0 \approx 1.2 \times 10^{-9} \text{ kg m}^{-3} \text{ s}$ using $\Omega_a h_{100} \approx 0.17$. Note that one can make a rough estimate for the surface mass density of the background by multiplying the density of axions by the size of the Universe given by the Hubble radius, that is, $\Sigma_{\text{back}} \approx \rho_a c/H_0 \approx 0.36 \text{ kg m}^{-2}$. This value is a factor of a few larger than the fiducial value we used for the halo surface mass density. To explain why this is the case, it is useful to notice that $\Sigma^{\text{halo}} \approx \rho_a \Delta_{\text{vir}} R$, where Δ_{vir} represents the virial overdensity of the halo. This quantity can be evaluated,

given a cosmological model, using the virial theorem (see the Appendix in [215] for details on the implementation and [216] for a recent discussion on the topic), but here we will consider it to be of the order of 200 (higher values are also often used). The ratio between the two expressions, $\Sigma^{\text{back}}/\Sigma^{\text{halo}} \approx \frac{c/H_0}{\Delta_{\text{vir}} R} \gg 1$ for our strawman object, but it is of the order of a few for $\Delta_{\text{vir}} \sim 200$ (a few hundred) and $R \sim 3 \text{ Mpc}$.

In fig. 4.2, we present estimates of the brightness temperature expected from a halo with a fixed velocity width $\Delta v = 200 \text{ kmsec}^{-1}$ and a range of values for Σ_{beam} computed using (4.11). We have fixed $g_{a\gamma\gamma} = 10^{-10} \text{ GeV}^{-1}$ which is close to the upper limit from the CAST experiment (and hence the target goal) and have included the effects of stimulated emission by the CMB which leads to an increase $\propto m_a^{-1}$ for $m_a \ll 470 \mu\text{eV}$. We have chosen $\Sigma_{\text{beam}} = 0.07 \text{ kgm}^{-2}$ which is Σ_{vir} for our strawman object, along with ten, hundred and a thousand times this value. In subsequent sections, we will discuss that such values might be attainable by observing more concentrated regions of the halo close to their centres.

In addition we have also added noise curves for a total integration time of 1 year with instantaneous sensitivities of $10 \text{ mK s}^{1/2}$, 100 and $1 \mu\text{K s}^{1/2}$ at $m_a c^2 = 250 \mu\text{eV}$ with the scaling $\propto (m_a/250 \mu\text{eV})^{-1/2}$ so that the noise level remains that for a fixed velocity width as m_a varies. We see that a sensitivity of $\sim 10 \text{ mK s}^{1/2}$ - which we will argue in section 4.2 is typical of a single pixel receiver at the relevant frequencies and bandwidths - is not sufficient to get anywhere near detecting the signal for $g_{a\gamma\gamma} = 10^{-10} \text{ GeV}^{-1}$, never mind that expected for the KSVZ and DFSZ models for typical values of Σ_{beam} as large as 7 kg m^{-2} . One might imagine that this can be reduced by having N receivers/telescopes in which case the instantaneous sensitivity will be $\approx 10 \text{ mK s}^{1/2}/\sqrt{N}$. Looking at fig. 4.2, it appears that $N \sim 10^2$ would be necessary to probe signals created

by $\Sigma_{\text{beam}} \approx 70 \text{ kg m}^{-2}$, $\sim 10^4$ to probe 7 kg m^{-2} , $\sim 10^6$ to probe 0.7 kg m^{-2} and $\sim 10^8$ for our strawman value of 0.07 kg m^{-2} . Therefore, it is clear that one would need to target sufficiently concentrated parts of haloes to probe this decay, which might be possible in haloes with supermassive black holes at their centres, although the local CDM density is highly uncertain in such environments. While this enhancement would not allow one to probe the benchmark QCD models for the axion, one could at least probe the parameter space below the well-established CAST limit [see fig.(4.2) for sensitivity estimates].

4.2 Sensitivity estimates for current and planned telescopes

Telescope	N	A_{eff} [m ²]	T_{sys} [K]	Frequency [GHz]	θ_{FWHM} [arcmin]	R_{beam} [kpc]
GBT	1	5500	30	30	0.3	0.5
FAST	1	50000	20	2.4	1.4	2.1
SKA1:Band 5	200	120	20	4.6-13.6	5.1-14.9	7.3-21.7
SKA2:Band 5	10000	120	20	4.6-13.6	5.1-14.9	7.3-21.7

Table 4.1: Table of telescope parameters which we have used in section 4.2 that are *indicative* of what might be possible using current and planned facilities. N is the number of dishes, A_{eff} the effective collecting area, T_{sys} the overall system temperature (in Rayleigh-Jeans regime), θ_{FWHM} the beam size and R_{beam} the radius corresponding to the beam size assuming a distance of 5 Mpc. GBT is the Green Bank Telescope and FAST is the Five hundred metre Aperture Spherical Telescope. They are currently operational and can cover a range of frequencies (up to ≈ 100 GHz in the case of GBT and up to ≈ 3 GHz for FAST). For the purposes of the discussion we have chosen to focus on one frequency for each and have chosen values of T_{sys} indicative of the noise levels that would be possible. We refer the reader to their webpages <https://greenbankobservatory.org> and <http://fast.bao.ac.cn/en/> for more detailed information about the capabilities. The Square Kilometre Array (SKA) is currently being designed/built in two phases. Phase I is much more certain than phase II. Again we believe that our numbers are indicative of what might ultimately transpire.

In this section we assess the possibility of detecting the decay of dark matter axions emitted from virialised halos using current and planned telescopes operating in the radio/mm waveband. We have tabulated the numbers we have used in the sensitivity calculations below in table 4.1. Typically, previous analyses have focused on comparing the flux density to the expected telescope noise. As we have already alluded to and indeed we will explain below that it is best to frame the discussion of sensitivity in terms of the intensity, or more commonly the brightness temperature.

4.2.1 Flux Density Signal

Having discussed the signal strength associated to axion decays in the previous sub-section, we turn now to another key parameter in determining the feasibility of detection - the integration time. The integration time required to detect a flux density S_σ in a bandwidth Δf_{obs} can be deduced from the radiometer equation

$$t_{\text{int}} = \left(\frac{2k_{\text{B}}T_{\text{sys}}}{A_{\text{eff}}S_\sigma} \right)^2 \frac{1}{\Delta f_{\text{obs}}}, \quad (4.17)$$

where T_{sys} is the system temperature, S_σ is the flux density noise level and A_{eff} is the effective area. For a signal-to-noise ratio of unity, $S_{\text{beam}} = S_\sigma$. For a single dish telescope with aperture efficiency η (typically $\approx 0.5 - 0.7$), this is given by $A_{\text{eff}} = \eta\pi D^2/4$. Using this, we can deduce that for a 1σ detection of the flux described by eq. (4.6) for a fiducial $M_{\text{beam}} = 10^{12}M_\odot$, the integration time is given by

$$t_{\text{int}} \approx \frac{10 \text{ days}}{(1 + \mathcal{F}_\gamma^{\text{eff}})^2(1 + z)} \left(\frac{T_{\text{sys}}}{30 \text{ K}} \right)^2 \left(\frac{A_{\text{eff}}}{5500 \text{ m}^2} \right)^{-2} \times \\ \left(\frac{\Delta v}{200 \text{ km s}^{-1}} \right) \left(\frac{g_{a\gamma\gamma}}{10^{-10} \text{ GeV}^{-1}} \right)^{-4} \times \\ \left(\frac{m_a c^2}{250 \text{ } \mu\text{eV}} \right)^{-5} \left(\frac{M_{\text{beam}}}{10^{12} M_\odot} \right)^{-2} \left(\frac{d_L(z)}{5 \text{ Mpc}} \right)^4, \quad (4.18)$$

where the specific choice for T_{sys} and A_{eff} have been chosen to be indicative of what might be possible for observations at 30 GHz with a 100 m telescope such as the GBT which would have a resolution ≈ 20 arcsec operating in a band around 30 GHz and an axion mass $m_a c^2 \approx 250 \mu\text{eV}$. Despite this particular choice, the expression for t_{int} should be applicable to the whole range of frequencies observed by the GBT, and indeed any single dish radio telescope, provided M_{beam} is chosen appropriately. We chose the GBT to illustrate this since it is the largest telescope

in the world operating at these frequencies and possibly as high as $\lesssim 100$ GHz. Setting a 95% exclusion limit - which is the standard thing to do in constraining dark matter - would require approximately 40 days. Detection at the 5σ level would take 25 times longer, i.e., 250 days of on-source integration time. Achieving an exclusion limit for the flux expected for the KSVZ model in this mass range would require ruling out $\tau_{2\gamma} \approx 6 \times 10^{40}$ s which would take 5×10^9 times longer, and the level expected for DFSZ will be even lower, neither of which are practical. We note that $\mathcal{F}_{\text{CMB}} \approx 0.5$ for $m_a c^2 = 250 \mu\text{eV}$ and ≈ 12 for $m_a c^2 = 20 \mu\text{eV}$ which will reduce the required integration times, but probably not enough to make much difference to the conclusions.

Despite this, one might think that integration times of a few tens of days might allow one to impose stronger limits than the CAST bounds. However, the numerical value in (4.18) is quite misleading since such a telescope would have a resolution of ≈ 20 arcsec at these frequencies and therefore we would expect $M_{\text{beam}} \ll M_{\text{vir}}$. From eq. (4.5) we have that $R_{\text{beam}} \approx 0.5$ kpc when the galaxy would be expected to have a total radius of $R_{\text{vir}} \approx 100$ kpc, which is a factor of 200 larger.

Mass inside the beam radius

We can obtain an estimate for the total halo mass contained within the beam by using the canonical halo dark matter distribution given by the Navarro-Frenk-White (NFW) profile [205] parameterised by the concentration parameter, \hat{c} , which is the ratio of the virial radius and the scale radius of the halo. It quantifies the amount of mass within the scale radius relative to that in the total halo, with large values of \hat{c} having more mass *concentrated* in the centre than lower values.

Consider a halo density profile $\rho(r) = \rho_s F(r/r_s)$ for $r < R_{\text{vir}}$ and zero otherwise. In the function $F(y)$, r_s is the scale radius, R_{vir} the virial radius and the ratio of the two $\hat{c} = R_{\text{vir}}/r_s$ is the concentration parameter. For the specific case of an Navarro-Frenk-White (NFW) profile [205], $F(y) = y^{-1}(1+y)^{-2}$. The mass inside the virial radius is given by

$$M_{\text{vir}} = 4\pi\rho_s r_s^3 \int_0^{\hat{c}} x^2 F(x) dx, \quad (4.19)$$

and the surface mass density at some radius, R , is

$$\Sigma(R) = 2r_s\rho_s \int_{\bar{R}}^{\hat{c}} \frac{yF(y)dy}{\sqrt{y^2 - \bar{R}^2}}, \quad (4.20)$$

where $\bar{R} = \hat{c}R/R_{\text{vir}}$. Both expressions (4.19) and (4.20) converge for $\bar{R} \rightarrow 0$.

In this work, we are particularly interested to the mass inside the radius of a telescope and defined by R_{beam} . We can evaluate this from

$$\begin{aligned} M_{\text{beam}} &= 2\pi \int_0^{R_{\text{beam}}} R \Sigma(R) dR, \\ &= M_{\text{vir}} \frac{\int_0^{\bar{R}_{\text{beam}}} x dx \int_x^{\hat{c}} \frac{yF(y)dy}{\sqrt{y^2 - x^2}}}{\int_0^{\hat{c}} x^2 F(x) dx}, \end{aligned} \quad (4.21)$$

where $\bar{R}_{\text{beam}} = \hat{c}R_{\text{beam}}/R_{\text{vir}}$. By manipulating the double integral, we can deduce that

$$\frac{M_{\text{beam}}}{M_{\text{vir}}} = 1 - \frac{\int_{\bar{R}_{\text{beam}}}^{\hat{c}} \sqrt{y^2 - \bar{R}_{\text{beam}}^2} F(y) dy}{\int_0^{\hat{c}} x^2 F(x) dx}. \quad (4.22)$$

For an NFW profile [217]

$$\frac{M_{\text{beam}}}{M_{\text{vir}}} \approx \frac{1}{f(\hat{c})} \left[\log \left(\frac{\bar{R}_{\text{beam}}}{2} \right) + \frac{1}{\sqrt{1 - \bar{R}_{\text{beam}}^2}} \cosh^{-1} \frac{1}{\bar{R}_{\text{beam}}} \right], \quad (4.23)$$

where $f(x) = \log(1+x) - \frac{x}{1+x}$. For small \bar{R} this is given by

$$\frac{M_{\text{beam}}}{M_{\text{vir}}} = -\bar{R}_{\text{beam}}^2 \frac{\log \left(\frac{\bar{R}_{\text{beam}}}{2} \right)}{2f(\hat{c})}. \quad (4.24)$$

The analytic approximation (4.24) and the exact results (4.22) are shown respectively as solid/dotted lines in fig. 4.3.

In appendix 4.2.1 we have calculated for $\hat{c}R_{\text{beam}}/R_{\text{vir}} = R_{\text{beam}}/r_s \ll 1$, that is, a beam size much less than the characteristic scale of the NFW profile, the following estimate for the halo mass contained within the telescope beam:

$$\frac{M_{\text{beam}}}{M_{\text{vir}}} = \frac{R_{\text{beam}}^2}{R_{\text{vir}}^2} \cdot \frac{\hat{c}^2}{2f(\hat{c})} \log \left(\frac{2R_{\text{vir}}}{\hat{c}R_{\text{beam}}} \right), \quad (4.25)$$

where $f(x) = \log(1+x) - \frac{x}{1+x}$. The behaviour of the beam mass is plotted in fig. 4.3. Using this expression we deduce that $M_{\text{beam}} \approx 0.8 \times 10^9 M_{\odot}$, $1.9 \times 10^9 M_{\odot}$ and $6.2 \times 10^9 M_{\odot}$ for $\hat{c} = 3, 5$ and 10 , respectively. As one would expect, there is a trend for M_{beam} to increase as \hat{c} decreases, since smaller values of \hat{c} correspond to larger haloes with greater mass concentrated in their centres. However, even for relatively large values we find that in this case $M_{\text{beam}} \ll M_{\text{vir}}$. Clearly, this reduction in M_{beam} has a deleterious effect on the ability of a single dish telescope to even post an upper limit on the spontaneous decay of dark matter axions since $t_{\text{int}} \propto M_{\text{beam}}^{-2}$ with $t_{\text{int}} \approx 3 \times 10^4$ years for $M_{\text{beam}} = 10^9 M_{\odot}$. Therefore, one needs

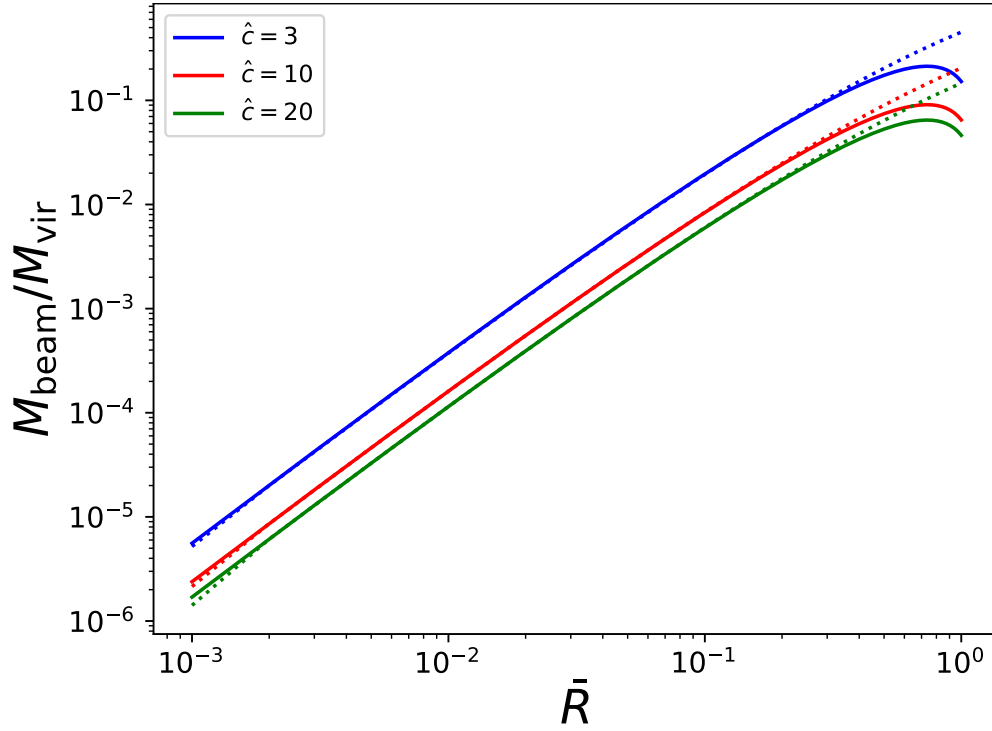


Figure 4.3: Projected mass within the beam as a function of $\bar{R} = cR_{\text{beam}}/R_{\text{vir}}$ assuming an NFW profile. From top to bottom, we consider three different concentration parameters, ranging from clusters to dwarf galaxies. The solid lines represent an analytic approximation for $\bar{R} \ll 1$, while the dotted lines are given by full numerical integration - see appendix 4.2.1 for details.

to be very careful in using (4.18).

It is possible to think in terms of the flux density, but as we have explained above one has to be very careful to use the mass inside the beam radius and not the total mass of the object since they will typically be very different. Our view is that it is much easier to think in terms of the brightness temperature (or equivalently the intensity, although telescope sensitivities are more commonly expressed in terms of a brightness temperature).

4.2.2 Brightness Temperature Signal

The calculation of the noise temperature is simpler. The noise level in intensity is simply given by $I_\sigma = S_\sigma/\Omega_{\text{beam}}$. Substituting for the intensity in terms of Rayleigh-Jean's law and setting $\Omega_{\text{beam}} = \lambda^2/D_{\text{tel}}^2$, we obtain the well-known Radiometer equation for the brightness temperature

$$T_\sigma = \frac{T_{\text{sys}}}{\eta\sqrt{\Delta f_{\text{obs}} t_{\text{int}}}}, \quad (4.26)$$

for a single telescope with system temperature T_{sys} and aperture efficiency η observing in a bandwidth of Δf_{obs} . The instantaneous sensitivity is just given by $T_{\text{sys}}/(\eta\sqrt{\Delta f_{\text{obs}}}) \approx 10 \text{ mK s}^{1/2} (T_{\text{sys}}/30 \text{ K}) (\Delta f_{\text{obs}}/20 \text{ MHz})^{-1/2}$ for $\eta = 0.7$ and hence the integration time required to detect a surface mass density of Σ_{beam} , which is that averaged over the beam radius, at 1σ is

$$\begin{aligned} t_{\text{int}} \approx & 3 \times 10^8 \text{ years} \frac{(1+z)^3}{(1+\mathcal{F}_\gamma^{\text{eff}})^2} \left(\frac{T_{\text{sys}}}{30 \text{ K}} \right)^2 \times \\ & \left(\frac{g_{a\gamma\gamma}}{10^{-10} \text{ GeV}^{-1}} \right)^{-4} \left(\frac{\Sigma_{\text{beam}}}{0.07 \text{ kg m}^{-2}} \right)^{-2} \times \\ & \left(\frac{\Delta v}{200 \text{ kmsec}^{-1}} \right) \left(\frac{m_a c^2}{250 \mu\text{eV}} \right)^{-1}. \end{aligned} \quad (4.27)$$

Note that this is independent of the telescope collecting area, as one would expect for an unresolved detection, and also there is no explicit dependence on the distance, although there is a dependence on the redshift. Many of the other dependencies, for example, on T_{sys} , Δv and $g_{a\gamma\gamma}$ are the same. Moreover, this expression (4.27) makes it very obvious that the discussion above based on (4.18) can be very misleading since the number at the front of the expression (remembering that the surface mass density of 0.07 kg m^{-2} was chosen to correspond to the average across an object of mass $10^{12} M_{\odot}$ and radius 100 kpc) is very much larger than in (4.18).

The fact that t_{int} is dependent on Σ_{beam} has two advantages. The first is that it is clear that in order to increase the size of the signal and hence reduce t_{int} to a practical length of time one has to increase Σ_{beam} . From our earlier discussion, we calculated, assuming an NFW profile, $M_{\text{beam}} \sim 10^9 M_{\odot}$ for our fiducial galaxy and telescope configuration for which $R_{\text{beam}} \approx 0.5 \text{ kpc}$, assuming a sensible range of concentration parameters. In this case the appropriate surface mass density would be¹

$$\Sigma_{\text{beam}} \approx 7 \text{ kg m}^{-2} \left(\frac{M_{\text{beam}}}{2.3 \times 10^9 M_{\odot}} \right) \left(\frac{R_{\text{beam}}}{0.5 \text{ kpc}} \right)^{-2}. \quad (4.28)$$

Of course this only gives one a factor of around 200 improvement but it makes it clear in what direction one might have to go in optimising the signal strength. We will return to this issue in sect. 4.3.

The other advantage is that it makes clear what one would have to do to establish an upper bound on the signal: one would need an estimate of Σ_{beam} over the region which one was observing. Fortunately, the amplitude of any gravitational lensing signal that one might measure is directly related to the surface mass density. The

¹We note that (4.27) and (4.18) would be identical if Σ_{beam} , M_{beam} and R_{beam} were chosen to be consistent with each other.

measurement of the amplification and shear can be related to the surface mass density of the lenses. One of the largest surface mass densities measured from strong lensing on the scale of a few kiloparsecs (which corresponds to the typical beam sizes) is 50 kg m^{-2} [218]. Such values are typically found towards the centre of virialised haloes. This motivates high resolution observations and a detailed study of high-density sources with rich ambient radio emission for an accurate estimate of Σ_{beam} and \mathcal{F}^{eff} .

The discussion so far has focused on the axion mass range $m_a c^2 \approx 250 \mu\text{eV}$, but we have also motivated searches at lower masses, for example, $m_a c^2 = 20 \mu\text{eV}$ which corresponds to $f_{\text{obs}} = 2.4 \text{ GHz}$. The Five hundred meter Aperture Spherical Telescope (FAST) might be a candidate large telescope for the detection of axions in this mass range. Despite its name, it can only illuminate beams with $D \approx 300 \text{ m}$ corresponding to a resolution of $\approx 1.4 \text{ arcmin}$ and $R_{\text{beam}} \approx 2 \text{ kpc} \ll R_{\text{vir}}$. The bandwidth corresponding to $\Delta v = 200 \text{ km sec}^{-1}$ at $z = 0$ is $\Delta f_{\text{obs}} = 1.6 \text{ MHz}$. The instantaneous sensitivity to such $T_{\text{sys}}/(\eta\sqrt{\Delta f_{\text{obs}}}) \approx 20 \text{ mK s}^{1/2} (T_{\text{sys}}/20 \text{ K}) (\Delta f_{\text{obs}}/1.6 \text{ MHz})^{-1/2}$ which is a little larger than for our estimate for the GBT at 30 GHz despite having a lower system temperature. The formula (4.27) should apply here as well with the values of T_{sys} and Σ_{beam} adjusted to take into account R_{beam} being a little larger. Ultimately, we come to the same conclusion.

If a focal plane array or phased array were fitted to the telescope, it might be possible to observe with N beams and this would reduce the amount of integration time required by a factor of $1/N$. However, there are practical limitations on the size of array which one can deploy on telescope since the physical size of the region over which one can focus is limited; much more than $N \sim 100$ would be difficult to imagine. Moreover, the beams cannot point at the same region of the

sky and just serve to increase the field-of-view. This does reduce the noise level, but over a wider area which would likely result in the decrease in the expected signal strength.

A number of recent works [211, 212, 219, 220] have suggested that it might be possible to use the Square Kilometre Array (SKA) to search for axions. Naively the very large collecting area of the SKA in the formula (4.18) would substantially reduce the necessary integration time. The proposed band 5 of the SKA, which has a frequency range of $4.6 - 13.7$ GHz, could potentially be of interest for the detection of axions in the mass range $40 - 110 \mu\text{eV}$. However, it is not valid to use the entire collecting area of the SKA in this way because the beam size, since it is an interferometer, is set by the longest baseline and this would be far too small. If one thinks in terms of brightness temperature, there is an extra factor, known as the filling factor, $\eta_{\text{FF}} \ll 1$, which will increase the noise level $\propto \eta_{\text{FF}}^{-1}$.

An interesting alternative approach would be to use each of the SKA telescopes as single telescopes in auto-correlation mode as it is envisaged for HI intensity mapping [221]. The SKA dishes will have a diameter of $D = 15$ m and a sensitivity defined by $A/T_{\text{sys}} \approx 6 \text{ m}^2 \text{ K}^{-1}$. Operating in band 5, this will have a resolution of $\theta_{\text{FWHM}} \approx 15$ arcsec at the lower end of the band and ≈ 6 arcsec at the higher end. In the first instance the SKA - SKA phase 1, sometimes called SKA1 - will have ≈ 200 such dishes but may eventually - SKA2 - have ≈ 10000 . As before, the integration time for the telescopes decreases by a factor of N , the number of telescopes, but unlike a phased array on a single telescope they can co-point at the same region of sky which is advantageous. With 200 telescopes, we estimate an integration time of about 1.5×10^6 years, while for 10^4 telescopes, we obtain $t_{\text{int}} \approx 3 \times 10^4$ years. This estimate will be smaller for lower masses (around 2 orders of magnitude at $m_a c^2 = 20 \mu\text{eV}$) due to the enhancement from

the stimulated decay. However, this will be mitigated to some extent by the factor $m_a c^2$ in the denominator of (4.27). The values used are for a strawman object, while if we use the surface mass density of (4.28), we would estimate integration times $\approx 10^4$ times smaller, which might bring this in the realms of possibility. We note that our integration time estimate for dwarf galaxies is consistent with that of reference [212] up to a factor of a few, although it is difficult to make a precise comparison. We believe that any minor discrepancies might be due to the fact that observational measurements of the size of the individual dwarf galaxies might lead to slight overestimation of the signal from them. This point is borne out in fig. (4.6), where we obtain slightly lower integration times for higher mass objects when we determine object size from the virial overdensity parameter, via the relationship between the virial mass and radius.

Reference [222] published an upper limit for $g_{a\gamma\gamma}$ based on 6 days of observations using the Haystack radio telescope for axions in the mass range around $m_a c^2 \approx 300 \mu\text{eV}$. In [222] they state that $T_{\text{sys}} \approx 100 \text{ K}$ and we estimate $A_{\text{eff}} \approx 750 \text{ m}^2$ (assuming $\eta \approx 0.6$) and hence flux density and brightness temperature sensitivities of $100 \text{ mJy s}^{1/2}$ and $40 \text{ mK s}^{1/2}$, respectively, in an observing bandwidth of $\Delta f_{\text{obs}} \approx 4 \text{ MHz}$. They assume a mass of $\approx 10^7 M_\odot$ and a diameter of $\approx 10 \text{ kpc}$ for the dwarf galaxies which they probe at distances in the range $d \approx 200 \text{ kpc}$ with velocity width of $\Delta v \approx 30 \text{ km s}^{-1}$ equivalent to $\Delta f_{\text{obs}} \approx 3.6 \text{ MHz}$. For $\tau_{2\gamma} = 5 \times 10^{33} \text{ s}$, which corresponds to their upper limit of $g_{a\gamma\gamma} < 10^{-9} \text{ GeV}^{-1}$, we predict a flux density of $S \approx 4 \text{ mJy}$ which would take $3 \times 10^3 \text{ s}$ to obtain a 95% exclusion limit. However, the typical angular diameter of these objects is $\approx 3 \text{ deg}$, which is very much larger - by more than a factor of 100 - than the beam size which would mean that $M_{\text{beam}} \ll M_{\text{vir}}$. For the reasons explained earlier, it is clear that they must have made some error in their calculations and this limit

should be discounted.

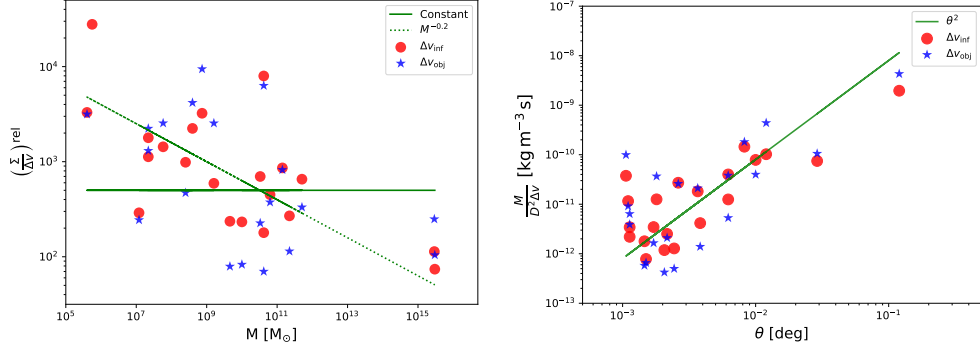


Figure 4.4: In the *left* panel. Signal strength as given by $\Sigma/\Delta v \propto T_{\text{RJ}}$. We assume an *identical* Strawman object (see the beginning of the chapter) and beam size $\Sigma = M_{\text{obj}}/(\theta_{\text{obj}} D_{\text{obj}})^2$ taking values from table 4.2. Note we normalised Σ by the background value $1.2 \times 10^{-9} \text{ kg m}^{-3} \text{ s}$. The trend appears relatively flat for the data in the table - the solid green line - and is compatible with the simple argument presented in the text, albeit with a somewhat higher value (≈ 500) relative to the background value. Possibly there is a trend with mass which we denoted with a line $\propto M^{-0.2}$ which could be due to the concentration parameter varying as a function of mass and the fact that the angular sizes are probably the scale radius for some fitted profile function rather than the virial radius. We note that much of this trend is driven by the outliers at low mass, ultra-faint dwarf spheroidal, and high mass, the galaxy clusters, Virgo and Coma. In the *right* panel, we present the quantity in (4.30) for the data in table 4.2 which clearly increases like θ_{obj}^2 as denoted by the line in the plot. Note that the starred data points, which use observational measurements of the velocity width Δv_{obj} , and the circular points, which correspond to the inferred width $\Delta v_{\text{inf}} \approx (GM_{\text{obj}}/R_{\text{obj}})^{1/2}$, show the same trend.

4.3 Optimising target objects

In the previous two sections we have explained that, if one targets a halo with surface mass density $\Sigma_{\text{beam}} \approx 0.07 \text{ kg m}^{-2}$ and velocity width $\Delta v \approx 200 \text{ km s}^{-1}$, the signal from stimulated emission from the CMB for $g_{a\gamma\gamma} = 10^{-10} \text{ GeV}^{-1}$ is too weak to be detected even for an array of receivers with $N \lesssim 10^6$. We came to this conclusion by estimating the integration time required to detect the signal focusing on the expression for the signal expressed in terms of the brightness temperature (4.12).

4.3.1 Maximising brightness temperature

Examination of equation (4.12) makes it clear that the largest possible signal is obtained by maximising $\Sigma_{\text{beam}}/\Delta v$. If the object is such that $\theta_{\text{FWHM}} \approx \theta_{\text{vir}}$, we estimate the quantity to be $\approx 3.5 \times 10^{-7} \text{ kg m}^{-3} \text{ s}^{-1}$ for the strawman object used in the previous section which is around 300 times larger than the background value. This value is based on what we think, at a level of better than a factor two, are realistic values, but precise knowledge of it is absolutely critical to any attempt to improve the CAST limits of $g_{a\gamma\gamma}$ using this approach. In this section, we will discuss, using theoretical arguments and comparing to observations, the range of values for $\Sigma_{\text{beam}}/\Delta v$ that might be available for us to be observed in the Universe.

Consider now the possibility that the effective beam size is sufficiently large to capture the full object flux so that $S_{\text{beam}} = S_{\text{tot}}$. From the beam geometry, one expects that $S_{\text{tot}} \propto M_{\text{vir}}$ - the scenario considered by [211]. Indeed this setup can be realised by considering the resolution of the SKA dishes at 2.4 GHz ($m_a c^2 = 20 \mu\text{eV}$) for which most of our candidate objects (table 4.2) are within the beam of the telescope. Put simply, this means that we are in the regime where the surface mass density within the beam is that of the whole object, i.e., $\Sigma_{\text{beam}} = \Sigma_{\text{vir}}$. Similarly, $M_{\text{beam}} = M_{\text{vir}}$. Throughout the subsequent discussion we therefore identify $\Sigma_{\text{beam}} = \Sigma_{\text{vir}}$ and phrase our analysis purely in terms of Σ_{vir} .

One might wonder how $\Sigma_{\text{vir}}/\Delta v$ depends on the size of the object. If we consider a halo with virial overdensity $\Delta_{\text{vir}} \sim 100$, then $M_{\text{vir}} = \frac{4\pi}{3} \Delta_{\text{vir}} \rho_a R_{\text{vir}}^3$, where $\rho_a = \Omega_a \rho_{\text{crit}}$ is the background density of axions and ρ_{crit} is the critical density. An estimate for the velocity width, up to order one factors, is $\Delta v = (GM_{\text{vir}}/R_{\text{vir}})^{1/2}$

and hence we find that

$$\frac{\Sigma_{\text{vir}}}{\Delta v} \approx 0.7 \left(\frac{\Delta_{\text{vir}} \rho_a}{G} \right)^{1/2} \approx 3.5 \times 10^{-7} \text{ kg m}^{-3} \text{ s}, \quad (4.29)$$

which is independent of the size of the object - that is, there is no dependence on M_{vir} or R_{vir} . If Δ_{vir} is universal and independent of the size of the object, as it is supposed to be almost by definition, then the expected brightness temperature averaged over a virialised halo will be independent of the size and hence the optimal detection for a specific halo size and telescope configuration would be obtained by matching the size of the object approximately to the telescope beam width. This is the standard practice to optimise detection efficiency in all branches of astronomy.

This suggestion, that there is no optimal size of object, appears to be contrary to the conclusions of [211], who claimed that the optimal detection would be for dwarf spheroidal galaxies, that is, the very lowest mass halos. They came to this conclusion considering the quantity

$$\frac{1}{\Delta v} \int d\Omega dl \rho_a \propto \frac{M_{\text{beam}}}{d^2 \Delta v} \propto S_{\text{beam}}, \quad (4.30)$$

where d is the distance to the object and the angular integration is over the angular size of the object - or, as they state it, for a telescope beam which has the same size as the object. This quantity is $\propto S_{\text{beam}}$ defined in (4.6) which is equivalent to (4.11) if one is careful with the choice of Σ_{beam} . But we have already explained that one can come to the wrong conclusion if one uses the wrong value of M_{beam} for a specific halo and that it is actually better to think in terms of the surface mass density Σ_{beam} .

In fig. 4.4, we have plotted the quantities in (4.30) and (4.29) using the data in

table 4.2 which is similar to, but not exactly the same as, that used in [211]. In particular, we have added some galaxies and galaxy clusters to the dwarf galaxies which they focus on that enables us to probe a wider lever arm in mass. The table contains values for the distance to and the mass of the object D_{obj} and M_{obj} , respectively, the angular size θ_{obj} and the velocity width Δv_{obj} . These are inferred in a heterogeneous way, but should at least be indicative of some truth. We would not necessarily expect these values to be those for a virialised halo and therefore we denoted them with the suffix “obj” to distinguish them as being observationally determined. From the observed information, we can infer the radius, $R_{\text{obj}} = \theta_{\text{obj}}/(2D_{\text{obj}})$ and also check consistency with our analytic estimates above by inferring $\Delta v_{\text{inf}} = (GM_{\text{obj}}/R_{\text{obj}})^{1/2}$, as well as calculating the surface mass density appropriate to an average over the object radius, $\Sigma_{\text{obj}} = M_{\text{obj}}/(\pi R_{\text{obj}}^2)$.

Firstly, we find in the right panel of fig. 4.4 that (4.30) which was plotted in [211] is indeed $\propto \theta_{\text{obj}}^2$ as claimed. But on the basis of the theoretical argument above, this is exactly what one would expect for the total flux density $S_{\text{tot}} \propto \Sigma_{\text{ave}} \theta^2 / \Delta v$, where Σ_{ave} is some average surface mass density for the objects, and hence, while it provides some confidence that the modelling is correct, it does not yield any obvious information about which objects would be optimal.

In the left panel of fig. 4.4 we have plotted $\Sigma_{\text{obj}}/\Delta v$ for the data presented in table 4.2, using both Δv_{obj} and Δv_{inf} with consistent results. We find that the data are compatible with $\Sigma_{\text{beam}}/\Delta v$ being a constant over eight orders of magnitude and for it to be ≈ 500 times the background value - slightly higher than for our strawman object - within the kind of uncertainties that we might expect coming from a heterogeneous sample such as the one which we have used. Visually, there could be some evidence for a trend $\sim M^{-0.2}$ which we have also included to guide

the eye, but the evidence for this is largely due to a few outliers at the low- and high-mass ends where perhaps the observational estimates are most uncertain. So it could be that there is some preference for lower mass halos over high mass halos, but the effect is not very dramatic. Note that on the y -axis, we plot $(\Sigma/\Delta v)^{\text{rel}} \equiv \frac{\Sigma/\Delta v}{1.2 \times 10^{-9} \text{ kg m}^{-3} \text{ s}}$, where the denominator is the value associated to the background.

It could be that the possible trend seen in the left panel of fig. 4.4 is related to the concentration parameter of the halo. It is likely that the observationally determined angular size, θ_{obj} , is not the virial radius but some scale radius from a fitting function used in conjunction with images. If this is the case, then we might expect a weak trend with mass.

The concentration parameter has been computed in numerical simulations and is usually assumed to be universal for halos of a given mass, M . A recently proposed expression is [209]

$$\hat{c}(M, z) = \hat{c}_0(z) \left(\frac{M}{M_0} \right)^{-\gamma(z)} \left[1 + \left(\frac{M}{M_1(z)} \right)^{0.4} \right], \quad (4.31)$$

where $M_0 = 10^{12} h_{100}^{-1} M_{\odot}$ and $\hat{c}_0(z)$, $\gamma(z)$ and $M_1(z)$ are fitted parameters which are redshift dependent. We will focus on low redshifts where $\hat{c}_0(z) \approx 7.4$, $\gamma(0) \approx 0.12$ and $M_1(0) = 5.5 \times 10^{17} h_{100}^{-1} M_{\odot}$. From this we see that at $z = 0$, $\hat{c} \propto M^{-0.12}$, that is, lower mass halos typically are more concentrated than higher mass halos, and therefore there will be more mass inside the scale radius, and for observations focusing on the region inside this scale radius Σ_{beam} might be larger.

This leads us on to an important caveat in this discussion: one does not have to choose to focus on trying to detect the entire signal from a halo and indeed it will be optimal, as well as practical, to not do this. Using (4.25), we can eliminate

Object	D_{obj}	$M_{\text{obj}} (M_{\odot})$	θ_{obj}	$\Delta v_{\text{obj}} [\text{km s}^{-1}]$	Reference(s)
Leo 1	250 kpc	2.2×10^7	12.6 arcmin	8.8	[223]
NGC 6822	490 kpc	1.6×10^9	40 arcmin	8	[223]
Draco	82 kpc	2.2×10^7	28.3 arcmin	9.5	[223]
Wilman 1	45 kpc	4×10^5	9 arcmin	4	[224]
Reticulum 2	30 kpc	5.6×10^5	3.6 arcmin	3.3	[225, 226]
Sextans B	1345 kpc	3.9×10^8	3.9 arcmin	18	[223]
Pegasus	955 kpc	5.8×10^7	3.9 arcmin	8.6	[223]
Antlia	1235 kpc	1.2×10^7	5.2 arcmin	6.3	[223]
NGC 205	815 kpc	7.4×10^8	6.2 arcmin	16	[223]
NGC 5128	3.8 Mpc	5.1×10^{11}	34.7 arcmin	477	[210]
NGC 5194	15.8 Mpc	4.2×10^{10}	8.4 arcmin	175	[210]
Maffei2	2.8 Mpc	4.2×10^{10}	3.8 arcmin	306	[210]
IC2574	4.0 Mpc	4.6×10^9	13.2 arcmin	107	[210]
SexA	1.3 Mpc	2.5×10^8	5.9 arcmin	46	[210]
NGC 3556	9.9 Mpc	3.3×10^{10}	5.0 arcmin	308	[210]
IC 0342	3.3 Mpc	1.4×10^{11}	21.4 arcmin	181	[210]
NGC 6744	8.3 Mpc	2.2×10^{11}	21.4 arcmin	323	[210]
ESO 300-014	9.8 Mpc	10^{10}	7.1 arcmin	130	[210]
NGC 3184	11.1 Mpc	6.3×10^{10}	7.4 arcmin	128	[210]
Virgo	18 Mpc	2.9×10^{15}	7 degrees	1100	[227, 228]
Coma	100 Mpc	3×10^{15}	100 arcmin	1100	[229, 230]

Table 4.2: Table of masses (M_{obj}), distances (D_{obj}), angular sizes (θ_{obj}) and velocity widths (Δv_{obj}) extracted from the literature and used in fig. 4.4. In each case we have specified the reference of the paper from which the numbers are extracted/calculated. From paper to paper the methods employed are different and hence the overall sample is relatively heterogeneous. For each object we can infer a radius $R_{\text{obj}} = \theta_{\text{obj}} D_{\text{obj}} / 2$ and a velocity width $\Delta v_{\text{inf}} = (GM_{\text{obj}} / R_{\text{obj}})^{1/2}$. We find that Δv_{obj} is strongly correlated with Δv_{inf} as we would expect and indeed that M_{obj} is also correlated with R_{obj} .

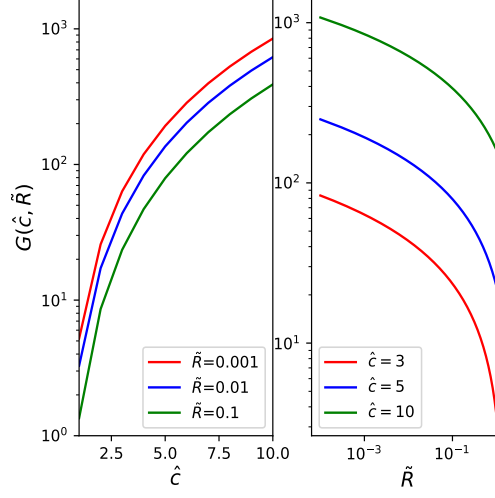


Figure 4.5: The function $G(\hat{c}, \tilde{R})$ as a function of its arguments. In the left panel, we plot G as a function of \hat{c} for different values constant \tilde{R} , and vice versa in the right panel.

M_{beam} and M_{vir} in terms of Σ_{beam} and Σ_{vir} . To do this we first recall the definition of the beam surface-mass density (see appendix 4.2.1)

$$\Sigma(R_{\text{beam}}) = \int_{R_{\text{beam}}}^{\hat{c}} \frac{r\rho(r)}{\sqrt{r^2 - R_{\text{beam}}^2}} dr, \quad (4.32)$$

$$M_{\text{beam}} = 2\pi \int_0^{R_{\text{beam}}} R\Sigma(R) dR, \quad (4.33)$$

where r is the radial coordinate of the object in question and R_{beam} is the projected distance which we identify to be given by the beam size. Explicitly for an NFW profile $\rho(r) = \rho_s F(r/r_s)$ with $F(y) = y^{-1}(1+y)^{-2}$, where r_s is the scale radius, R_{vir} the virial radius and the ratio of the two $\hat{c} = R_{\text{vir}}/r_s$. Next we can expand these integrals in small beam radius limit $\bar{R}_{\text{beam}} = \frac{R_{\text{beam}}}{R_{\text{vir}}} \ll 1$ to find the relation

$$\Sigma_{\text{beam}} \simeq G\left(\hat{c}, \frac{R_{\text{beam}}}{R_{\text{vir}}}\right) \Sigma_{\text{vir}}, \quad \bar{R}_{\text{beam}} \ll 1, \quad (4.34)$$

for an NFW profile $G(x, y) = x^2 \log(2y/x)/f(x)$ for $y/x \ll 1$. We anticipate that one could derive a similar expression for any halo profile.

We plot the function $G(\hat{c}, \frac{R_{\text{beam}}}{R_{\text{vir}}})$ as a function of \hat{c} and $\tilde{R} = R_{\text{beam}}/R_{\text{vir}}$, in fig. 4.5 which indicates that enhancements of up to 1000 might easily be possible and that these are likely to be larger in lower mass objects than those of higher mass. Therefore, at a first glance it would appear that, for a fixed experimental set up ($R_{\text{vir}}/R_{\text{beam}}$ fixed), one should search for an object with the largest concentration, a general result which we already anticipated in section 4.1. However, one should also note that for small \tilde{R} , which is fixed by the resolution of the telescope, the enhancement across the different concentration parameters is comparable. Furthermore, for a fixed resolution θ , $R_{\text{beam}}/R_{\text{vir}}$ is significantly smaller for larger mass halos, since R_{vir} is much larger. As a result, Σ_{beam} is larger for larger mass halos.

In conclusion, we have argued that maximising $\Sigma_{\text{beam}}/\Delta v$ will give the largest possible brightness temperature signal. Theoretical arguments suggest that if the beam encloses the virial radius of a particular object, this will be independent of mass and a very rudimentary search of the literature for specific values suggests that this could be true. However, for fixed observational setup, and hence fixed resolution, one might find a significant enhancement of the signal due to the fact that the surface mass density will increase as one probes the more central regions of a halo. These are likely to be larger for larger mass objects since the telescope beam probes denser regions of larger mass halos. This is the reason we have presented our sensitivity estimates as a function of Σ_{beam} and results for range of values $\Sigma_{\text{beam}} = 0.07 - 70 \text{ kg m}^{-2}$ in fig. 4.2.

4.3.2 Minimising Integration Time

From (4.18) and (4.27) we see that the integration time can be expressed either in terms of M_{beam} or Σ_{beam} . Here we shall use the latter measure. We have just seen

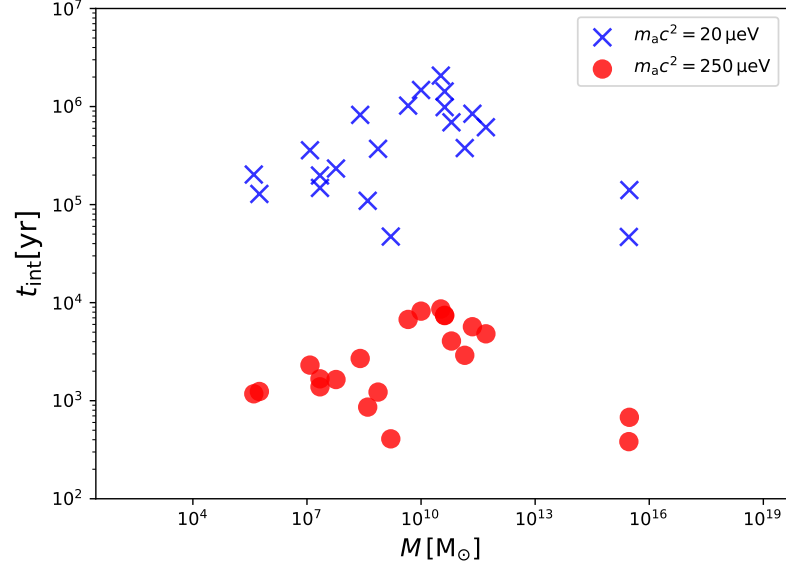


Figure 4.6: The integration time for the 1σ detection of the brightness temperature signal for the objects in table 4.2, assuming a single-pixel detector in a GBT-like telescope and the stimulated enhancement from both the CMB and the radio background. In this case, we have used (4.34) to evaluate Σ_{beam} assuming the resolution of the GBT, that is, the virial mass and the virial radii are related by the virial overdensity parameter, $M_{\text{vir}} \propto R_{\text{vir}}^3 \Delta_{\text{vir}}$. Note that we assume the fiducial signal strength corresponding to $g_{a\gamma\gamma} = 10^{-10} \text{ GeV}^{-1}$.

how brightness temperature is proportional to $\Sigma_{\text{beam}}/\Delta v$ and therefore largest when this ratio is maximal. However, whilst brightness temperature is a key observable, the ultimate arbiter of feasibility of detection is of course the integration time. From (4.18) we see the integration time has a slightly different dependence on the halo parameters Σ_{beam} and Δv to that of the brightness temperature, scaling instead as $t_{\text{int}} \propto \frac{1}{\Delta v} (\Sigma_{\text{beam}}/\Delta v)^{-2}$, with the additional factor of $1/\Delta v$ arising from the bandwidth of the signal. In light of the different parametric dependence of the integration time and brightness temperature on the halo parameters Σ_{beam} and Δv , and from table 4.2 since Δv varies significantly between objects, formally maximising $\Sigma_{\text{beam}}/\Delta v$ (brightness temperature) is slightly different to minimising $\Delta v/\Sigma_{\text{beam}}^2$ (integration time). Thus, it is natural to re-run the analysis of the previous discussion and check whether there is also no preferred object group for

t_{int} .

We can then estimate the beam surface mass density Σ_{beam} using the NFW profile as found in (4.34) and take values of Δv from table 4.2 as before. Thus, we must know R_{vir} , \hat{c} and Δv . We can infer the virial radius from the mass of the object $M_{\text{vir}} = M_{\text{obj}} = \frac{4\pi}{3}\Delta_{\text{vir}}\rho_a R_{\text{vir}}^3$, using the values in the table. The results for the integration time for different objects are plotted in fig. 4.6. We have assumed the resolution of the GBT, i.e., $\theta_{\text{FWHM}} \approx 10^{-4}$ at 30 GHz.

At $m_a c^2 = 250 \mu\text{eV}$, the stimulated enhancement factor is quite small. However, the decay time $\tau_{2\gamma}$ is significantly smaller than at $m_a c^2 = 20 \mu\text{eV}$. The values of $\mathcal{F}_\gamma^{\text{eff}}$ at lower mass aren't large enough to compensate for the increase of the decay time. Note that Σ_{beam} is roughly a factor of 2-3 smaller for lower mass, since the resolution is a factor ≈ 12 larger. Therefore, the integration time is lower at larger masses. As mentioned before, we see that the larger mass halos give a slightly lower integration time, since we are probing smaller values of \tilde{R} , i.e., denser regions of the halo. The Virgo cluster at $m_a c^2 = 250 \mu\text{eV}$ has an integration time of around 350 years. Ideally, one would want to find objects where $1 + \mathcal{F}_\gamma \gg 1$ at $m_a c^2 \geq 100 \mu\text{eV}$. Therefore, this motivates a more detailed study of the radio emission from the centre of the Virgo cluster.

In [212] it was suggested that the Galactic Centre could be a target since it would benefit from a large signal enhancement from the CMB, the measured radio background, but perhaps most importantly from the diffuse radio emission associated with the high density region and supermassive black hole located there. The size of the enhancement in this direction, $\mathcal{F}_\gamma^{\text{GC}}$, due to the photon occupation number density, will depend on the resolution of the telescope used in the measurement since $\mathcal{F} \approx I_\nu/E^3$. Hence, we need to estimate the intensity of radio emission from the Galactic Centre.

A measurement of the flux density of Sagittarius A* at 30 GHz is presented in the Planck Point Source Catalogue [231] and we will assume an intensity power law spectral index $\alpha = -2.8$ indicative of synchrotron emission and compatible with the spectrum of the Galactic Centre [232]. For any observation for which this source is effectively point-like, the intensity can be estimated as $I = S/\Omega_{\text{beam}} \times (f/30\text{GHz})^{-2.8}$ where $S \approx 200\text{Jy}$ is the flux density from the catalogue, f is the frequency of observation and Ω_{beam} is the area of the beam, which scales with frequency like f^{-2} .

For a GBT-like instrument, this gives us an intensity estimate $\approx 5 \times 10^5 \text{ Jy sr}^{-1}$ and hence the enhancement is

$$\mathcal{F}_{\gamma}^{\text{GC}} \approx 50 \left(\frac{250 \mu\text{eV}}{m_a c^2} \right)^{0.8}. \quad (4.35)$$

Clearly, this suggests that the galactic centre might be a good candidate to target for future studies. Of course, we are assuming in this calculation that the synchrotron index is the dominant contributor to the frequency dependence of the signal, which might be an oversimplification. However, this estimate clearly demonstrates that one can achieve similar sensitivity to the galactic centre with just a 100 m single-dish telescope rather than an array of many dishes used in auto-correlation mode, as done in reference [212] (which indicates that our order-of-magnitude estimate approximately agrees with their analysis). To make an accurate estimate of the stimulated enhancement factor, a dedicated study of the synchrotron, free-free as well as anomalous microwave emission(s) needs to be carried out, ideally on a pixel-by-pixel basis, from high-resolution observations of the galactic centre.

4.4 Observational conclusions

In the previous sections we have argued that the brightness temperature is a more robust quantity to measure, since one does not have to optimise to a specific solid angle for a given resolution. As a result, we have concluded that the appropriate quantity to optimise is $\Sigma_{\text{beam}}/\Delta v$. Higher resolution measurements of objects can benefit from an enhancement in the measured Σ_{beam} . For a flux density measurement, such an arrangement would result in $M_{\text{beam}} \ll M_{\text{vir}}$, which, of course, implies a weaker signal. Therefore, for single dish observations, the clear way forward is to target smaller regions of the Universe where one may obtain an enhancement for the surface mass density. Clearly, for such observations, one will require higher resolution which is easy for instruments like the GBT.²

We have also discussed the stimulated decay enhancement of the signal and noted that this enhancement is substantial at lower mass. A future experiment would greatly benefit from a dedicated study of specific sources for which high intensity radio emission has been measured. In our previous section, we motivated the Virgo cluster and the galactic centre. Note that for our sensitivity estimates for the galactic centre, we have assumed a constant Σ_{beam} for all axion masses, since the presence of the black hole results in a density spike at the galactic centre out to a few parsecs from the position of Sagittarius A*. For the radio background, we use the power law derived in [213], given by

$$T_{\text{ARCADE-2}} \approx 1.2 \text{ K} \left(\frac{1 \text{ GHz}}{f_{\text{obs}}} \right)^{2.62}. \quad (4.36)$$

²We thank Igor Irarstorza for sharing the CAST data.

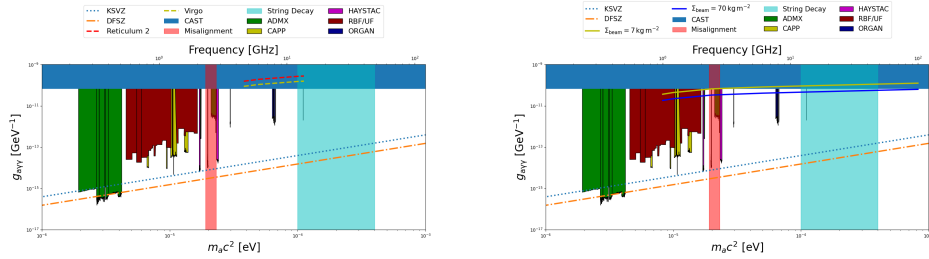


Figure 4.7: In the right panel, we show the sensitivity to axion-photon coupling as a function of axion mass observing a source with surface mass density Σ_{beam} and a velocity dispersion of 200 km s^{-1} which represent the typical values achievable by observations of the galactic centre. In the left panel, we assume $N = 10^4$ telescopes (SKA2:Band 5), used in single-dish mode for an integration time of 4 days and a system temperature of 30 K. The frequency coverage is as given on table 4.1. We include the enhancement due to the CMB and the radio background in this case, but note that the enhancement from the radio background is very uncertain. In the right panel, we show the sensitivity from observations between 1 and 100 GHz, assuming a 100 m single-dish telescope with a system temperature of 30 K, such as the GBT, and an integration time of 4 days. We included estimates of the stimulated emission enhancement from the CMB, the radio background and the synchrotron emission from the supermassive black hole, Sagittarius A* discussed in the text. We note that in reality, the system temperature for most radio telescope receivers varies with frequency, which would need to be modelled in an experiment. The sky-blue shaded region is the parameter region excluded by the CERN Axion Solar Telescope (CAST) [118]. The green and purple exclusions are from the ADMX [119–122] and HAYSTAC [123–125] haloscopes, respectively. The yellow exclusions are from the CAPP haloscope based in South Korea [128–130, 130, 131]. The dark red are from the RBF/UF haloscopes [132, 133]. Finally, the dark blue limits from the ORGAN collaboration [134, 135]. We also highlight the axion mass ranges predicted by the misalignment mechanism (red) and the string decay (cyan).

Substituting this expression back in, one obtains

$$\mathcal{F}_\gamma^{\text{RB}} \approx 1.6 \times 10^3 \left(\frac{1 \text{ GHz}}{f_{\text{obs}}} \right)^{3.62}. \quad (4.37)$$

We note that this is probably an over-estimate of \mathcal{F}^{RB} since the ARCADE measurement would require an additional population of radio sources at the relevant frequencies. In principle, there is also a free-free component as well as anomalous microwave emission from the galactic plane, some of which will contribute to the photon occupation number associated to the galactic centre. We remark that while a complete study of the sensitivity to the galactic centre is outside the purpose of this work, our order of magnitude estimate motivates a more detailed future study.

In the near future, the SKA will go into operation. With 1 km^2 of collecting area, the SKA brings the possibility of very high radio sensitivity. However, we note an sparse interferometer is, by construction, most suited to measuring flux densities with high resolution. One can use Rayleigh-Jeans law to convert the noise level on the flux density, which is set by the collecting area into a brightness temperature sensitivity

$$T_\sigma = \frac{T_{\text{sys}}}{\eta_{\text{FF}} \sqrt{\Delta f_{\text{obs}} t_{\text{obs}}}}. \quad (4.38)$$

The factor $\eta_{\text{FF}} \equiv (N A_{\text{eff}})/D_{\text{baseline}}^2 \ll 1$ is known as the filling factor and this increases the expected noise level for the brightness temperature. Here, N is the number of telescopes in the interferometric setup and A_{eff} is the effective collecting area of each telescope. However, if the telescopes are all used in single dish mode, then the integration time for a measurement decreases by a factor N since all the telescopes can point at the same region of the sky.

The high resolution associated with interferometers also means that their large

collecting area is offset by the small beam size, again decreasing M_{beam} by several orders of magnitude. As mentioned before, the flux density sensitivity can be increased by using the telescope in single-dish mode, which results in a factor of N decrease in integration time.

We conclude from our analysis that the brightness temperature is the appropriate quantity to optimise radio telescope searches for the spontaneous decay. In fig. 4.7 we show our estimates of the radio sensitivity to the spontaneous decay. In both the panels, we have set the integration time, t_{int} to be 4 days. The left panel shows the SKA2:Band 5 sensitivity operating in the single dish mode for the Virgo cluster and the Reticulum 2 dwarf galaxy using the numbers explained in the caption. Note that in principle, the sensitivity to the Virgo cluster could be significantly better, as we assume there is no radio emission from the centre of Virgo at frequencies larger than 10 GHz. In the right panel, we show the sensitivity to the galactic centre, assuming $\Sigma_{\text{beam}} \approx 7$ and 70 kg m^{-2} (values that are representative of what could be seen in highly dense environments such as the galactic centre) and a single pixel detector in a GBT-like telescope. It is clear the galactic centre is a promising target for future experiments, which motivates a more detailed study of the different sources of stimulated enhancement.

4.5 Summary

In the case of the detection of the spontaneous decay, previous work [211,212] has suggested that nearby dwarf spheroidal galaxies are ideal candidates to observe under the claim they maximise the flux density. In our analysis, we argue that a procedure to maximise the flux density signal can be non-trivial. This is because the resolution of most single-dish radio telescopes is such that the beam size is smaller than the apparent size of these dwarf galaxies, resolving them. As a result, it becomes confusing to optimise an experiment where one is interested in maximising the flux-density signal since it is difficult to observationally determine the virial radius of dwarf galaxies [233].

Our analysis highlights the fact that one need not carry out a matching procedure of sources to the resolution of the telescope. Indeed, the relevant quantity that determines the specific intensity is the ratio of the surface-mass density to the velocity dispersion, $\Sigma_{\text{beam}}/\Delta v$. Our results show that, except a weak trend in the halo concentration parameter with respect to the mass, this ratio is independent of the halo mass. We infer that a high resolution is in fact desirable, since the surface-mass density along the line of sight is enhanced for a more concentrated beam. This result motivates a search for structures that are characterised by large values of Σ_{beam} .

An important point that was first studied in [211,212] is the enhancement due to stimulated emission, since background radio/microwave photons are of the same frequency as the that corresponding to the De-Broglie wavelength of the axion. This causes the probability of the axion entering the transition state associated to the external dipole field of the photons to be greatly increased. Thus, the presence of an ambient radiation field at the same frequency as that of the axions

results in an effective enhancement of the decay. This is quantified by the photon occupation number.

Our analysis of the sensitivity to virialised objects shows that it is virtually impossible to design a conventional interferometer that can constrain the axion-photon coupling below the CAST limit. This is due to the fact that the sensitivity of an interferometer to any brightness temperature signal is weakened by a filling factor that increases the integration time to unachievable values. On the other hand, one may use an interferometer as a “light-bucket”, where all dishes are used in single-dish auto-correlation mode. We show that even in this case, one would require 4 days of on-source integration time with band 5 of SKA2 observing the Virgo cluster to improve on the CAST constraints [118] on the axion-photon coupling.

Our previous results indicate that the ideal source for detecting the spontaneous decay is characterised by large values of Σ_{beam} and large amounts of ambient radiation at the same frequency - corresponding to $\mathcal{F}_{\text{eff}} \gg 1$. Our order of magnitude estimate of the sensitivity to the galactic centre due to synchrotron emission (using the Planck Point Source catalogue [231]) from Sagittarius A* shows that this may be an ideal target to improve the CAST limit. This motivates a further detailed study of the radiation field in the galactic centre, which in principle could include components from Anomalous Microwave Emission (AME) (dust), free-free emission as well as synchrotron radiation.

Chapter 5

Axion-Photon Conversion in Pulsar Magnetospheres

In this chapter, we discuss the resonant mixing of photons and axion dark matter in pulsar magnetospheres [145–148]. The idea is a simple one: namely that in regions of the plasma where the photon plasma mass and axion mass become degenerate, there is enhanced conversion of dark matter axions to photons, just as in a regular haloscope whose geometry is tuned to a particular axion mass range. In addition, the ultra-strong magnetic fields of neutron stars also greatly enhance the overall magnitude of the effect. We examine the resonant mixing in the pulsar magnetosphere environment in section 5.1. Our analysis falls into roughly two parts. The first focuses on theoretical fundamentals of axion electrodynamics in magnetised plasma, beginning with an examination of one-dimensional (1D) propagation in planar geometries (the standard approach to axion-photon mixing). We are able to unify two apparently disparate analytic results for the conversion amplitude. The first is the perturbative $\mathcal{O}(g_{a\gamma\gamma}^2)$ formula for the conversion process of e.g., [147], while the second is non-perturbative and

given by the well-known Landau-Zener formula [146, 234] derived by computing the S-matrix for conversion as dictated by the mixing equations. Our analysis unifies these two approaches and shows the perturbative result to be a truncation of the full Landau-Zener formula in the non-adiabatic limit. For a given plasma background, this allows one to see precisely for what axion masses and momenta the evolution becomes non-adiabatic and therefore where a perturbative treatment is justified (see fig. 5.1). Our treatment reveals that infalling dark matter axions typically convert non-adiabatically in magnetospheres.

At present, a number of studies have begun to take data to constrain the pulsar signal for axion dark matter [235–237]. However, more work is required to properly characterise the shape and time-dependence of the radio line signal, including its (Doppler broadened) width (see section 5.1.3). The authors of [153] developed a ray tracing procedure for deriving more accurate observational properties of the signal. In sec. 5.2 we present the signal properties resulting from our ray tracing analysis, to self-consistently account for an inhomogeneous and time-dependent magnetosphere as well as including the effects of gravity. This allows us to incorporate the bending of the rays due to varying refractive index and compute the Doppler broadening of the signal from the time-dependence of the magnetosphere. We then combine our novel ray-tracing procedure with new and archival spectral observations of the Galactic Center magnetar PSR J1745–2900, henceforth GCM, using the Karl G. Jansky Very Large Array (VLA¹) to search for signatures of axion-photon conversion in the magnetar magnetosphere in section 5.3. The new observations are the most sensitive to date, and when combined with archival VLA observations of Sgr A* already used in [236, 237] that include the magnetar in the field of view, provide the strongest constraints on $g_{a\gamma\gamma}$ to

¹The National Radio Astronomy Observatory is a facility of the National Science Foundation operated under cooperative agreement by Associated Universities, Inc.

date over the mass range $4.2 - 60 \mu\text{eV}$ for a frequency range $\sim 1 - 15 \text{ GHz}$.

5.1 Axion-photon mixing

5.1.1 Axion Electrodynamics

Our starting point is the standard Lagrangian for the axion and photon, with medium effects described by a current j^μ :

$$\begin{aligned} \mathcal{L} = & -\frac{1}{4}F_{\mu\nu}F^{\mu\nu} - A_\mu j^\mu \\ & + \frac{1}{2}(\partial_\mu a \partial^\mu a - m_a^2 a^2) + \frac{1}{4}g_{a\gamma\gamma}aF_{\mu\nu}\tilde{F}^{\mu\nu}, \end{aligned} \quad (5.1)$$

where $F^{\mu\nu}$ and $\tilde{F}^{\mu\nu}$ are the electromagnetic field tensor and its dual, respectively. The equations of motion for the electromagnetic (EM) fields are given by

$$\nabla \cdot \mathbf{E} = \rho - g_{a\gamma\gamma} \mathbf{B} \cdot \nabla a, \quad (5.2)$$

$$\nabla \times \mathbf{B} - \dot{\mathbf{E}} = \mathbf{J} + g_{a\gamma\gamma} \dot{a} \mathbf{B} - g_{a\gamma\gamma} \mathbf{E} \times \nabla a, \quad (5.3)$$

$$\nabla \cdot \mathbf{B} = 0, \quad (5.4)$$

$$\dot{\mathbf{B}} + \nabla \times \mathbf{E} = 0. \quad (5.5)$$

Next, we linearise the equations of motion about the background solutions satisfying the $g_{a\gamma\gamma} = 0$ equations of motion by setting $\mathbf{E} \rightarrow \mathbf{E}_0 + \mathbf{E}$ and $\mathbf{B} \rightarrow \mathbf{B}_0 + \mathbf{B}$, with a corresponding ansatz for ρ and \mathbf{J} . We also neglect the background electric field, setting $\mathbf{E}_0 = 0$, since for neutron stars the magnetic component typically dominates in the magnetosphere, see, e.g., [238]. The electromagnetic fluctuations must be self-consistently accompanied by perturbations of charge carriers in the plasma via Lorentz forces. This can be modelled via an Ohm's law relation between the current and electric fluctuations \mathbf{E} and \mathbf{J} ,

$$\mathbf{J} = \sigma \cdot \mathbf{E}, \quad (5.6)$$

where the three-by-three matrix σ is the conductivity tensor. Note that together with current conservation $\dot{\rho} + \nabla \cdot \mathbf{J} = 0$, this closes the system of equations. To obtain a simple system of mixing equations, we specialise to a stationary background throughout the remainder of this section assuming \mathbf{B}_0 and σ to be time-independent, as would be the case for an aligned rotator neutron star model. One then obtains the following system of mixing equations for \mathbf{E} and a ,

$$\square a + m_a^2 a = g_{a\gamma\gamma} \mathbf{E} \cdot \mathbf{B}_0, \quad (5.7)$$

$$\square \mathbf{E} + \nabla(\nabla \cdot \mathbf{E}) + \sigma \cdot \dot{\mathbf{E}} = -g_{a\gamma\gamma} \ddot{a} \mathbf{B}_0, \quad (5.8)$$

where (5.8) was obtained by taking the curl of (5.5) and combining with (5.3) and (5.6). We have thus completely parametrised the axion-photon fluctuations in terms of two physical fields, \mathbf{E} and a . Note that the magnetic component is determined immediately from integration of (5.5). We see from (5.8) that, in general, different polarisations of \mathbf{E} will mix owing to the presence of a longitudinal mode $\nabla \cdot \mathbf{E} \neq 0$, which can be sourced via the axion [see eq. (5.2)] or when σ has off-diagonal components. Note, furthermore, that in a stationary background, the fields have simple harmonic time-dependence $\sim e^{-i\omega t}$. The conductivity in a magnetised plasma takes the form [239]

$$\sigma(\omega) = \frac{ie^2 n_e}{m_e} R_B(\theta) \begin{pmatrix} \frac{\omega}{\omega^2 - \omega_B^2} & \frac{i\omega_B}{\omega^2 - \omega_B^2} & 0 \\ -\frac{i\omega_B}{\omega^2 - \omega_B^2} & \frac{\omega}{\omega^2 - \omega_B^2} & 0 \\ 0 & 0 & \frac{1}{\omega} \end{pmatrix} R_B(\theta)^{-1}, \quad (5.9)$$

where $\theta = \theta(\mathbf{x})$, $\omega_B = eB_0/m_e$ is the gyrofrequency, $R_B(\theta)$ is the local rotation matrix which rotates \mathbf{B}_0 into the z -direction and $B_0 = |\mathbf{B}_0|$. We assume furthermore that $\omega \ll \omega_B$, which is easily satisfied for neutron stars with $B \simeq 10^9$ - 10^{14} G and frequencies $\omega \simeq m_a \sim \mu\text{eV}$ associated to non-relativistic axions. In this case,

one has $\sigma(\omega) \cdot \mathbf{E} = i(\omega_{\text{pl}}^2/\omega)\mathbf{E}_{\parallel}$, where \mathbf{E}_{\parallel} is the component of \mathbf{E} along \mathbf{B}_0 .

Here we spell out what are the precise physical assumptions needed to reduce the plasma (5.7)-(5.8) to a simple 1D problem.

We consider a planar geometry in which all background fields depend on a single parameter z , i.e., $\mathbf{B}_0 = \mathbf{B}_0(z)$. Then, since \mathbf{B}_0 is transverse ($\nabla \cdot \mathbf{B}_0 = 0$, note that this is fundamental, so long as $\partial_{[\mu} \tilde{F}_{\alpha\beta]} = 0$ is true, this condition has to hold), it follows immediately that \mathbf{B}_0 has no polarisation in the z -direction. Consider also that the wavefronts propagate in the same direction, such that $a = a(z)$ and $\mathbf{E} = \mathbf{E}(z)$. Crucially, these geometric assumptions ensure

$$\mathbf{B}_0(z) \cdot \nabla(\nabla \cdot \mathbf{E}(z)) = 0, \quad (5.10)$$

since by construction there are no gradients in the direction of \mathbf{B}_0 . Thus, by geometric considerations and assumptions, we are able to exclude the effects of a longitudinal component $\nabla \cdot \mathbf{E}$ from the mixing equations. One can then project (5.8) onto \mathbf{B}_0 to arrive at the following set of mixing equations,

$$\begin{pmatrix} \partial_z^2 - m_a^2 + \omega^2 & \omega g_{a\gamma\gamma} B_0(z) \\ \omega g_{a\gamma\gamma} B_0(z) & \partial_z^2 - \omega_{\text{pl}}^2(z) + \omega^2 \end{pmatrix} \begin{pmatrix} a \\ \mathcal{E} \end{pmatrix} = 0, \quad (5.11)$$

where $\mathcal{E} = E_{\parallel}/\omega$, $E_{\parallel} = \mathbf{E} \cdot \mathbf{B}_0/|\mathbf{B}_0|$ is the component of \mathbf{E} parallel to \mathbf{B}_0 and $\omega_{\text{pl}}^2 = e^2 n_e/m_e$ is the plasma frequency. The remaining component E_{\perp} normal to \mathbf{B}_0 , from Gauss' law can be seen to satisfy $\partial_z E_{\perp} = 0$ and thus by boundary conditions must vanish. Thus, in such a geometry, the mixing simplifies to only two degrees of freedom. To fully solve these equations, one should ensure that

solutions have the appropriate ingoing and outgoing waves at infinity,

$$z \rightarrow -\infty : \quad \begin{pmatrix} a \\ \mathcal{E} \end{pmatrix} = \begin{pmatrix} a_I e^{ik_a z} \\ 0 \end{pmatrix} + \begin{pmatrix} a_R e^{-ik_a z} \\ \gamma_R e^{-ik_\gamma z} \end{pmatrix}, \quad (5.12)$$

$$z \rightarrow \infty : \quad \begin{pmatrix} a \\ \mathcal{E} \end{pmatrix} = \begin{pmatrix} a_T e^{ik_a z} \\ \gamma_T e^{ik_\gamma z} \end{pmatrix}, \quad (5.13)$$

where a_I is the amplitude of the incident wave and γ_R and a_R , γ_T and a_T are the amplitudes of the reflected and transmitted waves, respectively.

5.1.2 Landau-Zener

The first step in deriving analytic results is to reduce the system to a first order equation. This involves two stages, firstly a gradient expansion with respect to background fields and secondly imparting information about local dispersion relations into the resulting equations. A somewhat heuristic derivation of a first order equation is given in the classic reference [240] for relativistic particles $k \gg \omega_{\text{pl}}, m_a$ with trivial dispersion $\omega \simeq k$. This is the so-called “weak dispersion” regime also examined in [146]. However, here we deal with non-relativistic dark matter axions which have $\omega \simeq m_a$, and since we are interested also in a photon whose dispersion varies locally according to $\omega^2 = k^2 + \omega_{\text{pl}}^2$, a more subtle analysis is required. One can define a density matrix for the system by writing:

$$\rho(z_1, z_2) = (a(z_1), \mathcal{E}(z_1)) \otimes (a(z_2), \mathcal{E}(z_2))^\dagger, \quad (5.14)$$

which satisfies

$$\begin{pmatrix} \partial_{z_1}^2 - m_a^2 + \omega^2 & \omega g_{a\gamma\gamma} B(z) \\ \omega g_{a\gamma\gamma} B(z) & \partial_{z_1}^2 - \omega_{\text{pl}}^2(z) + \omega^2 \end{pmatrix} \boldsymbol{\rho}(z_1, z_2) = 0. \quad (5.15)$$

One can introduce a local phase-space by performing a 1D Wigner transformation defined by

$$\boldsymbol{\rho}(k, z) = \int dy \boldsymbol{\rho}\left(z + \frac{y}{2}, z - \frac{y}{2}\right) e^{-iky}, \quad (5.16)$$

with $y = z_1 - z_2$ and $z = (z_1 + z_2)/2$, and using temporal translation invariance, one arrives at [241, 242]

$$\left[\omega^2 - k^2 + \frac{1}{4} \partial_z^2 - ik \partial_z - \mathbf{M}^2(z) e^{\frac{i}{2} \overleftarrow{\partial}_z \partial_k} \right] \rho(k, z) = 0, \quad (5.17)$$

where the Hermitian mass-mixing matrix is given by

$$\mathbf{M}^2 = \begin{pmatrix} m_a^2 & \omega g_{a\gamma\gamma} B(z) \\ \omega g_{a\gamma\gamma} B(z) & \omega_{\text{pl}}^2(z) \end{pmatrix}, \quad (5.18)$$

whose mass eigenvalues are

$$M_{1,2}^2 = \frac{1}{2} \left\{ m_a^2 + \omega_{\text{pl}}^2 \pm \left[(m_a^2 - \omega_{\text{pl}}^2(z))^2 + 4B^2 g_{a\gamma\gamma}^2 \omega^2 \right]^{1/2} \right\}. \quad (5.19)$$

Since local physical states are mass-diagonal states, in order to extract useful dispersion information, we first convert to the local mass basis:

$$\mathbf{M}_d^2 = U M^2 U^\dagger, \quad \boldsymbol{\rho}_d = U \boldsymbol{\rho} U^\dagger, \quad (5.20)$$

where

$$U = \begin{pmatrix} \cos \theta & -\imath \sin \theta \\ -\imath \sin \theta & \cos \theta \end{pmatrix}, \quad (5.21)$$

with $\tan 2\theta = \frac{\omega B(\mathbf{x}) g_{a\gamma\gamma}}{m_a^2 - m_\gamma^2}$, diagonalises the mass matrix, which amounts to the replacement

$$\partial \rightarrow D_z = \partial_z - \imath [\Xi, \cdot], \quad \Xi = \imath U \partial_z U^\dagger, \quad (5.22)$$

in eqs. (5.17), leading to

$$\left[\omega^2 - k^2 + \frac{1}{4} D_z^2 - \imath k \partial_z - \mathbf{M}_d^2(z) e^{\frac{\imath}{2} \overleftarrow{D}_z \partial_k} \right] \boldsymbol{\rho}_d(k, z) = 0, \quad (5.23)$$

where $\mathbf{M}_d^2 = \text{diag}(M_1^2, M_2^2)$. Taking the hermitian and antihermitian parts of (5.17) gives

$$\left(\omega^2 - k^2 + \frac{1}{4} D_z^2 \right) \boldsymbol{\rho} - \frac{1}{2} \{ \mathbf{M}_c^2, \boldsymbol{\rho} \} + \frac{\imath}{2} [\mathbf{M}_s^2, \boldsymbol{\rho}] = 0, \quad (5.24)$$

$$k D_z \boldsymbol{\rho} + \frac{1}{2} \{ \mathbf{M}_s^2, \boldsymbol{\rho} \} - \frac{\imath}{2} [\mathbf{M}_c^2, \boldsymbol{\rho}] = 0, \quad (5.25)$$

where

$$\mathbf{M}_c^2 = \mathbf{M}^2 \cos \left(\frac{1}{2} \overleftarrow{D}_z \partial_k \right), \quad (5.26a)$$

$$\mathbf{M}_s^2 = \mathbf{M}^2 \sin \left(\frac{1}{2} \overleftarrow{D}_z \partial_k \right). \quad (5.26b)$$

These are known as the *constraint* and *kinetic* equations respectively. The first contains information about dispersion relations and imposes appropriate mass-shell constraints, whilst the second controls the evolution of number densities. To leading order in gradients, the constraint equation (5.24) implies the following

Ansatz for the mass-basis density matrix $\boldsymbol{\rho}_d$

$$\rho_{d,ii}(z, k) = n_i(z, k) \delta(\omega^2 - k^2 - M_i), \quad (5.27a)$$

$$\rho_{d,ij}(z, k) = n_{ij}(z, k) \delta(\omega^2 - k^2 - \bar{M}^2), \quad (5.27b)$$

where $\bar{M} = (M_1^2 + M_2^2)/2$ is the average mass and any total derivatives in k drop out upon integration. In the present setup

$$\Xi = \begin{pmatrix} 0 & -\theta' \\ -\theta' & 0 \end{pmatrix}, \quad (5.28)$$

so that inserting (5.27) into eq. (5.25) and integrating over k to put all states on shell, leads to the following equations

$$i \frac{d\mathbf{N}(z)}{dz} = [\mathbf{H}, \mathbf{N}(z)], \quad (5.29a)$$

$$\mathbf{H} = \begin{pmatrix} M_1^2/2\bar{k} & \theta' \\ \theta' & M_2^2/2\bar{k} \end{pmatrix}, \quad (5.29b)$$

$$\mathbf{N} = \begin{pmatrix} n_1 & n_{12} \\ n_{21} & n_2 \end{pmatrix}, \quad (5.29c)$$

where $\bar{k}^2 = \omega^2 - \bar{M}^2$ is the “average momentum” arising from the off-diagonal coherence terms. Reverting to the flavour basis, one finds

$$i \frac{d\mathbf{N}_f}{dz} = \frac{1}{2\bar{k}} [\mathbf{M}^2, \mathbf{N}_f], \quad (5.30)$$

where \mathbf{M}^2 is the flavour mass matrix (5.18). For “pure state” solutions, the system can be realised via a wavefunction $\mathbf{N}_f = \boldsymbol{\Psi} \otimes \boldsymbol{\Psi}^\dagger$, where $\boldsymbol{\Psi} = (\psi_a, \psi_\gamma)$,

corresponding to an auxilliary Schödinger-like equation

$$i \frac{d}{dz} \begin{pmatrix} \psi_a \\ \psi_\gamma \end{pmatrix} = \frac{1}{2\bar{k}(z)} \begin{pmatrix} m_a^2 & \omega g_{a\gamma\gamma} B(z) \\ \omega g_{a\gamma\gamma} B(z) & \omega_{\text{pl}}^2(z) \end{pmatrix} \begin{pmatrix} \psi_a \\ \psi_\gamma \end{pmatrix}. \quad (5.31)$$

with $\bar{k} \equiv \sqrt{\omega^2 - \bar{M}^2}$ and where the key difference from refs. [147] or [146] is the realisation that the distinct axion and photon mass-shell conditions express themselves in a local *average momentum* associated to the average $\bar{M}^2 = (M_1^2 + M_2^2)/2 = (\omega_{\text{pl}}^2 + m_a^2)/2$ of the two eigenmasses. In particular, the average of the two eigenmasses also varies throughout space. Note that in the relativistic limit $\bar{k} \rightarrow \omega$ reproduces the weak dispersion equations of [146] and at the critical point (where $m_a = \omega_{\text{pl}}$), one can set $\bar{k} \rightarrow k$ to the axion momentum $\omega^2 = k^2 + m_a^2$, giving the localised version of ref. [147] about $z = z_c$, where z_c is the location of the resonance at which $m_a = \omega_{\text{pl}}$. Here ψ_a and ψ_γ defined above can be viewed as axion and photon states which have been put on-shell. For compactness of notation we also define

$$\Delta_a = m_a^2/2\bar{k}, \quad \Delta_\gamma = \omega_{\text{pl}}^2/2\bar{k}, \quad \Delta_B = \omega g_{a\gamma\gamma} B_0/2\bar{k}. \quad (5.32)$$

For a problem in which the mass-splitting varies linearly with the integration parameter such that the mass-mixing takes the form:

$$\mathbf{M}^2(z) = \begin{pmatrix} \epsilon_1 + \lambda_1 z & v^* \\ v & \epsilon_2 + \lambda_2 z \end{pmatrix}, \quad (5.33)$$

where $\epsilon_1, \lambda_1 \in \mathbb{R}$ and $v \in \mathbb{C}$ are constants, the S -matrix for conversion probabilities is given by the well-known Landau-Zener formula [234]

$$S_{\text{LZ}} = \begin{pmatrix} p & q \\ q & p \end{pmatrix}, \quad (5.34)$$

where $p = e^{-\pi\gamma}$, $q = \sqrt{1-p^2}$ and $\gamma = |v|^2/|\lambda_2 - \lambda_1|$. Thus, by linearising the plasma frequency in (5.31) about $z = z_c$ with $\omega_{\text{pl}}^2 \simeq m_a^2 + (z - z_c)(\omega_{\text{pl}}^2)'(z_c)$, we can immediately read off the form of γ , leading to

$$\gamma = \frac{g_{a\gamma\gamma}^2 B^2(z_c) \omega^2 / 2\bar{k}}{|(\omega_{\text{pl}}^2)'(z_c)|}. \quad (5.35)$$

The conversion probability is then given by the squared S -matrix elements:

$$P_{a \rightarrow \gamma} = 1 - e^{-2\pi\gamma}, \quad \gamma \simeq \frac{\Delta M^2(z_c)/2\bar{k}}{4|\theta'(z_c)|}, \quad (5.36)$$

where we used the definitions (5.21) and (5.19) to parameterise the probability in terms of the mass-splitting $\Delta M^2 = M_1^2 - M_2^2$ and mixing angle gradients, evaluated at the resonance, where we neglected gradients in $B(z)$ and $\bar{k}(z)$.

The physical interpretation of this result is that γ controls the *adiabaticity* of the evolution - i.e., how rapidly the background is varying. Formally this corresponds to the size of background plasma gradients. We see immediately that the perturbative result (5.38) (refs. [147, 240]) is precisely the truncation of the Landau-Zener probability (5.1.2) ([146, 243]) in the non-adiabatic limit for small γ . In other words, the smallness of the adiabaticity parameter determines the validity of the non-relativistic result in [147], as γ increases the probability $P_{\text{LZ}} \rightarrow 1$ which causes photons to convert back to axions.

It is intriguing to note the link between these results. Of course mathematically speaking, the stationary phase approximation used to compute (5.37) amounts to a linearisation of the plasma mass about the critical point and our use of the Landau-Zener result is formally valid in the limit for which the mass-splitting $m_a^2 - \omega_{\text{pl}}^2$ varies linearly with z implying the same implicit assumption. However, given that the derivation of each of these results seems a priori to be quite different - it is striking to see that their agreement is exact in the $\gamma \ll 1$ limit.

Perturbative calculation

As was done in [147] following the approach of [240], these equations can be solved perturbatively. Following the latter of these references, by going to the interaction picture, one can derive the following conversion probability

$$P_{a \rightarrow \gamma} = \left| \int_{-\infty}^{\infty} dz' \Delta_B(z') e^{i \int_0^{z'} dz'' [\Delta_\gamma(z'') - \Delta_a(z'')]} \right|^2. \quad (5.37)$$

The exponent is stationary at the resonance, allowing one to perform the integral using the stationary phase approximation to get

$$P_{a \rightarrow \gamma} = \frac{2\pi \Delta_B^2(z_c)}{|\Delta'_\gamma(z_c)|} \equiv 2\pi\gamma. \quad (5.38)$$

where z_c is defined by $\omega_{\text{pl}}(z_c) = m_a$ and the prime represents the derivative with respect to z . In order to make contact with the Landau-Zener formula for the conversion probability of ref. [146], we note that by using the definition of the mixing angle

$$\tan 2\theta = \frac{\omega B_0(z) g_{a\gamma\gamma}}{m_a^2 - \omega_{\text{pl}}^2}, \quad (5.39)$$

we can write

$$\gamma = 2\pi \frac{\Delta M^2(z_c)/2\bar{k}_c}{4|\theta'(z_c)|} + \mathcal{O}(\bar{k}'(z_c), B'_0(z_c)), \quad (5.40)$$

where $\Delta M^2 = M_1^2 - M_2^2$ is the mass-splitting in the mass-diagonal basis. Thus, up to gradients in the dispersion relation and the magnetic field, the result is precisely that of [146]. Note that by looking at the exponent in the stationary phase approximation, the width of the corresponding Gaussian gives the characteristic width Δz_c of the resonant region

$$(\Delta z_c)^2 = \frac{\pi}{|\Delta'_\gamma(z_c)|}. \quad (5.41)$$

We mimic the $\sim 1/r^3$ behaviour of the near-field dipole of the neutron star by taking

$$B_0(z) = \frac{B_* R^3}{z^3}, \quad (5.42)$$

and use the Goldreich-Julian density [244] for the plasma frequency, with $n_e = \Omega B_0(z)$ and Ω the rotation frequency of the neutron star, from which it follows that

$$\Delta z_c \simeq \sqrt{\frac{2\pi z_c \bar{k}}{3m_a^2}}, \quad z_c = R \left[\frac{B_* \Omega e^2}{m_e m_a^2} \right]^{1/3}. \quad (5.43)$$

This allows one to write the conversion probability explicitly as

$$P_{a \rightarrow \gamma} = \frac{1}{2} \frac{\omega^2}{\bar{k}^2(z_c)} g_{a\gamma\gamma}^2 B(z_c)^2 \Delta z_c^2. \quad (5.44)$$

There is a pleasing interpretation of this result in terms of a resonant forced oscillator solution - as can be seen from the form of (5.8). The photon field $\mathcal{E} = E_{\parallel}/\omega$ can be viewed as a harmonic oscillator with local “frequency” $k_\gamma = \sqrt{\omega^2 - \omega_{\text{pl}}^2}$ which becomes equal to that of the axion forcing $k_a = \sqrt{\omega^2 - m_a^2}$ when $\omega_{\text{pl}} = m_a$. Since the particular solution to the forced resonant oscillator grows linearly with z behaving as $\sim z e^{ik_\gamma z}$ and since the overall magnitude of the forcing is set by $\omega g_{a\gamma\gamma} B_0$, the total resonant growth in the photon amplitude is then given

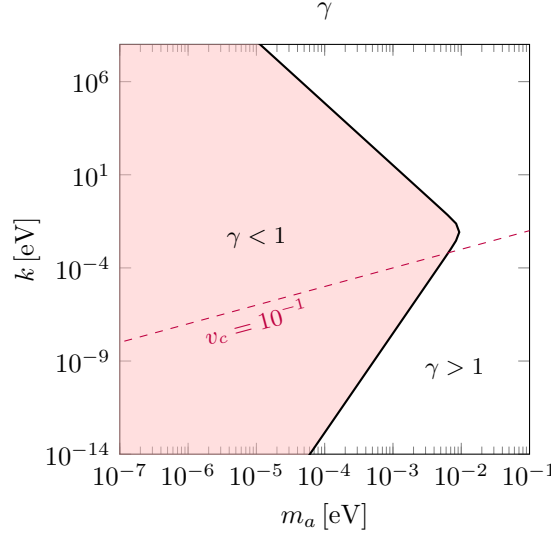


Figure 5.1: The adiabaticity parameter γ of (5.1.2) for the QCD axion with $g_{a\gamma\gamma}$ given by (1.65) with $E/N = 8/3$. We considered a magnetic field (5.42) with $B_* = 10^{14}\text{G}$, a rotation period $P = 0.1\text{s}$ with $R = 10\text{km}$. We also show the velocity at the critical point $v_c = k_c/m_a$ for the value 10^{-1} which can be reached via gravitational acceleration.

by multiplying the size of the region (linear z behaviour) by the magnitude of the forcing - which gives precisely the amplitude-squared of (5.44).

The size of γ – and therefore the regime in which a perturbative treatment is appropriate – is given in fig. 5.1 for the QCD axion with canonical neutron star parameters. Note that our systematic treatment of mass-shell constraints allows us to study γ across the full range of relativistic and non-relativistic axion parameter space.

Fig. 5.2 summarises our results for conversion in 1D and compares the full numerical results of the second order equation (5.11) against analytic approximations. The numerical conversion probability was computed by assuming an incident axion from $z \rightarrow -\infty$ with the magnetic field background (5.42) and solving the equations for the photon up to a finite depth inside the region of plasma

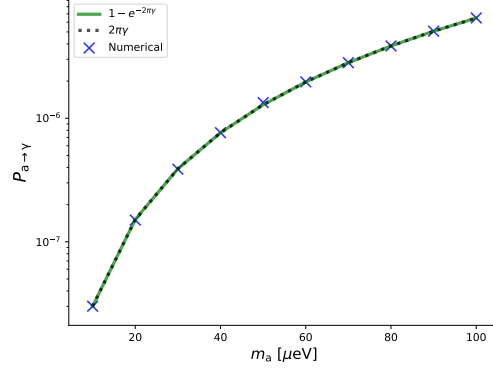


Figure 5.2: The analytic Landau-Zener probability, adiabaticity parameter γ and the numerical solution of the full second order equations of motion as a function of the axion mass. Here, we assume $g_{a\gamma\gamma} = 10^{-12} \text{ GeV}^{-1}$, $B_0 = 10^{14} \text{ G}$ and $k_a = 0.1m_a$. For these parameters, we find from energy conservation that the average velocity of the axion at the resonant conversion region $v_c \approx \frac{2GM}{z_c}$ is roughly 10% of the speed of light.

overdensity defined by $\omega_{\text{pl}} > \omega$ in which the photon amplitude becomes exponentially suppressed. This was implemented numerically as a Dirichlet and Neumann boundary condition by setting the electric field and its first derivative to zero at some finite depth inside the $\omega_{\text{pl}} > \omega$ region.

Figs. 5.1 and 5.2 show that the conversion of dark matter axions in neutron star magnetospheres typically involves non-adiabatic evolution for which a perturbative treatment in $g_{a\gamma\gamma}$ is valid. The fact that one does not stray into the adiabatic regime arises from two considerations: firstly, for asymptotic values of the axion velocity $v_a \equiv k_a/m_a$ given by 10^{-3} , gravitational acceleration $\frac{2GM_{\text{NS}}}{z_c}$ can bring these up to around 10^{-1} shown by the purple line in fig. 5.1. Secondly there is an upper limit on the axion mass beyond which the resonance region would be pushed inside the neutron star, as can be seen in (5.43). These two facts together restrict one to the non-adiabatic region of dark matter axions.

Of course there are some caveats to the above assumptions. Firstly axions with very high or very low momenta can in principle be pushed into the adiabatic

regime. However, the gravitational acceleration of the neutron star puts a lower bound $v_c \geq GM/z_c$, which is saturated by axions which are asymptotically at rest. Meanwhile for large v , the distribution is exponentially suppressed by the velocity dispersion v_0 .

5.1.3 Doppler broadening

Since the pulsar magnetosphere in general is not a stationary configuration, the energy of test particles moving in this background is not conserved. While a somewhat rich structure is indicated by simulations [245, 246], we consider here the minimal model of an oblique rotating magnetic dipole field that also determines the electron density according to Goldreich and Julian [244] and hence the critical surface. In order to arrive at an analytically transparent picture, we make some additional simplifying assumptions.

For an oblique rotator, the intersection of a plane perpendicular to the rotation axis with the critical surface takes the shape of an ellipse. When the lengths of the semi-major and semi-minor axes are a and b , respectively, the numerical eccentricity is $\varepsilon = \sqrt{1 - b^2/a^2}$. This ellipse rotates at an angular velocity Ω about its middle point.

Consider a corotating point on the critical surface, where an axion may be converted into a photon. We can further distinguish the cases of reflection and transmission. For reflection, an infalling axion reaches the critical surface from the outside and the photon is subsequently reflected when further climbing the potential barrier made up by the plasma. For transmission, the axion is coming from the inside region and the photon then continues to travel outbound. The instantaneous velocity of the tangential plane of the critical surface in general is not parallel to the plane itself (unless the point considered is aligned with one

of the axes of the ellipse or in the degenerate case of a circle). Physically, a particle that interacts with the critical surface transfers momentum to the magnetosphere, corresponding to the Doppler effect from the reflection by a moving mirror².

We therefore calculate the reflection or transmission of a ray of a particle of mass m_a in the xy -plane that approaches the origin at an angle α (all angles refer here to the x -axis), where it falls on a plane whose normal vector points in the direction φ . Upon reflection or transmission, the particle is converted into a massless state. The plane moves at a constant velocity v in the direction of the angle ϑ , see fig. 5.3. The calculation can be carried out by first boosting the four-momentum of the massive initial state from the rest frame of the observer to the rest frame of the critical surface. In that frame, the zero-component of the four-momentum is conserved as well as the spatial components of the momentum parallel to the surface. The component perpendicular to the surface is then found by imposing the energy-momentum relation of a massless particle. The final answer is obtained when boosting back to the frame of the observer.

To clarify this approach, we first quote the result for the situation where the surface moves toward the incoming massive particle, $\alpha = \vartheta = \varphi = 0$, such that we obtain

$$k^{0'} = \frac{c\sqrt{m_a^2 + k^2} + kv}{c \mp v}, \quad (5.45)$$

where k and k' are the moduli of the wave vectors of incoming and reflected wave, respectively. Throughout this section, an upper sign refers to the case of reflection and a lower one to transmission. Clearly, when setting $m_a = 0$, we obtain the

²We thank Georg Raffelt for bringing this issue to our attention.

classic result for Doppler shift for reflection as well as zero change in the frequency for transmission. We may therefore anticipate that for non-relativistic axions, the Doppler shift for axions leaving the magnetosphere is not suppressed compared to infalling axions.

To arrive at a conservative estimate of the Doppler broadening in the magnetosphere, we now assume that the shape is only mildly elliptical such that the misalignment angle $\varphi - \vartheta + \pi/2 \ll 1$ between the tangential plane and its velocity corresponds to a small parameter that we can expand in. The Doppler shift then takes the simple form

$$\frac{k'^0}{k^0} = 1 \mp \frac{v}{c} \frac{\sqrt{k^2 + m_a^2 - k^2 \cos^2(\alpha - \vartheta)} \pm k \sin(\alpha - \vartheta)}{\sqrt{k^2 + m_a^2} \sqrt{1 - \frac{v^2}{c^2}}} \times \\ [2(\varphi - \vartheta + \pi/2) + \mathcal{O}[(\varphi - \vartheta + \pi/2)^2]] , \quad (5.46)$$

In the limit of a relativistic incident particle, $m_a/k \rightarrow 0$, this reduces to

$$\frac{k'^0}{k^0} = 1 - \frac{v \sin(\alpha - \vartheta)}{c \sqrt{1 - \frac{v^2}{c^2}}} 2(\varphi - \vartheta + \pi/2) + \\ \mathcal{O}[(\varphi - \vartheta + \pi/2)^2] , \quad (5.47)$$

for reflections and $k'^0/k^0 \approx 1$ for transmissions. In the opposite limit, $m_a \gg k$, we find

$$\frac{k'^0}{k^0} = 1 \mp \frac{v}{c} \frac{1}{\sqrt{1 - \frac{v^2}{c^2}}} 2(\varphi - \vartheta + \pi/2) + \\ \mathcal{O}[(\varphi - \vartheta + \pi/2)^2] , \quad (5.48)$$

which is the expression useful for the present context.

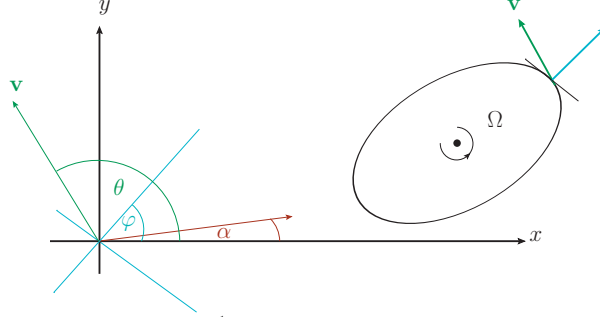


Figure 5.3: Parametrization of the Doppler shift on a moving, misaligned mirror.

In order to estimate the average effect for the conversion in the magnetosphere, we note that, for a given eccentricity, the angle $\varphi - \vartheta + \pi/2$ can assume values between $\pm\varepsilon^2/4$ within one rotation. Furthermore, depending on the impact parameter, the angle $\alpha - \theta$ approximately takes values between $-\pi/2$ (for trajectories that come very close to the core of the pulsar) and π (for trajectories that just about touch the critical surface on the far side of the pulsar). A full quantitative analysis involving the axion and photon trajectories should be straightforward, but it is probably not of obvious benefit since the oblique rotator model of the magnetosphere is likely to be oversimplified, and hence we just make an estimate of the size of the effect. Assuming further $v/c \ll 1$, we estimate that

$$\left\langle \left| \frac{k'^0}{k^0} - 1 \right| \right\rangle \sim \frac{\Omega r_c \varepsilon^2}{c} \approx 6 \times 10^{-4} \left(\frac{\Omega}{1 \text{ Hz}} \right) \left(\frac{r_c}{200 \text{ km}} \right) \varepsilon^2. \quad (5.49)$$

This is to be compared with the width from the velocity dispersion of the axion dark matter

$$\frac{1}{2} v_0^2 / c^2 \approx 8 \times 10^{-7} \left(\frac{v_0}{100 \text{ kms}^{-1}} \right)^2. \quad (5.50)$$

We see that the impact of Doppler broadening depends very strongly on the axion velocity in the resonant conversion region. When the axion is non-relativistic, the Doppler broadening dominates in the width of the spectral line over the

velocity dispersion. For axions that are relativistic at the point of conversion, there is the interesting possibility that the Doppler broadening for transmissions is strongly suppressed, which may be of importance for line searches. For our subsequent estimates, we use the non-relativistic expression (5.49) for the Doppler broadening.

As stated above, the oblique rotator model with the electron density proposed by Goldreich and Julian is chosen here because it is analytically tractable. Eventually, it should be replaced with a more realistic model of the magnetosphere. Even for the Goldreich–Julian model, we have made simplifying assumptions that we now comment on.

First, the conversion from the axion to the photon takes place during some finite time during which the location z_c of the critical surface, where the conversion takes place, changes its position due to acceleration. The width (5.43) of the surface in which the conversion occurs can be estimated as $\Delta z_c \sim (z_c m_a)^{1/2} v_c / c$. Assuming that the converting axion passes through this region at a speed $v_c / c \sim 0.1$ (created in the gravitational potential of the neutron star), it is clear that this takes a time much smaller than the rotation time, $2\pi/\Omega$, for axions in the GHz mass range.

Second, more important are corrections that should arise from the fact that the outgoing photon can only be considered relativistic when the Lorentz factor $\gamma \approx m_a / \omega_{\text{pl}}$ is large, which occurs for large $(z/z_c)^{3/2}$. Integration of time along the photon trajectory implies that the point z is reached after the time $z/c + \mathcal{O}(z_c/c)$. If during that time the background plasma changes significantly because of the rotation of the pulsar, one should anticipate order-one corrections to the Doppler effect.

Finally, due to the curvature of the contours of equal plasma mass and the finite distance to be traversed before it becomes relativistic, there should be corrections due to the continuous refraction of the escaping photon. For axions traversing the critical surface at a small angle, these can also be of order one.

In case there is additional structure in the magnetosphere beyond the Goldreich-Julian model, then the estimate (5.49) should be considered as conservative when applied within its range of validity, which is $\varepsilon \ll 1$. This is because for structures in the magnetosphere that are indicated by simulations, the critical surfaces appear to move at large velocities $\sim \Omega r_c$. It would, therefore, be desirable to numerically compute the broadening for realistic magnetosphere models on a full statistical average of axion trajectories and, if possible, to devise methods of correcting for the Doppler effect. We stress that since the estimate in (5.49) is significantly larger than the background velocity dispersion, the amplitude of the radio signal will be weaker, as we will show in the subsequent sections of the paper.

5.2 Ray-tracing Simulations

Ray tracing is a powerful technique for understanding the emission properties of astrophysical bodies and enables one to track the position, frequency and momentum of photons. The rays then contain all the information required to reconstruct the image of the object, as well as giving the angular power dependence, lensing effects and frequency distortions. Such techniques have been applied to both stars [247] and black holes [248–250], where in the latter case, the rays are geodesics of the spacetime metric rather than the plasma, but the principle is the same.

Ray tracing techniques were first applied to axion dark matter conversion in [153]. Here, the authors back-traced straight-line rays from the observer to the critical surface on which photons are produced, matching each ray onto its corresponding conversion amplitude. In this work, we examine how plasma affects ray tracing and the corresponding properties of the radio lines.

We shall see that the plasma has two very important effects which greatly modify signal properties in two important ways. The first is a new time-dependence resulting from the refraction of rays, which causes stronger pulsing of the signal. The plasma acts as a time-dependent lens, causing a variation in the number of rays reaching the observer, which fluctuates over the pulse period. The second effect involves the variation of frequency along rays, which allows us to determine the Doppler broadening of each photon, and by summing over all rays, derive the exact line shape of the signal in frequency space.

Our starting point for understanding the propagation is similar to the discussion found in [250], which is a generalisation of the flat space case discussed in [251] (and applied in refs. [252, 253]) which describes the propagation of photons in an

inhomogeneous and time-dependent plasma using Hamiltonian optics. We begin with a dispersion relation in a cold, isotropic plasma

$$g_{\mu\nu}k^\mu k^\nu + \omega_p^2 = 0, \quad (5.51)$$

where $g_{\mu\nu}$ is the space time metric. Taking covariant derivatives of this equation, we arrive at

$$k^\nu \nabla_\nu k^\mu = -\frac{1}{2} \partial^\mu \omega_p^2, \quad (5.52)$$

where we used $\nabla_\mu k_\nu = \nabla_\nu k_\mu$ since $k_\mu = \partial_\mu \Theta$ is the derivative on the eikonal phase Θ in the relevant WKB approximation. We then define worldlines $x^\mu(\lambda)$ associated to these rays satisfying

$$\frac{dx^\mu}{d\lambda} = k^\mu, \quad (5.53)$$

where λ is an arbitrary worldline parameter. Putting this together we arrive at

$$\frac{d^2 x^\mu}{d\lambda^2} + \Gamma_{\nu\rho}^\mu \frac{dx^\nu}{d\lambda} \frac{dx^\rho}{d\lambda} = -\frac{1}{2} \partial^\mu \omega_p^2, \quad (5.54)$$

where $\Gamma_{\nu\rho}^\mu$ are the Cristoffel symbols associated to the connection. We interpret the spatial components of the plasma derivatives on the right hand side of eq. (5.54) as an effective force, leading to the refraction of rays. Meanwhile, the temporal derivatives lead to frequency evolution along the worldline, as is apparent from eq. (5.52).

We choose a simple Schwarzschild metric to model the star's gravitational field

$$ds^2 = -f(r)dt^2 + \frac{dr^2}{f(r)} + d\Omega^2, \quad (5.55)$$

where $f(r) = 1 - r_s/r$ and $r_s = 2GM$ is the Schwarzschild radius for a neutron star of mass M . The refractive index n of the medium is defined by

$$n^2 = 1 - \frac{\omega_p^2}{\tilde{\omega}^2}, \quad (5.56)$$

where $\tilde{\omega}$ is the frequency in a coordinate system at rest with respect to the neutron star and includes the gravitational red-shift. Note that the dielectric constant only goes negative for $\omega < \omega_{\text{pl}}$ and therefore we neglect any attenuation due to the plasma, i.e., we only consider the real part of the refractive index.

$$\tilde{\omega}(r) = \left(1 - \frac{r_s}{r}\right)^{-1/2} \omega. \quad (5.57)$$

Here $\omega = -k_0$ is the co-moving frequency related to the temporal component of k_μ . In the absence of time-dependence in the plasma, ω is conserved along rays.

5.2.1 Frequency Broadening

When the plasma is time-dependent, ω evolves along rays according to eq. (5.52), which can be re-written in terms of coordinate time as

$$\frac{d\omega}{dt} = -\frac{f}{2\omega} \partial_t \omega_p^2. \quad (5.58)$$

The key point for this work, is to note that when the plasma background is time-dependent, as happens for the plasma around a neutron star, the photon

frequency evolves according to eq. (5.58). We can obtain an estimate for the Doppler broadening which gives a frequency shift $\delta\omega$ satisfying

$$\delta\omega \simeq \frac{1}{2\omega} \int dt \partial_t \omega_p^2(t, \mathbf{x}_0(t)), \quad (5.59)$$

where ω is frequency before broadening, and \mathbf{x}_0 gives the ray worldline. Formally we solve eq. (5.59) numerically for each ray, allowing us to build up the exact line shape for a given magnetosphere model.

5.2.2 Effect of Gravity

When taken in combination with refractive plasma effects, gravity plays an important role in influencing the characteristic size of the lensed image of the star. To understand how this happens, it is instructive to consider a simple spherically symmetric and stationary plasma with $\omega_p = \omega_p(r)$. In this case, one has two conserved quantities: the frequency ω_{obs} and angular momentum L which is related to the impact parameter b by $L = \omega b$. One can derive a simple energy conservation equation for the radial coordinates [250] corresponding to motion in an effective potential

$$\left(\frac{dr}{d\lambda}\right)^2 = \omega_{\text{obs}}^2 - \left(1 - \frac{r_s}{r}\right) \left(\frac{\omega_{\text{obs}}^2 b^2}{r^2} + \omega_p^2(r)\right). \quad (5.60)$$

Back-traced photons which are capable of reaching the critical surface, must have a distance of closest approach r_{min} satisfying $r_{\text{min}} \leq r_c$, where r_c is the radius of the critical surface. Since r_{min} is by definition a stationary point along the geodesic at $r = r_{\text{min}}$ we must have $dr/d\lambda = 0$. The maximum impact parameter b_{max} , corresponds to those rays which just skim the critical surface. For these rays $r_{\text{min}} = r_c$. We therefore have the maximum impact parameter for rays which

can reach the critical surface

$$b_{\max} = r_c \left[\frac{1}{1 - r_s/r_c} - \frac{m_a^2}{\omega_{\text{obs}}^2} \right]^{1/2}, \quad (5.61)$$

where we used the definition that at the critical surface, $\omega_p^2(r_c) = m_a^2$. The key point to note is that b_{\max} sets the characteristic size of the image in the image plane, which in the toy example we describe here, is a circle radius b_{\max} .

We also know that since ω_{obs} is the asymptotic frequency of photons, it satisfies $\omega_{\text{obs}}^2 \simeq m_a^2(1 + v_0^2)$ where v_0 is the asymptotic velocity of the axion, set by the velocity dispersion of dark matter. Putting this together, we see that to leading order in v_0 and r_s , we have that the characteristic size of the image (see fig. 5.4) is given by $r_{\text{image}} \simeq b_{\max}$

$$r_{\text{image}} \simeq r_c \left[\frac{r_s}{r_c} + v_0^2 \right]^{1/2}. \quad (5.62)$$

Let us now consider the scales at play. We can use a canonical model for the plasma density [244] (see eq.(5.43)) to estimate the size of r_c by equating $\omega_p(r_c) = m_a$. For the pulsar J0806.4-4123 used in this work and [153], we have $B_0 = 2.5 \times 10^{13}$ G and $P = 11.37$ sec so that for a mass $m_a = 0.5 \mu\text{eV}$ we obtain a characteristic radius $r_c \simeq 5R$. For a neutron star of mass $M = M_\odot$ and radius $R = 10\text{km}$ we have $r_s/R \simeq 0.3$. Note this value is quite high, owing to neutron stars being very compact, and quite close to being black holes.

Coming back to eq. (5.62), we see that for the NS values chosen above, $r_s/r_c \simeq 0.06 \gg v_0^2 \sim 10^{-6}$ so that gravity plays a vital role from a ray tracing perspective, in that it makes the area of the image $\mathcal{A}_{\text{image}} \sim r_{\text{image}}^2$ four orders of magnitude larger in comparison to a plasma analysis in flat space! Numerically, speaking, this greatly simplifies the task of locating and resolving the image of the critical

surface in the image plane. Locating a larger region, is of course much easier than hunting for a highly lensed “pin prick”. There is of course no such issue for the straight-line rays considered in [153] where the characteristic size of the image was just given by the geometric cross-section $\mathcal{A}_{\text{image}}^{\text{vac}} \sim r_c^2$. It is interesting to note that the authors of [153] claimed that gravity in the absence of plasma only produces a small percent-level correction to the total power. However, as explained above, when taken in combination with plasma, gravity in fact becomes an important component in making the problem numerically tractable by counter-balancing strong refraction from the magnetosphere. The relative image sizes with and without plasma can be seen by comparing the two panels in fig. 5.4.

5.2.3 Numerical Procedure

- Similar to the treatment in [153], we identify a region of interest of some angular size $\Delta\Omega$ containing the full set of trajectories that map the observer to the various possible lines of sight that cover this region. The regions where axion-photon conversion occur then form an image of the magnetosphere associated with the resonant conversion. We divide this region into pixels of size Δb , the centres are associated to trajectories of photons with observing angles $(\theta_{\text{obs}}, \psi_{\text{obs}})$. We back propagate each ray to the surface of the star and record a ‘hit’ or ‘miss’, depending on whether the trajectory contains a resonant conversion point.
- We then perform a coarse-grained scan across this region to identify the size of the image. Once this is done, we then re-scan across this image with a smaller pixel size, to maximise numerical efficiency. To ensure numerical convergence, we pick an angular resolution such that our final results do not change when the pixel size is halved.

- Each pixel is then assigned a radiant intensity calculated assuming the standard 1-dimensional axion-photon mixing described in [147]. The total intensity is then obtained by summing over all the rays and multiplying by the square of the pixel size Δb^2 (see appendix .3 [254] for more details).
- The Doppler broadening is computed by evolving the frequency evolution along each ray. This enables us to see how a line signal with frequency $\omega \sim m_a$ is broadened due to each ray i receiving a correction $\omega \rightarrow \omega + \delta\omega$. The final frequencies at the point of detection can then be binned, so as to derive the exact shape of the signal in the frequency domain.

The end product of these simulations is a ‘pulse-profile’, i.e., the radiated power $\frac{dP}{d\Omega}$ associated to a pulsar as a function of time/phase. To make contact with observations, one needs to then convert this power into a flux density according to the equation

$$S_{\text{obs}} = \frac{1}{D^2 \Delta f_{\text{obs}}} \frac{dP}{d\Omega}, \quad (5.63)$$

where S is the observed flux density, D is the distance to the pulsar and Δf_{obs} is the width of the frequency channels of the instrument.

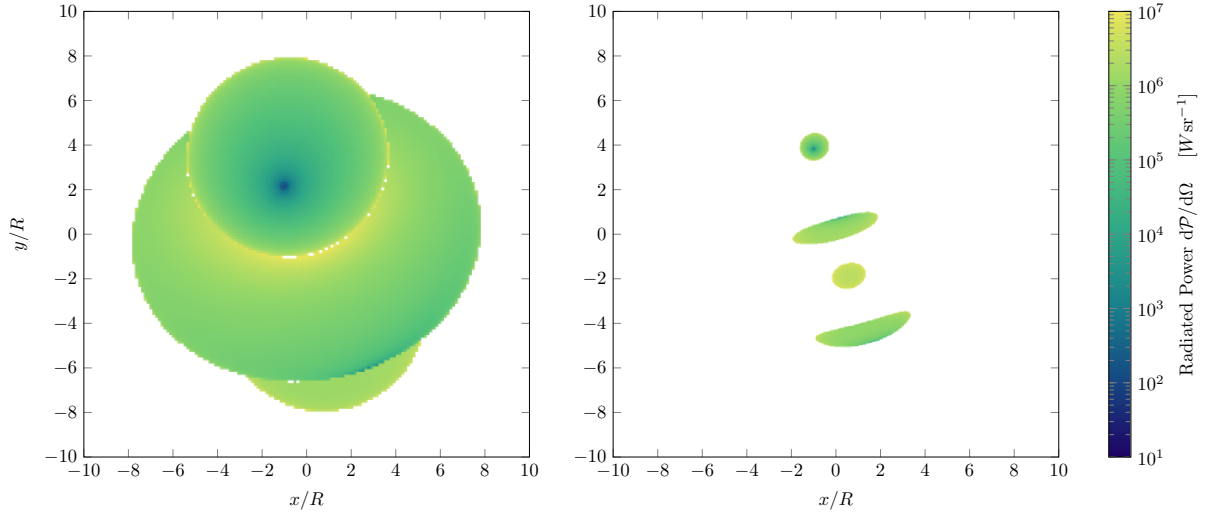


Figure 5.4: **Radiated power in image plane: vacuum vs. plasma.** The view of radio photons at frequency $\omega \simeq m_a$ produced by axion dark matter conversion, as seen in the image plane perpendicular to an observing angle $\theta = 36^\circ$. We chose model parameters compatible with observations of NS J0806.4-4123, with $B_0 = 2.5 \times 10^{13}\text{G}$, period $P = 11.37\text{sec}$ and magnetic misalignment angle $\alpha = 18^\circ$. The axion mass chosen was $m_a = 0.5\mu\text{eV}$ with a coupling $g_{a\gamma\gamma} = 10^{-12}\text{GeV}^{-1}$. The left image results from straight-line rays propagating through vacuum, reproducing the results of [153]. The right panel shows the presence of novel plasma effects considered in this work, computed via eq. (5.54). The time evolution of the image in the plasma case can be viewed [here](#) and can be contrasted against the [vacuum case](#) derived in [153].

5.3 Ray-tracing analysis applied to data

In this section, we combine our novel ray-tracing procedure [254] with new and archival spectral observations of the Galactic Center magnetar PSR J1745–2900, henceforth GCM, using the Karl G. Jansky Very Large Array (VLA³) to search for signatures of axion-photon conversion in the magnetar magnetosphere. The new observations are the most sensitive to date, and when combined with archival VLA observations of Sgr A* already used in [236, 237] that include the magnetar in the field of view, provide the strongest constraints on $g_{a\gamma\gamma}$ to date over the mass range $4.2 - 60 \mu\text{eV}$ for a frequency range $\sim 1 - 15 \text{ GHz}$.

Within the GJ model there is a maximum axion mass for conversion which is set by the critical surface having some part outside the star. After solving for r_c and maximising over θ and φ , which involves setting $\theta = \alpha/2$ and $\varphi = 0$, this is given by

$$m_a^{\text{max}} \approx 85 \mu\text{eV} \left(\frac{B_0}{10^{14} \text{ G}} \right)^{1/2} \left(\frac{P}{1 \text{ s}} \right)^{-1/2} \left(1 + \frac{1}{3} \cos \alpha \right)^{1/2}, \quad (5.64)$$

where α is the inclination of the magnetic axis relative to the rotation axis.

We have obtained upper limits on the time-averaged spectral line flux density in the direction of the GCM as a function of frequency from three sources. The first two are VLA archival data described in [236, 237]. The third is new VLA observations in its most extended configuration with maximum baseline 36.6 km that provides the angular resolution needed to separate the GCM emission from Sgr A*, which are $\approx 2.4''$ apart. Observations were obtained during seven single-transit sessions between MJD 59184 and 59253 (program 20B-154) in two circular polarizations with 8-bit sampling and 2 sec recording times. The new observations are in C-, X-, and Ku-bands (6–8 GHz, 10–12 GHz, and 12–13 GHz) and

³The National Radio Astronomy Observatory is a facility of the National Science Foundation operated under cooperative agreement by Associated Universities, Inc.

have integration times in the range $1.4 - 1.6 \times 10^4$ sec achieving r.m.s. noise levels in 4 MHz channels of 0.13 mJy in C-band and $\sim 50-60$ μ Jy in the higher frequency bands. The data were reduced and calibrated using standard techniques within the CASA package [255] following previous work [236, 237]. The continuum emission from Sgr A* is used for interferometric self-calibration (the magnetar continuum is detected but is 2–3 dex fainter than Sgr A*).

Continuum emission was removed by a linear uv subtraction to make null-centered spectral image cubes. We extracted the GCM spectrum from the cubes using an aperture slightly larger than the synthesized beam and the point source flux density was corrected channel-by-channel. To assess the significance of features in the spectra we form a sky noise spectrum using the r.m.s. noise in regions away from the GCM and Sgr A*, and these typically agree with the spectral noise in the GCM spectrum.

The new and archival GCM and sky spectra were Gaussian smoothed to 4 MHz channels, except for L-band (1–2 GHz), which was smoothed to 2 MHz channels. Noise values range from 0.57 mJy to 52 μ Jy (1.5 and 12.5 GHz). Unlike the lower-resolution observations presented in [236], no molecular or radio recombination lines were detected in 20B-154. Spatial filtering of the maximum-resolution array removed contaminating signals from the galactic center environment.

5.3.1 Limits on the axion-photon coupling

No significant ($> 4\sigma$) single-channel emission lines were detected at the position of the GCM⁴ and hence there are no candidate axion signals. These upper limits were then compared with model predictions as a function of m_a , θ and α in order

⁴One 5.1σ channel at 10.9 GHz was identified with a sidelobe of Sgr A* that was not captured in the sky noise spectrum.

to extract 95% confidence limits on $g_{a\gamma\gamma}$. The limits are presented in Fig. 5.5 for the two axion densities for halo models A and B described above. In both cases we have calculated limits for all values of the unconstrained angles θ and α and presented the range. We see that for halo model A the limits are similar to those from the CAST solar axion experiment [118], while they are a couple of orders of magnitude stronger (the limit on $g_{a\gamma\gamma}$ is $\propto \sqrt{\rho_a}$) for model B.

It is interesting to contrast this state-of-the-art treatment with the original toy-setup considered in ref. [147] that only considered radially outgoing photons where the angular dependence factorises and

$$\frac{dP^{\text{radial}}}{d\Omega}(\theta, \alpha, \varphi) \propto \frac{3 (\hat{\mathbf{m}} \cdot \hat{\mathbf{r}})^2 + 1}{|3 \cos \theta \hat{\mathbf{m}} \cdot \hat{\mathbf{r}} - \cos \alpha|^{4/3}}, \quad (5.65)$$

where \mathbf{m} is the magnetic dipole and hats denote unit vectors. We have also presented limits for these radial trajectories in Fig. 5.5. These are somewhat stronger than one gets from ray tracing, and also cut-off at a lower axion mass, $m_a \gtrsim 14 \mu\text{eV}$, due to the fact that beyond that there are points in the $\theta - \alpha$ plane where there is no predicted signal.

5.3.2 Conclusions

Our principle conclusion is that robust constraints on axion dark matter cannot be obtained using simplistic radial trajectories [147, 235] and therefore ray-tracing [153, 254, 256] becomes unavoidable. The principle reason for this is that radial trajectories connect each viewing angle in the sky with a single point on the emission surface resulting in a very undemocratic spread of power across the sky. This leads to very sharp angular variation in the signal with a few narrow bright-spots that are associated to trajectories with high emission rates and for

higher masses, so much angular variation that for many viewing angles the pulse averaged power vanishes entirely. As a result, in the radial approximation, one cannot be sure a signal is even present.

In future work it may be possible by modelling the pulsar beam and fitting to radio observations of the pulse width, one could infer something about α , and perhaps the viewing angle relative to the beam axis $\theta - \alpha$, this may allow us to attach some probability distribution to θ and α , reducing the parametric uncertainty. Nonetheless, at present the most conservative approach is to assume the viewing and magnetic angles are unknown parameters, and take those values (α, θ) for which the pulse-averaged power is minimal. With this in mind, the radial-trajectory approximations of [147] clearly make it impossible to place reliable bounds since the signal entirely vanishes for many viewing angles at higher masses.

Rather pleasingly, our analysis also reveals that the angular variation in power is actually under good control, typically around an order of magnitude for the values chosen in this paper. This translates to less than an order of magnitude uncertainty in the sensitivity to $g_{a\gamma\gamma}$ which scales as the square root of the power.

As stated in [257], sophisticated modelling of the axion-photon mixing incorporating 3D effects in mode excitation leads to corrections to the probability of conversion that may be several orders of magnitude. However, the important caveat to this statement is that this is true on the level of individual trajectories. When one integrates over all axion phase space, the corrections to the photon flux are $\sim \mathcal{O}(1)$, leading to a slightly stronger constraint on $g_{a\gamma\gamma}$. While it is important to carry out the full ray-tracing analysis with the 3D conversion probability in order to truly quantify these effects, we may conclude from recent results that

the 1D treatment is a reasonably conservative one.

To summarise, one can identify three principle uncertainties in axion-constraints. (i) The dark matter profile and therefore the dark matter density near the neutron star. (ii) The sensitivity of axion limits to the structure of the magnetosphere in terms of the magnetic field and plasma density profiles. (iii) The angular, frequency and time-dependence of the signal which depends on the propagation of photons through the magnetosphere. Point (i) is of course a challenge for any attempt to detect dark matter, even here on earth where the velocity and density is not necessarily known. It can also be that this uncertainty can be reduced by choosing pulsar further from the galactic centre where there is less disagreement between different halo models. Future observations may also allow better determination of the dark matter density around the magnetar. However, at the moment this is the primary uncertainty. It may be possible to ameliorate point (ii) in future work by applying state-of-the-art magnetosphere modelling and examining the variation in signal properties across different models. The subject of this section is point (iii), which has recently been resolved by sophisticated ray-tracing techniques as we have shown. In addition it may be necessary to include the full range of effects considered in refs. [256] and [152].

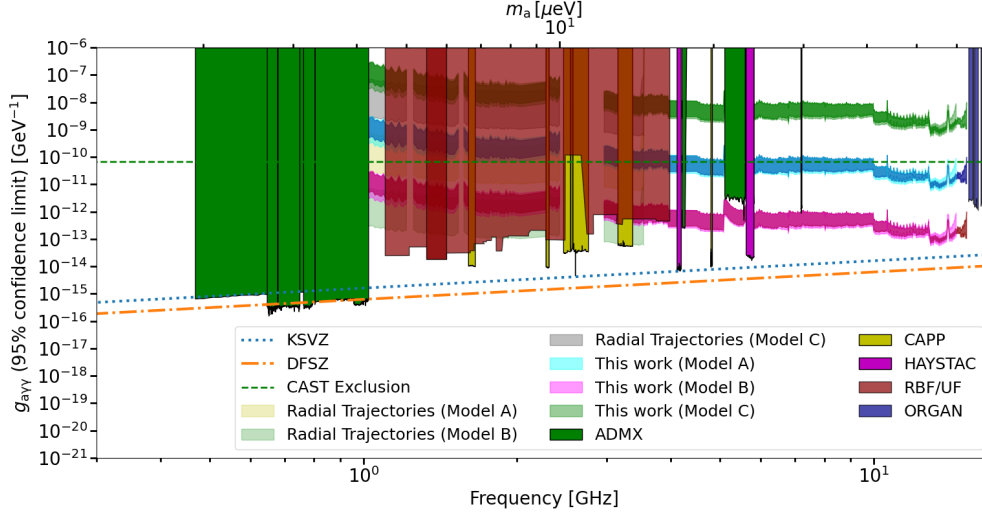


Figure 5.5: New exclusion limits on axion-dark matter combining archival and recent VLA data and novel plasma ray-tracing techniques [254]. The maximum value of m_a for which there is a signal corresponds to eq. (5.64), beyond which the critical surface disappears entirely inside the star. The thickness of the bands corresponds to the maximum and minimum limits of the signal with respect to the viewing angle θ and magnetic angle α . The dark coloured bands extremize over θ for a fixed value of the magnetic angle $\alpha = 18^\circ$, whilst the lighter bands extremize over both θ and α . We also display three possibilities for the axion dark matter density corresponding to models A, B and C described in the main text. Experimental limits from CAST [118], green and purple exclusions are from the ADMX [119–122] and HAYSTAC [123–125] haloscopes, respectively. The yellow exclusions are from the CAPP haloscope based in South Korea [128–130, 130, 131]. The dark red are from the RBF/UF haloscopes [132, 133]. Finally, the dark blue limits from the ORGAN collaboration [134, 135]. For comparison with our ray tracing analysis, we also display equivalent limits based on a single radial ray connecting the observer to the conversion surface also for $\alpha = 18^\circ$. For the radial formula, above a certain mass cutoff, the signal is zero for some values of θ and so there is no limit in those cases. For $\alpha = 18^\circ$, this cutoff occurs at when $m_a > 14.5 \mu\text{eV}$.

Chapter 6

Searching for the Resonant Axion-Photon Signal in the Time Domain

6.1 Introduction

In the previous chapter, we presented an analysis of the one-dimensional axion-photon mixing in neutron star magnetospheres valid for relativistic and non-relativistic dispersion relations and a ray-tracing analysis of the photon trajectories resulting from the resonant conversion. Our formalism took into account the refraction of the photons due to a) the charge density within the plasma and b) the gravitational field of the pulsar. We computed the radiated power as a function of the pulsar phase for a given set of observational parameters that we fixed for a given pulsar. We showed that the size of the ‘image’, i.e., the region over which the resonant conversion takes place projected onto the plane of the magnetosphere as seen by an observer on the Earth is regulated by the refractive index of the medium, which is a function of the plasma density (which acts as a repulsive medium) and gravity (which is attractive). We obtained a non-trivial time-dependence for the radiated power. This is due to the fact that the majority of the high-intensity emission appears to originate from specific regions in the pulsar magnetosphere, the so-called ‘throats’ of the charge distribution which are local maxima in the charge distribution. We also solve the full geodesic equations of motion to derive the frequency dependence of the signal, from which we showed the frequency width of the signal agreed with the order-of-magnitude estimate we made in [258]. We applied this numerical pipeline to real data taken by the Very Large Array (VLA) of the magnetar in the galactic centre in [259], to derive limits on the axion-photon coupling that supercede the CAST limit [118] over the axion mass range $1 \mu\text{eV} \leq m_a \leq 64 \mu\text{eV}$. We note our results differ from those in [256], most importantly in the prediction of the size of the amplitude of the time-dependence of the signal. In their analysis, they obtain a greater anisotropy across the magnetosphere, resulting in greater time-dependence, although they

neglect to take into account gravity. This formalism was recently applied to neutron star populations in the galactic centre to derive a limit on the axion photon coupling using the SETI Breakthrough Listen data [260].

With all the progress in the theoretical modelling of the axion-photon equations of motion as well as the ray-tracing of the photons through the magnetospheres, the challenge of sifting through real data to search for the signal and in the event of non-detection, setting a limit on the axion-photon coupling $g_{a\gamma\gamma}$ naturally arises. With large amounts of archival time-series data available on various pulsars, one might be tempted to make use of the information we obtain from the ray-tracing simulations on the time-dependence of the signal. This is especially important due to the difficulty associated with obtaining observational bandwidths required to resolve the features of the signal in frequency-space. In other words, one could envision using the results of the ray-tracing code, i.e., the predicted flux density as a function of the pulsar phase as a template that can be used as a filter to mine archival data for specific signal shapes (as a function of time). While there is currently debate on the amplitude of the time-dependence [256] and the amplitude of the probability of conversion [257], we remark that it would be counter-productive to not at the very least attempt to optimise searches for the signal in pulsar data with the ray-tracing results as a prior.

In this work, we introduce a matched filter approach towards searching for the signal in real data that is optimised to find signal profiles that match the ray-tracing simulation output. We stress that the advantage of indirect detection methods is their broadband nature, and therefore their usefulness lies in the ability to identify a signal if it does exist across wide ranges of frequency.

We begin by characterising the time-dependence of the signal and the effect of model parameters on the same in section 6.2, where we generate a database of

signals for different input parameters using which we create a tool that is able to interpolate between input parameters and predict the signal for arbitrary values. We then describe the mathematical formalism behind the matched-filter in section 6.3.1 and test the response of the filter in the presence of pure Gaussian noise in section 6.3.2. We then identify the pulsar B0834+06 with $B_0 = 2.98 \times 10^{12} \text{ G}$, $P = 0.785 \text{ s}$, $D = 0.785 \text{ kpc}$ as a test-case on which we test our formalism. We use this pulsar for two main reasons. The first being its proximity to the Earth that allows us to set the value of $\rho_{\text{DM}} = 0.45 \text{ GeVcm}^{-3}$, the local value. This is advantageous since the ρ_{DM} is highly uncertain for pulsars further away closer to the galactic centre, which makes the constraints from nearby pulsars much more reliable. Secondly, this pulsar was associated to among the largest values of on-source integration time in the JBCA pulsar catalogue in section 6.4.1. We discuss how one can model this data in section 6.4.2 and possible theoretical priors we may apply on observational parameters in order to set a limit on the axion-photon coupling in sections 6.4.3. We then apply the matched filter on the data in section 6.4.4. Finally, we describe our procedure for establishing an upper limit on the axion-photon coupling in 6.5. We conclude by discussing the validity of our results and commenting on future directions this line of research may take. We would like to particularly stress that this is a proof-of-principle study and therefore, the importance of the results in the landscape of the literature needs to be judged according to the potential strength of the technique rather than the constraints derived in this particular instance.

6.2 Characterising signal variability

6.2.1 Ray-tracing simulations

We model the axion-photon signal using the ray-tracing simulations described in the previous chapter [254]. In these simulations, we numerically calculate the angular, frequency and time-dependence of the signal resulting from the propagation of photons through the magnetosphere. This includes lensing, refraction and frequency distortions, leading, amongst other things, to the Doppler broadening of the line profile [258]. The end product of these simulations is a ‘pulse-profile’, i.e., the radiated power $\frac{dP}{d\Omega}$ associated to a pulsar as a function of time/phase. To make contact with observations, one needs to then convert this power into a flux density according to the equation

$$S_{\text{obs}} = \frac{1}{D^2 \Delta f_{\text{obs}}} \frac{dP}{d\Omega}, \quad (6.1)$$

where S is the observed flux density, D is the distance to the pulsar and Δf_{obs} is the width of the frequency channels of the instrument.

It is important to note the differences between the pulse profile associated to the pulsar itself and the dark matter signal due to the axion-photon resonance. The pulsar emission is typically periodic and persists only for a small duration of time, but has a wide bandwidth. The axion signal on the other hand has the opposite features, i.e., the signal will persist throughout the rotation phase of the neutron star but will typically be associated to a smaller frequency width.

In order to decouple the two signals, the simplest procedure is to simply excise those time channels that contain the pulsar signal. However, this would mean that one would unavoidably be subtracting some of the axion signal as well.

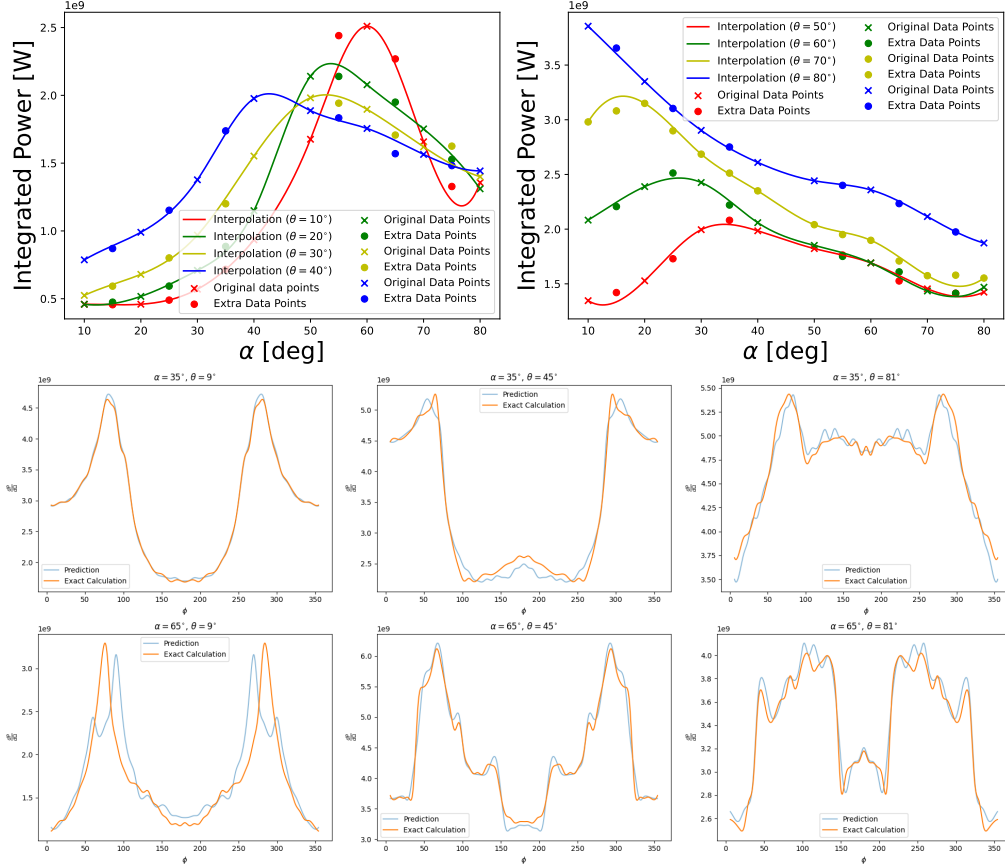


Figure 6.1: We present the integrated flux as a function of α for different values of the observing angle θ , where the original sampling is represented by the circle data points. An interpolation routine was used to calculate the signal at intermediate values, which was then compared to the cross data points evaluated by the ray-tracing code. In the bottom panels, we present examples of the agreement between the profiles as predicted using the interpolation routine and the profiles calculated from the ray-tracing code using the observational parameters for B0834+06.

Naively, one would expect that this would not be an issue, as this should represent only a small fraction of the total axion flux. However, depending on the phase relationship between the main pulsar beam and the axion signal, the effect of this subtraction can vary. Therefore, it is important to model the phase offset between the axion signal and pulsar emission ϕ_0 .

Based on our understanding of the ray-tracing simulations, we note that the axion signal is symmetric, and is π periodic. This is due to the fact that as the pulsar rotates, the resonant point r_c varies in position. When the resonant point occurs at the charge gaps, i.e., the so-called ‘throat’ regions of the Goldreich-Julian charge distribution there is a peak in the emission. Since the pulsar beam is supposed to emanate from the charge gaps, we set the phase offset $\phi_0 = \pi/4$.

6.2.2 Interpolation of simulation database

For a given pulsar, the input parameters required for our ray-tracing package are the magnetic field strength at the surface of the pulsar B_0 , the pulse-period P , the distance to the pulsar D , the dark matter density ρ_{DM} at the position of the pulsar, the observing angle θ between the line of sight and the rotation axis of the pulsar and the magnetic misalignment angle α which represents the angle between the magnetic axis and rotation axis of the pulsar. The period P is one of the best-measured quantities in astronomy, while the magnetic field strength of the pulsar is inferred from measurements of P and \dot{P} the spin-down rate of the pulsar combined with model-dependent parameters including the moment of inertia of the pulsar and its radius [261]. This calculation assumes that the energy released by the pulsar in the form of radio emission comes from the loss of rotational energy calculated from the spin-down rate. The large values of $\frac{\dot{P}}{P}$ observed for

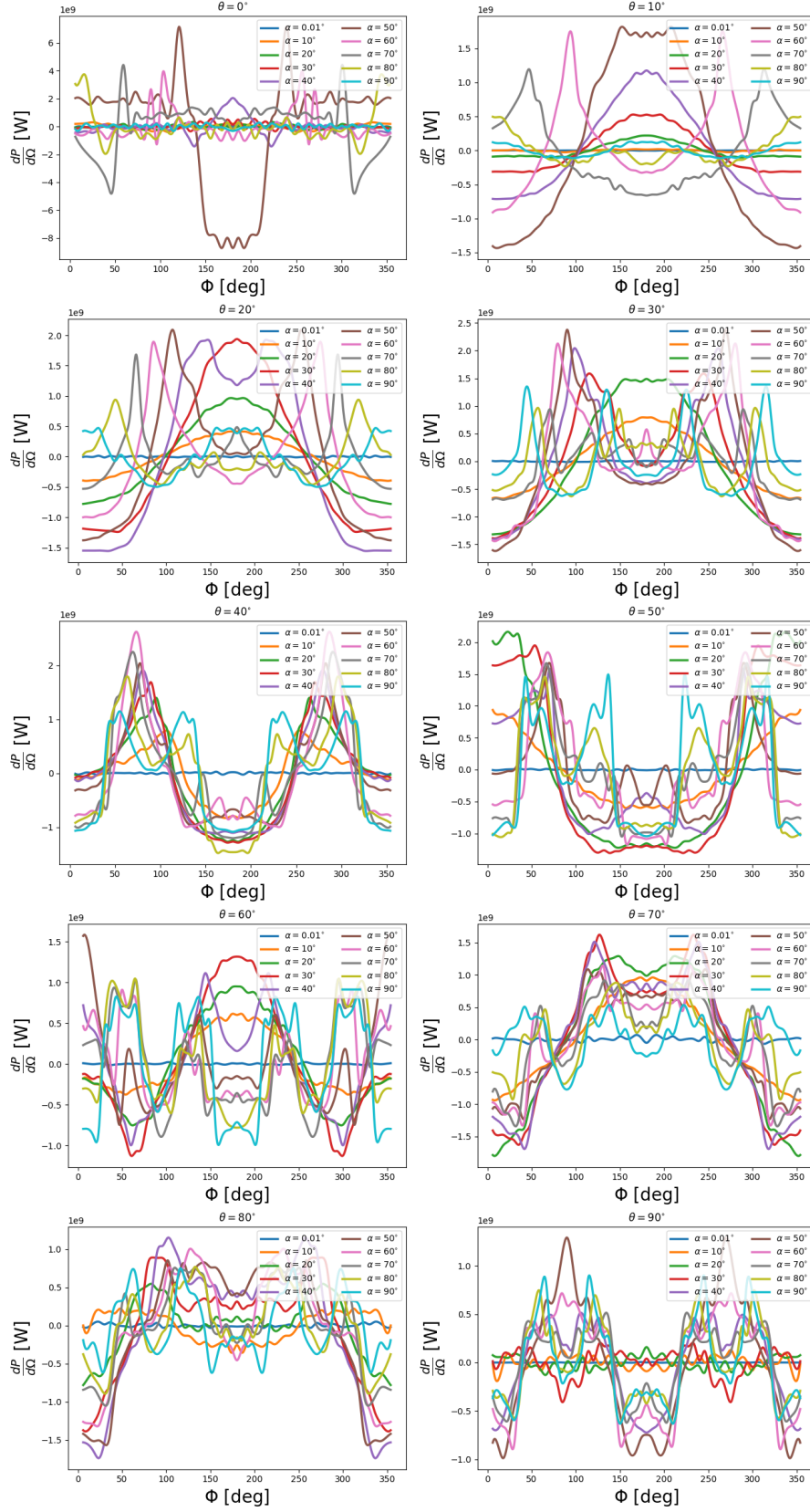


Figure 6.2: We present the time profiles as a function of the α for different observing angles. Clearly, for $\alpha \rightarrow 0$, the time dependence in the profiles becomes negligible. As mentioned before, the larger the time-dependence in the profile, the better the constraint on $g_{a\gamma\gamma}$. Therefore, one would expect that the profiles with the largest difference between the maximum and minimum flux as a function of time should give the best constraints, to leading order.

magnetars form the basis for their large inferred values of B_0 ¹. The distance to the pulsar is inferred from the dispersion of the pulse as a function of time, since the photons emitted in the main beam of the pulsar traverse through the galactic electron density along the line-of-sight. Given a model for the galactic electron density, one can estimate the distance to a pulsar. Galactic dark matter profiles allow one to predict the dark matter density at the position of the pulsar, but these models become highly uncertain as one gets closer to the galactic centre, where some models predict a spike in the density, while others predict a more cored profile.

This leaves the angles (α, θ) as parameters that are essentially unknown a-priori. Due to the computational cost of the ray-tracing simulations, that require ~ 24 hours to produce a pulse-profile when parallelised over 32 CPU cores, we require a faster alternative to predict the time-dependence of the signal for arbitrary input angles. Therefore, we generate a simulated database of flux profiles as a discrete function of (θ, α) , represented by the circular data points in the top panels of figure 6.1. Based on these datasets we generate an interpolation routine (where we use the SciPy package `scipy.interpolate`) that can then predict the signal for arbitrary values of α and θ , the performance of which can be seen in the bottom panels of figure 6.1, where we compare the prediction of our interpolation routine with crossed data points, that were not used to generate the interpolation. We show the time-variability as a function of the angles θ and α in fig. 6.2. We now have the tools necessary to test our matched filter formalism. Before we describe our matched filter formalism in detail, we would like some to develop some insight on the various kinds of profiles that our database contains and how one might expect the filter function to behave *a-priori*.

¹We note that the magnetars are known to emit large X-ray fluxes, the luminosity associated cannot be explained by spin-down alone.

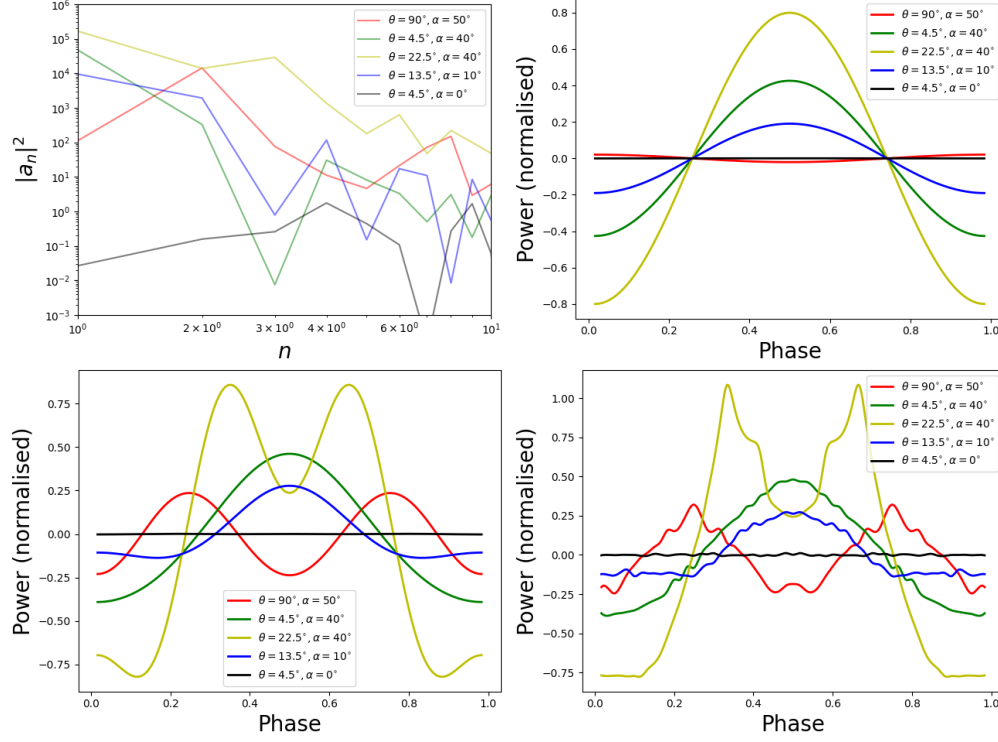


Figure 6.3: We present the power spectra for a representative set of profiles that display the variation in the shapes of the profiles seen in fig. 6.2. We see that amplitude in frequency space quickly drops as one moves to higher modes in frequency. This suggests that the filter function will respond to the largest features in our profiles, i.e., there is a cut-off value for the amplitude of time dependence below which the noise from the data should dominate the results. This is reflected in our plots of the axion-photon coupling in section 6.5. We also show the profiles obtained from inverting the FFT with only the first mode contributing (top right panel), the first 3 modes contributing (bottom left), and the full profiles are shown in the bottom-right panel.

6.2.3 Fourier analysis of profiles

We now turn to the profiles themselves. We are interested in developing some intuition on the response of a filter function on the time profiles generated by our interpolation. Naively, one would expect a signal with a larger amplitude in its time variation to return a larger signal-to-noise value as compared to a signal that is relatively flat as a function of time. Specifically, in our case, we are interested in understanding how one would expect the time variation in our signal as a function of (θ, α) is reflected in the limits that we obtain on the axion-photon coupling.

To develop this intuition, we compute the real discrete Fourier transform of our profiles. This will enable us to understand which modes will contribute to the filter function and therefore understand the most significant individual features in the shapes of the profiles. As we will see in section 6.3, the signal to noise returned by the matched filter is simply the magnitude of the overlap integral of the data with the normalised profiles, and therefore if one decomposes the profiles into Fourier modes, is simply a sum over the contributing terms in the discrete FFT of the profiles times the appropriate noise term. We can see the results of the Fourier analysis in fig. 6.3. Clearly, we see that the amplitude of the FFT for the various profiles considered falls fairly quickly as one goes to higher frequency modes. Clearly, this suggests that the most important features in the profiles are those with the largest amplitude on time variation over most of the pulsar period. As a result, one would expect that the difference between the maximum and the minimum flux should be a reasonable representation of the filter response, even in the presence of noise. As we will see later, this simple prediction is largely borne out in our analysis of the axion-photon coupling limit obtained from application of the matched filter to the the complete pulsar data set in section 6.5.

6.3 Matched Filter

6.3.1 Mathematical formalism

Matched filters have been implemented for precision cosmology in the past few decades, in the context of detecting galaxy clusters in the Universe from observations of distortions of the black body spectrum associated to the CMB using the thermal Sunyaev-Zeldovic (tSZ) effect [262]. The usefulness of the technique lies in the fact that it provides a natural quantity, the detection confidence or signal-to-noise q that associates the data-set under consideration to each input signal. Therefore, one is able to perform studies of the parametric dependence of the SNR on the model parameters, which allows one to marginalise over nuisance parameters or set theoretical priors on them.

Let the amplitude of the flux density signal be S_0 . We assume that the shape of the signal $\mathbf{F}(\mathbf{p})$ is determined by the some set of parameters \mathbf{p} . The vector that completely characterised the data as seen by the telescope may then be written as

$$\mathbf{d} = S_0 \mathbf{F}(\mathbf{p}) + \hat{\mathbf{n}}, \quad (6.2)$$

where $\hat{\mathbf{n}}$ is a Gaussian random noise vector. Note that we assume Gaussian noise since the average-subtracted pulsar data is very close to being Gaussian. One can then solve for the signal amplitude S_0 to obtain

$$S_0 = \frac{\mathbf{F}^T C^{-1} \mathbf{d}}{\mathbf{F}^T C^{-1} \mathbf{F}}, \quad (6.3)$$

where T represents the transpose and C^{-1} is the inverse of the covariance matrix

associated with $\hat{\mathbf{n}}$. The variance σ is written as

$$\sigma = (\mathbf{F}^T C^{-1} \mathbf{F})^{-1} \quad (6.4)$$

The signal-to-noise ratio q may then be written as

$$q = \frac{S_0}{\sigma} = \frac{\mathbf{F}^T C^{-1} \mathbf{d}}{(\mathbf{F}^T C^{-1} \mathbf{F})^{1/2}}. \quad (6.5)$$

If the shape of the signal in time and in frequency is known to be $\mathbf{F} = \bar{\mathbf{F}}$, one can then optimise the filter to return a non-zero (modulo fluctuations about the mean due to the noise) signal-to-noise value q only when the data vector contains such a signal.

We now implement this procedure to look for the signal in mock data generated by our interpolation routine that we generated from our simulation data (see section 6.2). We are essentially interested in testing the response of the filter as we vary the input parameters (m_a, θ, α) , which we first test in the presence of simulated noise. Note that $g_{a\gamma\gamma}$ only sets the amplitude of the profiles and therefore can be integrated out of the analysis. The value of the coupling is only required to infer a limit from data, as will be explained in section 6.5.

6.3.2 Simulated Data

We first implement our matched filter on simulated data, where we add the expected signal (at $m_a = 6.3 \mu\text{eV}$) to a Gaussian random noise vector whose amplitude and variance are chosen to be about the same as the typical values (~ 0.01 Jy) in archival data within the JBCA catalogue. We generate the flux profiles as a function of pulsar rotational phase with pulsar parameters for the pulsar B0834+06. These values are associated to the pulsar B0843+06 in the

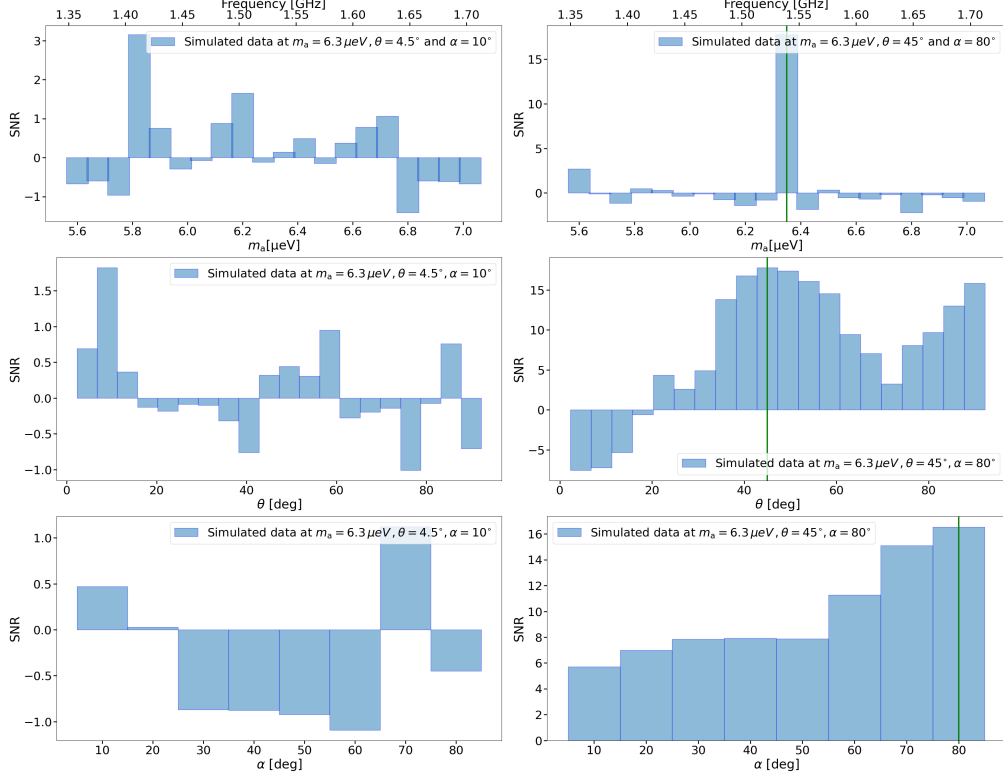


Figure 6.4: Here we plot SNR as a function of (θ, α) for constant (m_a, θ) with the time-averaged signal at each frequency channel is subtracted (which is what pulsar observers do typically). In the left panels, we present the filter response to a profile with negligible time-dependence (profile A). In the right panels, we present the filter response to a profile with significant time-variation (profile B). Now we see that the SNR is consistent with no signal for profile A, since the time variation is practically negligible, leading to an almost complete subtraction of the signal from the data. Therefore, due to the specific data available from pulsar observations, greater time-variability is more desirable, and avoids the absence of constraints for certain mass values where the profile is flat for specific values of (α, θ) . We obtain identical results, with the filter performing better for profile B and the signal disappearing for profile A when the time-averaged signal is subtracted at each frequency bin.

JBCA pulsar catalogue, a test case that was chosen mainly due to its proximity to the Earth, but also due to the fact that this pulsar was associated to among the largest values of on-source integration time. Given the proximity of this pulsar, we set the value of $\rho_{\text{DM}} = 0.45 \text{ GeVcm}^{-3}$, the local value. We choose two fiducial profiles that contain almost no time variation ($\theta = 4.5^\circ, \alpha = 10^\circ$) (profile A) and relatively large time variation ($\theta = 45^\circ, \alpha = 80^\circ$) (profile B), respectively.

We show in fig. 6.4 the SNR values returned by the filter when we insert the signal profiles A and B into the frequency channel corresponding to an axion mass $m_a = 6.3 \mu\text{eV}$, where we vary the input values of m_a, θ and α in the top, middle and bottom panels, respectively. As can be seen in fig. 6.4, the amplitude and time-variation associated to profile B leads to the the SNR curve peaking at the input value of the relevant parameter, which means the filter correctly associates the input profile with the maximum SNR. Note that while the $q - m_a$ curve sharply peaks at the input value of m_a , the trend with respect to θ and α is more complex. In contrast, the filter associates profile A (top and middle panels) with zero SNR despite explicit insertion of the profile into the data vector. This is due to the subtraction of the time-averaged signal from each frequency channel (bottom panel). The flat nature of profile A leads to a complete removal of the signal from the data. These results show that it is not possible to rule out all values of θ, α for a given value of m_a if the profiles for certain values of the angles are flat. However, for profiles with significant time variation (like profile B), one notices that while there is additional structure in the signal-to-noise as a function of θ , one is still able to detect the signal.

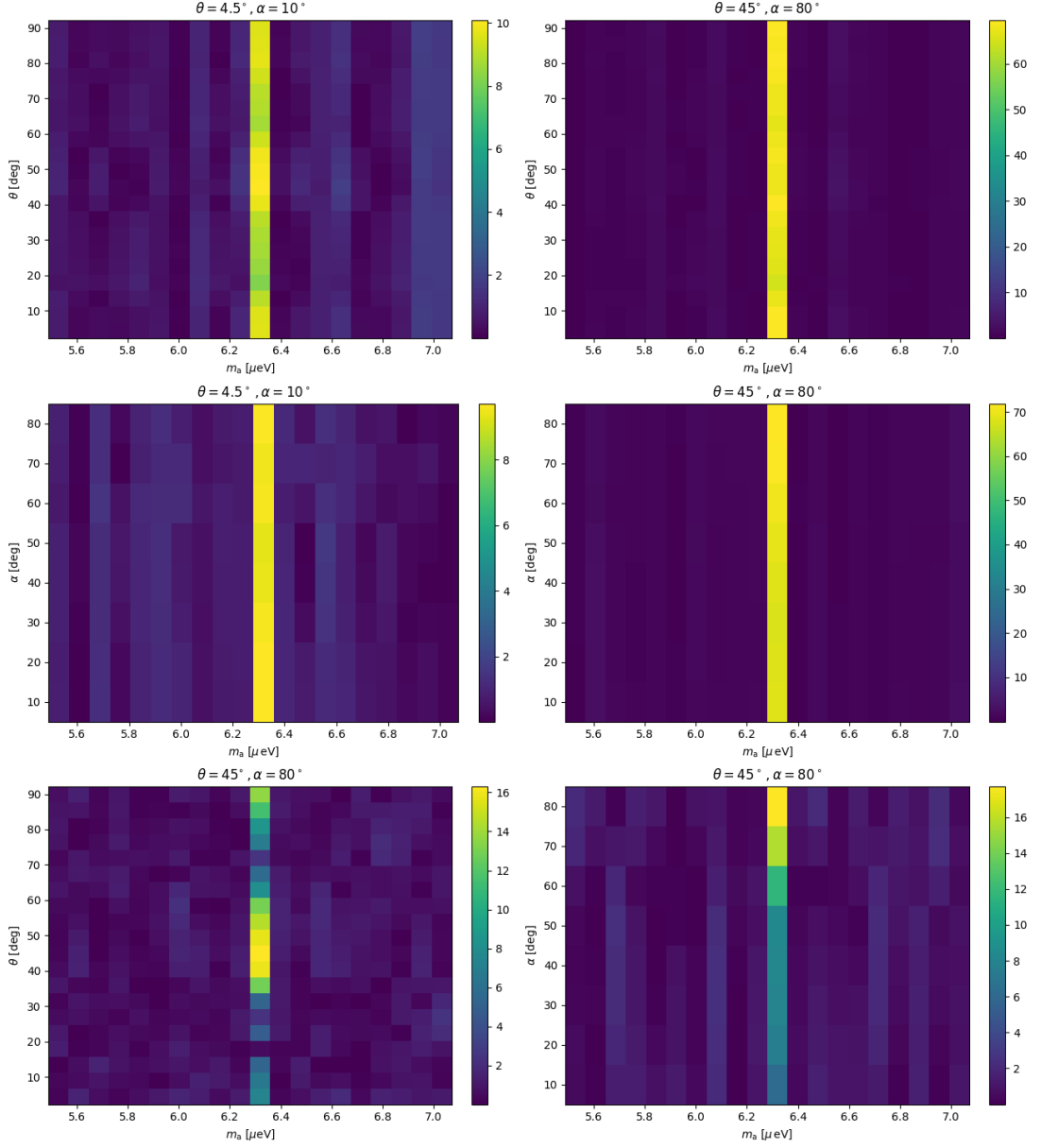


Figure 6.5: We plot the SNR as a function of (m_a, θ) and (m_a, α) , respectively. The top and middle panels contain the full signals for both profile A and B. The bottom panels contain the average subtracted signal from profile B (since it disappears for profile A). These results summarise our understanding of the performance of the filter for different profiles and data-vectors. When the data-vector contains purely the total amplitude of flux detected by the receiver, the only relevant parameter that affects the matched filter is axion mass. The SNR contains minimal structure from θ, α , in this case. However, when one subtracts the time-averaged profile from each frequency channel in the data-vector, we see additional structure, indicating the variability of profile shape as a function of the observing and magnetic misalignment angles.

These results may be summarised in fig. 6.5, where we plot the the SNR as a function of (m_a, θ) and (m_a, α) , respectively. We see that when one applies the matched filter on the data-vector without the time-average in each frequency channel subtracted, one has almost no uncertainty from the observing and magnetic misalignment angles on the SNR and therefore, on the resulting constraints on $g_{a\gamma\gamma}$. However, when the data vector has the time-averaged signal subtracted from each frequency bin, one has a non-trivial dependence on θ, α in the SNR. Essentially, we can conclude that in the presence of noise, the filter returns a greater signal-to-noise when the amplitude of the average difference between the maximum and minimum signal as a function of time is large. In other words, pulse-profiles where the difference between the instantaneous power and the power averaged over the period is large over a significant portion of the period give rise to a larger signal-to-noise ratio. As a simple test, one would expect that the signal-to-noise to scale with (θ, α) in an *opposite* manner to $\Delta \frac{dP}{d\Omega}$, the difference in the maximum and minimum of the pulse-profile (see fig. 6.3 and the attached discussion for some more intuition on the filter response). We will return to this point later in section 6.5.

6.4 B0834+06: The data from the catalogue

6.4.1 Archival Pulsar Data from JBCA catalogue

We now work with data from the Jodrell Bank Centre for Astrophysics (JBCA) catalogue on the pulsar B0834+06 for the values of B_0 , P and D associated with this pulsar). This data was processed by the pulsar group at JBCA, consisting of Michael Keith, Patrick Weltevrede and Ben Stappers. The data contains pulse-subtracted flux-densities across 768 channels in frequency and 1024 channels in phase. The pulsar data are observed with the 76-m Lovell Telescope at Jodrell Bank Observatory at a central frequency of 1520 MHz and a nominally useable bandwidth of 400 MHz, though some portions of this band will later be excised to remove radio frequency interference (RFI). The data are captured with the DFB, a digital filterbank clone of the PDFB3 instrument described in [263]. The data are recorded in the PSRFITS format and processed using psrchive [264]. The data are aligned in pulse phase using a Fourier-basis Gaussian process model of the pulse phase fit using `run_enterprise` [265], which makes use of `enterprise` [266] and `tempo2` [267].

For this experiment we are looking for faint off-pulse signals, and so it is important to remove as much RFI from the data as possible. RFI is initially excised by manual identification of outliers in individual frequency channels and 30-s ‘sub-integrations’. This is typically sufficient for general pulsar timing science. Further RFI removal on individual observations is performed using ‘clfd’ which removes outlier channels and sub-integrations using an inter-quartile range filter on the variance, range and spectral power of each pulse profile [268]. Further inspection of the dataset as a whole is performed by fully averaging each observation in frequency and appending every sub-integration into a single dataset. We then

remote outlier sub-integrations from the entire dataset based on inspection of the skew, kurtosis and cross-correlation of the off-pulse region of the profile. The RFI removal process, which is far in excess of that usually performed for pulsar timing, removed nearly half of the recorded sub-integrations.

Once the RFI affected data had been zero-weighted, the data are then averaged in time and de-dispersed. A flux calibration is applied by using the known spectral index and time-averaged flux density of the pulsar (for B0834+06, this comes from [269]).

6.4.2 Modelling the Data

In our tests with the simulated data, we modelled the noise as a Gaussian with a constant amplitude and variance across frequency. In order to test this assumption, we calculate the mean and the standard deviation of the data per frequency channel. The results may be seen in fig. 6.6. The variability of the data over frequency is mostly likely due to the imperfections in the RFI subtraction algorithm used to clean the data. One could attempt to model this variation, but as an initial more conservative approach, we employ a cut to the data that removes the frequency channels associated with $\sigma > 0.013$ Jy. The results after the cut can be seen in figs. 6.7, 6.10, . Clearly, the top panel that contains the Gaussian noise model in fig. 6.7 is almost indistinguishable from the bottom panel which contains the data.

Although we obtain agreement between the noise model and the data, it is worth noting that the data is still not a perfect Gaussian. This may be seen comparing a Gaussian distribution with the same variance as the data to the data itself. This is shown in fig. 6.6, from which it is clear the data contains a non-zero kurtosis.

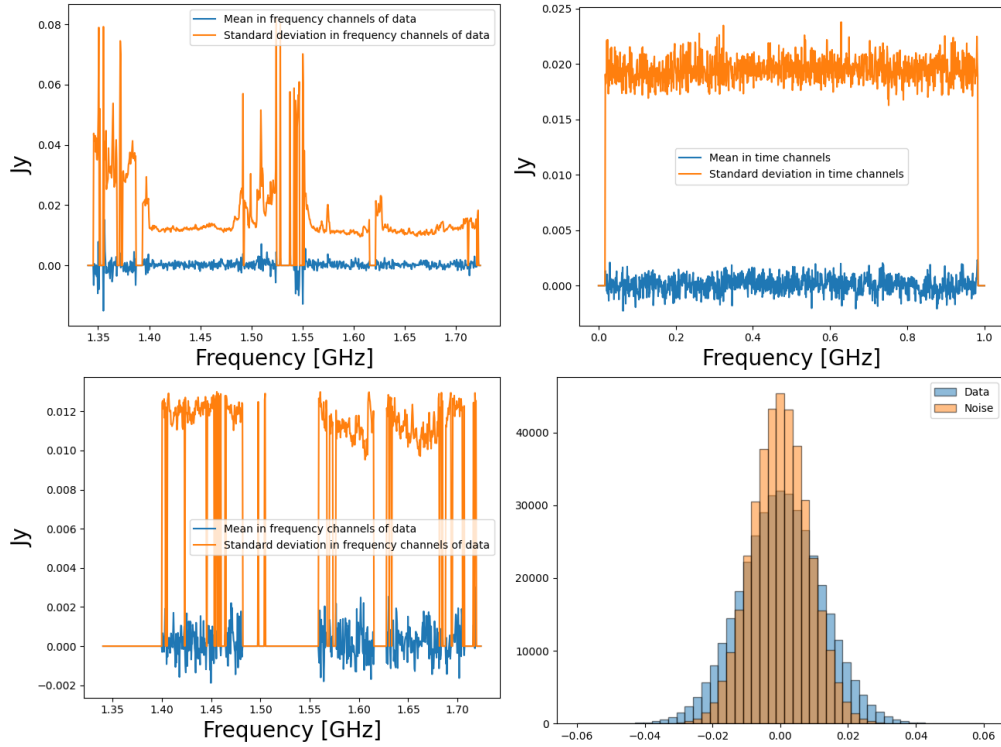


Figure 6.6: We plot the standard deviation and the mean in the frequency channels (left panel) and the time channels (right panel). This shows that the data is not perfectly equivalent to a Gaussian noise matrix with a constant σ . The trend in frequency is most likely due to an imperfect subtraction of RFI. In the bottom right, we show the histogram of the data vector from the pulsar catalogue and the Gaussian with the same variance and mean, which shows that the data vector is not a perfect Gaussian but a distribution with a non-zero kurtosis.

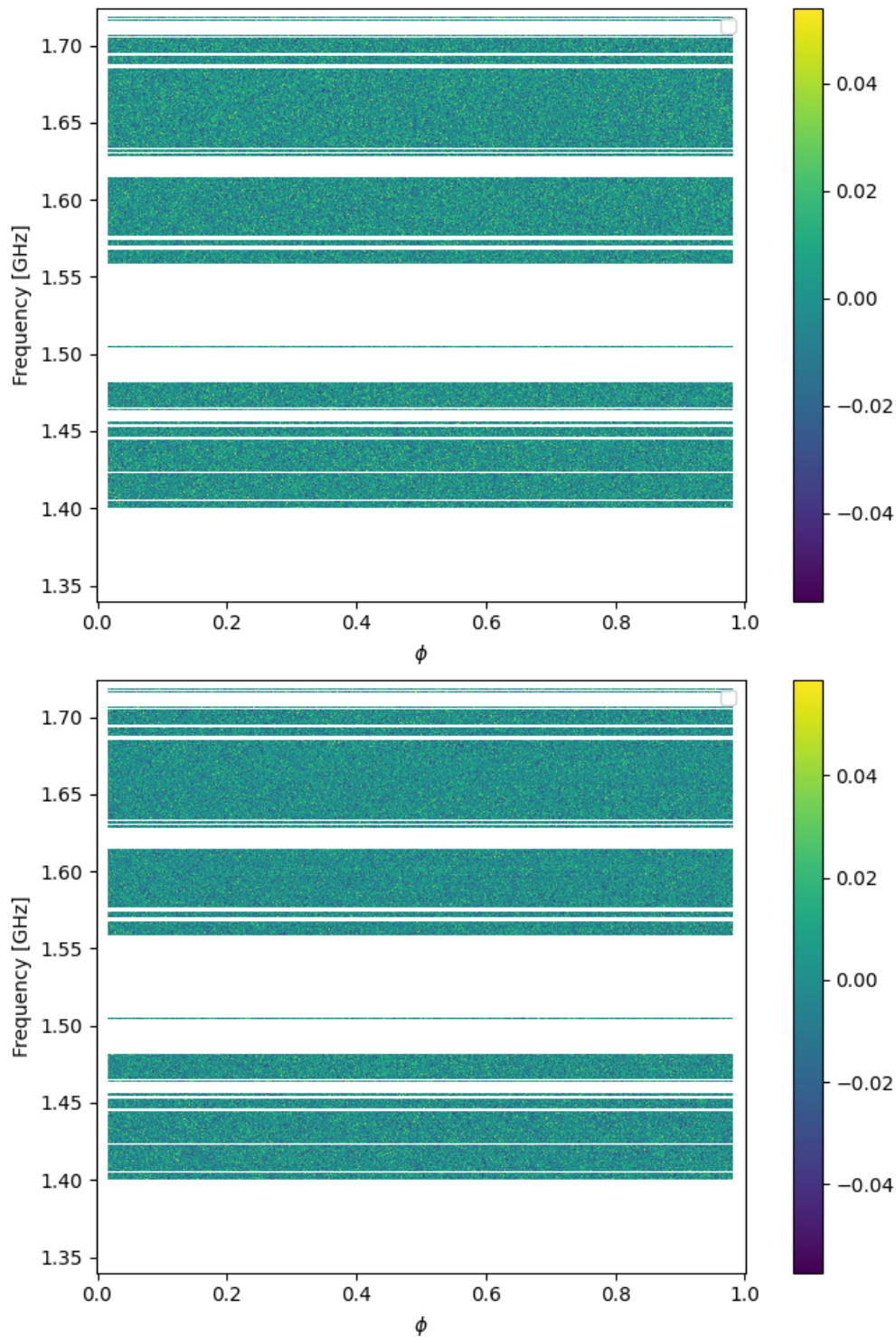


Figure 6.7: Dynamical spectra with the RFI dominated channels excised. The top panel contains our simulated noise model, while the bottom panel is the real data from the catalogue. In this case, we have employed a cut in frequency space that excised channels with $\sigma > 0.013$.

Our main goal in this analysis is to design a pipeline that can not only search the data for the signal, but also derive limits on the axion-photon coupling as a function of mass. For the former, we simply apply the filter to the data across all frequency channels that survive our standard deviation cut, with the profile templates generated by the interpolation routine described in section 6.2. Essentially, we associate each profile to a signal-to-noise q . Assuming the signal is absent, one would expect a Gaussian distribution for the q values obtained from scanning the data that is statistically compatible the distribution obtained from applying the filter to Gaussian noise with an identical variance. Any outliers to this distribution would imply that the filter favours the presence of a particular template within the data. We set a signal-to-noise threshold of $q = 4$ to identify outliers. Given that the various profile templates are obtained by the variation of three parameters (m_a, θ, α) , it is possible for the filter to fit random noise to a particular profile, leading to relatively large q values for a few profiles that are anomalous. In order to minimise the likelihood of this, we vary the σ of our noise model across frequency to match the trend shown by the data.

6.4.3 Prior on $\theta - \alpha$ plane

The constraint on the beam geometry comes from the following equation that relates the half-opening angle of the radiation beam ρ (assumed to be circular), the inclination angle of the magnetic axis α (relative to the rotation axis), the angle θ between the line of sight and the rotation axis and the pulse width W [272, 273]

$$\cos \rho = \cos \alpha \cos \theta + \sin \alpha \sin \theta \cos(W/2). \quad (6.6)$$

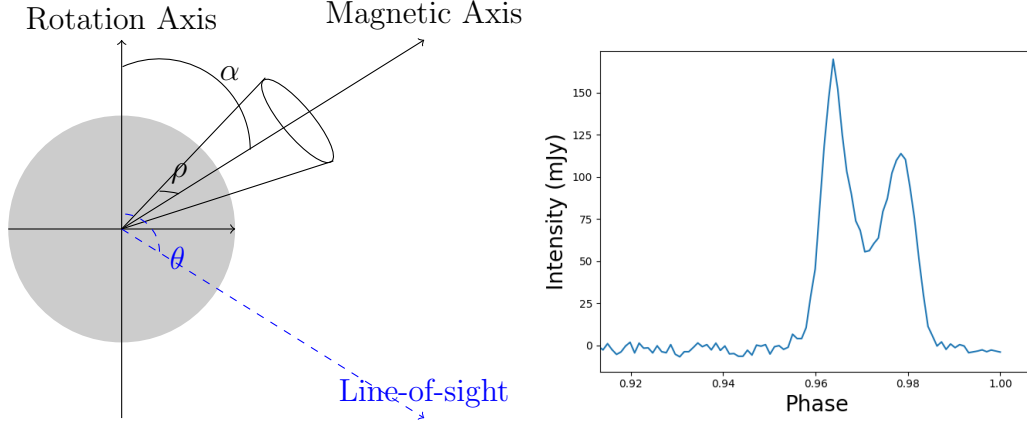


Figure 6.8: LEFT PANEL: Representation of the pulsar beam geometry. The emission height h_{em} corresponds to the distance between the centre of the pulsar and region beyond the last open field lines. Analytically, this can be approximated to be the surface cut by the last open field line at the polar cap $h_{\text{em}} = r_c \sin \theta_{\text{PC}}$ where θ_{PC} is the angular radius of the last open field line and $r_c = \frac{2\pi}{cP}$ is the radius of the light cylinder corresponding to the emitted beam [270]. Of course, this is only an approximate estimate, as the real emission mechanism is unknown. RIGHT PANEL: The intensity measurement for B0834+06 as a function of phase or the so-called pulse-profile. The measured FWHM of this profile corresponds to the value of W in eq. (6.6) [271].

There are two possible sources of uncertainty in the above expression, i.e., the pulse-width W and the pulsar beam opening angle ρ .

Here, W is the expected pulse width corresponding to a fully illuminated beam within ρ , assuming spherical geometry. See fig. 6.8 for a visual representation of the geometry. The opening angle of the beam ρ will depend on the pulsar considered. One can estimate the ρ for a given pulsar by calculating the height h_{em} at which the emission occurs, assuming that the emission region co-rotates with the pulsar with respect to the observer. In this case, the beam is bounded by the tangents to the last open magnetic field lines assuming a dipole field

configuration. Then, the following relation will hold [274]

$$\rho = \theta_{\text{PC}} + \arctan\left(\frac{1}{2} \tan \theta_{\text{PC}}\right), \quad (6.7)$$

$$\rho \simeq \frac{3}{2} \sqrt{\frac{h_{\text{em}}}{R_c}} = \sqrt{\frac{9\pi h_{\text{em}}}{2cP}}. \quad (6.8)$$

where we used the small angle approximation for θ_{PC} . Here the light cylinder radius R_c is used, which depends on the pulse period P . The measured FWHM of the profile gives $W = 7.19 \pm 0.06$ deg (more info about fit procedure can be found in [275]). one possible issue is that profiles are often asymmetric. So assuming that the full open field line region is active is not necessarily true and hence the W in the equation above should be taken as the pulse width that would be observed if the full beam is active. In rare cases, the middle of the open field line region is centred at one of the profile peaks, and part of the otherwise maybe triple profile is missing. However, pulse profiles for B0834+06 obtained at different frequencies show that there is no evidence for a missing component. As a result, we fix the value of W to be equal to the measured value.

We now turn to the uncertainty in the estimation of ρ , which mainly stems from lack of knowledge on the value of h_{em} . Estimations of the emission height depend on simulations of the pulse-beam in which the period of the pulsar and the filling fraction of the beam among other model parameters, and has been constrained to be in the range of 200 to 400 km irrespective of pulse period [276] at 1.4 GHz. However, not only does this range contradict historical data [277] that indicates that pulsars with lower periods are associated with emission heights of several thousand metres, but is also associated to uncertainties involving the methodology used to measure the pulse width. In fig. 6.9, we show the constraint on the $\theta - \alpha$ plane for a range $100 \text{ km} \leq h_{\text{em}} \leq 3500 \text{ km}$, which translates to

$4^\circ \leq \rho \leq 31^\circ$. The allowed range in W and ρ therefore defines a range of values in $\alpha - \theta$ space. We also show the scaling of the signal-to-noise returned by the matched filter for different values of (α, θ) representative of the variation in the phase-profile of the signal. In the following sections, we impose the constraint $\alpha > 20^\circ$, which corresponds to $h_{\text{em}} = 3200 \text{ km}$. While this might appear to be on the edge of the range we considered in fig. 6.9, we stress that our approach is best suited to search for a signal that might otherwise be buried in the data and would require years of slowly scanning across frequencies in laboratory-based experiments. In any case, such a value is has been associated to pulsars with $P < 1 \text{ s}$ [277].

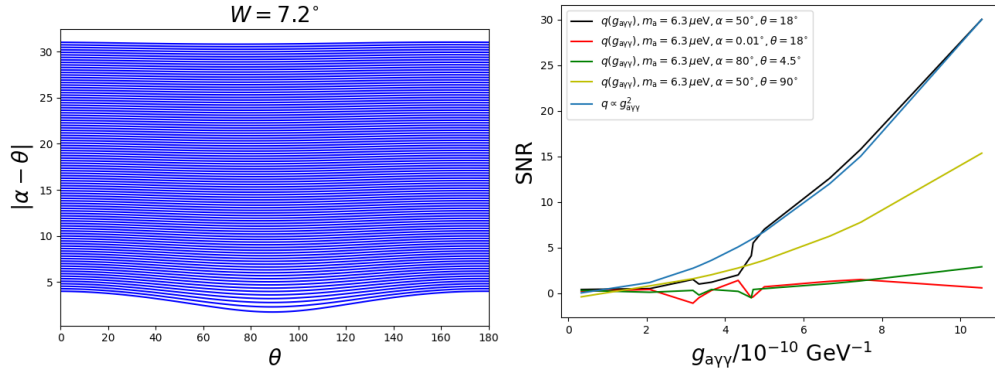


Figure 6.9: LEFT : The constraint on the $\alpha - \theta$ plane for $W = 7.2^\circ$ and $3.5^\circ \leq \rho \leq 11^\circ$. RIGHT: Signal-to-noise ratio as a function $g_{a\gamma\gamma}$ for different input parameters. The SNR value returned by the filter when applied to real data with various signals injected. Clearly, one can see that that in cases where the average subtraction has a significant effect on the filter response, in cases where the scaling is essentially flat, oscillating about zero. In cases where the time variability is significant, the SNR scales as $g_{a\gamma\gamma}^2$ until some cut-off value, below which the the curve flattens off and eventually oscillates about zero, indicating that the noise dominates at this amplitude. This turnover also shows that the limit one sets is insensitive to the value q_{ref} , so long as one is close to the turnover region.

6.4.4 Searching for the signal

We now discuss the results from applying the matched filter to the real data with the RFI dominated frequency channels excised as mentioned before. We apply the matched filter to the data vector from the pulsar catalogue against the profiles generated by the interpolation routine (see section 6.2). We then repeat the same procedure with the Gaussian noise model where we match the variance in each frequency channel to the corresponding value in the pulsar data. We plot a histogram of the resulting distribution of q (SNR) values in fig. 6.10. In the absence of the signal, we would expect the two distributions to be statistically equivalent to each other, while in the presence of an axion signal, one would expect to see an outlier in the histogram associated to the pulsar data, which would not be present in the one associated to the noise model. In fig. 6.10, we show that the histogram of the SNR obtained by applying the matched filter to pure Gaussian noise is statistically consistent with the the distribution obtained from applying it to the data. We see a slight excess in the number of profiles associated to the SNR range $5 \leq q \leq 6$ in the blue histogram (associated to the real data). We associate this slight excess to two main factors, the first being that one is varying two nuisance parameters (θ, α) to obtain the profiles. Secondly, our noise model, while accurate enough to produce statistically compatible results with the real data, is not a perfect reproduction of the data. The input $g_{a\gamma\gamma}$ value for the profiles was set to be $10^{-10} \text{ GeV}^{-1}$, which sets the overall amplitude of the profiles and therefore the expected q one would measure for the profiles if they are present in the data.

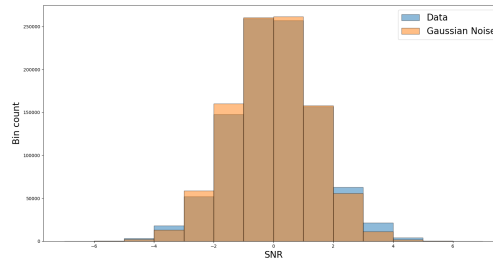


Figure 6.10: SNR histogram with the cut employed on both the Gaussian noise model as well as the pulsar catalogue data. For our noise model, we vary the standard deviation in each frequency channel to be the same as in the data vector. The resulting distributions of the SNR are statistically equivalent to each other. The matched filter calculates bin $5 \leq q \leq 6$ for more profiles in the data compared to the noise model. We associate this slight mismatch to the fact that our noise model is not a perfect reproduction of the noise (see fig. 6.6).

6.5 Establishing an upper limit

We employ a $2\text{-}\sigma$ SNR cut in order to calculate an upper limit on the axion coupling. We know that the signal scales with $g_{a\gamma\gamma}$ as $S \propto g_{a\gamma\gamma}^2$. One can see the various regimes of scaling of the filter response with $g_{a\gamma\gamma}$ in fig. 6.9. From this fact, we obtain

$$g_{a\gamma\gamma}^{\text{limit}} = g_{a\gamma\gamma}^{\text{fiducial}} \left(\frac{q_{\text{ref}}}{q} \right)^{1/2}, \quad (6.9)$$

where we set $g_{a\gamma\gamma}^{\text{fiducial}} = 10^{-9} \text{ GeV}^{-1}$ and $q_{\text{ref}} = 4$. By injecting the signal into the data and measuring the signal-to-noise returned by the matched filter, one can use (6.9) to obtain an upper limit on the axion-photon coupling. In fig. 6.11, we show the upper limit on $g_{a\gamma\gamma}$ obtained from non-detection of the profiles in the data at a frequency corresponding to $m_a = 6.3 \mu\text{eV}$ in the top right panel as a function of (θ, α) . In the top left panel, we show the difference between the maximum and minimum radiated power for each profile as a function of input (θ, α) . Note that the profiles associated to a large value of $\Delta \frac{dP}{d\Omega}$ lead to a smaller limit on $g_{a\gamma\gamma}$. In other words, the simplest metric that measures the amplitude of the time variation for each profile informs the limit that one obtains from the data. This is further shown in fig. 6.12, where we identify profiles corresponding to different regions in the colourmap of $g_{a\gamma\gamma}^{\text{lim}}$, where the limit is strong (blue), the limit is moderate (green) and finally, where the limit is either extremely weak or doesn't exist (yellow) due to the flatness of the profiles. Clearly, one can see that the blue profiles, that lead to the best limits display maximal time variation, followed by the green profiles, and finally, the yellow profiles are essentially flat.

In the bottom panel of fig. 6.11, we show $g_{a\gamma\gamma}^{\text{limit}}$ along the diagonal in the plot above, where $\alpha = \theta$. Note that there are two regions in which the limit scales differently as a function of α . As indicated in section 6.2, the flatness of the

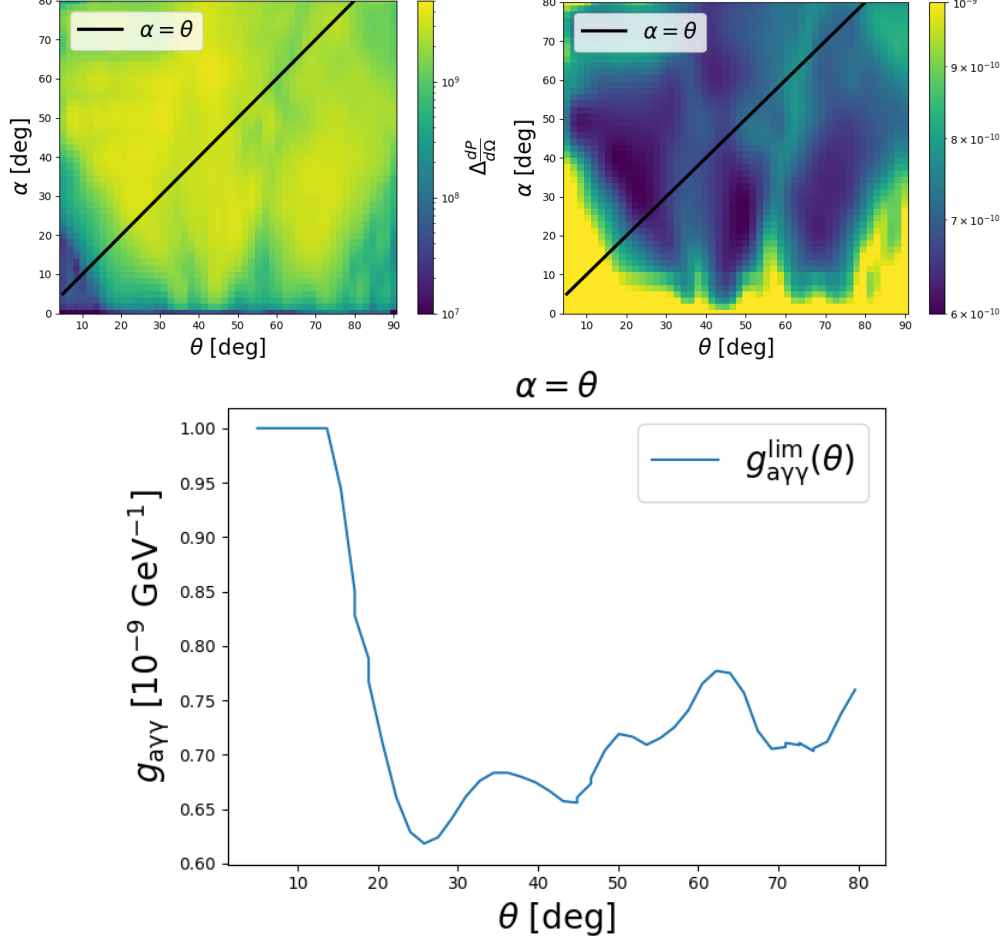


Figure 6.11: LEFT: We show the difference between the maximum and the minimum of the average subtracted profiles, which should correlate with the q values returned by the filter which in turn correlates with the limit on $g_{a\gamma\gamma}$. Note that the bright spots correspond to geometric configurations that lead to the ‘throat’ regions of the charge distribution (where the emission is large) to be beamed towards the observer over significant portions of the pulse period. RIGHT: The corresponding upper limit on $g_{a\gamma\gamma}$ from the non-detection of any profiles at the level $2\text{-}\sigma$ in the data. Note that this corresponds to $q = 4$, due to the fact that we are varying (θ, α) to obtain our profile shapes. This is for $m_a = 6.3 \mu\text{eV}$. BOTTOM: We show the limit on the axion coupling along the line $\alpha = \theta$. Note that the variation in the limit is from varying values of θ , i.e., sampling different trajectories in the magnetosphere leading to variation in time-dependence and hence the inferred limit.

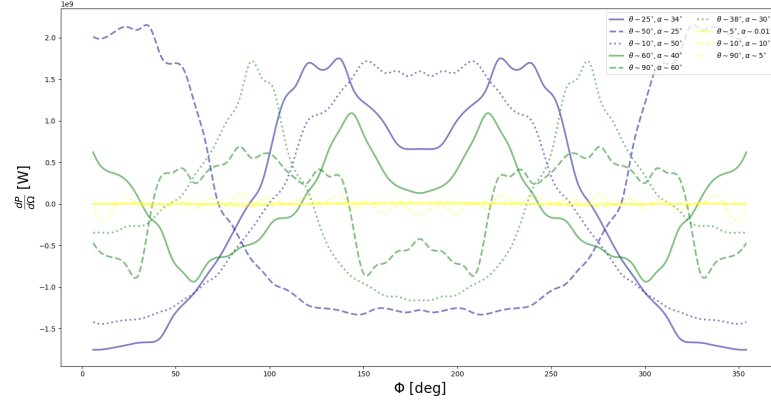


Figure 6.12: Sample of the profiles from the interpolation routine at various values of (θ, α) chosen such that one has a subset that is representative of the variation in shape as a function of these parameters.

profiles at low values of α means that the constraint on the coupling rapidly increases as $\alpha \rightarrow 0$. Using the arguments presented in section 6.4.3, we exclude values of $\alpha < 20^\circ$. Therefore, the limit is then obtained from the supremum of the set of all coupling values associated with the remaining values of α .

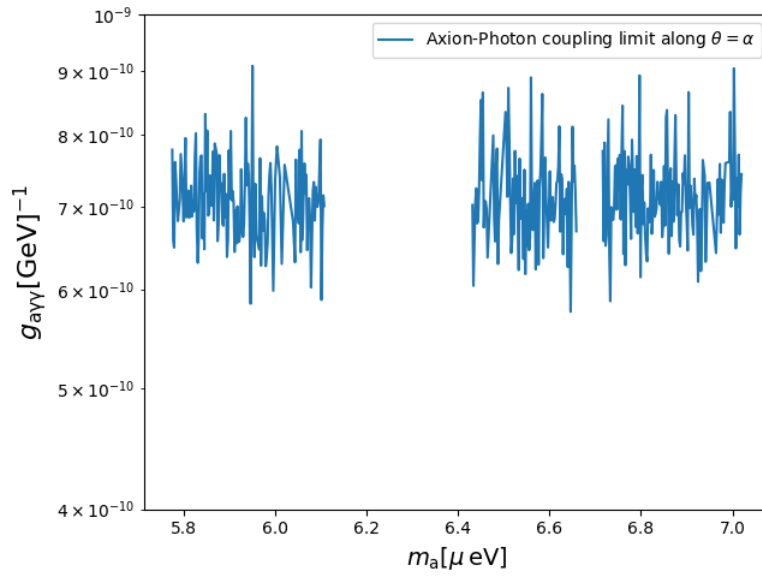


Figure 6.13: The upper limit on $g_{a\gamma\gamma}$ at the 95% confidence level on the frequency channels that survive the cut-off.

6.6 Summary and conclusion

The resonant conversion of axions to photons in neutron star magnetospheres is an active area of research, particularly due to the fact that it is complimentary to direct detection experiments such as the ADMX experiment. This is because one is able to scan across a large mass range relatively quickly in comparison to laboratory experiments. Therefore, while the road to a positive detection contains many challenges, not least of which is that it is very difficult to obtain enough sensitivity to rule out the benchmark QCD model axions (KSVZ and DFSZ), such a detection if made could easily be verified by laboratory experiments, potentially accelerating the experiment.

In this work, we have presented a matched filter technique to analyse radio pulsar data to search for the resonant axion-photon signal. Recent theoretical developments in the field have led to a clearer understanding of the shape of the signal as a function of time/pulsar phase. The crucial point is that one can take advantage of the knowledge of the signal profile when searching for it, optimising the filter to look for specific profile shapes. We began by summarising our numerical ray-tracing procedure and results (see [\[254\]](#)). We designed an interpolating routine that can generate signal profiles for different values of the input parameters (m_a, θ, α) . Our results indicated that the time-dependence in the profiles generated by our ray-tracing procedure had varying amplitudes of time variation as a function of the angles (θ, α) . This is especially important since most observational pulsar radio data has the average baseline flux subtracted. Therefore, a profile that contains little to no time-dependence would be subtracted away by this procedure.

In order to understand how this would impact our results, we computed the power

spectra of a subset of our profiles that were representative of the various levels of time variation in all the profiles. We noted that the amplitude of the power spectra associated to profiles with significant time variation fell relatively sharply as a function wavenumber, which implies that the first few modes contain most of the useful information on the profile shapes. In contrast, the power spectra of the flat profile was several orders of magnitude lower than the other spectra. This was confirmed by computing the inverse FFT of the profiles with the modes associated to large wavenumbers suppressed. We showed that including modes up $n = 3$ is sufficient to recover the shape of the profiles modulo small scale structure, so long as they contain appreciable time variation. More importantly, this gives one some intuition regarding the expected performance of the matched filter where one would expect profiles associated to a large difference between the maximum and minimum flux should be more likely to be detected by the filter, while a flat profile is practically impossible to detect.

We present our matched filter formalism in section 6.3, which we test out on simulated data. We generated flux profiles for pulsar parameters for a fiducial candidate pulsar, B0843+06 in the JBCA pulsar catalogue. This candidate was identified as a test case mainly due to its proximity to the Earth, but also due to the fact that this pulsar was associated to among the largest values of on-source integration time. We showed that when inserting the signal into a Gaussian noise vector with a variance identical to the actual radio data from the JBCA pulsar catalogue, the matched filter is able to successfully infer the values of the input parameters of the inserted signal, so long as the profile is not flat.

We then turned towards implementing our matched filter formalism on archival radio pulsar data from the JBCA catalogue. The data contains pulse-subtracted

flux-densities across 768 channels in frequency and 1024 channels in phase. The pulsar data were observed with the 76-m Lovell Telescope at Jodrell Bank Observatory at a central frequency of 1520 MHz and a nominally useable bandwidth of 400 MHz, though some portions were excised to remove radio frequency interference (RFI). We excised the frequency channels from the data in which the standard deviation exceeded the threshold $\sigma = 0.013$ Jy. The resulting data vector was almost identical to a Gaussian distribution, but still had some non-Gaussian features such as a non-zero kurtosis.

As mentioned before, the time-dependence of the signal is strongly dependent on the value of (α, θ) , more specifically becoming negligibly small in the limit $\alpha \rightarrow 0$. In sec. 6.4.3, we describe the procedure we adopted to obtain a prior on the $\alpha - \theta$ plane, which allowed us to constrain the region $\alpha < 20^\circ$ using the measured value of the pulse-width as well as the dipole geometry of the pulsar magnetic field.

To search for the signal within the data, we applied the filter formalism to the data and calculated the distribution of SNR values associated to each profile corresponding to all possible values of m_a, α, θ . We then repeated this procedure with a Gaussian noise vector, with the same number of frequency and time channels. We varied the variance in each frequency channel in the noise vector to match that measured in the corresponding frequency channel of the data vector. We obtained statistically equivalent distributions in SNR values when applying the filter to the data and when applying it to our noise model, indicating that the signal is absent.

To infer a limit on $g_{a\gamma\gamma}$ from the absence of a positive detection, we inserted the signal corresponding to each value of the input parameters into the data and calculated the SNR value that filter would measure if the signal were to be

present in the data. From the value of q , we reverse-engineer the limit on the axion-photon coupling using eq. (6.9).

Chapter 7

Conclusion

In this thesis, we discussed two different ways of tackling the open problem of the nature of dark matter and dark energy. We began by discussing modifying the law of gravity (GR) as a way of explaining the observational data without the need for a cosmological constant. Modified gravity has been parameterised on linear cosmological scales (where the density contrast is small) using cosmological perturbation theory. Cosmological surveys in the next decade will produce a multitude of data on non-linear scales. We presented a way of constraining modified gravity in a model-independent manner using data on non-linear scales.

In chapters 2 and 3, we presented the world’s first model-independent N -body simulations based on a theoretical framework for examining modified gravity in a consistent way across all cosmological scales. In these simulations, the modifications to gravity are encoded in a single parameter often dubbed the effective gravitational parameter, μ (in GR, $\mu = 1$) as specified in the post-Friedmann formalism [83]. Essentially, this parameter represents the strength of gravitational interactions. $\mu > 1$ signifies that the gravitational force is stronger than that

predicted by GR and vice-versa for $\mu < 1$. While μ can in principle be any general function of space and time, as a logical first step, we concentrate on purely time-dependent modifications to μ (see sec. 2.2 for a detailed discussion on the usefulness of making this choice as a first step). Essentially, we parametrise modified gravity by the value of μ in different time bins (see table 2.1 and fig. 2.2). This is a realisation of the model-independent approach initially put forward in [83]. We computed the matter power spectrum $P(k)$ from our simulations (see fig. 3.2), thereby quantifying the effect of modifying μ at different epochs and different duration in redshift. We found that time-dependent modifications to the strength of gravity induce scale-dependent modifications to $P(k)$. More precisely, we found that modifying μ at early times, i.e., when the smallest haloes are in the process of forming induces an excess on non-linear scales on the non-linear $P(k)$ relative to Λ CDM (when $\mu > 1$, without loss of generality. The opposite occurs when $\mu < 1$). In contrast, when μ is modified at late times, when largest haloes form via mergers of smaller haloes, we see an excess on quasi-linear scales followed by a dip in non-linear scales. We explained that this behaviour is likely due to a transfer of power due to mergers between smaller haloes that only occur at late times. We also discussed how one can compute weak-lensing observables from the measured $P(k)$ in our simulations to probe the full 2-parameter family of modified gravity (see sec. 2.5). In fig. 2.10 we show the usefulness of modelling non-linear scales in the weak-lensing convergence power spectrum with respect to the quantity of data that will be generated in those scales as well as in order to break degeneracies that exist on linear scales between modified gravity parameters.

We also presented a comparison of the various tools that exist in the literature today that attempt to predict the effects modifying gravity on the clustering

of matter on various scales, i.e., the matter power spectrum. These tools are typically dubbed ‘fitting functions’ in the literature. Designing precise, accurate and fast fitting functions is very important for the community given the huge computational expense associated to simulations. A key result was that the halo model reaction formalism (**ReACT**) [86] performed significantly better than the others. We also saw that we can achieve greater accuracy over a larger range of scales with **ReACT** relative to our simulations by modifying the concentration-mass relation (see fig. 2.7 and sec. 3.3). Looking to the future, in order to run a full Fisher forecast using our pipeline, one requires a fitting function that can predict $P(k)$ quickly and reliably over most of the relevant parameter space.

In chapter 3, we ran a suite of simulations (see table 3.2) in order to validate **ReACT**. We also varied the amplitude concentration-mass relation in order to increase the range of scales over which we achieve 1% accuracy relative to our simulations, i.e., in order to maximise k_{fail} . In Λ CDM, $c(M)$ has a weak inverse dependence on halo mass [209]. This is because at late times, the accretion of mass only occurs around the outer edges of haloes, outside the scale radius. Conversely, at early times, the mass accretion is relatively uniform. Since more massive haloes form at late times, larger haloes are associated with smaller values of concentration and vice-versa for small haloes. In fig. 3.4, we show that the amplitude of the concentration-mass relation decreases when μ is modified at late times, indicating an excess of higher-mass haloes relative to Λ CDM and vice-versa at high redshift. We develop a procedure to fit the variation of the $c(M)$ in our simulations by dividing our redshift range into two regimes. We showed that A is linear in redshift within the high redshift regime. On the other hand, the redshift dependence in the low redshift regime depends on the value of μ and the choice of the growth factor associated to the bins, which varies depending on

the size and location of the bin. In order to predict the general variation of $c(M)$ for arbitrary $\mu(z)$, we plan to run additional simulations with varying $D(z)$ for constant values of μ .

As mentioned earlier, an important immediate future direction to take is to use the machinery that we have developed in chapters 2 and 3 to run Fisher forecasts for a Euclid/LSST-like survey. While such a forecast may not be accurate to the 1% level, it will provide valuable information on the constraining power of the experiment as a function of the number of input parameters (such as the number of redshift bins for μ). Furthermore, such an analysis would provide valuable insight into the nature of the pixelised μ approach, which will inform the full time and scale dependent analysis. With improved performance of fitting functions that are built into the forecast, one can also understand the impact of incorporating additional effects such as intrinsic alignment of galaxies, baryonic feedback on the non-linear regime for the first time in the model-independent context. Such model-independent forecasts will prove to be very useful in the next decade of data-driven cosmology.

The axion is one of the well-motivated candidates for dark matter [114]. In chapters 4, 5 and 6 we explore the possibility of detecting the axion assuming that it accounts for the observed Ω_{CDM} of the Universe via its coupling to electromagnetism $g_{a\gamma\gamma}$. Due to the mass range predicted for the CDM axion, the photons produced lie in the frequency range probed by radio telescopes. There are two mechanisms by which axions can convert to photons. In chapter 4, we concentrate on the spontaneous decay of axions to photons. The characteristic decay time-scale is of the order of the age of the Universe, which makes any detection at the level $g_{a\gamma\gamma} < 10^{-10} \text{ GeV}^{-1}$ very difficult. Nevertheless, we show that one can optimise detection strategies to take advantage of the fact that the spontaneous

decay is enhanced via stimulated emission by the ambient radio emission at the galactic centre. In fig. 4.7, we show that one could go beyond the constraints from the CAST telescope using a 100 m dish such as the Green Bank Telescope.

A lot of recent work has studied the resonant conversion of axions to photons in neutron star (NS) magnetospheres [145, 147, 153, 256–259]. When the axion mass m_a is equal to the plasma mass of the photon ω_{pl} , the interaction term in the equations of motion dominate, representing a resonance. In chapter 5, we showed that one-dimensional probability of conversion of axions to photons is described by the canonical Landau-Zener relation irrespective of the dispersion relation of the axion. Crucially, we also showed that the signal is not merely a spectral line, but is actually Doppler broadened due to the rotation of the neutron star [258]. It has been shown that the photons thus produced are then lensed as they traverse through the magnetosphere due to both the plasma and the curved spacetime associated to the neutron star [153, 254, 256]. In fig. 6.11, we compute the constraint on the axion-photon coupling using the VLA data of the galactic centre magnetar using our ray-tracing formalism. We showed that the previous constraints which assumed straight-line trajectories most likely over-estimates the strength of the signal and predicts the incorrect profile as a function of time.

As theoretical modelling of the resonant signal improves, the challenge of searching for the signal through archival or new time-series data becomes apparent. In particular, the difficulty in resolving the features of the signal in frequency-space due to bandwidth limitations makes the time-domain analysis more attractive. Essentially, our approach involves an optimised search for the signal using a filter that is matched to the results of the ray-tracing code, i.e., the predicted flux density as a function of the pulsar phase as a template. While there is currently debate on the amplitude of the time-dependence [256] and the amplitude of the

probability of conversion [257], we remark that it would be counter-productive to not at the very least attempt perform a time-domain analysis with our knowledge of the shapes as a prior.

In chapter 6, we introduce our matched filter analysis to find resonant axion-photon signals in the time-domain using the ray-tracing simulation output. We stress that the advantage of indirect detection methods is their broadband nature, and therefore their usefulness lies in the ability to identify a signal if it does exist across a wide range in frequency. In section 6.2 we constructed a database of signals as a function of input parameters (the axion mass m_a , the viewing angle θ and the angle between the magnetic axis and the axis of rotation α) by interpolating the ray-tracing results. Thus, we have a tool that is able to predict the signal for arbitrary input parameters. We quantified the time-dependence in our profiles as a function of (α, θ) and showed the largest modes in frequency space (see fig. 6.3) are sufficient to reproduce the main features of the profiles relevant for the matched filter. This gives us valuable intuition on how one can expect the response of the matched filter to vary in the (α, θ) plane. We used B0834+06 as a candidate pulsar to test our formalism for which real data was obtained from the JBCA pulsar catalogue in section 6.4.1. Assuming a dipole magnetic structure and measurements of the pulse-profile, we imposed theoretical priors on the parameter space of (θ, α) (see fig. 6.9). We established a constraint $\alpha > 20^\circ$, using which we reverse-engineered an upper limit on $g_{a\gamma\gamma}$ based on the non-detection of any signals with $q > 3$. We particularly stress that this is a proof-of-principle study and therefore, the importance of the results in the landscape of the literature needs to be judged according to the potential strength of the technique rather than the constraints derived in this particular instance.

We have shown that it is possible to mine radio pulsar data for the resonant

axion-photon signal and have described a pipeline that one could implement to carry out this task. As mentioned earlier, it has been pointed out [256] that the time-dependence in the signal could be much larger than our current estimates. This would have a strong bearing on the eventual limit that we are able to set on $g_{a\gamma\gamma}$, since our methodology is more powerful for strongly time-dependent signal profiles. This represents exciting future prospects in the what could be achieved from data taken using telescopes like the MeerKat array that are capable of achieving relatively low noise temperatures.

Bibliography

- [1] Planck Collaboration, N. Aghanim, Y. Akrami, M. Ashdown, J. Aumont, C. Baccigalupi, M. Ballardini, A. J. Banday, R. B. Barreiro, N. Bartolo, S. Basak, R. Battye, K. Benabed, J. P. Bernard, M. Bersanelli, P. Bielewicz, J. J. Bock, J. R. Bond, J. Borrill, F. R. Bouchet, F. Boulanger, M. Bucher, C. Burigana, R. C. Butler, E. Calabrese, J. F. Cardoso, J. Carron, A. Challinor, H. C. Chiang, J. Chluba, L. P. L. Colombo, C. Combet, D. Contreras, B. P. Crill, F. Cuttaia, P. de Bernardis, G. de Zotti, J. Delabrouille, J. M. Delouis, E. Di Valentino, J. M. Diego, O. Doré, M. Douspis, A. Ducout, X. Dupac, S. Dusini, G. Efstathiou, F. Elsner, T. A. Enßlin, H. K. Eriksen, Y. Fantaye, M. Farhang, J. Fergusson, R. Fernandez-Cobos, F. Finelli, F. Forastieri, M. Frailis, A. A. Fraisse, E. Franceschi, A. Frolov, S. Galeotta, S. Galli, K. Ganga, R. T. Génova-Santos, M. Gerbino, T. Ghosh, J. González-Nuevo, K. M. Górski, S. Gratton, A. Gruppuso, J. E. Gudmundsson, J. Hamann, W. Handley, F. K. Hansen, D. Herranz, S. R. Hildebrandt, E. Hivon, Z. Huang, A. H. Jaffe, W. C. Jones, A. Karakci, E. Keihänen, R. Keskitalo, K. Kiiveri, J. Kim, T. S. Kisner, L. Knox, N. Krachmalnicoff, M. Kunz, H. Kurki-Suonio, G. Lagache, J. M. Lamarre,

- A. Lasenby, M. Lattanzi, C. R. Lawrence, M. Le Jeune, P. Lemos, J. Lesgourgues, F. Levrier, A. Lewis, M. Liguori, P. B. Lilje, M. Lilley, V. Lindholm, M. López-Caniego, P. M. Lubin, Y. Z. Ma, J. F. Macías-Pérez, G. Maggio, D. Maino, N. Mandolesi, A. Mangilli, A. Marcos-Caballero, M. Maris, P. G. Martin, M. Martinelli, E. Martínez-González, S. Matarrese, N. Mauri, J. D. McEwen, P. R. Meinhold, A. Melchiorri, A. Mennella, M. Migliaccio, M. Millea, S. Mitra, M. A. Miville-Deschênes, D. Molinari, L. Montier, G. Morgante, A. Moss, P. Natoli, H. U. Nørgaard-Nielsen, L. Pagano, D. Paoletti, B. Partridge, G. Patanchon, H. V. Peiris, F. Perrotta, V. Pettorino, F. Piacentini, L. Polastri, G. Polenta, J. L. Puget, J. P. Rachen, M. Reinecke, M. Remazeilles, A. Renzi, G. Rocha, C. Rosset, G. Roudier, J. A. Rubiño-Martín, B. Ruiz-Granados, L. Salvati, M. Sandri, M. Savelainen, D. Scott, E. P. S. Shellard, C. Sirignano, G. Sirri, L. D. Spencer, R. Sunyaev, A. S. Suur-Uski, J. A. Tauber, D. Tavagnacco, M. Tenti, L. Toffolatti, M. Tomasi, T. Trombetti, L. Valenziano, J. Valiviita, B. Van Tent, L. Vibert, P. Vielva, F. Villa, N. Vittorio, B. D. Wandelt, I. K. Wehus, M. White, S. D. M. White, A. Zacchei, and A. Zonca. Planck 2018 results. VI. Cosmological parameters. *Astronomy and Astrophysics*, 641:A6, September 2020.
- [2] Santiago Casas, Martin Kunz, Matteo Martinelli, and Valeria Pettorino. Linear and non-linear Modified Gravity forecasts with future surveys. *Physics of the Dark Universe*, 18:73–104, December 2017.
- [3] A. Einstein. Die Grundlage der allgemeinen Relativitätstheorie. *Annalen der Physik*, 354(7):769–822, January 1916.
- [4] A. Friedmann. Über die Krümmung des Raumes. *Zeitschrift für Physik*, 10:377–386, 1922.

- [5] G. Lemaître. Un Univers homogène de masse constante et de rayon croissant rendant compte de la vitesse radiale des nébuleuses extra-galactiques. *Annales de la Société Scientifique de Bruxelles*, 47:49–59, 1927.
- [6] H. P. Robertson. Dynamical space-times which contain a conformal Euclidean 3-space. *Transactions of the American Mathematical Society*, Vol. 29, pp. 481–496, 29:481–496, 1927.
- [7] A. G. Walker. On Milne’s Theory of World-Structure. *Proceedings of the London Mathematical Society, (Series 2) volume 42, p. 90–127*, 42:90–127, 1937.
- [8] A. G. Riess, A. V. Filippenko, P. Challis, A. Clocchiatti, A. Diercks, P. M. Garnavich, R. L. Gilliland, C. J. Hogan, S. Jha, R. P. Kirshner, B. Leibundgut, M. M. Phillips, D. Reiss, B. P. Schmidt, R. A. Schommer, R. C. Smith, J. Spyromilio, C. Stubbs, N. B. Suntzeff, and J. Tonry. Observational Evidence from Supernovae for an Accelerating Universe and a Cosmological Constant. *The Astronomical Journal*, 116:1009–1038, September 1998.
- [9] Steven Weinberg. The cosmological constant problem. *Rev. Mod. Phys.*, 61:1–23, Jan 1989.
- [10] T. M. C. Abbott, M. Agüena, A. Alarcon, S. Allam, O. Alves, A. Amon, F. Andrade-Oliveira, J. Annis, S. Avila, D. Bacon, E. Baxter, K. Bechtol, M. R. Becker, G. M. Bernstein, S. Bhargava, S. Birrer, J. Blazek, A. Brandao-Souza, S. L. Bridle, D. Brooks, E. Buckley-Geer, D. L. Burke, H. Camacho, A. Campos, A. Carnero Rosell, M. Carrasco Kind, J. Carretero, F. J. Castander, R. Cawthon, C. Chang, A. Chen, R. Chen, A. Choi, C. Conselice, J. Cordero, M. Costanzi, M. Crocce, L. N. da Costa, M. E.

da Silva Pereira, C. Davis, T. M. Davis, J. De Vicente, J. DeRose, S. Desai, E. Di Valentino, H. T. Diehl, J. P. Dietrich, S. Dodelson, P. Doel, C. Doux, A. Drlica-Wagner, K. Eckert, T. F. Eifler, F. Elsner, J. Elvin-Poole, S. Everett, A. E. Evrard, X. Fang, A. Farahi, E. Fernandez, I. Ferrero, A. Ferté, P. Fosalba, O. Friedrich, J. Frieman, J. García-Bellido, M. Gatti, E. Gaztanaga, D. W. Gerdes, T. Giannantonio, G. Giannini, D. Gruen, R. A. Gruendl, J. Gschwend, G. Gutierrez, I. Harrison, W. G. Hartley, K. Herner, S. R. Hinton, D. L. Hollowood, K. Honscheid, B. Hoyle, E. M. Huff, D. Huterer, B. Jain, D. J. James, M. Jarvis, N. Jeffrey, T. Jeltema, A. Kovacs, E. Krause, R. Kron, K. Kuehn, N. Kuropatkin, O. Lahav, P. F. Leget, P. Lemos, A. R. Liddle, C. Lidman, M. Lima, H. Lin, N. McCrann, M. A. G. Maia, J. L. Marshall, P. Martini, J. McCullough, P. Melchior, J. Mena-Fernández, F. Menanteau, R. Miquel, J. J. Mohr, R. Morgan, J. Muir, J. Myles, S. Nadathur, A. Navarro-Alsina, R. C. Nichol, R. L. C. Ogando, Y. Omori, A. Palmese, S. Pandey, Y. Park, F. Paz-Chinchón, D. Petravick, A. Pieres, A. A. Plazas Malagón, A. Porredon, J. Prat, M. Raveri, M. Rodriguez-Monroy, R. P. Rollins, A. K. Romer, A. Roodman, R. Rosenfeld, A. J. Ross, E. S. Rykoff, S. Samuroff, C. Sánchez, E. Sanchez, J. Sanchez, D. Sanchez Cid, V. Scarpine, M. Schubnell, D. Scolnic, L. F. Secco, S. Serrano, I. Sevilla-Noarbe, E. Sheldon, T. Shin, M. Smith, M. Soares-Santos, E. Suchyta, M. E. C. Swanson, M. Tabbutt, G. Tarle, D. Thomas, C. To, A. Troja, M. A. Troxel, D. L. Tucker, I. Tutusaus, T. N. Varga, A. R. Walker, N. Weaverdyck, R. Wechsler, J. Weller, B. Yanny, B. Yin, Y. Zhang, J. Zuntz, and DES Collaboration. Dark Energy Survey Year 3 results: Cosmological constraints from galaxy clustering and weak lensing. *Phys. Rev. D*, 105(2):023520, January 2022.

- [11] Beth A. Reid, Will J. Percival, Daniel J. Eisenstein, Licia Verde, David N. Spergel, Ramin A. Skibba, Neta A. Bahcall, Tamas Budavari, Joshua A. Frieman, Masataka Fukugita, J. Richard Gott, James E. Gunn, Zeljko Ivezic, Gillian R. Knapp, Richard G. Kron, Robert H. Lupton, Timothy A. McKay, Avery Meiksin, Robert C. Nichol, Adrian C. Pope, David J. Schlegel, Donald P. Schneider, Chris Stoughton, Michael A. Strauss, Alexander S. Szalay, Max Tegmark, Michael S. Vogeley, David H. Weinberg, Donald G. York, and Idit Zehavi. Cosmological constraints from the clustering of the Sloan Digital Sky Survey DR7 luminous red galaxies. *Monthly Notices of the Royal Astronomical Society*, 404(1):60–85, 04 2010.
- [12] Alvise Raccanelli, Daniele Bertacca, Davide Pietrobon, Fabian Schmidt, Lado Samushia, Nicola Bartolo, Olivier Doré, Sabino Matarrese, and Will J. Percival. Testing gravity using large-scale redshift-space distortions. *Monthly Notices of the Royal Astronomical Society*, 436(1):89–100, 09 2013.
- [13] Volker Springel, Simon D. M. White, Adrian Jenkins, Carlos S. Frenk, Naoki Yoshida, Liang Gao, Julio Navarro, Robert Thacker, Darren Croton, John Helly, John A. Peacock, Shaun Cole, Peter Thomas, Hugh Couchman, August Evrard, Jörg Colberg, and Frazer Pearce. Simulations of the formation, evolution and clustering of galaxies and quasars. *Nature*, 435(7042):629–636, June 2005.
- [14] Planck Collaboration XIII., P. A. R. Ade, N. Aghanim, M. Arnaud, M. Ashdown, J. Aumont, C. Baccigalupi, A. J. Banday, R. B. Barreiro, J. G. Bartlett, and et al. Planck 2015 results. XIII. Cosmological parameters. *Astronomy and Astrophysics*, 594:A13, September 2016.

- [15] David Tytler, John M. O’Meara, Nao Suzuki, and Dan Lubin. Review of Big Bang Nucleosynthesis and Primordial Abundances. *Physica Scripta Volume T*, 85:12, January 2000.
- [16] S. Weinberg. *Cosmology*. Oxford University Press, 2008.
- [17] Timothy Clifton, Pedro G. Ferreira, Antonio Padilla, and Constantinos Skordis. Modified gravity and cosmology. *Physics Reports*, 513:1–189, March 2012.
- [18] J. L. Feng. Dark Matter Candidates from Particle Physics and Methods of Detection. *Annual Review of Astronomy and Astrophysics*, 48:495–545, September 2010.
- [19] Julien Billard, Mark Boulay, Susana Cebrián, Laura Covi, Giuliana Fiorillo, Anne Green, Joachim Kopp, Béla Majorovits, Kimberly Palladino, Federica Petricca, Leszek Roszkowski, and Marc Schumann. Direct Detection of Dark Matter – APPEC Committee Report. *arXiv e-prints*, page arXiv:2104.07634, April 2021.
- [20] Dmitry S. Gorbunov and V. A. Rubakov. *Introduction to the theory of the early universe*. 2011.
- [21] Alan H. Guth. Inflationary universe: A possible solution to the horizon and flatness problems. *Phys. Rev. D*, 23(2):347–356, January 1981.
- [22] Katsuhiko Sato. Cosmological baryon-number domain structure and the first order phase transition of a vacuum. *Physics Letters B*, 99(1):66–70, February 1981.
- [23] A. A. Starobinsky. A new type of isotropic cosmological models without singularity. *Physics Letters B*, 91(1):99–102, March 1980.

- [24] A. Albrecht and P. J. Steinhardt. Cosmology for Grand Unified Theories with Radiatively Induced Symmetry Breaking. *Phys. Rev. Letters*, 48(17):1220–1223, April 1982.
- [25] A. D. Linde. Chaotic inflation. *Physics Letters B*, 129(3-4):177–181, September 1983.
- [26] Enrico Pajer and Marco Peloso. A review of axion inflation in the era of planck. *Classical and Quantum Gravity*, 30(21):214002, oct 2013.
- [27] Eleonora Di Valentino, Olga Mena, Supriya Pan, Luca Visinelli, Weiqiang Yang, Alessandro Melchiorri, David F Mota, Adam G Riess, and Joseph Silk. In the realm of the hubble tension—a review of solutions. *Classical and Quantum Gravity*, 38(15):153001, Jul 2021.
- [28] Adam G. Riess, Stefano Casertano, Wenlong Yuan, J. Bradley Bowers, Lucas Macri, Joel C. Zinn, and Dan Scolnic. Cosmic distances calibrated to 1and hubble space telescope photometry of 75 milky way cepheids confirm tension with Λ cdm. *The Astrophysical Journal Letters*, 908(1):L6, Feb 2021.
- [29] Laura Salvati, Marian Douspis, and Nabila Aghanim. Constraints from thermal Sunyaev-Zel’dovich cluster counts and power spectrum combined with CMB. *Astronomy and Astrophysics*, 614:A13, June 2018.
- [30] The LIGO Scientific Collaboration, the Virgo Collaboration, B. P. Abbott, R. Abbott, T. D. Abbott, S. Abraham, F. Acernese, K. Ackley, C. Adams, R. X. Adhikari, and et al. GWTC-1: A Gravitational-Wave Transient Catalog of Compact Binary Mergers Observed by LIGO and Virgo during the First and Second Observing Runs. *arXiv e-prints*, November 2018.
- [31] G. F. Smoot. Cosmic Microwave Background Anisotropy Large Angular

- Scales / COBE DMR Results. In N. Sanchez and A. Zichichi, editors, *NATO Advanced Science Institutes (ASI) Series C*, volume 467 of *NATO Advanced Science Institutes (ASI) Series C*, pages 301–311, 1995.
- [32] D. J. Fixsen, E. S. Cheng, D. A. Cottingham, R. E. Eplee, Jr., R. B. Isaacman, J. C. Mather, S. S. Meyer, P. D. Noerdlinger, R. A. Shafer, R. Weiss, E. L. Wright, C. L. Bennett, N. W. Boggess, T. Kelsall, S. H. Moseley, R. F. Silverberg, G. F. Smoot, and D. T. Wilkinson. Cosmic microwave background dipole spectrum measured by the COBE FIRAS instrument. *The Astrophysical Journal*, 420:445–449, January 1994.
- [33] D. N. Spergel, L. Verde, H. V. Peiris, E. Komatsu, M. R. Nolta, C. L. Bennett, M. Halpern, G. Hinshaw, N. Jarosik, A. Kogut, M. Limon, S. S. Meyer, L. Page, G. S. Tucker, J. L. Weiland, E. Wollack, and E. L. Wright. First-Year Wilkinson Microwave Anisotropy Probe (WMAP) Observations: Determination of Cosmological Parameters. *Astrophysical Journal Supplements*, 148:175–194, September 2003.
- [34] D. N. Spergel, R. Bean, O. Doré, M. R. Nolta, C. L. Bennett, J. Dunkley, G. Hinshaw, N. Jarosik, E. Komatsu, L. Page, H. V. Peiris, L. Verde, M. Halpern, R. S. Hill, A. Kogut, M. Limon, S. S. Meyer, N. Odegard, G. S. Tucker, J. L. Weiland, E. Wollack, and E. L. Wright. Three-Year Wilkinson Microwave Anisotropy Probe (WMAP) Observations: Implications for Cosmology. *Astrophysical Journal Supplements*, 170:377–408, June 2007.
- [35] S. Perlmutter, G. Aldering, G. Goldhaber, R. A. Knop, P. Nugent, P. G. Castro, S. Deustua, S. Fabbro, A. Goobar, D. E. Groom, I. M. Hook, A. G. Kim, M. Y. Kim, J. C. Lee, N. J. Nunes, R. Pain, C. R. Pennyacker, R. Quimby, C. Lidman, R. S. Ellis, M. Irwin, R. G. McMahon,

- P. Ruiz-Lapuente, N. Walton, B. Schaefer, B. J. Boyle, A. V. Filippenko, T. Matheson, A. S. Fruchter, N. Panagia, H. J. M. Newberg, W. J. Couch, and T. S. C. Project. Measurements of Ω and Λ from 42 High-Redshift Supernovae. *The Astrophysical Journal*, 517:565–586, June 1999.
- [36] C. W. Misner, K. S. Thorne, and J. A. Wheeler. *Gravitation*. 2017.
- [37] Enis Belgacem, Yves Dirian, Stefano Foffa, and Michele Maggiore. Non-local gravity. conceptual aspects and cosmological predictions. *Journal of Cosmology and Astroparticle Physics*, 2018(03):002–002, mar 2018.
- [38] Peter G. Bergmann. Comments on the scalar-tensor theory. *International Journal of Theoretical Physics*, 1(1):25–36, May 1968.
- [39] Jr. Nordtvedt, Kenneth. Post-Newtonian Metric for a General Class of Scalar-Tensor Gravitational Theories and Observational Consequences. *The Astrophysical Journal*, 161:1059, September 1970.
- [40] Robert V. Wagoner. Scalar-Tensor Theory and Gravitational Waves. *Phys. Rev. D*, 1(12):3209–3216, June 1970.
- [41] Clifford M. Will and Jr. Nordtvedt, Kenneth. Conservation Laws and Preferred Frames in Relativistic Gravity. I. Preferred-Frame Theories and an Extended PPN Formalism. *The Astrophysical Journal*, 177:757, November 1972.
- [42] Jr. Nordtvedt, Kenneth and Clifford M. Will. Conservation Laws and Preferred Frames in Relativistic Gravity. II. Experimental Evidence to Rule Out Preferred-Frame Theories of Gravity. *The Astrophysical Journal*, 177:775, November 1972.

- [43] Richard A. Battye, Francesco Pace, and Damien Trinh. Cosmological perturbation theory in generalized Einstein-Aether models. *Phys. Rev. D*, 96:064041, September 2017.
- [44] C. Brans and R. H. Dicke. Mach’s Principle and a Relativistic Theory of Gravitation. *Physical Review*, 124:925–935, November 1961.
- [45] Gregory Walter Horndeski. Second-Order Scalar-Tensor Field Equations in a Four-Dimensional Space. *International Journal of Theoretical Physics*, 10:363–384, September 1974.
- [46] Peter G. Bergmann. Comments on the scalar-tensor theory. *International Journal of Theoretical Physics*, 1:25–36, May 1968.
- [47] A. A. Starobinsky. A new type of isotropic cosmological models without singularity. *Physics Letters B*, 91:99–102, March 1980.
- [48] T. V. Ruzmaïkina and A. A. Ruzmaïkin. Quadratic Corrections to the Lagrangian Density of the Gravitational Field and the Singularity. *Soviet Journal of Experimental and Theoretical Physics*, 30:372, January 1969.
- [49] Yasunori Fujii. Origin of the gravitational constant and particle masses in a scale-invariant scalar-tensor theory. *Phys. Rev. D*, 26:2580–2588, November 1982.
- [50] L. H. Ford. Cosmological-constant damping by unstable scalar fields. *Phys. Rev. D*, 35:2339–2344, April 1987.
- [51] Bharat Ratra and P. J. E. Peebles. Cosmological consequences of a rolling homogeneous scalar field. *Phys. Rev. D*, 37:3406–3427, June 1988.
- [52] C. Wetterich. Cosmology and the fate of dilatation symmetry. *Nuclear Physics B*, 302:668–696, June 1988.

- [53] Takeshi Chiba, Naoshi Sugiyama, and Takashi Nakamura. Cosmology with x-matter. *Monthly Notices of the Royal Astronomical Society*, 289:L5–L9, August 1997.
- [54] Takeshi Chiba, Naoshi Sugiyama, and Takashi Nakamura. Observational tests of x-matter models. *Monthly Notices of the Royal Astronomical Society*, 301:72–80, November 1998.
- [55] Pedro G. Ferreira and Michael Joyce. Structure Formation with a Self-Tuning Scalar Field. *Phys. Rev. Letters*, 79:4740–4743, December 1997.
- [56] Pedro G. Ferreira and Michael Joyce. Cosmology with a primordial scaling field. *Phys. Rev. D*, 58:023503, July 1998.
- [57] Iyaylo Zlatev, Limin Wang, and Paul J. Steinhardt. Quintessence, Cosmic Coincidence, and the Cosmological Constant. *Phys. Rev. Letters*, 82:896–899, February 1999.
- [58] R. R. Caldwell, Rahul Dave, and Paul J. Steinhardt. Cosmological Imprint of an Energy Component with General Equation of State. *Phys. Rev. Letters*, 80:1582–1585, February 1998.
- [59] C. Armendáriz-Picón, T. Damour, and V. Mukhanov. k-Inflation. *Physics Letters B*, 458:209–218, July 1999.
- [60] Takeshi Chiba, Takahiro Okabe, and Masahide Yamaguchi. Kinetically driven quintessence. *Phys. Rev. D*, 62:023511, July 2000.
- [61] C. Armendariz-Picon, V. Mukhanov, and Paul J. Steinhardt. Dynamical Solution to the Problem of a Small Cosmological Constant and Late-Time Cosmic Acceleration. *Phys. Rev. Letters*, 85:4438–4441, November 2000.

- [62] C. Armendariz-Picon, V. Mukhanov, and Paul J. Steinhardt. Essentials of k-essence. *Phys. Rev. D*, 63:103510, May 2001.
- [63] Ryotaro Kase and Shinji Tsujikawa. Dark energy in Horndeski theories after GW170817: A review. *arXiv e-prints*, page arXiv:1809.08735, September 2018.
- [64] A. I. Vainshtein. To the problem of nonvanishing gravitation mass. *Physics Letters B*, 39(3):393–394, May 1972.
- [65] Sean M. Carroll and Eugene A. Lim. Lorentz-violating vector fields slow the universe down. *Phys. Rev. D*, 70:123525, December 2004.
- [66] Eugene A. Lim. *Can we see Lorentz-violating vector fields in the CMB?* PhD thesis, THE UNIVERSITY OF CHICAGO, December 2004.
- [67] Chung-Pei Ma and Edmund Bertschinger. Cosmological perturbation theory in the synchronous and conformal newtonian gauges. *The Astrophysical Journal*, 455:7, dec 1995.
- [68] Richard A. Battye and Jonathan A. Pearson. Effective action approach to cosmological perturbations in dark energy and modified gravity. *Journal of Cosmology and Astro-Particle Physics*, 2012:019, July 2012.
- [69] Richard A. Battye and Jonathan A. Pearson. Parametrizing dark sector perturbations via equations of state. *Phys. Rev. D*, 88:061301, September 2013.
- [70] Richard A. Battye and Jonathan A. Pearson. Computing model independent perturbations in dark energy and modified gravity. *Journal of Cosmology and Astro-Particle Physics*, 2014:051, March 2014.

- [71] Richard A. Battye, Boris Bolliet, and Francesco Pace. Do cosmological data rule out $f(R)$ with $w \neq -1$? *Phys. Rev. D*, 97:104070, May 2018.
- [72] Richard A. Battye, Boris Bolliet, and Jonathan A. Pearson. $f(R)$ gravity as a dark energy fluid. *Phys. Rev. D*, 93:044026, February 2016.
- [73] Francesco Pace, Richard A. Battye, Boris Bolliet, and Damien Trinh. Dark sector evolution in Horndeski models. *Journal of Cosmology and Astroparticle Physics*, 2019(9):018, September 2019.
- [74] Giulia Gubitosi, Federico Piazza, and Filippo Vernizzi. The effective field theory of dark energy. *Journal of Cosmology and Astro-Particle Physics*, 2013:032, February 2013.
- [75] Jérôme Gleyzes, David Langlois, and Filippo Vernizzi. A unifying description of dark energy. *International Journal of Modern Physics D*, 23:1443010, January 2014.
- [76] Clifford M. Will. *Theory and Experiment in Gravitational Physics*. 1993.
- [77] S. S. Shapiro, J. L. Davis, D. E. Lebach, and J. S. Gregory. Measurement of the Solar Gravitational Deflection of Radio Waves using Geodetic Very-Long-Baseline Interferometry Data, 1979–1999. *Phys. Rev. Letters*, 92:121101, March 2004.
- [78] B. Bertotti, L. Iess, and P. Tortora. A test of general relativity using radio links with the Cassini spacecraft. *Nature*, 425:374–376, September 2003.
- [79] Levon Pogosian, Alessandra Silvestri, Kazuya Koyama, and Gong-Bo Zhao. How to optimally parametrize deviations from general relativity in the evolution of cosmological perturbations. *Phys. Rev. D*, 81:104023, May 2010.
- [80] Irene Milillo, Daniele Bertacca, Marco Bruni, and Andrea Maselli. Missing

- link: A nonlinear post-Friedmann framework for small and large scales. *Phys. Rev. D*, 92:023519, July 2015.
- [81] Timothy Clifton, Christopher S. Gallagher, Sophia Goldberg, and Karim A. Malik. Viable gauge choices in cosmologies with nonlinear structures. *Phys. Rev. D*, 101(6):063530, March 2020.
- [82] Daniel B. Thomas, Marco Bruni, and David Wands. The fully non-linear post-Friedmann frame-dragging vector potential: magnitude and time evolution from N-body simulations. *Monthly Notices of the Royal Astronomical Society*, 452:1727–1742, September 2015.
- [83] Daniel B. Thomas. Cosmological gravity on all scales: Simple equations, required conditions, and a framework for modified gravity. *Physical Review D*, 101(12), Jun 2020.
- [84] Hans A. Winther, Fabian Schmidt, Alexandre Barreira, Christian Arnold, Sownak Bose, Claudio Llinares, Marco Baldi, Bridget Falck, Wojciech A. Hellwing, Kazuya Koyama, Baojiu Li, David F. Mota, Ewald Puchwein, Robert E. Smith, and Gong-Bo Zhao. Modified gravity n-body code comparison project. *Monthly Notices of the Royal Astronomical Society*, 454(4):4208–4234, Oct 2015.
- [85] Tessa Baker, Alexandre Barreira, Harry Desmond, Pedro Ferreira, Bhuvnesh Jain, Kazuya Koyama, Baojiu Li, Lucas Lombriser, Andrina Nicola, Jeremy Sakstein, and Fabian Schmidt. Novel probes project: Tests of gravity on astrophysical scales. *Reviews of Modern Physics*, 93(1), Feb 2021.
- [86] Benjamin Bose, Matteo Cataneo, Tilman Tröster, Qianli Xia, Catherine Heymans, and Lucas Lombriser. On the road to percent accuracy IV: REACT – computing the non-linear power spectrum beyond Λ CDM. *arXiv*

e-prints, page arXiv:2005.12184, May 2020.

- [87] M. Cataneo, L. Lombriser, C. Heymans, A. J. Mead, A. Barreira, S. Bose, and B. Li. On the road to percent accuracy: non-linear reaction of the matter power spectrum to dark energy and modified gravity. *Monthly Notices of the Royal Astronomical Society*, 488(2):2121–2142, September 2019.
- [88] R. E. Smith, J. A. Peacock, A. Jenkins, S. D. M. White, C. S. Frenk, F. R. Pearce, P. A. Thomas, G. Efstathiou, and H. M. P. Couchman. Stable clustering, the halo model and non-linear cosmological power spectra. *Monthly Notices of the Royal Astronomical Society*, 341(4):1311–1332, 06 2003.
- [89] Ryuichi Takahashi, Masanori Sato, Takahiro Nishimichi, Atsushi Taruya, and Masamune Oguri. REVISING THE HALOFIT MODEL FOR THE NONLINEAR MATTER POWER SPECTRUM. *The Astrophysical Journal*, 761(2):152, dec 2012.
- [90] Simeon Bird, Matteo Viel, and Martin G. Haehnelt. Massive neutrinos and the non-linear matter power spectrum. *Monthly Notices of the Royal Astronomical Society*, 420(3):2551–2561, 02 2012.
- [91] C. Abel, N. J. Ayres, G. Ban, G. Bison, K. Bodek, V. Bondar, M. Daum, M. Fairbairn, V. V. Flambaum, P. Geltenbort, K. Green, W. C. Griffith, M. van der Grinten, Z. D. Grujić, P. G. Harris, N. Hild, P. Iaydjiev, S. N. Ivanov, M. Kasprzak, Y. Kermaidic, K. Kirch, H.-C. Koch, S. Komposch, P. A. Koss, A. Kozela, J. Krempel, B. Lauss, T. Lefort, Y. Lemièrre, D. J. E. Marsh, P. Mohanmurthy, A. Mtchedlishvili, M. Musgrave, F. M. Piegsa, G. Pignol, M. Rawlik, D. Rebreyend, D. Ries, S. Roccia, D. Rozpędzik, P. Schmidt-Wellenburg, N. Severijns, D. Shiers, Y. V. Stadnik, A. Weis, E. Wursten, J. Zejma, and G. Zsigmond. Search for axion-like dark matter

- through nuclear spin precession in electric and magnetic fields. *ArXiv e-prints*, August 2017.
- [92] J. H. Christenson, J. W. Cronin, V. L. Fitch, and R. Turlay. Evidence for the 2π decay of the K_2^0 meson. *Phys. Rev. Lett.*, 13:138–140, Jul 1964.
- [93] R. D. Peccei and H. R. Quinn. Constraints imposed by CP conservation in the presence of pseudoparticles. *Phys. Rev. D*, 16:1791–1797, September 1977.
- [94] S. Weinberg. A new light boson? *Physical Review Letters*, 40:223–226, January 1978.
- [95] F. Wilczek. Problem of strong P and T invariance in the presence of instantons. *Physical Review Letters*, 40:279–282, January 1978.
- [96] J. E. Kim. Weak-interaction singlet and strong CP invariance. *Physical Review Letters*, 43:103–107, July 1979.
- [97] M. A. Shifman, A. I. Vainshtein, and V. I. Zakharov. Can confinement ensure natural CP invariance of strong interactions? *Nuclear Physics B*, 166:493–506, April 1980.
- [98] M. Dine, W. Fischler, and M. Srednicki. A simple solution to the strong CP problem with a harmless axion. *Physics Letters B*, 104:199–202, August 1981.
- [99] A. R. Zhitnitsky. On Possible Suppression of the Axion Hadron Interactions. (In Russian). *Sov. J. Nucl. Phys.*, 31:260, 1980. [*Yad. Fiz.*31,497(1980)].
- [100] John Preskill, Mark B. Wise, and Frank Wilczek. Cosmology of the invisible axion. *Physics Letters B*, 120(1):127–132, 1983.

- [101] L.F. Abbott and P. Sikivie. A cosmological bound on the invisible axion. *Physics Letters B*, 120(1):133–136, 1983.
- [102] Michael Dine and Willy Fischler. The not-so-harmless axion. *Physics Letters B*, 120(1):137–141, 1983.
- [103] Michael S. Turner. Coherent scalar-field oscillations in an expanding universe. *Phys. Rev. D*, 28:1243–1247, Sep 1983.
- [104] Michael S. Turner. Cosmic and local mass density of “invisible” axions. *Phys. Rev. D*, 33:889–896, Feb 1986.
- [105] Paola Arias, Davide Cadamuro, Mark Goodsell, Joerg Jaeckel, Javier Redondo, and Andreas Ringwald. Wispy cold dark matter. *Journal of Cosmology and Astroparticle Physics*, 2012(06):013, jun 2012.
- [106] T W B Kibble. Topology of cosmic domains and strings. *Journal of Physics A: Mathematical and General*, 9(8):1387, aug 1976.
- [107] T.W.B. Kibble. Some implications of a cosmological phase transition. *Physics Reports*, 67(1):183–199, 1980.
- [108] Giovanni Grilli di Cortona, Edward Hardy, Javier Pardo Vega, and Giovanni Villadoro. The QCD axion, precisely. *Journal of High Energy Physics*, 2016:34, Jan 2016.
- [109] Kyu Jung Bae, Ji-Haeng Huh, and Jihn E. Kim. Updating the axion cold dark matter energy density. *Journal of Cosmology and Astro-Particle Physics*, 2008:005, Sep 2008.
- [110] Masahiro Kawasaki and Kazunori Nakayama. Axions: Theory and Cosmological Role. *Annual Review of Nuclear and Particle Science*, 63:69–95, Oct 2013.

- [111] D. J. E. Marsh. Axion cosmology. *Physics Reports*, 643:1–79, July 2016.
- [112] Jonas Enander, Andreas Pargner, and Thomas Schwetz. Axion minicluster power spectrum and mass function. *Journal of Cosmology and Astroparticle Physics*, 2017(12):038, Dec 2017.
- [113] Mark P. Hertzberg, Max Tegmark, and Frank Wilczek. Axion cosmology and the energy scale of inflation. *Physical Review D*, 78(8), oct 2008.
- [114] O. Wantz and E. P. S. Shellard. Axion cosmology revisited. *Phys. Rev. D*, 82(12):123508, December 2010.
- [115] R. A. Battye and E. P. S. Shellard. Axion string constraints. *Physical Review Letters*, 73:2954–2957, November 1994.
- [116] R. A. Battye and E. P. S. Shellard. Axion string cosmology and its controversies. *ArXiv Astrophysics e-prints*, September 1999.
- [117] P. Sikivie. Experimental tests of the ‘invisible’ axion. *Physical Review Letters*, 51:1415–1417, October 1983.
- [118] V. Anastassopoulos, S. Aune, Barth, et al. New CAST limit on the axion-photon interaction. *Nature Physics*, 13:584–590, June 2017.
- [119] C. Bartram, T. Braine, E. Burns, R. Cervantes, N. Crisosto, N. Du, H. Korranda, G. Leum, P. Mohapatra, T. Nitta, L. J Rosenberg, G. Rybka, J. Yang, John Clarke, I. Siddiqi, A. Agrawal, A. V. Dixit, M. H. Awida, A. S. Chou, M. Hollister, S. Knirck, A. Sonnenschein, W. Wester, J. R. Gleason, A. T. Hipp, S. Jois, P. Sikivie, N. S. Sullivan, D. B. Tanner, E. Lentz, R. Khatiwada, G. Carosi, N. Robertson, N. Woollett, L. D. Duffy, C. Boutan, M. Jones, B. H. LaRoque, N. S. Oblath, M. S. Taubman, E. J. Daw, M. G. Perry, J. H. Buckley, C. Gaikwad, J. Hoffman, K. W. Murch,

- M. Goryachev, B. T. McAllister, A. Quiskamp, C. Thomson, and M. E. Tobar. Search for invisible axion dark matter in the $3.3 - 4.2 \mu\text{eV}$ mass range. *Phys. Rev. Lett.*, 127:261803, Dec 2021.
- [120] T. Braine, R. Cervantes, N. Crisosto, N. Du, S. Kimes, L. J. Rosenberg, G. Rybka, J. Yang, D. Bowring, A. S. Chou, R. Khatiwada, A. Sonnenschein, W. Wester, G. Carosi, N. Woollett, L. D. Duffy, R. Bradley, C. Boutan, M. Jones, B. H. LaRoque, N. S. Oblath, M. S. Taubman, J. Clarke, A. Dove, A. Eddins, S. R. O’Kelley, S. Nawaz, I. Siddiqi, N. Stevenson, A. Agrawal, A. V. Dixit, J. R. Gleason, S. Jois, P. Sikivie, J. A. Solomon, N. S. Sullivan, D. B. Tanner, E. Lentz, E. J. Daw, J. H. Buckley, P. M. Harrington, E. A. Henriksen, and K. W. Murch. Extended search for the invisible axion with the axion dark matter experiment. *Phys. Rev. Lett.*, 124:101303, Mar 2020.
- [121] C. Boutan, M. Jones, B. H. LaRoque, N. S. Oblath, R. Cervantes, N. Du, N. Force, S. Kimes, R. Ottens, L. J. Rosenberg, G. Rybka, J. Yang, G. Carosi, N. Woollett, D. Bowring, A. S. Chou, R. Khatiwada, A. Sonnenschein, W. Wester, R. Bradley, E. J. Daw, A. Agrawal, A. V. Dixit, J. Clarke, S. R. O’Kelley, N. Crisosto, J. R. Gleason, S. Jois, P. Sikivie, I. Stern, N. S. Sullivan, D. B. Tanner, P. M. Harrington, and E. Lentz. Piezoelectrically tuned multimode cavity search for axion dark matter. *Phys. Rev. Lett.*, 121:261302, Dec 2018.
- [122] N. Du, N. Force, R. Khatiwada, E. Lentz, R. Ottens, L. J. Rosenberg, G. Rybka, G. Carosi, N. Woollett, D. Bowring, A. S. Chou, A. Sonnenschein, W. Wester, C. Boutan, N. S. Oblath, R. Bradley, E. J. Daw, A. V. Dixit, J. Clarke, S. R. O’Kelley, N. Crisosto, J. R. Gleason, S. Jois, P. Sikivie, I. Stern, N. S. Sullivan, D. B. Tanner, and G. C. Hilton. Search for invisible

- axion dark matter with the axion dark matter experiment. *Phys. Rev. Lett.*, 120:151301, Apr 2018.
- [123] B.M. Brubaker, L. Zhong, S.K. Lamoreaux, K.W. Lehnert, and K.A. van Bibber. Haystac axion search analysis procedure. *Physical Review D*, 96(12), Dec 2017.
- [124] L. Zhong, S. Al Kenany, K.M. Backes, B.M. Brubaker, S.B. Cahn, G. Carosi, Y.V. Gurevich, W.F. Kindel, S.K. Lamoreaux, K.W. Lehnert, S.M. Lewis, M. Malnou, R.H. Maruyama, D.A. Palken, N.M. Rapidis, J.R. Root, M. Simanovskaia, T.M. Shokair, D.H. Speller, I. Urdinaran, and K.A. van Bibber. Results from phase 1 of the haystac microwave cavity axion experiment. *Physical Review D*, 97(9), May 2018.
- [125] K. M. Backes, D. A. Palken, S. Al Kenany, B. M. Brubaker, S. B. Cahn, A. Droster, Gene C. Hilton, Sumita Ghosh, H. Jackson, S. K. Lamoreaux, A. F. Leder, K. W. Lehnert, S. M. Lewis, M. Malnou, R. H. Maruyama, N. M. Rapidis, M. Simanovskaia, Sukhman Singh, D. H. Speller, I. Urdinaran, Leila R. Vale, E. C. van Assendelft, K. van Bibber, and H. Wang. A quantum enhanced search for dark matter axions. *Nature*, 590(7845):238–242, Feb 2021.
- [126] Alexander J. Millar, Javier Redondo, and Frank D. Steffen. Dielectric haloscopes: sensitivity to the axion dark matter velocity. *Journal of Cosmology and Astroparticle Physics*, 2017(10):006, October 2017.
- [127] Allen Caldwell, Gia Dvali, Béla Majorovits, Alexander Millar, Georg Raffelt, Javier Redondo, Olaf Reimann, Frank Simon, and Frank Steffen. Dielectric haloscopes: A new way to detect axion dark matter. *Phys. Rev. Lett.*, 118:091801, Mar 2017.

- [128] S. Lee, S. Ahn, J. Choi, B. R. Ko, and Y.K. Semertzidis. Axion dark matter search around $6.7 \mu\text{ev}$. *Physical Review Letters*, 124(10), mar 2020.
- [129] Junu Jeong, SungWoo Youn, Sungjae Bae, Jihungeun Kim, Taehyeon Seong, Jihn E. Kim, and Yannis K. Semertzidis. Search for invisible axion dark matter with a multiple-cell haloscope. *Physical Review Letters*, 125(22), nov 2020.
- [130] Ohjoon Kwon, Doyu Lee, Woohyun Chung, Danho Ahn, HeeSu Byun, Fritz Caspers, Hyoungsoon Choi, Jihoon Choi, Yonuk Chong, Hoyong Jeong, Junu Jeong, Jihn E. Kim, Jinsu Kim, Çağlar Kutlu, Jihnhwan Lee, MyeongJae Lee, Soohyung Lee, Andrei Matlashov, Seonjeong Oh, Seongtae Park, Sergey Uchaikin, SungWoo Youn, and Yannis K. Semertzidis. First results from an axion haloscope at CAPP. *Physical Review Letters*, 126(19), may 2021.
- [131] Jinsu Kim, Ohjoon Kwon, Çağlar Kutlu, Woohyun Chung, Andrei Matlashov, Sergey Uchaikin, Arjan Ferdinand van Loo, Yasunobu Nakamura, Seonjeong Oh, HeeSu Byun, Danho Ahn, and Yannis K. Semertzidis. Near-quantum-noise axion dark matter search at capp around 9.5 ev, 2022.
- [132] S. DePanfilis, A. C. Melissinos, B. E. Moskowitz, J. T. Rogers, Y. K. Semertzidis, W. U. Wuensch, H. J. Halama, A. G. Prodell, W. B. Fowler, and F. A. Nezrick. Limits on the abundance and coupling of cosmic axions at 4.5μ and $5\mu\text{ev}$. *Phys. Rev. Lett.*, 59:839–842, Aug 1987.
- [133] C. Hagmann, P. Sikivie, N. S. Sullivan, and D. B. Tanner. Results from a search for cosmic axions. *Phys. Rev. D*, 42:1297–1300, Aug 1990.
- [134] Ben T. McAllister, Graeme Flower, Eugene N. Ivanov, Maxim Goryachev, Jeremy Bourhill, and Michael E. Tobar. The ORGAN experiment: An

- axion haloscope above 15 GHz. *Physics of the Dark Universe*, 18:67–72, dec 2017.
- [135] Aaron Quiskamp, Ben T. McAllister, Paul Altin, Eugene N. Ivanov, Maxim Goryachev, and Michael E. Tobar. Direct search for dark matter axions excluding ALPogenesis in the 63- to 67- μeV range with the ORGAN experiment. *Science Advances*, 8(27), jul 2022.
- [136] G. G. Raffelt. *Stars as laboratories for fundamental physics: The astrophysics of neutrinos, axions, and other weakly interacting particles*. 5 1996.
- [137] Francesca V. Day and Jamie I. McDonald. Axion superradiance in rotating neutron stars. *JCAP*, 10:051, 2019.
- [138] Ciaran A. J. O’Hare, Andrea Caputo, Alexander J. Millar, and Edoardo Vitagliano. Axion helioscopes as solar magnetometers. *Phys. Rev. D*, 102(4):043019, 2020.
- [139] B. Garbrecht and J. I. McDonald. Axion configurations around pulsars. *JCAP*, 07:044, 2018.
- [140] Anirudh Prabhu and Nicholas M. Rapidis. Resonant Conversion of Dark Matter Oscillons in Pulsar Magnetospheres. *JCAP*, 10:054, 2020.
- [141] Thomas D. P. Edwards, Bradley J. Kavanagh, Luca Visinelli, and Christoph Weniger. Transient Radio Signatures from Neutron Star Encounters with QCD Axion Miniclusters. *Phys. Rev. Letters*, 127(13):131103, September 2021.
- [142] Jean-François Fortin, Huai-Ke Guo, Steven P. Harris, Elijah Sheridan, and Kuver Sinha. Magnetars and axion-like particles: probes with the hard X-ray spectrum. *Journal of Cosmology and Astroparticle Physics*, 2021(6):036,

June 2021.

- [143] Tanmay Kumar Poddar and Subhendra Mohanty. Probing the angle of birefringence due to long range axion hair from pulsars. *Phys. Rev. D*, 102(8):083029, 2020.
- [144] Steven P. Harris, Jean-Francois Fortin, Kuver Sinha, and Mark G. Alford. Axions in neutron star mergers. *JCAP*, 07:023, 2020.
- [145] M. S. Pshirkov and S. B. Popov. Conversion of Dark matter axions to photons in magnetospheres of neutron stars. *J. Exp. Theor. Phys.*, 108:384–388, 2009.
- [146] D. Lai and J. Heyl. Probing axions with radiation from magnetic stars. *Phys. Rev. D*, 74(12):123003, December 2006.
- [147] Anson Hook, Yonatan Kahn, Benjamin R. Safdi, and Zhiqun Sun. Radio Signals from Axion Dark Matter Conversion in Neutron Star Magnetospheres. *Phys. Rev. Letters*, 121(24):241102, Dec 2018.
- [148] Fa Peng Huang, Kenji Kadota, Toyokazu Sekiguchi, and Hiroyuki Tashiro. Radio telescope search for the resonant conversion of cold dark matter axions from the magnetized astrophysical sources. *Phys. Rev. D*, 97(12):123001, Jun 2018.
- [149] Daniel A. Camargo, Farinaldo S. Queiroz, and Riccardo Sturani. Detecting dark matter with neutron star spectroscopy. *Journal of Cosmology and Astroparticle Physics*, 2019(9):051, Sep 2019.
- [150] Benjamin R. Safdi, Zhiqun Sun, and Alexander Y. Chen. Detecting Axion Dark Matter with Radio Lines from Neutron Star Populations. *Phys. Rev.*, D99(12):123021, 2019.

- [151] Thomas D. P. Edwards, Marco Chianese, Bradley J. Kavanagh, Samaya M. Nissanke, and Christoph Weniger. Unique Multimessenger Signal of QCD Axion Dark Matter. *Phys. Rev. Lett.*, 124(16):161101, 2020.
- [152] R.A. Battye, B. Garbrecht, J.I. McDonald, F. Pace, and S. Srinivasan. Dark matter axion detection in the radio/mm waveband. *Physical Review D*, 102(2), Jul 2020.
- [153] Mikaël Leroy, Marco Chianese, Thomas D. P. Edwards, and Christoph Weniger. Radio Signal of Axion-Photon Conversion in Neutron Stars: A Ray Tracing Analysis. *Phys. Rev. D*, 101(12):123003, 2020.
- [154] A. G. Riess, L.-G. Strolger, S. Casertano, H. C. Ferguson, B. Mobasher, B. Gold, P. J. Challis, and et al. New Hubble Space Telescope Discoveries of Type Ia Supernovae at $z \geq 1$: Narrowing Constraints on the Early Behavior of Dark Energy. *The Astrophysical Journal*, 659:98–121, April 2007.
- [155] Planck Collaboration VIII. Planck 2018 results. VIII. Gravitational lensing. *ArXiv e-prints*, July 2018.
- [156] DES Collaboration. Dark Energy Survey year 1 results: Cosmological constraints from galaxy clustering and weak lensing. *Phys. Rev. D*, 98(4):043526, August 2018.
- [157] D. Gruen, O. Friedrich, E. Krause, J. DeRose, R. Cawthon, C. Davis, J. Elvin-Poole, E. S. Rykoff, R. H. Wechsler, and et al. Density split statistics: Cosmological constraints from counts and lensing in cells in DES Y1 and SDSS data. *Phys. Rev. D*, 98(2):023507, July 2018.
- [158] Lucas Lombriser. A parametrisation of modified gravity on nonlinear

- cosmological scales. *Journal of Cosmology and Astro-Particle Physics*, 2016:039, November 2016.
- [159] Timothy Clifton and Viraj A. A. Sanghai. Parametrizing theories of gravity on large and small scales in cosmology. *Phys. Rev. Lett.*, 122:011301, Jan 2019.
- [160] H. A. Buchdahl. Non-Linear Lagrangians and Cosmological Theory. *Monthly Notices of the Royal Astronomical Society*, 150(1):1–8, 09 1970.
- [161] Gia Dvali, Gregory Gabadadze, and Massimo Porrati. 4d gravity on a brane in 5d minkowski space. *Physics Letters B*, 485(1):208 – 214, 2000.
- [162] Hans A. Winther, Fabian Schmidt, Alexandre Barreira, Christian Arnold, Sownak Bose, Claudio Llinares, Marco Baldi, Bridget Falck, Wojciech A. Hellwing, Kazuya Koyama, Baojiu Li, David F. Mota, Ewald Puchwein, Robert E. Smith, and Gong-Bo Zhao. Modified gravity N-body code comparison project. *Monthly Notices of the Royal Astronomical Society*, 454(4):4208–4234, December 2015.
- [163] Hans A. Winther, Kazuya Koyama, Marc Manera, Bill S. Wright, and Gong-Bo Zhao. COLA with scale-dependent growth: applications to screened modified gravity models. *Journal of Cosmology and Astroparticle Physics*, 2017(8):006, August 2017.
- [164] Marco Bruni, Daniel B. Thomas, and David Wands. Computing general-relativistic effects from Newtonian N-body simulations: Frame dragging in the post-Friedmann approach. *Phys. Rev. D*, 89(4):044010, February 2014.
- [165] Julian Adamek, David Daverio, Ruth Durrer, and Martin Kunz. gevolution: a cosmological N-body code based on General Relativity. *Journal of*

Cosmology and Astroparticle Physics, 2016(7):053, July 2016.

- [166] Gong-Bo Zhao, Tommaso Giannantonio, Levon Pogosian, Alessandra Silvestri, David J. Bacon, Kazuya Koyama, Robert C. Nichol, and Yong-Seon Song. Probing modifications of general relativity using current cosmological observations. *Phys. Rev. D*, 81(10):103510, May 2010.
- [167] G. Zhao, D. Bacon, R. Maartens, M. Santos, and A. Raccanelli. Model-independent constraints on dark energy and modified gravity with the SKA. In *Advancing Astrophysics with the Square Kilometre Array (AASKA14)*, page 165, April 2015.
- [168] Alireza Hojjati, Gong-Bo Zhao, Levon Pogosian, Alessandra Silvestri, Robert Crittenden, and Kazuya Koyama. Cosmological tests of general relativity: A principal component analysis. *Phys. Rev. D*, 85(4):043508, February 2012.
- [169] Michael Kopp, Constantinos Skordis, Daniel B. Thomas, and Stéphanie Ilić. Dark Matter Equation of State through Cosmic History. *Phys. Rev. Letters*, 120(22):221102, June 2018.
- [170] D.B. Thomas, M. Bruni, K. Koyama, B. Li, and G.-B. Zhao. $f(r)$ gravity on non-linear scales: the post-friedmann expansion and the vector potential. *Journal of Cosmology and Astroparticle Physics*, 2015(07):051–051, Jul 2015.
- [171] Farbod Hassani and Lucas Lombriser. N -body simulations for parametrised modified gravity. *arXiv e-prints*, page arXiv:2003.05927, March 2020.
- [172] Cristhian Garcia-Quintero, Mustapha Ishak, and Orion Ning. Current constraints on deviations from General Relativity using binning in redshift and

- scale. *arXiv e-prints*, page arXiv:2010.12519, October 2020.
- [173] Michael Kopp, Constantinos Skordis, Daniel B Thomas, and Stéphane Ilić. Dark matter equation of state through cosmic history. *Physical Review Letters*, 120(22), Jun 2018.
- [174] Weiguang Cui, Pengjie Zhang, and Xiaohu Yang. Nonlinearities in modified gravity cosmology: Signatures of modified gravity in the nonlinear matter power spectrum. *Phys. Rev. D*, 81(10):103528, May 2010.
- [175] Youcai Zhang, Pengjie Zhang, Xiaohu Yang, and Weiguang Cui. Nonlinearities in modified gravity cosmology. II. Impacts of modified gravity on the halo properties. *Phys. Rev. D*, 87(2):023521, January 2013.
- [176] Hans F. Stabenau and Bhuvnesh Jain. n -body simulations of alternative gravity models. *Phys. Rev. D*, 74:084007, Oct 2006.
- [177] Istvan Laszlo and Rachel Bean. Nonlinear growth in modified gravity theories of dark energy. *Phys. Rev. D*, 77:024048, Jan 2008.
- [178] Daniel B. Thomas and Carlo R. Contaldi. Viability of the cluster mass function formalism in parametrised modified gravity, 2011.
- [179] Jiajun Zhang, Rui An, Shihong Liao, Wentao Luo, Zhaozhou Li, and Bin Wang. Fully self-consistent cosmological simulation pipeline for interacting dark energy models. *Phys. Rev. D*, 98(10):103530, November 2018.
- [180] Marco Baldi. Clarifying the effects of interacting dark energy on linear and non-linear structure formation processes. *Monthly Notices of the Royal Astronomical Society*, 414(1):116–128, June 2011.
- [181] Farbod Hassani, Julian Adamek, Martin Kunz, and Filippo Vernizzi. k -evolution: a relativistic N -body code for clustering dark energy. *Journal of*

- Cosmology and Astroparticle Physics*, 2019(12):011, December 2019.
- [182] Santiago Casas, Martin Kunz, Matteo Martinelli, and Valeria Pettorino. Linear and non-linear Modified Gravity forecasts with future surveys. *Physics of the Dark Universe*, 18:73–104, December 2017.
- [183] Wayne Hu and Ignacy Sawicki. Parametrized post-friedmann framework for modified gravity. *Phys. Rev. D*, 76:104043, Nov 2007.
- [184] Volker Springel. The cosmological simulation code GADGET-2. *Monthly Notices of the Royal Astronomical Society*, 364(4):1105–1134, December 2005.
- [185] Volker Springel, Simon D. M. White, Adrian Jenkins, Carlos S. Frenk, Naoki Yoshida, Liang Gao, Julio Navarro, Robert Thacker, Darren Croton, John Helly, John A. Peacock, Shaun Cole, Peter Thomas, Hugh Couchman, August Evrard, Jörg Colberg, and Frazer Pearce. Simulations of the formation, evolution and clustering of galaxies and quasars. *Nature*, 435(7042):629–636, June 2005.
- [186] Michael Boylan-Kolchin, Volker Springel, Simon D. M. White, Adrian Jenkins, and Gerard Lemson. Resolving cosmic structure formation with the Millennium-II Simulation. *Monthly Notices of the Royal Astronomical Society*, 398(3):1150–1164, September 2009.
- [187] R. E. Angulo, V. Springel, S. D. M. White, A. Jenkins, C. M. Baugh, and C. S. Frenk. Scaling relations for galaxy clusters in the Millennium-XXL simulation. *Monthly Notices of the Royal Astronomical Society*, 426(3):2046–2062, November 2012.

- [188] Daniel B. Thomas and Carlo R. Contaldi. Testing model independent modified gravity with future large scale surveys. *Journal of Cosmology and Astroparticle Physics*, 2011(12):013, December 2011.
- [189] Adrian Jenkins. Second-order Lagrangian perturbation theory initial conditions for resimulations. *Monthly Notices of the Royal Astronomical Society*, 403(4):1859–1872, 04 2010.
- [190] Martín Crocce, Sebastián Pueblas, and Román Scoccimarro. Transients from initial conditions in cosmological simulations. *Monthly Notices of the Royal Astronomical Society*, 373(1):369–381, November 2006.
- [191] Patrick McDonald, Hy Trac, and Carlo Contaldi. Dependence of the non-linear mass power spectrum on the equation of state of dark energy. *Monthly Notices of the Royal Astronomical Society*, 366(2):547–556, February 2006.
- [192] J. Lesgourgues. The Cosmic Linear Anisotropy Solving System (CLASS) I: Overview. *ArXiv e-prints*, April 2011.
- [193] Stephane Colombi and Dmitri Novikov. POWMES: Measuring the Power Spectrum in an N-body Simulation, October 2011.
- [194] Stéphane Colombi, Andrew Jaffe, Dmitri Novikov, and Christophe Pichon. Accurate estimators of power spectra in N-body simulations. *Monthly Notices of the Royal Astronomical Society*, 393(2):511–526, February 2009.
- [195] R. K. Sheth and G. Tormen. Large-scale bias and the peak background split. *Monthly Notices of the Royal Astronomical Society*, 308:119–126, September 1999.
- [196] R. K. Sheth and G. Tormen. An excursion set model of hierarchical clustering: ellipsoidal collapse and the moving barrier. *Monthly Notices of the*

- Royal Astronomical Society*, 329:61–75, January 2002.
- [197] F. Bernardeau, S. Colombi, E. Gaztañaga, and R. Scoccimarro. Large-scale structure of the Universe and cosmological perturbation theory. *Physics Reports*, 367(1-3):1–248, September 2002.
- [198] I. Smail, R. S. Ellis, and M. J. Fitchett. Gravitational lensing of distant field galaxies by rich clusters - I. Faint galaxy redshift distributions. *Monthly Notices of the Royal Astronomical Society*, 270:245–270, September 1994.
- [199] Wayne Hu. Power Spectrum Tomography with Weak Lensing. *The Astrophysical Journal Letters*, 522(1):L21–L24, September 1999.
- [200] P. G. Castro, A. F. Heavens, and T. D. Kitching. Weak lensing analysis in three dimensions. *Phys. Rev. D*, 72(2):023516, July 2005.
- [201] A. Spurio Mancini, R. Reischke, V. Pettorino, B. M. Schäfer, and M. Zumalacárregui. Testing (modified) gravity with 3D and tomographic cosmic shear. *Monthly Notices of the Royal Astronomical Society*, 480(3):3725–3738, November 2018.
- [202] Euclid Collaboration, A. Blanchard, S. Camera, C. Carbone, V. F. Cardone, S. Casas, S. Clesse, S. Ilić, M. Kilbinger, T. Kitching, M. Kunz, F. Lacasa, E. Linder, E. Majerotto, K. Markovič, M. Martinelli, V. Pettorino, A. Pourtsidou, Z. Sakr, A. G. Sánchez, D. Sapone, I. Tutusaus, S. Yahia-Cherif, V. Yankelevich, S. Andreon, H. Aussel, A. Balaguera-Antolínez, M. Baldi, S. Bardelli, R. Bender, A. Biviano, D. Bonino, A. Boucaud, E. Bozzo, E. Branchini, S. Brau-Nogue, M. Brescia, J. Brinchmann, C. Burigana, R. Cabanac, V. Capobianco, A. Cappi, J. Carretero, C. S. Carvalho, R. Casas, F. J. Castander, M. Castellano, S. Cavuoti, A. Cimatti, R. Cledassou, C. Colodro-Conde, G. Congedo, C. J. Conselice, L. Conversi,

- Y. Copin, L. Corcione, J. Coupon, H. M. Courtois, M. Cropper, A. Da Silva, S. de la Torre, D. Di Ferdinando, F. Dubath, F. Ducret, C. A. J. Duncan, X. Dupac, S. Dusini, G. Fabbian, M. Fabricius, S. Farrens, P. Fosalba, S. Fotopoulou, N. Fourmanoit, M. Frailis, E. Franceschi, P. Franzetti, M. Fumana, S. Galeotta, W. Gillard, B. Gillis, C. Giocoli, P. Gómez-Alvarez, J. Graciá-Carpio, F. Grupp, L. Guzzo, H. Hoekstra, F. Hormuth, H. Israel, K. Jahnke, E. Keihanen, S. Kermiche, C. C. Kirkpatrick, R. Kohley, B. Kubik, H. Kurki-Suonio, S. Ligori, P. B. Lilje, I. Lloro, D. Maino, E. Maiorano, O. Marggraf, N. Martinet, F. Marulli, R. Massey, E. Medinaceli, S. Mei, Y. Mellier, B. Metcalf, J. J. Metge, G. Meylan, M. Moresco, L. Moscardini, E. Munari, R. C. Nichol, S. Niemi, A. A. Nucita, C. Padilla, S. Paltani, F. Pasian, W. J. Percival, S. Pires, G. Polenta, M. Poncet, L. Pozzetti, G. D. Racca, F. Raison, A. Renzi, J. Rhodes, E. Romelli, M. Roncarelli, E. Rossetti, R. Saglia, P. Schneider, V. Scottez, A. Secroun, G. Sirri, L. Stanco, J. L. Starck, F. Sureau, P. Tallada-Crespí, D. Tavagnacco, A. N. Taylor, M. Tenti, I. Tereno, R. Toledo-Moreo, F. Torradeflot, L. Valenziano, T. Vassallo, G. A. Verdoes Kleijn, M. Viel, Y. Wang, A. Zacchei, J. Zoubian, and E. Zucca. Euclid preparation. VII. Forecast validation for Euclid cosmological probes. *Astronomy and Astrophysics*, 642:A191, October 2020.
- [203] J. Zuntz, M. Paterno, E. Jennings, D. Rudd, A. Manzotti, S. Dodelson, S. Bridle, S. Sehrish, and J. Kowalkowski. CosmoSIS: Modular cosmological parameter estimation. *Astronomy and Computing*, 12:45–59, September 2015.
- [204] T.M.C. Abbott, F.B. Abdalla, S. Avila, M. Banerji, E. Baxter, K. Bechtol, M.R. Becker, E. Bertin, J. Blazek, S.L. Bridle, and et al. Dark energy

- survey year 1 results: Constraints on extended cosmological models from galaxy clustering and weak lensing. *Physical Review D*, 99(12), Jun 2019.
- [205] J. F. Navarro, C. S. Frenk, and S. D. M. White. The Structure of Cold Dark Matter Halos. *The Astrophysical Journal*, 462:563, May 1996.
- [206] Alexander Knebe, Steffen R. Knollmann, Stuart I. Muldrew, Frazer R. Pearce, Miguel Angel Aragon-Calvo, Yago Ascasibar, Peter S. Behroozi, Daniel Ceverino, Stephane Colombi, Juerg Diemand, Klaus Dolag, Bridget L. Falck, Patricia Fasel, Jeff Gardner, Stefan Gottlöber, Chung-Hsing Hsu, Francesca Iannuzzi, Anatoly Klypin, Zarija Lukić, Michal Maciejewski, Cameron McBride, Mark C. Neyrinck, Susana Planelles, Doug Potter, Vicent Quilis, Yann Rasera, Justin I. Read, Paul M. Ricker, Fabrice Roy, Volker Springel, Joachim Stadel, Greg Stinson, P. M. Sutter, Victor Turchaninov, Dylan Tweed, Gustavo Yepes, and Marcel Zemp. Haloes gone MAD14: The Halo-Finder Comparison Project. *Monthly Notices of the Royal Astronomical Society*, 415(3):2293–2318, 08 2011.
- [207] Peter S. Behroozi, Risa H. Wechsler, and Hao-Yi Wu. THE ROCKSTAR PHASE-SPACE TEMPORAL HALO FINDER AND THE VELOCITY OFFSETS OF CLUSTER CORES. *The Astrophysical Journal*, 762(2):109, dec 2012.
- [208] Greg L. Bryan and Michael L. Norman. Statistical Properties of X-Ray Clusters: Analytic and Numerical Comparisons. *The Astrophysical Journal*, 495(1):80–99, March 1998.
- [209] Anatoly Klypin, Gustavo Yepes, Stefan Gottlöber, Francisco Prada, and Steffen Heß. MultiDark simulations: the story of dark matter halo concentrations and density profiles. *Monthly Notices of the Royal Astronomical*

- Society*, 457(4):4340–4359, 02 2016.
- [210] Igor D. Karachentsev, Elena I. Kaisina, and Olga G. Kashibadze Nasonova. The Local Tully-Fisher Relation for Dwarf Galaxies. *The Astronomical Journal*, 153(1):6, Jan 2017.
- [211] Andrea Caputo, Carlos Peña Garay, and Samuel J. Witte. Looking for axion dark matter in dwarf spheroidal galaxies. *Phys. Rev. D*, 98(8):083024, Oct 2018.
- [212] Andrea Caputo, Marco Regis, Marco Taoso, and Samuel J. Witte. Detecting the stimulated decay of axions at radio frequencies. *Journal of Cosmology and Astro-Particle Physics*, 2019:027, Mar 2019.
- [213] D. J. Fixsen, A. Kogut, S. Levin, M. Limon, P. Lubin, P. Mirel, M. Seiffert, J. Singal, E. Wollack, T. Villela, and C. A. Wuensche. ARCADE 2 Measurement of the Absolute Sky Brightness at 3-90 GHz. *The Astrophysical Journal*, 734(1):5, Jun 2011.
- [214] Nicolao Fornengo, Roberto A. Lineros, Marco Regis, and Marco Taoso. The isotropic radio background revisited. *Journal of Cosmology and Astroparticle Physics*, 2014(4):008, Apr 2014.
- [215] F. Pace, S. Meyer, and M. Bartelmann. On the implementation of the spherical collapse model for dark energy models. *Journal of Cosmology and Astroparticle Physics*, 10:040, October 2017.
- [216] Francesco Pace, Carlo Schmid, David F. Mota, and Antonino Del Popolo. Halo collapse: virialization by shear and rotation in dynamical dark-energy models. Effects on weak-lensing peaks. *Journal of Cosmology and Astroparticle Physics*, 2019(9):060, Sep 2019.

- [217] Dan Coe. Dark Matter Halo Mass Profiles. *arXiv e-prints*, page arXiv:1005.0411, May 2010.
- [218] Joshua N. Winn, David Rusin, and Christopher S. Kochanek. The central image of a gravitationally lensed quasar. *Nature*, 427(6975):613–615, Feb 2004.
- [219] K. Kelley and P. J. Quinn. A Radio Astronomy Search for Cold Dark Matter Axions. *The Astrophysical Journal Letters*, 845:L4, August 2017.
- [220] Katharine Kelley and P. J. Quinn. Searching for Axion Dark Matter using Radio Telescopes. In *Proceedings, 13th Patras Workshop on Axions, WIMPs and WISPs, (PATRAS 2017): Thessaloniki, Greece, 15 May 2017 - 19, 2017*, pages 43–46, 2018.
- [221] Philip Bull, Pedro G. Ferreira, Prina Patel, and Mario G. Santos. Late-time cosmology with 21cm intensity mapping experiments. *Astrophys. J.*, 803(1):21, 2015.
- [222] B. D. Blout, E. J. Daw, M. P. Decowski, P. T. P. Ho, L. J. Rosenberg, and D. B. Yu. A Radio Telescope Search for Axions. *The Astrophysical Journal*, 546:825–828, January 2001.
- [223] M. L. Mateo. Dwarf Galaxies of the Local Group. *Annual Review of Astronomy and Astrophysics*, 36:435–506, 1998.
- [224] Joe Wolf, Gregory D. Martinez, James S. Bullock, Manoj Kaplinghat, Marla Geha, Ricardo R. Muñoz, Joshua D. Simon, and Frank F. Avedo. Accurate masses for dispersion-supported galaxies. *Monthly Notices of the Royal Astronomical Society*, 406(2):1220–1237, Aug 2010.
- [225] Sergey E. Koposov, Vasily Belokurov, Gabriel Torrealba, and N. Wyn

- Evans. Beasts of the Southern Wild: Discovery of Nine Ultra Faint Satellites in the Vicinity of the Magellanic Clouds. *The Astrophysical Journal*, 805(2):130, Jun 2015.
- [226] J. D. Simon, A. Drlica-Wagner, T. S. Li, B. Nord, M. Geha, K. Bechtol, E. Balbinot, E. Buckley-Geer, H. Lin, J. Marshall, B. Santiago, L. Strigari, M. Wang, R. H. Wechsler, B. Yanny, T. Abbott, A. H. Bauer, G. M. Bernstein, E. Bertin, D. Brooks, D. L. Burke, D. Capozzi, A. Carnero Rosell, M. Carrasco Kind, C. B. D’Andrea, L. N. da Costa, D. L. DePoy, S. Desai, H. T. Diehl, S. Dodelson, C. E. Cunha, J. Estrada, A. E. Evrard, A. Fausti Neto, E. Fernandez, D. A. Finley, B. Flaugher, J. Frieman, E. Gaztanaga, D. Gerdes, D. Gruen, R. A. Gruendl, K. Honscheid, D. James, S. Kent, K. Kuehn, N. Kuropatkin, O. Lahav, M. A. G. Maia, M. March, P. Martini, C. J. Miller, R. Miquel, R. Ogando, A. K. Romer, A. Roodman, E. S. Rykoff, M. Sako, E. Sanchez, M. Schubnell, I. Sevilla, R. C. Smith, M. Soares-Santos, F. Sobreira, E. Suchyta, M. E. C. Swanson, G. Tarle, J. Thaler, D. Tucker, V. Vikram, A. R. Walker, W. Wester, and DES Collaboration. Stellar Kinematics and Metallicities in the Ultrafaint Dwarf Galaxy Reticulum II. *The Astrophysical Journal*, 808(1):95, Jul 2015.
- [227] Jounghun Lee, Suk Kim, and Soo-Chang Rey. A New Dynamical Mass Measurement for the VIRGO Cluster Using the Radial Velocity Profile of the Filament Galaxies. *The Astrophysical Journal*, 807:122, July 2015.
- [228] P. Fouqué, J. M. Solanes, T. Sanchis, and C. Balkowski. Structure, mass and distance of the Virgo cluster from a Tolman-Bondi model. *Astronomy and Astrophysics*, 375:770–780, September 2001.

- [229] Jeffrey M. Kubo, Albert Stebbins, James Annis, Ian P. Dell’Antonio, Huan Lin, Hossein Khiabani, and Joshua A. Frieman. The Mass of the Coma Cluster from Weak Lensing in the Sloan Digital Sky Survey. *The Astrophysical Journal*, 671:1466–1470, December 2007.
- [230] Bjarne Thomsen, William A. Baum, Mark Hammergren, and Guy Worthey. The Distance to the Coma Cluster from Surface Brightness Fluctuations. *The Astrophysical Journal*, 483:L37–L40, July 1997.
- [231] Planck Collaboration XXVI. Planck 2015 results. XXVI. The Second Planck Catalogue of Compact Sources. *Astronomy and Astrophysics*, 594:A26, Sep 2016.
- [232] Planck Collaboration IV. Planck 2018 results. IV. Diffuse component separation. *arXiv e-prints*, page arXiv:1807.06208, Jul 2018.
- [233] E. Battaner and E. Florido. The Rotation Curve of Spiral Galaxies and its Cosmological Implications. *Fundamental Cosmic Physics*, 21:1–154, Jan 2000.
- [234] S Brundobler and Veit Elser. S-matrix for generalized landau-zener problem. *Journal of Physics A: Mathematical and General*, 26(5):1211, 1993.
- [235] Joshua W. Foster, Yonatan Kahn, Oscar Macias, Zhiquan Sun, Ralph P. Eatough, Vladislav I. Kondratiev, Wendy M. Peters, Christoph Weniger, and Benjamin R. Safdi. Green Bank and Effelsberg Radio Telescope Searches for Axion Dark Matter Conversion in Neutron Star Magnetospheres. *Phys. Rev. Lett.*, 125(17):171301, 2020.
- [236] Jeremy Darling. New Limits on Axionic Dark Matter from the Magnetar PSR J1745-2900. *Astrophys. J. Lett.*, 900(2):L28, 2020.

- [237] Jeremy Darling. Search for Axionic Dark Matter Using the Magnetar PSR J1745-2900. *Phys. Rev. Lett.*, 125(12):121103, 2020.
- [238] D. B. Melrose and R. Yuen. Pulsar Electrodynamics: an unsolved problem. *J. Plasma Phys.*, 82(2):635820202, 2016.
- [239] A. V. Gurevich, V. S. Beskin, and Y. N. Istomin. *Physics of the Pulsar Magnetosphere*. Cambridge University Press (November 23, 2006), November 2006.
- [240] Georg Raffelt and Leo Stodolsky. Mixing of the Photon with Low Mass Particles. *Phys. Rev.*, D37:1237, 1988.
- [241] Tomislav Prokopec, Michael G. Schmidt, and Steffen Weinstock. Transport equations for chiral fermions to order \hbar and electroweak baryogenesis. Part 1. *Annals Phys.*, 314:208–265, 2004.
- [242] Bjorn Garbrecht, Tomislav Prokopec, and Michael G. Schmidt. Particle number in kinetic theory. *Eur. Phys. J.*, C38:135–143, 2004.
- [243] Tzee-Ke Kuo and James T. Pantaleone. Neutrino Oscillations in Matter. *Rev. Mod. Phys.*, 61:937, 1989.
- [244] P. Goldreich and W. H. Julian. Pulsar Electrodynamics. *The Astrophysical Journal*, 157:869, August 1969.
- [245] Alexander A. Philippov, Anatoly Spitkovsky, and Benoit Cerutti. Ab-initio pulsar magnetosphere: three-dimensional particle-in-cell simulations of oblique pulsars. *Astrophys. J.*, 801(1):L19, 2015.

- [246] Constantinos Kalapotharakos, Gabriele Brambilla, Andrey Timokhin, Alice K. Harding, and Demosthenes Kazanas. Three-dimensional Kinetic Pulsar Magnetosphere Models: Connecting to Gamma-Ray Observations. *Astrophys. J.*, 857(1):44, 2018.
- [247] Frederic H. Vincent et al. Accurate Ray-tracing of Realistic Neutron Star Atmospheres for Constraining Their Parameters. *Astrophys. J.*, 855(2):116, 2018.
- [248] Dimitrios Psaltis and Tim Johannsen. A Ray-Tracing Algorithm for Spinning Compact Object Spacetimes with Arbitrary Quadrupole Moments. I. Quasi-Kerr Black Holes. *Astrophys. J.*, 745:1, 2012.
- [249] Tim Johannsen and Dimitrios Psaltis. Testing the No-Hair Theorem with Observations in the Electromagnetic Spectrum: II. Black-Hole Images. *Astrophys. J.*, 718:446–454, 2010.
- [250] Adam Rogers. Frequency-dependent effects of gravitational lensing within plasma. *Mon. Not. Roy. Astron. Soc.*, 451(1):17–25, 2015.
- [251] Steven Weinberg. Eikonal method in magnetohydrodynamics. *Phys. Rev.*, 126:1899–1909, Jun 1962.
- [252] Jamie I. McDonald and Luís B. Ventura. Bending of light in axion backgrounds. 8 2020.
- [253] Jamie I. McDonald and Luís B. Ventura. Optical properties of dynamical axion backgrounds. *Phys. Rev. D*, 101(12):123503, 2020.
- [254] R. A. Battye, B. Garbrecht, J. McDonald, and S. Srinivasan. Radio line properties of axion dark matter conversion in neutron stars. *Journal of High Energy Physics*, 2021(9):105, September 2021.

- [255] J. P. McMullin, B. Waters, D. Schiebel, W. Young, and K. Golap. volume 376 of *Astronomical Society of the Pacific Conference Series*, page 127. 2007.
- [256] Samuel J. Witte, Dion Noordhuis, Thomas D. P. Edwards, and Christoph Weniger. Axion-photon conversion in neutron star magnetospheres: The role of the plasma in the Goldreich-Julian model. *Phys. Rev. D*, 104(10):103030, November 2021.
- [257] Alexander J. Millar, Sebastian Baum, Matthew Lawson, and M. C. David Marsh. Axion-photon conversion in strongly magnetised plasmas. *arXiv e-prints*, page arXiv:2107.07399, July 2021.
- [258] R.A. Battye, B. Garbrecht, J.I. McDonald, F. Pace, and S. Srinivasan. Dark matter axion detection in the radio/mm waveband. *Physical Review D*, 102(2), Jul 2020.
- [259] R. A. Battye, J. Darling, J. I. McDonald, and S. Srinivasan. Towards robust constraints on axion dark matter using PSR J1745-2900. *Phys. Rev. D*, 105(2):L021305, January 2022.
- [260] Joshua W. Foster, Samuel J. Witte, Matthew Lawson, Tim Linden, Vishal Gajjar, Christoph Weniger, and Benjamin R. Safdi. Extraterrestrial Axion Search with the Breakthrough Listen Galactic Center Survey. *arXiv e-prints*, page arXiv:2202.08274, February 2022.
- [261] R. Belvedere, Jorge A. Rueda, and R. Ruffini. ON THE MAGNETIC FIELD OF PULSARS WITH REALISTIC NEUTRON STAR CONFIGURATIONS. *The Astrophysical Journal*, 799(1):23, jan 2015.

- [262] Íñigo Zubeldia, Aditya Rotti, Jens Chluba, and Richard Battye. Understanding matched filters for precision cosmology. *Monthly Notices of the Royal Astronomical Society*, 507(4):4852–4863, November 2021.
- [263] R. N. Manchester, G. Hobbs, M. Bailes, W. A. Coles, W. van Straten, M. J. Keith, R. M. Shannon, N. D. R. Bhat, A. Brown, S. G. Burke-Spolaor, D. J. Champion, A. Chaudhary, R. T. Edwards, G. Hampson, A. W. Hotan, A. Jameson, F. A. Jenet, M. J. Kesteven, J. Khoo, J. Kocz, K. Maciesiak, S. Osłowski, V. Ravi, J. R. Reynolds, J. M. Sarkissian, J. P. W. Verbiest, Z. L. Wen, W. E. Wilson, D. Yardley, W. M. Yan, and X. P. You. The Parkes Pulsar Timing Array Project. *Publications of the Astronomical Society of Australia*, 30:e017, January 2013.
- [264] A. W. Hotan, W. van Straten, and R. N. Manchester. PSRCHIVE and PSRFITS: An Open Approach to Radio Pulsar Data Storage and Analysis. *Publications of the Astronomical Society of Australia*, 21(3):302–309, January 2004.
- [265] Michael John Keith, Iuliana C. Nițu, and Yang Liu. run_enterprise, January 2022.
- [266] Justin A. Ellis, Michele Vallisneri, Stephen R. Taylor, and Paul T. Baker. ENTERPRISE: Enhanced Numerical Toolbox Enabling a Robust Pulsar Inference Suite, September 2020.
- [267] G. B. Hobbs, R. T. Edwards, and R. N. Manchester. TEMPO2, a new pulsar-timing package - I. An overview. *Monthly Notices of the Royal Astronomical Society*, 369(2):655–672, June 2006.
- [268] V. Morello, E. D. Barr, S. Cooper, M. Bailes, S. Bates, N. D. R. Bhat, M. Burgay, S. Burke-Spolaor, A. D. Cameron, D. J. Champion, R. P.

- Eatough, C. M. L. Flynn, A. Jameson, S. Johnston, M. J. Keith, E. F. Keane, M. Kramer, L. Levin, C. Ng, E. Petroff, A. Possenti, B. W. Stappers, W. van Straten, and C. Tiburzi. The High Time Resolution Universe survey - XIV. Discovery of 23 pulsars through GPU-accelerated reprocessing. *Monthly Notices of the Royal Astronomical Society*, 483(3):3673–3685, March 2019.
- [269] F. Jankowski, W. van Straten, E. F. Keane, M. Bailes, E. D. Barr, S. Johnston, and M. Kerr. Spectral properties of 441 radio pulsars. *Monthly Notices of the Royal Astronomical Society*, 473(4):4436–4458, February 2018.
- [270] Andrew Lyne and Francis Graham-Smith. *Pulsar Astronomy*. 2012.
- [271] Simon Johnston and Matthew Kerr. Polarimetry of 600 pulsars from observations at 1.4 GHz with the Parkes radio telescope. *Monthly Notices of the Royal Astronomical Society*, 474(4):4629–4636, March 2018.
- [272] D. R. Lorimer and M. Kramer. *Handbook of Pulsar Astronomy*. 2012.
- [273] J. Gil, P. Gronkowski, and W. Rudnicki. Geometry of the emission region of PSR 0950+08. *Astronomy and Astrophysics*, 132:312–316, March 1984.
- [274] S. C. Rookyard, P. Weltevrede, and S. Johnston. Constraints on viewing geometries from radio observations of γ -ray-loud pulsars using a novel method. *Monthly Notices of the Royal Astronomical Society*, 446(4):3367–3388, February 2015.
- [275] X. Song, P. Weltevrede, M. J. Keith, S. Johnston, A. Karastergiou, M. Bailes, E. D. Barr, S. Buchner, M. Geyer, B. V. Hugo, A. Jameson, A. Parthasarathy, D. J. Reardon, M. Serylak, R. M. Shannon, R. Spiewak,

- W. van Straten, and V. Venkatraman Krishnan. The Thousand-Pulsar-Array programme on MeerKAT - II. Observing strategy for pulsar monitoring with subarrays. *Monthly Notices of the Royal Astronomical Society*, 505(3):4456–4467, August 2021.
- [276] Simon Johnston and A. Karastergiou. The period-width relationship for radio pulsars revisited. *Monthly Notices of the Royal Astronomical Society*, 485(1):640–647, May 2019.
- [277] Aris Karastergiou and Simon Johnston. An empirical model for the beams of radio pulsars. *Monthly Notices of the Royal Astronomical Society*, 380(4):1678–1684, October 2007.
- [278] A. Zucca, L. Pogosian, A. Silvestri, and G. B. Zhao. MGCAMB with massive neutrinos and dynamical dark energy. *Journal of Cosmology and Astroparticle Physics*, 2019(5):001, May 2019.
- [279] J. Bicak and P. Hadrava. General-relativistic radiative transfer theory in refractive and dispersive media. *Astronomy and Astrophysics*, 44(2):389–399, November 1975.

.1 Convergence Tests for Simulations

We now show that we have achieved the same level of convergence in our modified gravity simulations. In the left panel of fig. 1, we compute the ratio of the matter spectrum from Λ CDM simulations with respect to our highest resolution reference simulation, increasing the particle in steps. The green line denotes the k value at which the second-highest resolution simulation (512^3 particles) disagrees with our highest resolution (1024^3 particles) simulation, which is an indicator of the scale up to which our results are reliable. In the right panel, we show the convergence of our modified gravity simulations by plotting a ratio of ratios. We evaluate the ratio of matter power spectra from the simulation with 512^3 particles with the simulation with 1024^3 particles in both our Λ CDM simulations as well as our modified gravity simulations. We then plot S_{512}/S_{1024} , and show that they agree up to the same wavenumber as the left-hand-side panel, again shown by the green line. The fact that the vertical green line is at an identical wavenumber on both our panels demonstrates that we have achieved convergence for both our Λ CDM simulations as well as our modified gravity simulations. Therefore, we show that our simulations in are insensitive to realisation-dependent effects in the model parameters up to a wavenumber $k \sim 5 h \text{ Mpc}^{-1}$ that was validated by convergence tests as shown in fig. 1.

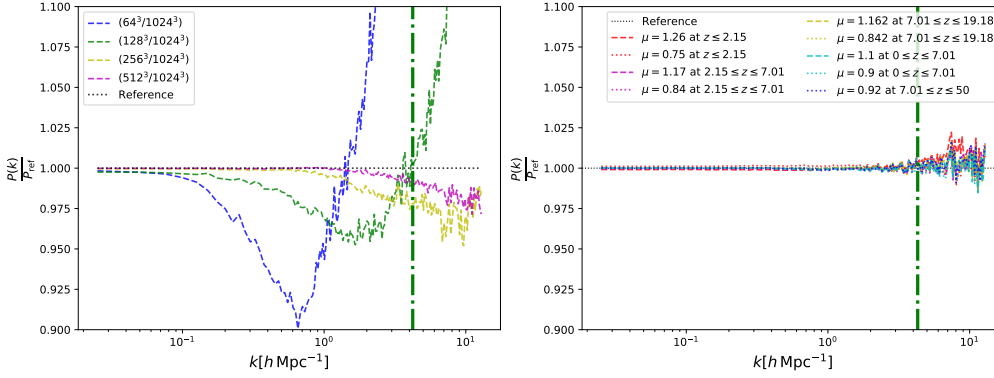


Figure 1: *Left panel:* The ratio of the power spectra as a function of scale, with each line labelled by the particle number of the simulation they represent. All simulations have a box size of $250 \text{ Mpc } h^{-1}$ comoving. The green vertical line represents the wavelength at which the ratio of the power spectra deviates at the level of 1% from the simulations with the best resolution. This panel shows the level of convergence we obtain in our Λ CDM simulations. *Right panel:* A similar procedure was carried out for the modified gravity simulations, but with a key difference. For each simulation, we calculate the ratio $S(k)$ of the power spectrum from the simulation to the power spectrum from the Λ CDM simulation. We then plot the ratio of $S(k)$ computed from simulations with 512^3 particles to simulations with 1024^3 particles. The green vertical line is plotted at the identical point as before. Therefore, we show that our modified gravity simulations have similar convergence both with respect to each other as well as with respect to our Λ CDM simulations. Note that on linear scales, all the ratios are within 0.5% of 1, which justifies our choice of μ in each bin. For our production simulations, we use a particle number of 1024^3 (with an equally fine mesh) and a box size of $250 \text{ Mpc } h^{-1}$.

.2 Linear growth and smoothing

.2.1 The Linear Growth Factor

In the case where we have 2 redshift bins for μ , we have that $D^{\Lambda\text{CDM}}(z_1)/D^{\Lambda\text{CDM}}(z_2) = D^{\Lambda\text{CDM}}(z_2)/D^{\Lambda\text{CDM}}(z_3)$. Setting $z_1 = 0$ and $z_3 = 50$, we obtain

$$D(z_2)^2 = D(z_1)D(z_3), \quad (1)$$

from which we can compute $z_2 \approx 7.01$. We follow a similar procedure in the case where we have 4 bins in redshift. We consider the bin $0 \leq z \leq 7.01$ as our reference in the context of choosing the value of μ . We set $\mu = 1.1$ and 0.9 , in this bin, respectively, and compute $D(0)$. For all the other bins, we choose μ such that the growth factor at $z = 0$ is identical to the value we computed for our reference bin. In this way, we obtain the μ values in table 2.1. In order to confirm that these values of μ indeed correspond to identical growth factors at $z = 0$, we implemented our time-dependent formalism into the Boltzmann solver **CLASS** as described in [278]. In fig. 2 we show that the relative differences in the linear power spectra for all the cases in table 2.1 are within 0.5%, in accordance with the right panel in fig. 1, which shows that our modified **CLASS** code performs as expected. Therefore, we run two sets of seven simulations in which $\mu \neq 1$ in one, two or four redshift bins, with the matter power spectrum measured from all the simulations being equal on linear scales at $z = 0$.

This allows an additional consistency check for our simulations, since the matter power spectrum at $z = 0$ for all our simulations should differ from the standard ΛCDM result by a factor $[D(z)]^2$.

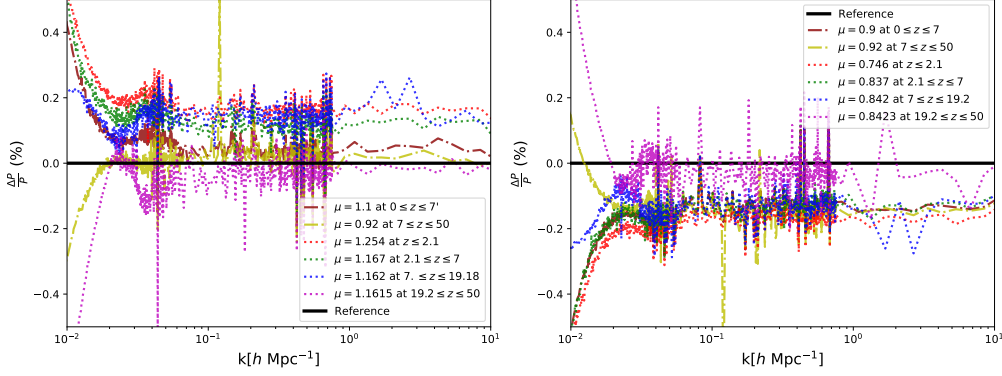


Figure 2: The relative difference in the linear power spectra at redshift zero to the reference case (chosen to be the case where μ is constant) from runs of our modified CLASS code.

.2.2 Smoothing bin-transitions

As mentioned in 2, we implement smoothing between μ values in our redshift bins, in order to test if the width of the transition between different values of μ affects our results. We assume that the input to the code includes an array of values for μ as well as an array of redshifts that denote the bins. We then use a combination of two error functions given by

$$E_1 = C_1 \text{erf}((z_{\text{array}}[i] - z)/X) + C_2, \quad (2)$$

$$E_2 = C_1 \text{erf}(-(z_{\text{array}}[i+1] - z)/X) + C_2, \quad (3)$$

where C_1 , C_2 and X are parameters that determine the amplitude, midpoint and width of the error function, respectively, to determine μ at each redshift. The iterative variable i is incremented once the current redshift (associated to the timestep in the code) is lower than the midpoint of the current bin, i.e., when $z < (z_{\text{array}}[i+1] + z_{\text{array}}[i])/2$. The constants C_1 and C_2 are given by

$$C_1 = \mu_{\text{array}}[i+1] - \mu_{\text{array}}[i]/2, \quad (4)$$

$$C_2 = \mu_{\text{array}}[i+1] + \mu_{\text{array}}[i]/2, \quad (5)$$

The value of μ is given by

$$\mu = E_1 \text{ if } z > z_{\text{array}}[i+1] - z[i]/2, \quad (6)$$

$$\mu = E_2 \text{ if } z < z_{\text{array}}[i+1] - z[i]/2. \quad (7)$$

We have chosen the width function $X = (1/A) \ln(\Delta z_{\text{bin}})$ with A being a tolerance parameter that determines the width of the transition and Δz_{bin} is the bin-width. This choice ensures that the width of the transition naturally becomes shorter at lower redshifts where the growth factor is more sensitive to redshift (where the timestep in the code is small).

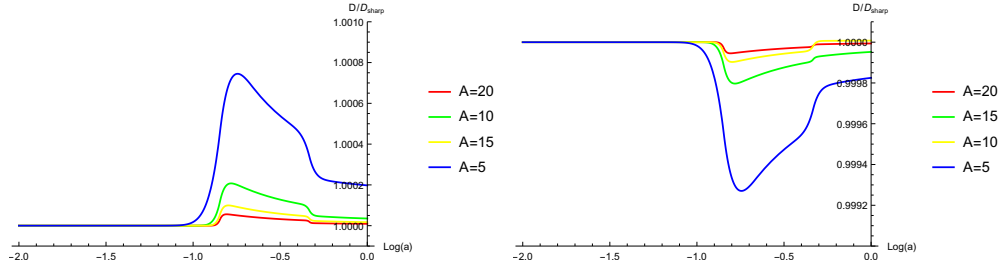


Figure 3: The plot of the growth factor as a function of redshift in the case where $\mu > 1$ (left) and $\mu < 1$ (right) at $2.15 \leq z \leq 7.01$.

.3 Covariant radiative transport in plasmas

The specific intensity at the point of emission can then be related to that at detection by using the property

$$\frac{I}{n^2\omega^3} = \text{constant}, \quad (8)$$

along rays where n is the refractive index. Hence we have the following relation

$$\frac{I_{\text{obs}}}{n_{\text{obs}}^2\omega_{\text{obs}}^3} = \frac{I_{\text{em}}}{n_{\text{em}}^2\omega_{\text{em}}^3}, \quad (9)$$

where n_{em} and n_{obs} and ω_{em} and ω_{obs} etc. are measured in a coordinate system at rest with respect to the star. Combining this relation together with the definition

$$I_{\text{em}}(\mathbf{x}_{\text{em}}, \mathbf{v}_{\text{em}}^a) = \frac{1}{4\pi} m_a v_{\text{em}}^a \rho_{\text{DM}}(\mathbf{x}_{\text{em}}) P_{a \rightarrow \gamma}(\mathbf{x}_{\text{em}}, \mathbf{v}_{\text{em}}^a), \quad (10)$$

for the intensity at emission and using the fact that far from the star $n_{\text{obs}} \simeq 1$ we arrive at

$$F = \frac{1}{D^2} \sum_i \frac{(\Delta b)^2}{(n_{\text{em}}^i)^2} \tilde{f}(r_{\text{em}}, r_s) \frac{\rho_{\text{DM}}(\mathbf{x}_{\text{em}}^i) v_{\text{em}}^a P_{a \rightarrow \gamma}}{4\pi}, \quad (11)$$

We now derive the relation (9). By definition, the phase space distribution for photons satisfies

$$\mathcal{F}(x^i, k^i) = \frac{dN}{d\mathcal{V}} = \frac{dN}{d^3\mathbf{x}d^3\mathbf{k}}. \quad (12)$$

where dN is the number of photons in the phase space volume $d^3\mathbf{x}d^3\mathbf{k}$. Formally, one must define phase space using a local coordinate system, since the background

is inhomogeneous [279]. The infinitesimal energy carried by photons frequency $\omega = \omega(\mathbf{k})$ is then given by $dE_\omega = \omega dN$. Using the expression (12) for dN , we arrive at

$$dE_\omega = \omega \mathcal{F}(x^i, p^i) d^3\mathbf{k} d^3\mathbf{x}, \quad (13)$$

We now re-write the momentum phase space element in terms of the refractive index

$$n = k/\omega, \quad k = |\mathbf{k}|. \quad (14)$$

Firstly we change to spherical coordinates

$$d^3\mathbf{k} = k^2 dk d\Omega(\hat{\mathbf{k}}), \quad (15)$$

where $d\Omega(\hat{\mathbf{k}}) = \sin\theta_{\mathbf{k}} d\theta_{\mathbf{k}} d\varphi_{\mathbf{k}}$ is the solid angle element in momentum space, defined with respect to some axis. Next we write dk in terms of the refractive index by using

$$dk = d(n\omega) = d\omega \left[n + \omega \frac{dn}{d\omega} \right]. \quad (16)$$

The final term can be re-written in terms of the group velocity

$$v_g = \left[n + \omega \frac{dn}{d\omega} \right]^{-1}. \quad (17)$$

Putting this together and combining eqs. (13)-(17) we can re-write the momentum volume element as

$$d^3\mathbf{k} = \frac{n^2 \omega^2}{v_g} d\omega d\Omega(\hat{\mathbf{k}}). \quad (18)$$

This leads immediately to

$$dE_\omega = \frac{\omega^3 n^2}{v_g} \mathcal{F}(x^i, k^i) d\omega d\Omega(\hat{\mathbf{k}}) d^3\mathbf{x}. \quad (19)$$

Finally, we invoke *Liouville's theorem*, which states that by definition, the phase space density \mathcal{F} is conserved along geodesics of Hamilton's equations. Hence we have

$$\frac{d}{d\lambda} \mathcal{F}(x(\lambda), k(\lambda)) = 0, \quad (20)$$

where λ is the wordline parameter and $x(\lambda), k(\lambda)$ satisfy eqs. (5.53) and (5.54).

To understand the power flow through a surface perpendicular to the wordlines, we introduce coordinates

$$\mathbf{x} = (x_\perp^1, x_\perp^2, x_\parallel), \quad (21)$$

where x_\perp^1, x_\perp^2 lie in the plane perpendicular to the direction of propagation, corresponding to x_\parallel . The surface area element $dA = dx_\perp^1 dx_\perp^2$. If the group velocity along the worldline is v_g , then we have $dx_\parallel = v_g dt$. In this coordinate system, the spatial volume element then becomes

$$d^3\mathbf{x} \rightarrow v_g dA dt. \quad (22)$$

Hence in these coordinates, eq. (19) reads

$$dE_\omega = \frac{\omega^3 n^2}{v_g} \mathcal{F}(x^i, k^i) d\omega d\Omega(\hat{\mathbf{k}}) dA dt. \quad (23)$$

This allows one to connect the distribution function \mathcal{F} to the Poynting flux which

is the energy per unit time per unit area:

$$|\mathbf{S}| = \frac{dE}{dA dt}, \quad (24)$$

The specific intensity is then defined as

$$I = \left| \frac{d\mathbf{S}}{d\Omega d\omega} \right|, \quad (25)$$

where $d\Omega$ gives the solid angle in the direction of propagation. On comparing eq. (13) with (25), one obtains that

$$\mathcal{F} = \frac{I}{n^2 \omega^3}, \quad (26)$$

and hence from eq. (20) conservation of \mathcal{F} along worldlines implies that

$$\frac{I}{n^2 \omega^3} = \text{constant}, \quad (27)$$

along light rays. Hence we have the following relation between quantities at the point of emission on the critical surface, and points in the image plane:

$$\frac{I_{\text{obs}}}{n_{\text{obs}}^2 \omega_{\text{obs}}^3} = \frac{I_{\text{em}}}{n_{\text{em}}^2 \omega_{\text{em}}^3}, \quad (28)$$

where ω_{obs} and ω_{em} etc. are measured in fixed (i.e. accelerated rather than freely falling) frames.